



Nanoparticles of lanthanide and transition metal oxysulfides : from colloidal synthesis to structure, surface, optical and magnetic properties

Clément Larquet

► To cite this version:

Clément Larquet. Nanoparticles of lanthanide and transition metal oxysulfides : from colloidal synthesis to structure, surface, optical and magnetic properties. Material chemistry. Sorbonne Université, 2018. English. NNT : 2018SORUS432 . tel-02950055

HAL Id: tel-02950055

<https://theses.hal.science/tel-02950055>

Submitted on 27 Sep 2020

HAL is a multi-disciplinary open access archive for the deposit and dissemination of scientific research documents, whether they are published or not. The documents may come from teaching and research institutions in France or abroad, or from public or private research centers.

L'archive ouverte pluridisciplinaire **HAL**, est destinée au dépôt et à la diffusion de documents scientifiques de niveau recherche, publiés ou non, émanant des établissements d'enseignement et de recherche français ou étrangers, des laboratoires publics ou privés.

Sorbonne Université

Ecole doctorale 397 : Physique et chimie des matériaux

Laboratoire de Chimie de la Matière Condensée de Paris (LCMCP)

Institut de Minéralogie, de Physique des Matériaux et de Cosmochimie (IMPMC)

Nanoparticles of lanthanide and transition metal oxysulfides: from colloidal synthesis to structure, surface, optical and magnetic properties

Par M. Clément Larquet

Thèse de doctorat de Sorbonne Université

Dirigée par Clément Sanchez et Andrea Gauzzi

Présentée et soutenue publiquement le 25 septembre 2018

Devant un jury composé de :

Mme. Elsje Alessandra Quadrelli	Directrice de recherches - CPE Lyon	Rapporteur
M. Stéphane Jobic	Directeur de recherches - IEMN	Rapporteur
Mme. Catherine Louis	Directrice de recherches - SU	Examinatrice
Mme. Asma Tougeri	Chargée de recherches – Univ. Lille	Examinatrice
M. Patrick Maestro	Directeur scientifique - Solvay	Examineur
Mme. Sophie Carencó	Chargée de recherches - SU	Encadrant principal
M. Andrea Gauzzi	Professeur - SU	Directeur de thèse
M. Clément Sanchez	Professeur - Collège de France	Directeur de thèse

Introduction

Among the various combinations of metal with chalcogens, the association of a metal with oxygen and sulfur anions is peculiar. It was given the name of metal oxysulfide. Because these two anions present dissimilar sizes and electronic properties, associating them with a metal in a single compound is a synthetic challenge. Notably, metal oxysulfides are scarcer in nature than their oxide or sulfide cousins despite the abundance of the two chalcogens.

From a synthetic point of view, even if the first oxysulfides were described in the XIXth century, their preparation was developed only at the beginning of the 1950's with the advent of the first lanthanide- and actinide-based chalcogenides.

Remarkably, the *d*-block transition metal oxysulfides are rarely involved in monometallic oxysulfide compounds. However, the formation of bimetallic oxysulfides enriched the number of elements that could crystallize in oxysulfide structures. Since 1967, bimetallic oxysulfides are regularly reported and more complex compositions (quinary oxysulfides and more) started to emerge at the beginning of the 1980's.

Since 2000, the hype for nanoparticles has reached the oxysulfides. Twenty years later, $\text{Ln}_2\text{O}_2\text{S}$ crystalline phase and the other oxysulfides are now studied within two segregated chemists communities. Great efforts were made on the development of various syntheses of $\text{Ln}_2\text{O}_2\text{S}$ nanoparticles whose applications in luminescence are diverse and were previously identified in the bulk phases. On the contrary, few works on other nanoscaled oxysulfides were reported in the same period.

In the Laboratory of the Chemistry of Condensed Matter of Paris (LCMCP) was noted that lanthanide oxysulfide nanoparticles were almost exclusively studied for luminescence despite their intriguing bichalcogenide nature. At the beginning of the project, the works of Ishikawa *et al.* on the photocatalytic properties of $\text{Sm}_2\text{Ti}_2\text{S}_2\text{O}_5$ and He *et al.* on the magnetic properties of $\text{Eu}_{2-x}\text{O}_2\text{S}$ nanoparticles were already reported since a few years. Building from the know-how the LCMCP developed on the synthesis of complex nanostructures, collaboration started with the Institute of Mineralogy, Physics of Materials and Cosmochemistry (IMPMC) whose expertise on the electronic, optical and magnetic properties of complex materials was extremely valuable and complementary.

The strategy of the project was first to acquire some know-how from the $\text{Ln}_2\text{O}_2\text{S}$ nanoparticles synthesis and then switch to the *d*-block oxysulfide nanoparticles, for which novel structures and properties were expected. We did not expect that lanthanide oxysulfide nanoparticles would be such a complex and surprising system despite the dozens of reported works on the subject.

Following this strategy, the manuscript is divided in two independent parts. The first one is dedicated to the lanthanide oxysulfide nanoparticles. We will see from a detailed bibliographic study that the synthesis of $\text{Ln}_2\text{O}_2\text{S}$ nanoparticles is now well controlled both in aqueous and organic solvents, with various morphologies, surfaces, and applications (Chapter I). Then, the challenging case of cerium oxysulfide nanoparticles is handled (Chapter II). For the first time, unsupported $\text{Ce}_2\text{O}_2\text{S}$ nanoparticles are obtained *via* a colloidal synthesis in organic surfactants, using $\text{Ce}(\text{acac})_3$, elemental sulfur and a sodium complex. The peculiar reactivity of the entire series of the oxysulfide solid solution of $(\text{Gd,Ce})_2\text{O}_2\text{S}$ nanoparticles is evaluated with *in situ* X-ray absorption near edge spectroscopy (XANES) and near ambient pressure X-ray photoemission spectroscopy (NAP-XPS). Following this work, an investigation on the structure and the surface of the $\text{Ln}_2\text{O}_2\text{S}$ nano-objects is conducted through the case study of $\text{Gd}_2\text{O}_2\text{S}$ (Chapter III). The sulfur amount, the ligands quantity and coordination mode, the sodium localization and role in the synthesis are discussed, leading to a more precise vision of the final nanoparticles contradictory on several points with previous works on the subject. Also, the study of colloidal solution samples during the nanoparticles nucleation and growth allow us to propose a detail formation mechanism for $\text{Ln}_2\text{O}_2\text{S}$ nanoparticles. This work on the description of the structure is a milestone for the quantification of the magnetic and optical properties of the $(\text{Gd,Ce})_2\text{O}_2\text{S}$ nanocrystals. The electronic properties of cerium in the oxysulfide structure leads to significant evolutions of these properties (Chapter IV).

In the second part, transition metal oxysulfides were investigated. The bibliographic study underlines the lack of monometallic structures and reviews the several syntheses of transition metal oxysulfides syntheses (Chapter V). An exploratory approach is conducted to reach monometallic and bimetallic oxysulfides with *d*-block transition metals at the nanoscale (Chapter VI). Confronted with mitigated results, a new strategy is developed to obtain at mild temperatures the concomitant oxidation and sulfidation of a metal (0) complex, leading to an unprecedented synthesis of amorphous nickel oxysulfide (Chapter VII).

Note: Part of this manuscript was written using the manuscripts of several journal articles (published, submitted or to be submitted) for which I wrote the first draft. Whenever an extract of an article was used, the corresponding sections are clearly delimited in the text. At the end of the manuscript, an experimental section references details on the various conducted syntheses and techniques throughout the project.

Now is the time to dive in the fascinating world of the metal oxysulfides.

Table of contents

Introduction	3
Table of contents	7
Part I: Lanthanide oxysulfide nanoparticles.....	9
Chapter I - Lanthanide oxysulfide syntheses: from bulk to nanoparticles	11
Chapter II - Synthesizing and storing $\text{Ln}_2\text{O}_2\text{S}$ nanoparticles: from $\text{Gd}_2\text{O}_2\text{S}$ to $\text{Ce}_2\text{O}_2\text{S}$.....	63
Chapter III - Unveiling the structure of $\text{Ln}_2\text{O}_2\text{S}$ nanoplates in high boiling point organic solvents with an alkaline source: $\text{Gd}_2\text{O}_2\text{S}$ as a case study.....	93
Chapter IV - Benefits of bimetallic composition: the tunable optical and magnetic properties of $\text{Gd}_{2(1-y)}\text{Ce}_{2y}\text{O}_2\text{S}$ nanoparticles	137
Part II: <i>d</i>-Block transition metal oxysulfide nanoparticles.....	159
Chapter V - The synthesis of bulk and nanoscaled transition metal oxysulfides: a burgeoning challenge.....	161
Chapter VI - Attempts at transposing $\text{Ln}_2\text{O}_2\text{S}$ synthesis to nanoscaled transition metal oxysulfides.....	195
Chapter VII - Towards nickel oxysulfide nanoparticles.....	217
Conclusion and perspectives.....	245
Experimental section	253

Part I

Lanthanide Oxysulfide

Nanoparticles

Chapter I

Lanthanide oxysulfide syntheses: from bulk to nanoparticles

Table of Content

I.1. Introduction.....	13
I.1.1. Definition	13
I.1.2. Discovery and first phases	13
I.1.3. Applications of bulk lanthanide oxysulfides.....	16
I.1.3.1. Screens	16
I.1.3.2. Laser: emission and absorption.....	17
I.1.3.3. Scintillators	18
I.1.3.4. Patents	19
I.2. Nanoscaled ternary lanthanide oxysulfides $\text{Ln}_2\text{O}_2\text{S}$	20
I.2.1. Introduction.....	20
I.2.1.1. Examples of oxysulfide nanoparticles applications	20
I.2.1.2. Synthetic strategies for lanthanide oxysulfide nanoparticles	23
I.2.2. Exotic syntheses.....	25
I.2.2.1. Boron-sulfur method.....	26
I.2.2.2. Combustion synthesis	26
I.2.2.3. N,S dual doped carbon supported $\text{Ce}_2\text{O}_2\text{S}$	27
I.2.2.4. Emulsion liquid membrane system (ELM).....	27
I.2.2.5. Synthesis in molten sodium chloride	28
I.2.2.6. Composite-hydroxide-mediated method.....	29

I.2.2.7. Electrospinning	30
I.2.2.8. Anodic aluminum oxide template	30
I.2.3. Water-based syntheses	30
I.2.3.1. Gelatin-templated synthesis	31
I.2.3.2. Sol-gel polymer thermolysis	32
I.2.3.3. Syntheses in water at atmospheric pressure	33
I.2.3.4. Aqueous reactions under autogenic pressure	42
I.2.3.5. Conclusion	46
I.2.4. Syntheses in organic medium	47
I.2.4.1. Decomposition of sulfur-containing single-source precursors	48
I.2.4.2. Syntheses with high boiling-point organic solvents at atmospheric pressure.....	52
I.2.4.3. Solvothermal syntheses in autoclave	55
I.2.3. Conclusion: selecting the best synthetic strategy.....	57
References	58

I.1. Introduction

Note: This chapter I is an excerpt from the following review titled “*Metal Oxysulfides: From Bulk Compounds to Nanomaterials*”, by Larquet, C. and Carencu, S. to be submitted soon.

I.1.1. Definition

A “metal oxysulfide” is a compound composed of at least a metal, oxygen and sulfur, with negative oxidation states (eg. –II) for both oxygen and sulfur. The generic formula for ternary oxysulfide is $M_xO_yS_z$. Due to its negative oxidation state, sulfur forms no bounds with oxygen in oxysulfides, in contrast with more common metal sulfates $M_x(S^{VI}O_4)_y$ where the sulfur is at oxidation state +IV.

In 1951, Eastman *et al.* recommended the following distinction:¹ $M_xO_yS_z$ compounds should be designed by the general term “oxide-sulfide” and named after the similarities of their crystalline structure with the corresponding oxide or sulfide. If the oxide-sulfide has the same crystalline structure than the oxide, it should be named “thio-oxide”; if its crystalline structure is the same than the sulfide, it should be called “oxy-sulfide” and if its structure is none of the two, it should be called “sulfoxide”.

However, in an article of 1958 published in French, Flahaut *et al.* questioned this nomenclature.² They argued that all the Ln_2O_2S (Ln = lanthanide) compounds crystallize in the same structure and showed similar chemical properties. With Eastman’s nomenclature, because Ln_2O_3 oxides crystallize in the two different structures Ce_2O_3 and Tl_2O_3 , the Ln_2O_2S compounds would have been named “thioxyde” (French word for thio-oxide) from lanthanum to praseodymium and “sulfoxyde” (sulfoxide) for the others.

Although the terms “thio-oxide” and “oxide-sulfide” are still present in the literature, “oxysulfide” is now employed in a large majority of the works to name any combination on one or several metals to oxygen and sulfur anions.

I.1.2. Discovery and first phases

Oxysulfides are scarce in nature and are the most often artificial (not found in nature). To the best of our knowledge, the first occurrence of an oxysulfide compound was reported in 1827 by Mosander, who was working on the sulfidation of Ce_2O_3 into Ce_2S_3 using H_2S . He noticed the presence of oxygen and sulfur combined with the metal in a single product, along with the formation of cerium sulfate. Later, Sterba in 1904³ and Biltz in 1908⁴ also reported this observation. Biltz even proposed the formula $Ce_2S_{2.5}O \cdot S$ as he identified remaining sulfur as

polysulfide on the final product. Without knowing it, Klemm *et al.* were probably the first to obtain a pure phase of $\text{Ln}_2\text{O}_2\text{S}$ by heating $\text{Er}(\text{SO}_4)_3$ in H_2S and consequently forming $\text{Er}_2\text{O}_2\text{S}$, which they only described as pale pink and resistant to other heating treatments in H_2S .⁵

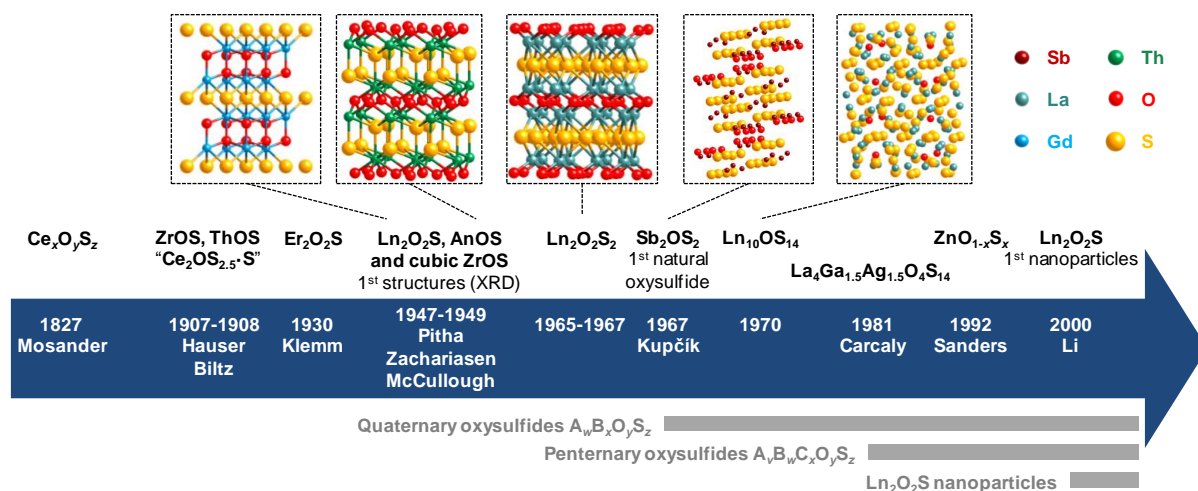


Figure 1: Key dates and authors of the oxysulfide research with some related structures. Ln stands for lanthanide and An for actinide. $\text{An}_2\text{O}_2\text{S}$ compounds are also known since 1949 ($\text{Pu}_2\text{O}_2\text{S}$) and possess the same structure as $\text{Ln}_2\text{O}_2\text{S}$.

The first crystalline oxysulfide structures were elucidated by Pitha in 1947 ($\text{La}_2\text{O}_2\text{S}$)⁶ and Zachariasen in 1949 ($\text{La}_2\text{O}_2\text{S}$, $\text{Ce}_2\text{O}_2\text{S}$ and $\text{Pu}_2\text{O}_2\text{S}$).⁷ Flahaut et al. indicated the enthalpy of formation of $\text{Ce}_2\text{O}_2\text{S}$ $\Delta H = -1800$ kJ/mol. The samples often contained impurities and were prepared either by reducing the corresponding sulfate $\text{Ln}_2(\text{SO}_4)_3$ using H_2 or by gently heating sesquisulfide compounds (Ln_2S_3) in air. The two authors noticed that the metal was coordinated to seven atoms: four atoms of oxygen and three atoms of sulfur. The $\text{Ln}_2\text{O}_2\text{S}$ structure derives from the hexagonal oxide Ln_2O_3 and crystallizes in the $P-3m1$ space group. This lamellar structure can be described as alternating sheets of $[\text{Ln}_2\text{O}_2]^{2+}$ and S^{2-} (Figure 2). Since this discovery, the entire series of lanthanide oxysulfide $\text{Ln}_2\text{O}_2\text{S}$ (except promethium) was prepared.²

In the 1960's and the 1970's, more $\text{M}_2\text{O}_2\text{S}$ compounds were also reported. The work on radioactive elements gave the actinide oxysulfides $\text{Np}_2\text{O}_2\text{S}$,⁸ $\text{Am}_2\text{O}_2\text{S}$,⁹ $\text{Cm}_2\text{O}_2\text{S}$,⁹ $\text{Bk}_2\text{O}_2\text{S}$ ⁹ and $\text{Cf}_2\text{O}_2\text{S}$.¹⁰ Similarly to $\text{Ln}_2\text{O}_2\text{S}$ compounds, $\text{An}_2\text{O}_2\text{S}$ (An = actinide) materials crystallize in the $P-3m1$ space group. On the contrary, $\text{Sc}_2\text{O}_2\text{S}$ crystallizes in the hexagonal $P6_3/mmc$ space group. Its structure remains very close to $\text{Ln}_2\text{O}_2\text{S}$ with a coordination of seven for scandium atoms and a structure based on alternative layers of $[\text{Sc}_2\text{O}_2]^{2+}$ and S^{2-} .¹¹ In 1949, Zachariasen described the structure of tetravalent actinide oxysulfides ThOS , UOS and NpOS as presenting a PbFCl structure type with tetragonal symmetry in $P4/nmm$ space group.

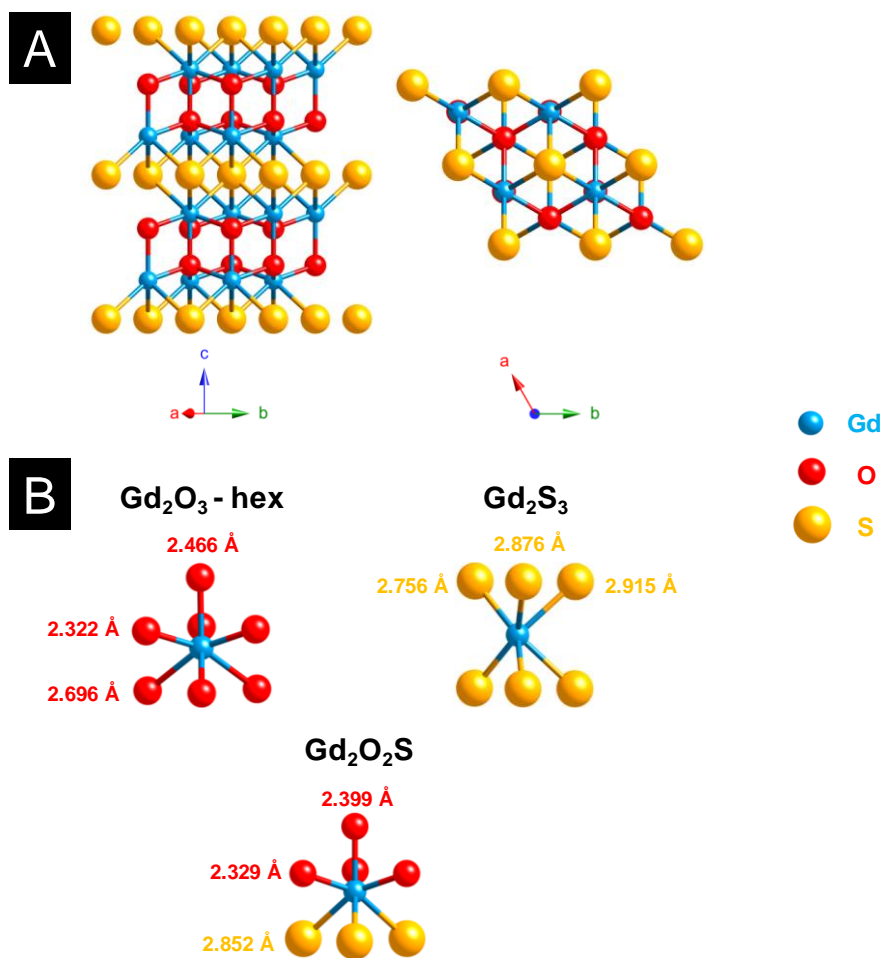


Figure 2: (A) $\text{Ln}_2\text{O}_2\text{S}$ structure: a hexagonal layered structure ($\text{Ln} = \text{Gd}$). (B) Lanthanide environment in hexagonal lanthanide oxide Ln_2O_3 (JCPDS 02-1878), lanthanide sesquisulfide Ln_2S_3 (JCPDS 03-2364) and lanthanide oxysulfide $\text{Ln}_2\text{O}_2\text{S}$ (JCPDS 06-8819) with the example of gadolinium.

A few years later, Khodadad *et al.* and Ballestracci demonstrated the existence of several $\text{Ln}_2\text{O}_2\text{S}_2$ compounds ($\text{Ln} = \text{La}$, Pr and Nd), where the disulfide $[\text{S}_2]^{2-}$ anion is present.^{12–14} They have to be distinguished from AnOS ($\text{An} = \text{actinide}$) compounds in which the actinide is at the +IV oxidation state while the lanthanide in $\text{Ln}_2\text{O}_2\text{S}_2$ remains at the +III oxidation state.

Oxydisulfides M_2OS_2 were also synthetically obtained for lanthanide compounds Ln_2OS_2 ($\text{Ln} = \text{Sm}$,¹⁵ Gd ,¹⁶ Tb ,¹⁷ Dy ,¹⁸ Er ,¹⁹ Tm ,¹⁹ Yb ,¹⁹ Y^{20}). The erbium, thulium and ytterbium compounds were obtained at 10 kbar and 1600 °C.

A sulfur-rich phase was also discovered by trying to solve the crystalline structure of what was thought to be $\beta\text{-Ln}_2\text{S}_3$. It happened to be $\text{Ln}_{10}\text{OS}_{14}$ ($\text{Ln} = \text{La}$, Ce , Pr , Nd , Sm) that formed because of traces of water or oxygen during the reaction.^{21,22} Besançon *et al.* showed that the oxygen content of $\text{Ln}_{10}\text{S}_{14}\text{O}_x\text{S}_{1-x}$ can be lowered to a value close to 0.1 mol% for La , Ce and Pr .^{23,24} Later, Schleid *et al.* also reported the gadolinium compound $\text{Gd}_{10}\text{OS}_{14}$.²⁵

The work of Marcon with actinides led to the first description of more complex compounds, namely $M^{III}_2M^{IV}_2O_4S_3$ ($Pu_4O_4S_3$, $U_2Pu_2O_4S_3$, $U_2Gd_2O_4S_3$ and $Ce_4O_4S_3$), based on composition analysis.²⁶ He also completed the work of Zachariassen by obtaining $PuOS$.²⁶ In the same time, based on the work of Marcon, the compositions of cerium oxysulfides $Ce_4O_4S_3$ ^{27,28} and $Ce_6O_6S_4$ ²⁹ were confirmed and their structures were elucidated by X-Ray diffraction on monocrystals by Dugué *et al.* and Wichelhaus. $Ce_4O_4S_3$ and $Ce_6O_6S_4$ monocrystals were obtained by heating Ce_2O_2S and sulfur or CeO_2 , Ce_2S_3 and sulfur together. In the lanthanide series, only cerium allows both oxidation states +III and +IV. In $Ce^{III}_2O_2S$, partial oxidation of cerium led to $Ce^{III}_2Ce^{IV}_2O_4S_3$ and $Ce^{III}_4Ce^{IV}_2O_6S_4$.

I.1.3. Applications of bulk lanthanide oxysulfides

In the 1980's, potential applications in optics for doped Ln_2O_2S materials were identified and led to their use as lamps, lasers, scintillators, screens, etc. Often, Y_2O_2S , La_2O_2S or Gd_2O_2S are used as the lattice and doped with one or several lanthanide ions to obtain the desirable luminescence features. Also, electrochemical properties of transition metal oxysulfides were investigated for their use in lithium-ion batteries. A brief summary is given below on these applications.

I.1.3.1. Screens

Doped oxysulfides were primary employed in cathode ray tubes (CRTs) of television screens and later in computer monitors. In 1968, Royce patented a “family of new cathodoluminescent phosphors” by describing the potential use of doped Y_2O_2S and Gd_2O_2S .³⁰ Lutetium and lanthanum were also envisaged as efficient matrixes for the doping ions (mainly Sm^{III} or Eu^{III}).

Three classes of phosphors, respectively associated to red, blue and green, are necessary for a proper screen to emit the colors of the visible spectrum. Thanks to their good luminescence properties, lanthanide doping ions equip the main phosphors used for industrial applications.³¹ Red color is provided by Eu^{III} : $Y_2O_3:Eu$, $Y_2O_2S:Eu$, $YVO_4:Eu$, $Y_2(WO_4)_3:Eu$; blue emission is enabled by Eu^{II} in compounds such as: $Sr_5(PO_4)_3Cl:Eu$, $BaMgAl_{11}O_7:Eu$, $Sr_2Al_6O_{11}:Eu$; and green is emitted thanks to Tb^{III} : $CeMgAl_{11}O_{19}:Tb$, $(Ce,Gd)MgB_5O_{10}:Tb$, $(La,Ce)PO_4:Tb$, $Y_2SiO_5:Tb$, $Y_3Al_5O_{12}:Tb$.³² However, for CRTs, blue and green are preferentially obtained with $ZnS:Ag$ and $ZnS:(Cu,Au)$, respectively.

In current computer monitors, the amount of europium-doped yttrium oxysulfide $\text{Y}_2\text{O}_2\text{S:Eu}$ (0.73 wt% for Eu, 13.4 wt% for Y) used for red emission has become large enough to implement and develop the rare-earths recovery.³³

I.1.3.2. Laser: emission and absorption

I.1.3.2.1. Stimulated emission in lanthanum oxysulfide

The first study on metal oxysulfides as laser-emitting material was reported in the earliest years of the design of laser devices. “Laser” stands for light amplification by stimulated emission of radiation and is a general term for a device that emits light through a process of optical amplification based on the stimulated emission of electromagnetic radiation. It is characterized and differs from other light sources by the spatial and temporal coherences of the resulting light. Thus, there are countless applications of the laser devices. Two kinds of applications can be distinguished: information transfer (fiber-optic communication, length measurements, fingerprint detection, barcode scanner, thermometers, laser pointers, weapon guidance...) and power transfer (cutting, welding, superficial fusion, marking materials...).

In 1971, while the most famous laser crystal, namely YAG:Nd (neodymium-doped yttrium aluminum garnet), had already been extensively studied, Alves *et al.* carried out the first experiments dealing with an oxysulfide-based laser.³⁴ They grew and studied millimetric $\text{La}_2\text{O}_2\text{S:Nd}$ crystals with many defects, but also estimated the properties of crystals with less imperfections. Similarly to YAG:Nd, the stimulated emission takes place between the $^4\text{F}_{3/2}$ and $^4\text{I}_{11/2}$ energy levels of the Nd^{III} ion in $\text{La}_2\text{O}_2\text{S:Nd}$ with an emission wavelength of 1075 nm (9300 cm^{-1}), while YAG:Nd emits at 1064 nm (9400 cm^{-1}).

In 1990, Markushev *et al.* presented preliminary results on the stimulation emission kinetics at the temperature of liquid nitrogen for 1 mol% of neodymium.³⁵ In 2012, the stimulated emission properties of $\text{La}_2\text{O}_2\text{S:Nd}$ were studied with oxysulfide powders.³⁶ In particular, Iparraguirre *et al.* estimated and experimentally investigated the influence of the doping ion concentration and pumping wavelengths on the different laser properties.³⁶

I.1.3.2.2. Laser absorption of samarium oxysulfide

The counterpart of laser emission is laser absorption. Because of the coherence of the emitted light, laser devices can be harmful for human skin or eyes. Protecting glasses or clothes are then required for safety issues. Absorption materials must display a low reflectivity and a good thermal stability because of local heating induced by the laser beam.

The research on absorption devices deals with materials that can absorb the 1064 nm radiation of the widespread YAG:Nd³⁺ laser. In particular, samarium-based compounds were found to be efficient absorption materials because of electronic transitions between the ground state ⁶H_{5/2} to the ⁶F_{9/2} excited state.

Undoped Sm₂O₂S was found to absorb a large proportion of the 1064 nm laser radiation with a reflectivity of around 0.74 % and it is stable up to 2000 °C.³⁷ In comparison, SmBO₃ presents a reflectivity of 0.6 % but endures a phase transition at 1200 °C.³⁸ Doping with erbium or thulium may also be an efficient way to slightly enhance the absorption properties of Sm₂O₂S.³⁹

I.1.3.3. Scintillators

A scintillator is a material that emits light when it is excited by an ionizing radiation (X-rays or gamma rays for example). Scintillators are mainly used in the field of medical imaging. Their role is to lower the dose of X-rays endured by a patient during an analysis. To enable a good absorption of the X-ray beam, the requirements for a good scintillator phosphor is the presence of heavy atoms (cadmium, bismuth, lanthanides, tungsten for instance), a high material density ($\geq 4 \text{ g.cm}^{-3}$) and a high stability regarding the radiations. The photon must be converted into photons in the visible range (500 - 800 nm) with a good efficiency, a fast decay and a short afterglow. Moreover, mechanical strength, absence of toxicity, and chemical stability are desired features.⁴⁰

Thus, a scintillator is generally composed by a dense ceramic and converts X-rays in visible light. It is connected to photodiodes that convert the visible photons in electrons that form an image on a layer of amorphous silica. Considering their efficient absorption of X-rays, Y₂O₂S:Tb, La₂O₂S:Tb, Gd₂O₂S:Tb were considered to replace CaWO₄, which was commonly used as scintillator.⁴¹ Gd₂O₂S:Tb was finally chosen for its higher density and better absorption properties in comparison to the other lanthanides.⁴¹ Later, Gd₂O₂S:Pr was shown to be an efficient scintillator by Rossner *et al.* They demonstrated that the main differences between the Pr^{III} and the Tb^{III} doping lie in the incident beam conversion efficiency (for a 40 - 80 keV X-ray beam, 8.5 % for Gd₂O₂S:Pr,Ce,F and 15 % for Gd₂O₂S:Tb) and the luminescence lifetime of the doping ion ($\sim 3 \mu\text{s}$ for Gd₂O₂S:Pr,Ce,F; 600 μs for Gd₂O₂S:Tb).⁴⁰ Pr^{III} shows a very rapid decay, cerium decreases the trap states and fluorine causes an important decrease of the afterglow. Gd₂O₂S:Eu was also studied. Its absorption and luminescence properties were competitive enough and it enables the emission of red photons

(instead of green photons for Pr and Tb), which can be useful for compatibility issues with digital imaging systems.⁴²

Nowadays, gadolinium oxysulfides are used as scintillators for Single-Photon Emission Computed Tomography (SPECT), X-ray Computed Tomography (CT) and Positron Emitting Tomography (PET).

I.1.3.4. Patents

Among the several hundreds of patents which deal with lanthanide oxysulfides, most of them focus on the preparation of bulk oxysulfides and their use as screens or scintillators. Because of their huge amount and redundancy, they are not referenced here.

I.2. Nanoscaled ternary lanthanide oxysulfides $\text{Ln}_2\text{O}_2\text{S}$

I.2.1. Introduction

Oxysulfide nanoparticles

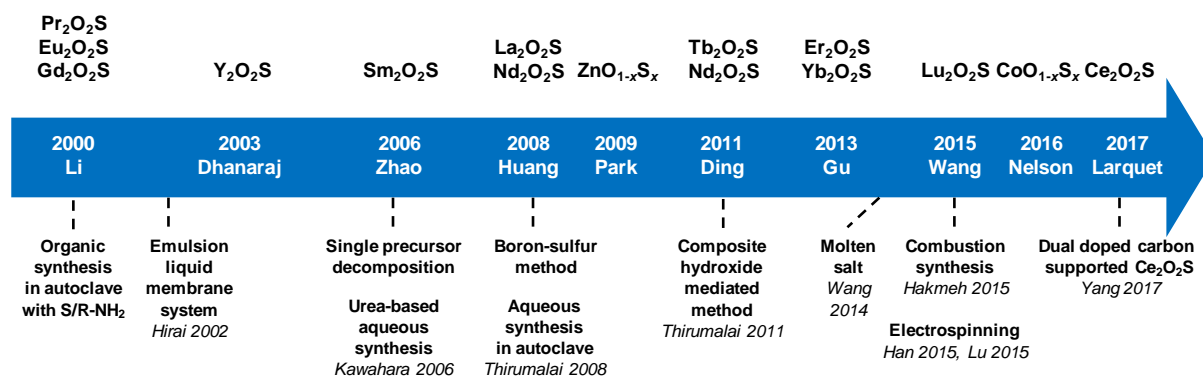


Figure 3: Key dates, authors and techniques of the oxysulfide nanoparticles research.

Following the hype for nanotechnology in the 21st century, researchers have recently worked on producing metal oxysulfide materials as nanoparticles. This trend is justified by the applications that could emerge from nanomaterials, especially in the domain of biology and medicine. In particular, nano-scale objects can cross biologic barriers and be metabolized by living beings. Also, because of their wide range of morphologies, compositions and grafting, the nanoparticles can reach targeted zones using specific interactions to provide local information, deliver drugs at precise places or stimulate organs and tissues with an internal or external stimulus.

Lanthanide oxysulfide nanomaterials present many advantages for imaging in biological medium. They have a good chemical and thermal stability. Their size and shape is highly tunable from very small crystals around 5 nm to micrometer spheres, rods, belts, tubes and so on. Moreover, the $\text{Ln}_2\text{O}_2\text{S}$ crystalline phase bears many lanthanide/transition metal or lanthanide/lanthanide substitutions, which guarantees a generous variety of luminescent properties.

I.2.1.1. Examples of oxysulfide nanoparticles applications

I.2.1.1.1. Upconversion

In the fields of therapy and *in vivo* imaging, using direct light composed of high energy photons, typically X-rays or gamma rays, leads to potential harmful effects for the patient. Organic dyes, radioisotopes and quantum dots are currently used in order to perform

bioimaging. However, toxicity of radioactive isotopes and quantum dots is problematic. Also, organic fluorophores and quantum dots (QD) are excited through ultraviolet (UV) irradiation that can lead to autofluorescence (excitation of natural targets, such as elastin, collagen...), photobleaching (destruction of the dye) and luminescence blinking.

Another indirect but efficient way to excite phosphors at low energy for bioimaging is infrared (IR) irradiation. The main advantage is the high signal-to-noise ratio, because biological tissues absorb less light in this spectral range, while light absorption is high both in the 400 – 600 nm range (due to tissues constituents such as melanin or hemoglobin) and above 1300 nm (due to water). Consequently, IR bioimaging does not result in parasitic fluorescence in the 800 – 1200 nm region. Moreover, it causes low tissue damage and enables local irradiation along with high penetration depth.

Lanthanide-based upconverting phosphors are based (in the simplest case) on the combination of two absorbed low-energy photons in one of a higher energy, resulting for instance in the absorption of IR wavelengths and emission of visible light.⁴³ This way, many advantages are conferred to the imaging system:⁴⁴ the chemical stability and low toxicity of rare-earth compounds, the absence of photo-bleaching, the low and easy available required energy.

Oxysulfide nanomaterials based on the upconverting properties of lanthanide dopants have been studied as potential upconverting phosphors for biomedical imaging. Ytterbium and erbium co-doped materials are being investigated in detail, but other dopants, such as holmium and thulium have also been reported for upconverting materials.

1.2.1.1.2. Persistent luminescence

The phenomenon of persistent luminescence is the emission of light by a material after excitation has stopped. It must be distinguished from fluorescence and phosphorescence. Its mechanism is complex and still debated.⁴⁵ In persistent luminescence, the origin of the extended emission in an insulator or semi-conductor is the entrapment of electrons or holes that are progressively released.⁴⁶ Either an electron is trapped in an energy level near the conduction band or a hole is trapped in an energy level near the valence band.

The traps can be point defects with intrinsic defects of the lattice such as vacancies, interstitial defects, antisite defects or extrinsic defects when doping ions substitute lattice atoms or occupy interstitial sites. Extended defects (dislocations, surface, or grain boundaries) of the lattice can also play the role of traps.

Oxysulfide materials containing titanium and europium have been developed for persistent luminescence. Here, the doping ions substitute the rare-earth of the matrix and correspond to extrinsic defects. $\text{Y}_2\text{O}_2\text{S}:\text{Ti}$ in 2005 was the first example,⁴⁷ but numerous articles focused on the promising properties of $\text{Ln}_2\text{O}_2\text{S}:\text{Eu}^{3+}, \text{Mg}^{2+}, \text{Ti}^{4+}$ ($\text{Ln} = \text{Gd}, \text{Y}$).

1.2.1.1.3. Magnetic probes

Because of their remaining $4f$ electrons, most of the lanthanide ions present magnetic properties. Lanthanide oxysulfides were found to be paramagnetic in a large range of temperatures, and their magnetic properties at low temperatures were extensively studied.^{48–50}

Lanthanides can exhibit high magnetic susceptibility, which is major interest for chemicals that can be injected in a living organism. For instance, Gd^{III} complexes are used as positive contrast agents in magnetic resonance imaging (MRI) due to the $4f^7$ electronic configuration of the ion ($\mu = 7.94 \mu_{\text{B}}$). The role of a contrast agent is to enhance the MRI signal by locally perturbing the magnetic field. The spin relaxation time of Gd^{III} is long enough to optimize the dipole-dipole interactions of electron and protons (biological tissues, water) in the neighborhood of the contrast agent. The MRI signal is then enhanced by the acceleration of the spin relaxation of the protons caused by these interactions. Gadolinium ions in molecular complexes remain toxic because of polarizing effects and competition with calcium. Special hydrosoluble complexes were then developed to mitigate the toxicity of Gd^{III} .⁵¹

An alternative to lanthanide complexes is lanthanide nanoparticles. A better relaxation occurs as the consequence of the concentration of several thousand atoms in a little volume. Iron oxide nanoparticles were widely studied and used as negative contrast agents, but many artefacts were observed on the resulting images.⁵² Gd_2O_3 nanoparticles were found to have a similar or better relaxivity than gadolinium complexes, without the drawbacks of iron oxides. They were then chosen for the precise visualization of locally injected cells.^{53,54}

With doping ions, gadolinium oxide nanoparticles were then applied for bimodal imaging (MRI and luminescence).⁵⁵ Because of their very good luminescence properties, similar results are expected for oxysulfide $\text{Gd}_2\text{O}_2\text{S}$ nanoparticles. Bimodal agents are especially useful to get various information of the environment of the nanoparticles from the luminescence properties (wavelength, lifetime, and so on) in short times coupled with long term data and precise localization with magnetic resonance imaging.⁵⁶ Ajithkumar *et al.* demonstrated the possibility of performing multimodal bioimaging using oxysulfide material choosing the $\text{Gd}_2\text{O}_2\text{S}:\text{Yb}, \text{Er}$ phosphor.⁴⁴

1.2.1.1.4. Catalysis

Because the majority of lanthanides are often restricted to the +III oxidation state, catalysis based on oxido-reduction reactions is not the preferential application of oxysulfide materials. Nevertheless, cerium (Ce^{III} and Ce^{IV}) and europium (Eu^{II} and Eu^{III}) are notable exceptions. In particular, $\text{Ce}_2\text{O}_2\text{S}$ nanoparticles on carbon was tested for oxygen reduction reaction (ORR).⁵⁷ Also, $\text{Eu}_2\text{O}_2\text{S}$ nanoparticles showed catalytic activity for the water-gas shift reaction (reaction of CO with water that yields CO_2 and H_2).⁵⁸ They can also act as a peroxidase mimic for the catalytic oxidation of 3,3',5,5'-tetramethylbenzidine (TMB).⁵⁹

1.2.1.2. Synthetic strategies for lanthanide oxysulfide nanoparticles

1.2.1.2.1. General pathways towards $\text{Ln}_2\text{O}_2\text{S}$ nanoparticles

Several strategies can be employed to yield oxysulfides nanoparticles. Historically, bulk oxysulfides were formed by partial sulfidation of oxides, oxidation of sulfides or reduction of sulfates (Figure 4). However, solid-gas or solid-solid reactions at high temperatures inevitably lead to sintering and large particles. This should be avoided to control the growth of nanoparticles. Moreover, avoiding sulfates is challenging: their formation is a competitive reaction.

Four major strategies are employed to yield $\text{Ln}_2\text{O}_2\text{S}$ (bulk and nanoparticles). The two first methods are the sulfidation of an oxygenated phase such as an oxide or a hydroxide (Figure 4, pathway A) and the oxidation of sulfides (Figure 4, pathway B). In the latter case, the term “oxidation” names a substitution between sulfur and oxygen and does not imply oxido-reduction processes. This process is challenging: the partial oxygenation of sulfides is hard to control because sulfates are easily formed. To the best of our knowledge, only bulk materials were synthesized this way.

The reduction of sulfates and oxysulfates is also possible (Figure 4, pathway C). It is generally excluded for the formation of nanoparticles as it demands high temperatures ($\geq 800^\circ\text{C}$). Finally, another way to achieve the synthesis of metal oxysulfides is the co-insertion of oxygen and sulfur anions. Decompositions of organic precursors containing oxygen or sulfur are especially helpful for this method (Figure 4, pathway D). For syntheses in which oxygen rate has to be finely controlled, inert atmosphere assured by N_2 or argon is mandatory.

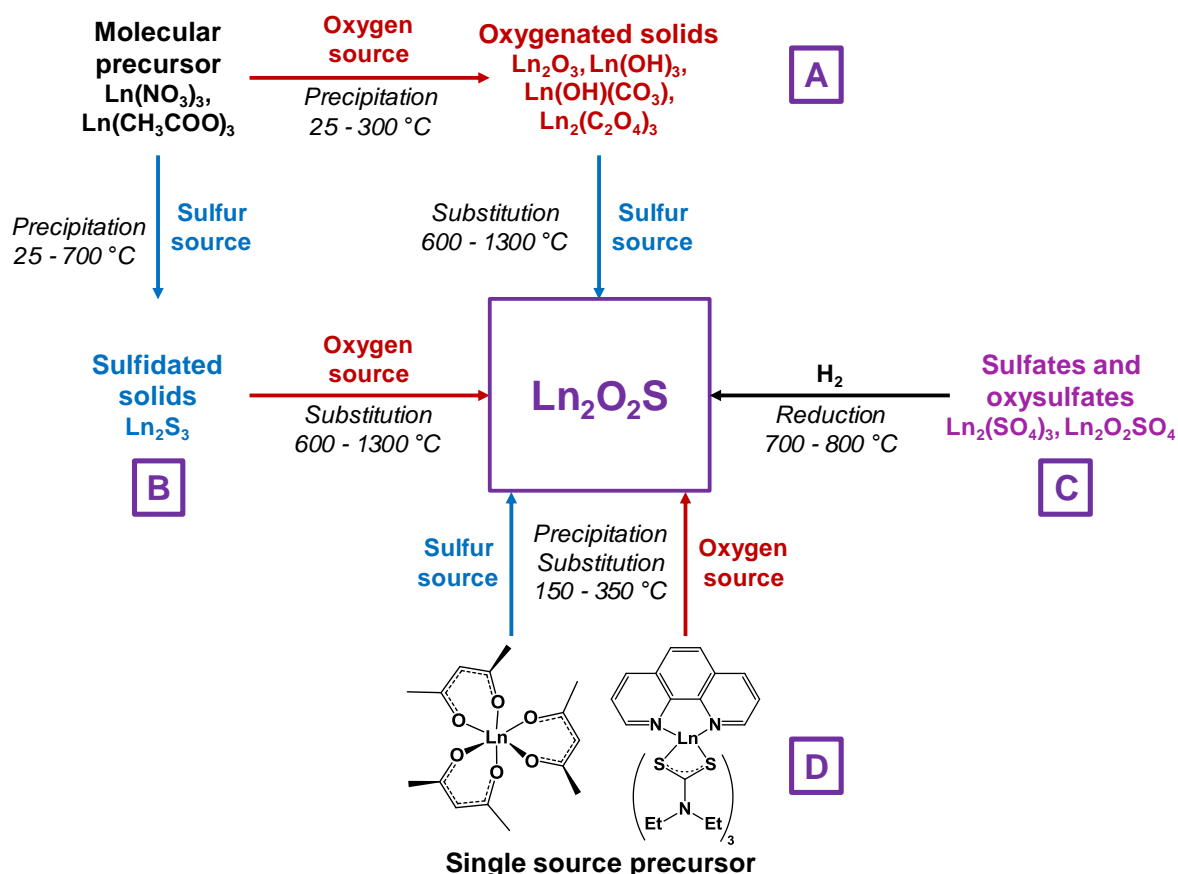


Figure 4: Synthetic strategies for $\text{Ln}_2\text{O}_2\text{S}$.

Since twenty years, a broad spectrum of techniques has been developed to yield $\text{Ln}_2\text{O}_2\text{S}$ nanoparticles, which remains by far the center of the oxysulfide research. Here, we chose to classify them in three groups mainly depending on the reaction medium: water, organic solvent and others.

I.2.1.2.2. Typical oxygen and sulfur sources in $\text{Ln}_2\text{O}_2\text{S}$ nanoparticles syntheses

I.2.1.2.2.1. Oxygen sources

The oxygen source for the formation of $\text{Ln}_2\text{O}_2\text{S}$ nanoparticles highly depends on the synthetic route (Figure 4).

Commonly, in the water-based syntheses, oxygen is brought by hydroxide or carbonate ions with the precipitation of an intermediate oxygenated phase in basic medium. Oxygen insertion in sulfides Ln_2S_3 has never been performed for nanoparticles, to the best of our knowledge. Molecular precursors such as lanthanide formate or lanthanide acetylacetonate contain enough oxygen for the targeted composition. In organic medium, the use of ketones as ligands enables the formation of *in situ* water when an amine is present. The thermal decomposition of single-

source precursors with sulfide ligands can be performed in air or pure dioxygen to give $\text{Ln}_2\text{O}_2\text{S}$ nanoparticles. In the case of reduction of sulfates and oxysulfates, no additional source of oxygen is required.

I.2.1.2.2.2. Sulfur sources

In water, sulfidation is mainly carried out by solid-gas reaction with H_2S or in situ formed CS_2 using elemental sulfur heated in graphite or in presence of carbon. Nevertheless, a significant amount of syntheses also use sulfur sources soluble in water, such as thiourea or thioacetamide that initiate the sulfidation process. Elemental sulfur can also be used in organic medium especially dissolved in amines. Recently, substitution of oxygen by sulfur was carried out by ammonium sulfide and hexamethyldisilathiane (HMDTS).⁶⁰

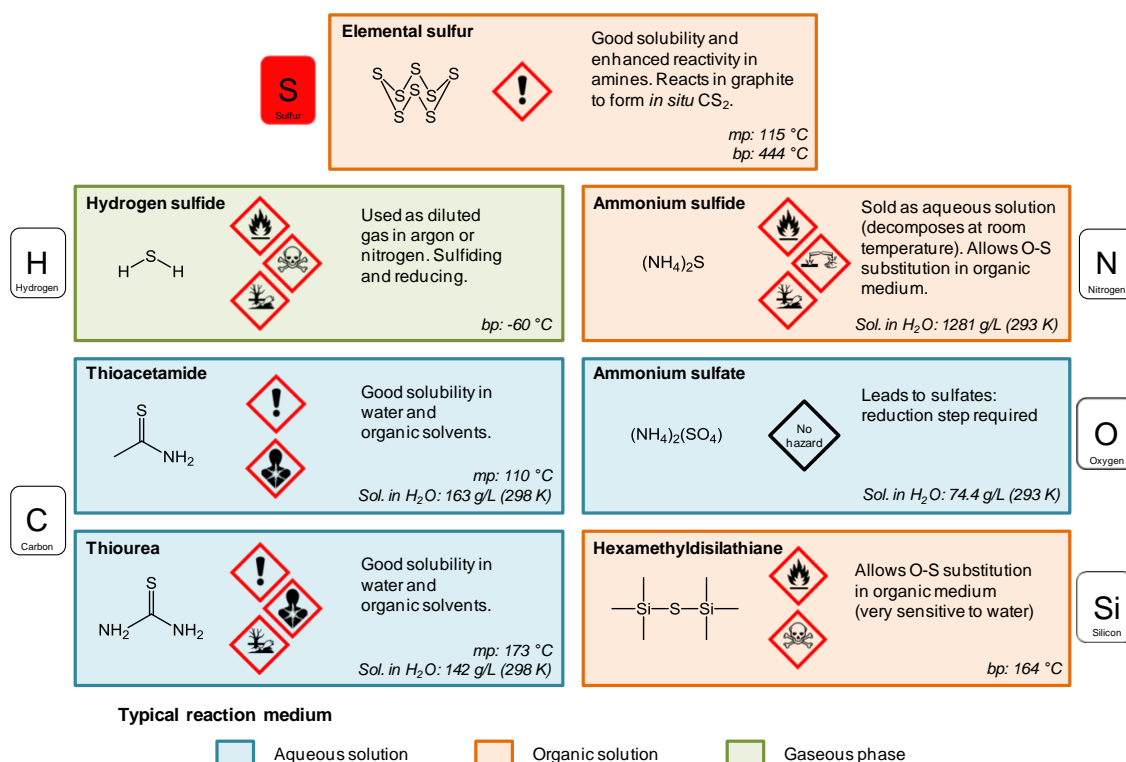


Figure 5: Sulfur sources typically used for the sulfidation processes leading to oxysulfides (mp = melting point, bp = boiling point, Sol. = solubility). The first neighbor of sulfur in the molecule is indicated.

I.2.2. Exotic syntheses

Classical nanoparticles syntheses consist in heating hydrophobic or water-soluble inorganic precursors in organic or aqueous media, possibly sealed and/or pressurized and often followed by a thermal treatment which helps sulfidation and/or crystallization. In marge of these techniques, unconventional synthetic methods can be found. They involve unusual solvents,

like molten salts, or are performed in uncommon conditions (electrospinning, combustion, and so on). This section describes such syntheses.

I.2.2.1. Boron-sulfur method

In 2008, Huang *et al.* adapted the boron-sulfur method, originally destined to the synthesis of sulfides, to the synthesis of $\text{La}_2\text{O}_2\text{S}$ and $\text{Nd}_2\text{O}_2\text{S}$.⁶¹ In this synthesis, nanowires of the lanthanide hydroxide $\text{Ln}(\text{OH})_3$ (formed by reaction between $\text{Ln}(\text{NO}_3)_3$ and KOH) are directly heated in presence of boron and elemental sulfur S_8 placed in a neighboring crucible. The driving force of the reaction is the strong affinity of boron with oxygen, which leads to the formation of B_2O_3 as a by-product.

When the reaction is maintained for 24 hours at 400 °C, LnS_2 nanowires are obtained. Using shorter reactions times (500 °C, 10 min), sulfidation of the wire is partial and $\text{Ln}_2\text{O}_2\text{S}$ can be obtained (Figure 6A).

This solid-state reaction preserves the shape of the precursor. Also, it is one of the rare techniques that enable the formation of $\text{Ln}_2\text{O}_2\text{S}_2$ nanomaterials using in some conditions an excess amount of sulfur compared with the targeted stoichiometry to ensure complete reactions. Nevertheless, only a small quantity of reactants was loaded in the crucible, leading to less than 15 mg of product per reaction. Also, the remaining species (B_2O_3 , sulfur in excess) were washed with toxic CS_2 .

I.2.2.2. Combustion synthesis

In order to get a swift synthesis, Hakmeh *et al.* developed a combustion synthesis by mixing lanthanide nitrates ($\text{La}(\text{NO}_3)_3$, $\text{Er}(\text{NO}_3)_3$ and $\text{Yb}(\text{NO}_3)_3$) with thioacetamide in ethanol.⁶² The precursors were rapidly inserted in a furnace at 500 °C. Two successive flames evidenced first the ignition of ethanol, then the exothermic decomposition of the organic compounds, leading to an increase of the temperature and eventually to the formation of particles. A post-treatment at high temperature was also necessary (H_2S in N_2 , 2 hours, 1000 °C) and resulted in large particles with a typical size around 300 – 500 nm (Figure 6B).

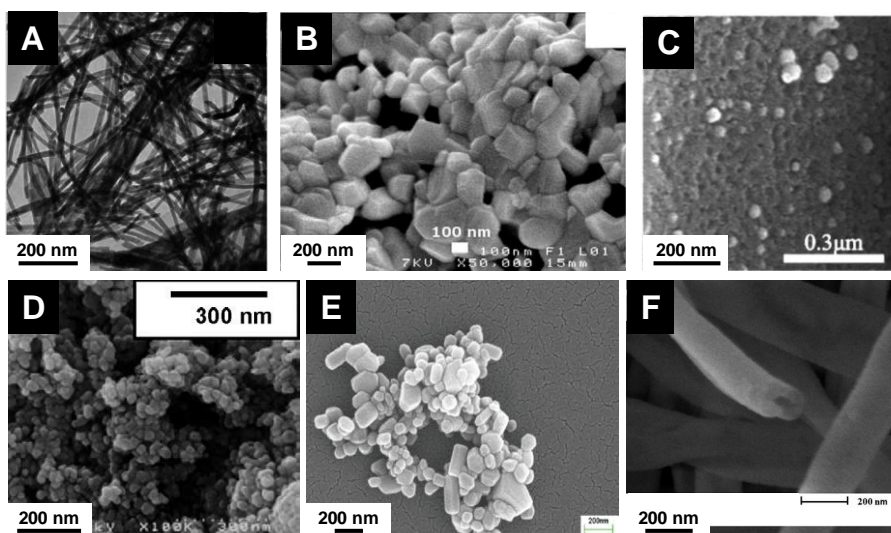


Figure 6: $\text{Ln}_2\text{O}_2\text{S}$ nanoparticles obtained from unconventional synthetic methods: (A) Boron-sulfur method ($\text{La}_2\text{O}_2\text{S}:\text{Eu}$ nanowires); (B) Combustion ($\text{La}_2\text{O}_2\text{S}:\text{Yb,Er}$ nanoparticles); (C) Thermal decomposition of a gel of Pomelo skins ($\text{Ce}_2\text{O}_2\text{S}$ nanoparticles supported on carbon); (D) Emulsion liquid membrane system ($\text{Y}_2\text{O}_2\text{S}:\text{Yb,Er}$ nanoparticles); (E) Synthesis in molten NaCl ($\text{Y}_2\text{O}_2\text{S}:\text{Eu}$ nanoparticles); (F) Electrospinning ($\text{Y}_2\text{O}_2\text{S}:\text{Yb,Er}$ hollow nanofiber).

I.2.2.3. N,S dual doped carbon supported $\text{Ce}_2\text{O}_2\text{S}$

Recently, an original catalyst for oxygen reduction reaction (ORR) was obtained by using the thermal decomposition of a vegetal, which provides the carbon support for the inorganic catalyst.⁵⁷ Cerium nitrate ($\text{Ce}(\text{NO}_3)_3$) was dissolved in water along with thiourea and then pomelo skins were added to the solution in order to form a gel. After drying, the gel was annealed at 900 – 950 °C for 2 hours to get $\text{Ce}_2\text{O}_2\text{S}$ supported on carbon doped by nitrogen and sulfur. When the reaction temperature was set to 850 °C or 1000 °C, the reaction led to the formation of CeO_2 . The TEM observation of the catalyst shows 50–100 nm crystals of $\text{Ce}_2\text{O}_2\text{S}$ disseminated on the surface of the samples (Figure 6C). The porous structure, inherited from the pomelo precursor and the oxygen vacancies evidenced by the authors make this material suitable for the ORR.

I.2.2.4. Emulsion liquid membrane system (ELM)

Emulsion Liquid Membrane System (ELM) employs a water-in-oil-in-water (W/O/W) double emulsion. Originally, ELM was applied to separate metals. Here, the double emulsion is used for the formation of doped yttrium and gadolinium oxalates. These intermediates are converted to oxysulfides, $\text{Y}_2\text{O}_2\text{S}:\text{Yb,Er}$ and $\text{Gd}_2\text{O}_2\text{S}:\text{Eu}$, by a solid-state reaction with sulfur vapor.^{63,64} Typically, a first emulsion is obtained by mechanical agitation of an organic phase containing kerosene with bis(1,1,3,3-tetramethylbutyl)phosphinic acid (DTMBPA) (or 2-

methyl-2-ethylheptanoic acid, VA-10) as extractant and sorbitan sesquioleate as surfactant and an aqueous phase containing oxalic acid. This emulsion is then added to the external water phase which contains the metal ions (chloride or nitrates) and the double emulsion is produced by mechanical stirring. The oxalate compounds are thus produced at ambient temperature, and the system is demulsified using ethylene glycol. Oxysulfides nanoparticles of 50 – 100 nm are then obtained by annealing the powders at 600 – 1000 °C in sulfur vapor generated at 200 °C by elemental sulfur and carried by a N₂ flow (Figure 6D).

I.2.2.5. Synthesis in molten sodium chloride

The synthesis in molten salts is an emerging technique which consists in the use of one or several salts as solvents for an inorganic reaction. An eutectic mixture can even be used to benefit from a lower melting point. Molten salts are typically suitable for reaction temperatures between 300 °C and 1000 °C, which enable the formation of nanoparticles while avoiding their sintering.^{65,66} After cooling, the particles are obtained in a matrix composed by the salts that are washed with water or alcohols.

Molten sodium chloride (melting point: 801 °C) was chosen for the one-pot synthesis of Y₂O₂S:Eu. Y(NO₃)₃, Eu(NO₃)₃ and NaOH were mixed and stirred before the addition of NaCl, S₈ and a surfactant.⁶⁷ After grinding, the mixture was heated to 850 °C in a CO atmosphere for 4 hours, and then cooled and washed.

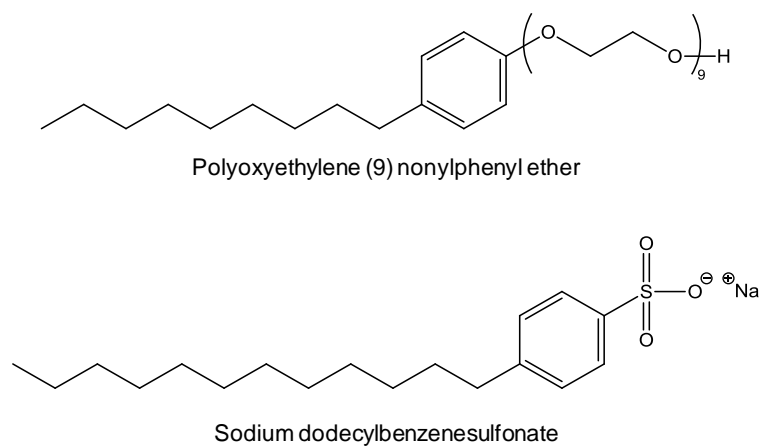


Figure 7: Examples of surfactants employed by Wang *et al.* to synthesize Y₂O₂S:Eu in molten NaCl.⁶⁷

Depending on the surfactant, the particles were either sub-micrometric or nanoscaled, but the morphology was quite irregular and the size polydisperse in all cases. For instance, polyoxyethylene (9) nonylphenyl ether (Figure 7) gave 150 – 250 nm particles (Figure 6E) while sodium dodecylbenzenesulfonate (Figure 7) gave 0.5 – 1.5 μm particles.

I.2.2.6. Composite-hydroxide-mediated method

The composite-hydroxide-mediated method is also a synthesis in molten salts, but with hydroxides. Thirumalai *et al.* adapted this method to the synthesis of Eu-doped yttrium oxysulfide by heating concentrated yttrium acetate $\text{Y}(\text{CH}_3\text{COO})_3$ in an eutectic mixture of NaOH and KOH in an autoclave.⁶⁸ As the melting temperature of the mixture is 165 °C, the autoclave was heated at 200 °C to yield $\text{Y}(\text{OH})_3$ nanobelts (48 h) and nanorods (24 h) (Figure 8).

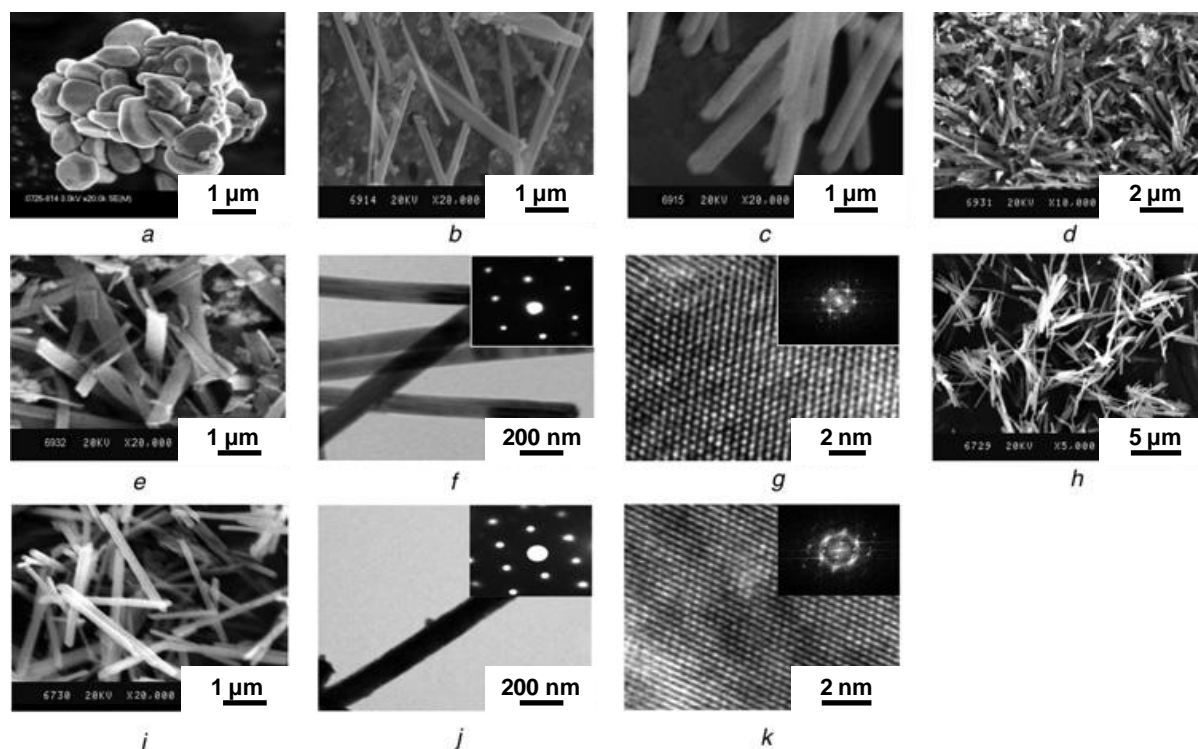


Figure 8: Europium-doped yttrium oxysulfide nanoparticles with different morphologies obtained *via* the composite-hydroxide-mediated method and their precursors.⁶⁸ (a) SEM image of bulk $\text{Y}_2\text{O}_2\text{S}:\text{Eu}$. (b) SEM image of $\text{Y}(\text{OH})_3$ nanobelts. (c) SEM image of $\text{Y}(\text{OH})_3$ nanorods. (d) SEM image of $\text{Y}_2\text{O}_2\text{S}:\text{Eu}$ nanobelts. (e) SEM image of $\text{Y}_2\text{O}_2\text{S}:\text{Eu}$ nanorods. (f) TEM and (g) HRTEM images of $\text{Y}_2\text{O}_2\text{S}:\text{Eu}$ nanobelts. (h) High-magnification SEM image of $\text{Y}_2\text{O}_2\text{S}:\text{Eu}$ nanobelts. (i) High-magnification SEM image of $\text{Y}_2\text{O}_2\text{S}:\text{Eu}$ nanorods. (j) TEM and (k) HRTEM images of $\text{Y}_2\text{O}_2\text{S}:\text{Eu}$ nanorods. Insets are corresponding SAED patterns.

Europium and S_8 were then mixed with the $\text{Y}(\text{OH})_3$ nanomaterial at 70–80 °C and underwent an undescribed sulfidation process. In any case, the product was then annealed at 600 °C for 2 hours in an (Ar or N_2)/sulfur atmosphere to form $\text{Y}_2\text{O}_2\text{S}:\text{Eu}$. Interestingly, the final product retained the morphology of the $\text{Y}(\text{OH})_3$ precursor. On the other hand, the step where the product was sulfidated was particularly unclear here, as three sulfidation processes are mentioned.

I.2.2.7. Electrospinning

Electrospinning is based on the application of a high potential difference between a polymer solution or a polymer melt and a collector. The electrical field creates charged threads that can be assembled depending on the experimental parameters such as tension, temperature, relative humidity (RH), concentration of the precursors, viscosity, distance between capillary screen and collection screen, etc.

Lanthanide nitrates $\text{Y}(\text{NO}_3)_3$, $\text{Yb}(\text{NO}_3)_3$ and $\text{Er}(\text{NO}_3)_3$ and polyvinyl pyrrolidone (PVP) were dissolved in DMF and stirred eight hours.⁶⁹ Fibers were produced by electrospinning. They were annealed twice: (i) at 700 °C for 8 hours under air to get $\text{Y}_2\text{O}_3\text{:Tb,Er}$ fibers and (ii) at 800 °C for 4 hours in a CS_2 atmosphere (obtained by heating S_8 in presence of carbon) to yield $\text{Y}_2\text{O}_2\text{S:Yb,Er}$ hollow nanofibers (Figure 6F). The same strategy was used to yield $\text{Y}_2\text{O}_2\text{S:Er}$ hollow nanofibers.⁷⁰ With slightly different electrospinning parameters, full nanofibers of $\text{Y}_2\text{O}_2\text{S:Yb,Er}$ with a diameter comprised between 80 and 140 nm were obtained and studied by Lu *et al.*⁷¹

I.2.2.8. Anodic aluminum oxide template

In 2013, Cui *et al.* elaborated a synthesis for doped oxysulfide nanoarrays using an anodic aluminum oxide template (AAO).^{72,73} A nitrate solution obtained by dissolution of Y_2O_3 , Eu_2O_3 and $\text{Mg}(\text{OH})_2 \cdot 4\text{MgCO}_3 \cdot 2\text{H}_2\text{O}$ in hot HNO_3 (65 %) was diluted by ethanol. Titanium doping was then obtained by adding the reaction product of $\text{Ti}(\text{OBu})_4$ with acetylacetone. The pH was adjusted to 1 with HNO_3 . The sol was eventually obtained by evaporation at 80 - 90 °C. The AAO template was dipped in the sol, dried, calcined at 600 °C for 2 hours and etched by NaOH (2.0 M) to give $\text{Y}_2\text{O}_3\text{:Eu,Mg,Ti}$ nanoarrays. The whole process involved numerous steps and the resulting nanoarrays had to be sulfurated to $\text{Y}_2\text{O}_2\text{S:Eu,Mg,Ti}$ using S_8 in graphite at 850 °C sharp.⁷² Lower and higher temperatures were indeed not adequate: they resulted respectively in uncomplete sulfidation or oxide formation. Besides, an optimal concentration of europium dopant for the luminescence properties was determined (6.5 mol% Eu vs. Y).⁷³

I.2.3. Water-based syntheses

In the following syntheses, the reaction medium is water. It is an available, green, and ideal solvent for the dissolution of numerous metallic precursors, especially nitrates and chlorides.

Water also brings two main advantages: first, the availability of lanthanide precursors, and especially nitrates (that can be prepared from oxides in HNO_3) and water-soluble sulfur

sources (thioacetamide, thiourea, ammonium sulfide, sodium sulfide and so on; see Figure 5); second, the substantial knowledge on inorganic polymerization in water. So far, in more than 90 % of the articles dealing with $\text{Ln}_2\text{O}_2\text{S}$ nanoparticles, the desired feature of the material was luminescence. Luminescence is due to a controlled doping of the oxysulfide phase ($\text{Ln}^1_2\text{O}_2\text{S}:\text{Ln}^2,\text{M}^3,\text{M}^4$) that is achieved by co-precipitation of the main cation (Ln^1) with the cations that trigger the luminescence and influence its properties (Ln^2 , and possibly M^3 , M^4 ,...).

Water is however limiting metal oxysulfide synthesis by its relatively low boiling point. Even hydrothermal syntheses with autoclaves do not provide enough energy to obtain crystalline oxysulfide nanoparticles. In general, syntheses lead to an intermediate nanoscaled phase (which sometimes already contains sulfur) that is subsequently fully converted in oxysulfide nanoparticles with a solid-gas sulfidation (Figure 4). This last step remains an important drawback. It requires relatively high temperatures for nanoparticles synthesis (typically between 600 °C and 1100 °C) and a large excess of inert gas and sulfur which is often present under the active but toxic gaseous forms of H_2S or CS_2 . Also, it can affect the morphology of the solid by sintering or degradation of the desired phase.

The high-temperature sulfidation step remains the most challenging process here, but can be useful for other features. For luminescence purposes, the energy provided during the thermal treatment gives better-crystallized nanoparticles that present better photoluminescence properties. Moreover, doping ions can be inserted during this step.

I.2.3.1. Gelatin-templated synthesis

Reported in 2008 by Liu *et al*, this synthesis stands out through the original use of gelatin and the way the oxysulfide phase is obtained.⁷⁴

First, the appropriate amounts of lanthanum, terbium and europium nitrates obtained from dissolution of La_2O_3 , Tb_4O_7 and Eu_2O_3 in nitric acid are mixed and heated with gelatin at 80 °C in H_2O . The obtained translucent gelatin sol turns into a gel at 0 °C. Small pieces of the gel are soaked into $\text{NH}_3\cdot\text{H}_2\text{O}$ and $\text{La}(\text{OH})_3:\text{Eu},\text{Tb}$ precipitates inside the gel. Violent stirring can then turn the gel into sol again, and $(\text{NH}_4)_2(\text{SO}_4)$ is added in stoichiometric amount. After drying and annealing at 500 °C for 2 hours in air, a powder of oxysulfate $\text{La}_2\text{O}_2\text{SO}_4:\text{Eu},\text{Tb}$ nanoparticles is formed. The oxysulfate nanoparticles are then converted to oxysulfide nanoparticles by solid-gas reaction using H_2 as reducing gas (700 - 800 °C, 2 hours).

The pathway of oxysulfate reduction is quite rare in the oxysulfide nanoparticles literature, as it often requires high temperatures and long reaction times. Here, the nanoparticles however keep a reasonable 50 nm diameter. On the other hand, this synthesis comprises a myriad of steps, generates two intermediary phases and requires two heat treatments above 500 °C.

I.2.3.2. Sol-gel polymer thermolysis

This strategy is based on the elaboration of an organic network in which the inorganic nanoparticles nucleate and grow in a controlled way. The network is then burnt to free the nanoparticles. It is analogous to the Pechini method used for oxide synthesis for which a tridimensional polyester network is elaborated by reaction of trisodium citrate and ethylene glycol for instance.⁷⁵

Dhanaraj *et al.* published in 2003 a first version of a sol-gel polymer thermolysis strategy to yield $\text{Y}_2\text{O}_2\text{S:Eu}$ nanoparticles.⁷⁶ $\text{Y}(\text{NO}_3)_3$ and $\text{Eu}(\text{NO}_3)_3$ were obtained from the corresponding oxides. Urea, formaldehyde and elemental sulfur were then added and the network was formed at 60 °C. By condensation of urea and formaldehyde along with water evaporation, a gel was obtained. After thermolysis at 500 °C in sulfidating atmosphere, $\text{Y}_2\text{O}_2\text{S:Eu}$ nanoparticles were formed. Based on the XRD pattern, the product was not pure (small peaks of impurities). Despite the treatment at 500 °C, the nanoparticles were quite small (around 30 to 50 nm) but presented an unclear morphology and aggregation. The work of Dai *et al.* in 2008 on $\text{La}_2\text{O}_2\text{S:Eu}$ which deals with the effects of Eu^{3+} concentration on the photoluminescence is based on the same synthetic route.⁷⁷

One year later, Dhanaraj *et al.* published a second version of the protocol that led to hexagonal nanoplates with a size between 7 nm and 15 nm, tunable *via* the reactants concentrations.⁷⁸ The thermolysis process was divided in two steps: first, the sol/network solid was heated at 500 °C for 2 hours to get $\text{Y}_2\text{O}_3\text{:Eu}$ nanoparticles, and was subsequently digested by a thiosulfate solution. After water evaporation, a second thermal treatment at 500 °C (1 hour) burnt the mixture to yield $\text{Y}_2\text{O}_2\text{S:Eu}$ nanoparticles. The authors did not obtain a pure product yet, based on XRD analysis, but this time they identified sodium polysulfides as side-products. Later, Thirumalai and Nakkiran reused this strategy, succeeded in washing the by-products⁷⁹ and deeply investigated the nanoparticles: optical^{79,80} and electronic properties⁸⁰ were discussed as well as the photo-assisted relaxation of surface states.⁸¹

I.2.3.3. Syntheses in water at atmospheric pressure

Element	Ln_2O_3 99.99 %, €/100 g ^a	$\text{Ln}(\text{NO}_3)_3 \cdot x\text{H}_2\text{O}$ 99.9 %, €/100 g ^a	Cost ^b
Y	230	140 (99.8 %)	●
La	139	89	●
Ce	/	359	●
Pr	1850 (99.9 %)	236 (99.99 %)	●
Nd	722	113	●
Sm	796	271	●
Eu	3140	2608	●
Gd	2560	235	●
Tb	3900	1420	●
Dy	1040	166	●
Ho	806 (99.9 %)	776	●
Er	1064	233	●
Tm	17500	3300	●
Yb	2120	430	●
Lu	10820	5040	●

^a Prices on Sigma-Aldrich on January 8th 2018 for France. ^b From more affordable to more expensive: blue-green-yellow-red.

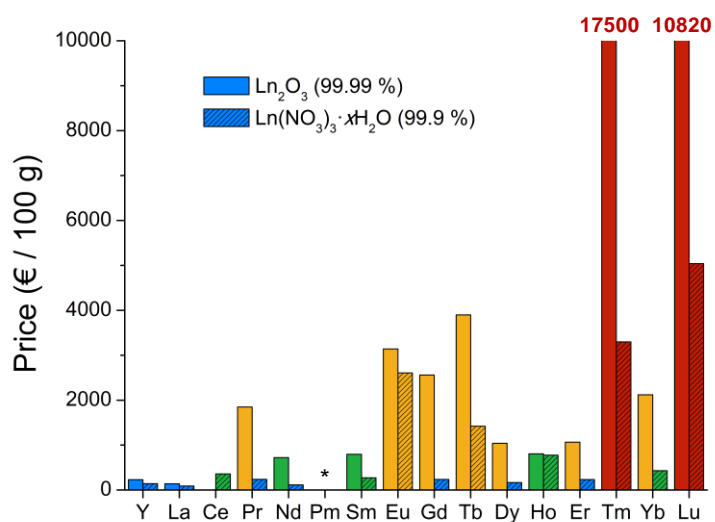


Table 1: Lanthanide oxide and nitrate prices (January 2018).

Because of the attractiveness of luminescent water-dispersible nanoparticles, the pursuit of doped oxysulfide nanoparticles led to the publication and the refinement of synthetic strategies in water. However, the reported syntheses illustrate the complexity of obtaining oxysulfides at low temperatures in water: most often, the authors choose to precipitate an unsulfurated intermediary doped phase ($\text{Ln}(\text{OH})_3$, $\text{Ln}(\text{OH})(\text{CO}_3)$ for instance) that can be amorphous or not. Thus, the syntheses presented in this section are worthwhile for oxide-, hydroxide- or hydroxycarbonate-based nanomaterials. The intermediate nanoparticles are then sulfidated, most often with a solid-gas or alternatively with a solid-solid reaction.

Interestingly, the conditions for lanthanide oxysulfide nanoparticles syntheses in water are majorly optimized on $\text{Gd}_2\text{O}_2\text{S}$ and $\text{Y}_2\text{O}_2\text{S}$ because of their well-known luminescent properties and also maybe for the relatively low price of the related precursors (Table 1).

I.2.3.3.1. Urea-based syntheses

I.2.3.3.1.1. Decomposition of urea in water

Generally, the precipitation of the lanthanide salts is performed *via* the basification of the reaction medium. Thus, a significant amount of research has focused on the cheap, safe, highly available and water-soluble urea. Urea is indeed known to decompose in ammonia ($\text{pK}_a(\text{NH}_4^+, \text{NH}_3) = 9.25$) and aqueous carbon dioxide which can carbonate aqueous lanthanide species (Figure 9).

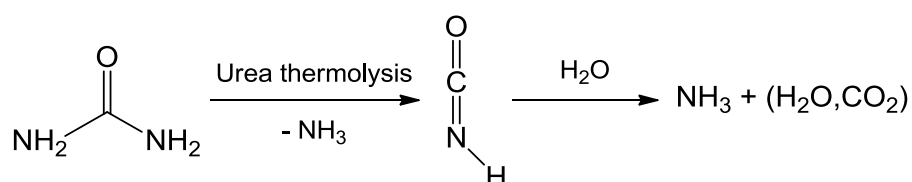


Figure 9: Urea decomposition in water. Isocyanic acid is slowly obtained by urea thermolysis and ammoniac release. A second ammoniac molecule is released by hydrolysis which gives aqueous carbon dioxide “ H_2CO_3 ”.

The concomitant release of ammonia and aqueous carbon dioxide is used in particular for the precipitation of lanthanide hydroxycarbonates $\text{Ln}(\text{OH})\text{CO}_3$ that turned out to be a suitable precursor of lanthanide oxysulfide nanoparticles.

I.2.3.3.1.2. Syntheses with urea in water

The first aqueous synthesis of oxysulfide nanoparticles was reported by Kawahara *et al.* in 2006.⁸² Using yttrium and europium nitrates $\text{Y}(\text{NO}_3)_3$ and $\text{Eu}(\text{NO}_3)_3$ along with urea, an

europium-doped hydroxide precursor $\text{Y}(\text{OH})_3\text{:Eu}$ was obtained by heating the mixture possibly in the presence of a glycol (ethylene glycol, propylene glycol, or hexamethylene glycol). The isolated powder of $\text{Y}(\text{OH})_3\text{:Eu}$ was then heated between 800 °C and 1200 °C with Na_2CO_3 and sulfur to create a sulfidating vapor and yield $\text{Y}_2\text{O}_2\text{S:Eu}$ nanoparticles. XRD showed that the crystalline phase was pure $\text{Y}_2\text{O}_2\text{S}$. The obtained nanoparticles were faceted crystals of 100–300 nm length. Above 1100 °C, sintering made the particles sub-micrometric (≥ 600 nm).

Xing *et al.* then developed an inspiring but complex protocol to synthesize $\text{Y}_2\text{O}_2\text{S:Yb, Ho}$ upconversion nanoparticles.⁸³ A solution of lanthanide nitrates $\text{Y}(\text{NO}_3)_3$, $\text{Yb}(\text{NO}_3)_3$ and $\text{Ho}(\text{NO}_3)_3$ and a solution of urea were separately prepared. The latter solution was added to the first that had been pre-heated at 60 °C and the mixture was then heated at 82 °C. After cooling and aging during 48 hours, a white amorphous precipitate (likely $\text{Y}(\text{OH})\text{CO}_3$)⁸⁴ was dried and converted to $\text{Y}_2\text{O}_3\text{:Yb, Ho}$ *via* calcination (600 °C, 1 hour, air). Then, the oxide was sulfidated at 800 °C for 1 hour with a sulfur vapor created by S_8 at 400 °C and conveyed by an argon flow. It enabled the formation of size-monodisperse and non-aggregated nanoparticles with an average diameter of *ca* 80 nm. The diameter could also be tuned by adjusting the reaction time (aging step). Several works are based on Xing's synthesis with slight modifications. Luo *et al.* added a small amount of oleic acid in the urea mixture and performed the sulfidation at only 600 °C to form the same $\text{Y}_2\text{O}_2\text{S:Yb, Ho}$ nanoparticles.⁸⁵ In the same group, Pang *et al.* reported additional reactions that coated the nanoparticles with functionalized silica using a derived Stöber process with polyvinylpyrrolidone (PVP), aqueous ammonia, tetraethylorthosilicate (TEOS) and aminopropyltriethoxysilane (APTES) in a second step (Figure 10).⁸⁶

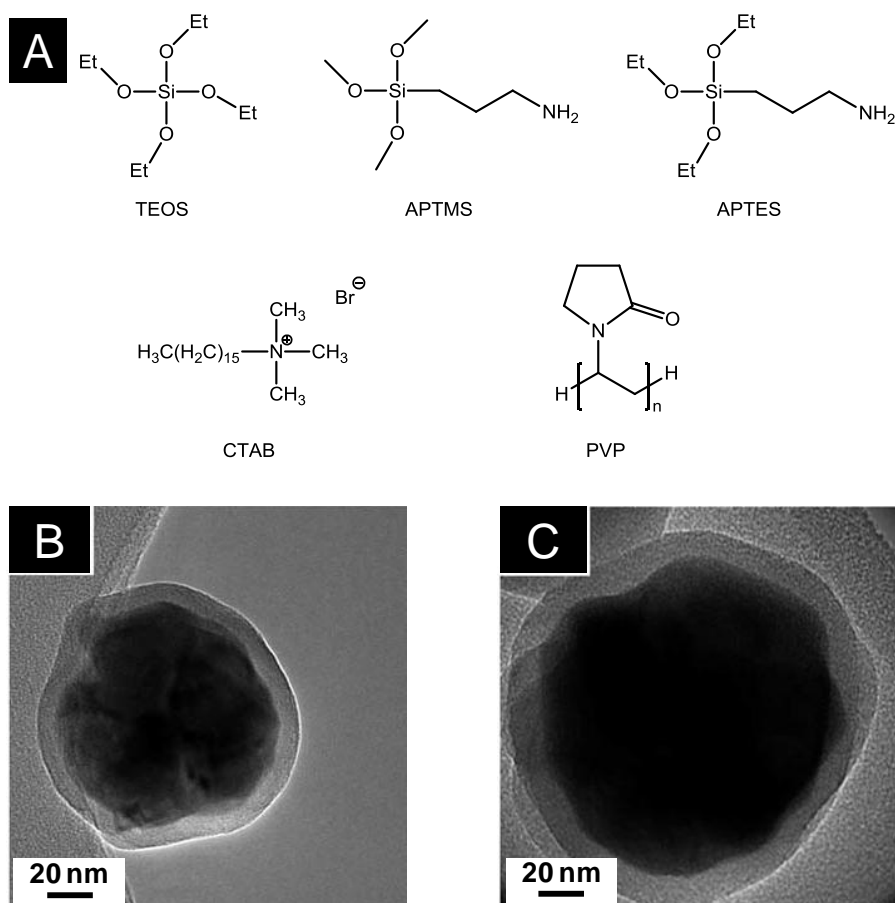


Figure 10: (A) Precursors and additives commonly used for nanoparticles silica coating. Tetraethylorthosilicate (TEOS) is used as silica precursor; 3-aminopropyltrimethoxysilane (APTMS) and 3-aminopropyltriethoxysilane (APTES) are rather employed for silica functionalisation. TEM micrographs of $\text{Gd}_2\text{O}_2\text{S}:\text{Eu}@\text{SiO}_2\text{-APTMS}$ (B) and $\text{Gd}_2\text{O}_2\text{S}:\text{Eu}@\text{mSiO}_2$ (C) nanoparticles from Osseni *et al.* (mSiO₂ stands for mesoporous silica).⁸⁷

Also based on Xing's work, Bakhtiari *et al.* later studied the effect of europium concentration on $\text{Y}_2\text{O}_2\text{S}:\text{Eu}$ nanoparticles size and luminescence.⁸⁸ Very recently, Tian *et al.* succeeded in forming upconverting core-shell nanoparticles $\text{Y}_2\text{O}_2\text{S}:\text{Er}@\text{Y}_2\text{O}_2\text{S}:\text{Yb,Tm}$ by applying Xing's method twice to form the oxide-oxide compound $\text{Y}_2\text{O}_3:\text{Er}@\text{Y}_2\text{O}_3:\text{Yb,Tm}$ as an intermediate.⁸⁴ Solid-gas reaction with sulfur vapor at 800 °C finally provided the oxysulfide nanoparticles. After the shell formation, $\text{Y}_2\text{O}_3:\text{Er}@\text{Y}_2\text{O}_3:\text{Yb,Tm}$ nanoparticles were well separated (Figure 11A). After sulfidation, the nanoparticles were aggregated because of sintering (Figure 11B). Nevertheless, the shell prevented the quenching of the Er^{III} luminescence and multicolor fluorescence was achieved thanks to $\text{Er}^{\text{III}}/\text{Tm}^{\text{III}}$ co-doping (Figure 11C).

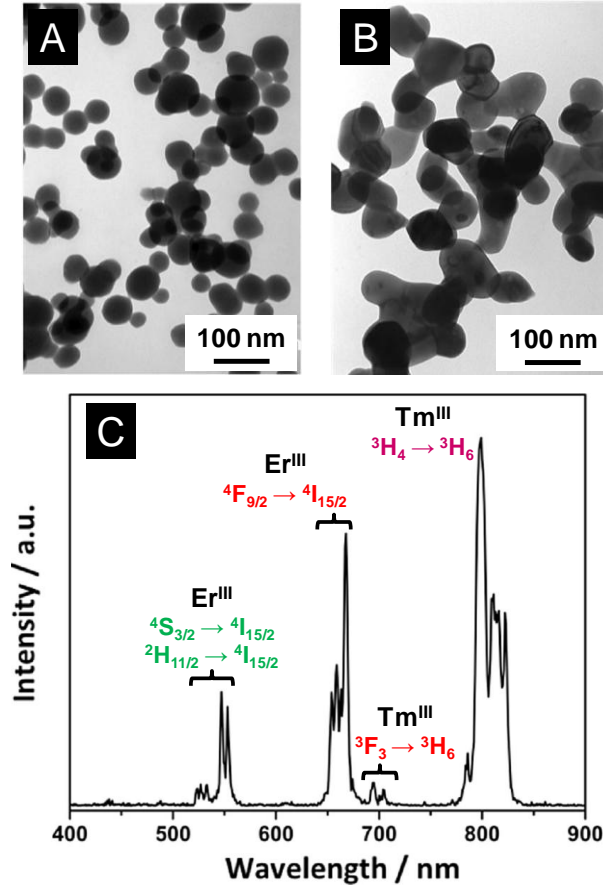


Figure 11: TEM micrographs of $\text{Y}_2\text{O}_3\text{:Er}$ (A) and $\text{Y}_2\text{O}_2\text{S:Er@Y}_2\text{O}_2\text{S:Yb,Tm}$ nanoparticles (B) synthesized by Tian *et al.*⁸⁴ (C) Luminescence spectrum of $\text{Y}_2\text{O}_2\text{S:Er@Y}_2\text{O}_2\text{S:Yb,Tm}$ nanoparticles under 1550 nm excitation that exhibits the multicolor fluorescence of the core-shell nanoparticles (in the near-infrared region, between 780-830 nm, the $^4\text{I}_{9/2} \rightarrow ^4\text{I}_{15/2}$ transition of Er^{III} was proven to play a minor role).

$\text{Y}_2\text{O}_2\text{S:Eu,Mg,Ti}$ nanoparticles were also synthesized for persistent luminescence applications by Ai *et al.* in 2010.⁸⁹ $\text{Y(OH)CO}_3\text{:Eu}$ was obtained by heating a mixture of $\text{Y(NO}_3)_3$, $\text{Eu(NO}_3)_3$ and urea at 90 °C for 2 hours. The final product is obtained by a two-step thermal treatment developed by Li *et al.* in 2009.⁹⁰ It involves first S_8 in graphite at 800 °C for 4 hours, which creates *in situ* reactive CS_2 , and then solid-solid reaction with doping solids (here $\text{Mg(OH)}_2 \cdot 4\text{MgCO}_3 \cdot 6\text{H}_2\text{O}$ and TiO_2). The same year, Ai *et al.* presented an original morphology for the same phase.⁹¹ Hollow submicrospheres were obtained using templating 350 - 400 nm carbon submicrospheres obtained by hydrothermal glucose decomposition (autoclave, 160 °C, 9 h). Before sulfidation and Mg/Ti doping, $\text{Y}_2\text{O}_3\text{:Eu}$ was obtained when removing carbon by thermal treatment at 700 °C (2 h, air).

In 2011, Osseni *et al.* reported the first synthesis of $\text{Gd}_2\text{O}_2\text{S:Eu}$ nanoparticles starting from nitrates and urea in a water/ethanol mixture ($\text{H}_2\text{O/EtOH} = 80/20 \text{ v/v}$).⁸⁷ After dissolution, the

reactants were heated to 85 °C to form a doped hydroxycarbonate precursor $\text{Gd}(\text{OH})\text{CO}_3 \cdot \text{H}_2\text{O}:\text{Eu}$. After isolation and drying, a heat treatment in two steps was performed. First, sulfidation was performed by $\text{Ar}/\text{H}_2\text{S}$ at 750 °C for 90 min and then the nanoparticles were maintained at 850 °C for 4 hours under argon atmosphere only. The final nanoparticles were crystalline and spherical. Diameter was tunable by varying the $\text{H}_2\text{O}/\text{EtOH}$ ratio and reaction time. Interestingly, two techniques of deposition of silica on the nanoparticles were presented. The shell was either formed of mesoporous silica using TEOS and cetyltrimethylammonium bromide (CTAB) or functionalized by a silica/APTMS shell using TEOS and 3-aminopropyltrimethoxysilane (APTMS). In particular, mesoporous silica was found to enhance the luminescence properties of the nanoparticles.

A slightly different strategy, close to the work of Xing *et al.* on yttrium, was adopted in 2013 by Yan *et al.* for the formation of terbium-doped oxysulfide nanoparticles of gadolinium and yttrium.⁹² $\text{Tb}(\text{NO}_3)_3$ and $\text{Gd}(\text{NO}_3)_3$ were dissolved in water around 100 °C, and then urea was added. After filtration and drying, $\text{Gd}(\text{OH})\text{CO}_3 \cdot \text{H}_2\text{O}:\text{Tb}$ was obtained. The sulfidation process was quite complex: the precursor is mixed with Na_2CO_3 and sulfur but is also covered by a second mixture composed of Gd_2O_3 , Na_2CO_3 and S_8 . The bottom layer was washed in hot water and filtrated after being fired at 900 °C for 1 hour. The crystalline phases $\text{Gd}_2\text{O}_2\text{S}$ or alternatively $\text{Y}_2\text{O}_2\text{S}$ were pure (based on XRD) and the polydispersity of the diameter was significant (average diameter around 100 - 120 nm). Yan *et al.* also studied the role of the doping ions in the luminescence mechanism of $\text{Y}_2\text{O}_2\text{S}:\text{Tb},\text{Er}$ nanoparticles.⁹³ In 2016, Bagheri *et al.* fabricated a scintillator screen composed of $\text{Gd}_2\text{O}_2\text{S}:\text{Pr}$ nanoparticles synthesized *via* a similar nitrate/urea reaction.⁹⁴ However, the sulfidation process is a solid-solid reaction with S_8 at 900 °C for 1 hour.

In 2014, Hernández-Adame *et al.* extensively studied the influence of the reaction conditions on the morphology of $\text{Gd}(\text{OH})\text{CO}_3:\text{Tb}$ and $\text{Gd}_2\text{O}_2\text{S}:\text{Tb}$, by mixing an urea aqueous solution with an aqueous solution of $\text{Tb}(\text{NO}_3)_3$ and $\text{Gd}(\text{NO}_3)_3$, and performing two thermal treatments (at 800 °C under air and at 900 °C under a N_2/S atmosphere).⁹⁵ The precursor concentrations, the temperature of the stock solutions of nitrates and urea and the time and temperature of reactions were varied (Figure 12). Eventually, only one set of conditions gave regular spherical nanoparticles ($\varnothing \approx 100$ nm) : a nitrate solution at $6.0 \cdot 10^{-3}$ M, pre-heated at 65 °C, and a urea solution at 0.5 M, at room temperature, reacting for 90 min at 85 °C (Figure 12B).

Recently, Cichos *et al.* studied three different syntheses of europium-doped $\text{Gd}_2\text{O}_2\text{S}$ nanoparticles starting from nitrates and urea: (i) heating water at around 100 °C for 2 hours

using an oil bath, (ii) heating a Teflon bottle at 100 °C for 24 hours and (iii) heating an autoclave at 120 °C for 12 hours (see the autoclave section).⁹⁶ After reaction, the isolated solids were heated with an excess of sulfur under argon at 950 °C for 1 hour to yield Gd₂O₂S:Eu particles. In case (i), the intermediary solid was amorphous but the particles were spherical and quite monodisperse in diameter (Figure 13A). After sulfidation, crystalline Gd₂O₂S:Eu nanoparticles with a diameter close to 135 nm were obtained. The surface was rougher than the amorphous precursor's one. The Teflon bottle method (case (ii)) gave micrometric hydroxycarbonate Gd(OH)CO₃ particles (Figure 13B) that were converted to Gd₂O₂S:Eu micrometric crystals and was thus not suitable for nanoparticles synthesis.

1.2.3.3.2. Other precipitation routes from aqueous solutions

Closely related to urea's precipitating method, an aqueous ammonia/ammonium hydrogenocarbonate precipitation of nitrates was reported by Tian *et al.* in 2015.⁹⁷ A NH₄HCO₃/NH₃·H₂O solution was added dropwise to a nitrate solution including Y(NO₃)₃, Yb(NO₃)₃ and Er(NO₃)₃. A white precipitate of Y(OH)_x(CO₃)_y:Yb,Er was obtained and dried. The Y₂O₂S:Yb,Er nanoparticles were obtained using sulfur vapor (S₈ heated at 400 °C) carried by N₂ at 900 °C for 1 hour. The small but aggregated crystalline nanoparticles (Ø ≈ 30 nm) were phase-pure, based on XRD. Here, the use of ammonium hydrogenocarbonate and aqueous ammonia enabled the authors to carry out the reaction without heating whereas urea needed thermolysis.

Regarding upconverting oxysulfide nanoparticles, Fu *et al.* chose Na₂CO₃ to form intermediate solids which were then sulfidated.⁹⁸ After dissolution of Y(NO₃)₃, Yb(NO₃)₃ and Ho(NO₃)₃, the nitrate solution was added in a 0.1 M solution of Na₂CO₃ containing PEG 4000 as surfactant. A solid precipitated, was isolated and dried. It was heated at 600 °C to yield Y₂O₃:Yb,Ho. Then, the oxide was converted to oxysulfide using Xing's thermal treatment described in the previous section. Interestingly, Na₂CO₃ enables the authors to work at ambient temperature in the first step whereas urea required thermolysis. However, two thermal treatments were necessary to reach the oxysulfide product. Moreover, an irregular faceted morphology and a significant polydispersity in size were found in the final sample.

Author – Year Phase	Metal sources	Precipitation step(s)	Annealing step(s)	Intermediary phase(s)	Final Morphology (Final Size)
Kawahara 2006 ⁸² Y₂O₂S:Eu	Y(NO ₃) ₃ Eu(NO ₃) ₃	<u>1/</u> Urea, glycol 100 °C, 5 h	<u>2/</u> S ₈ , Na ₂ CO ₃ 800-1200 °C, 2 h	<u>1/</u> Y(OH) ₃ :Eu	Nanocrystals (100 - 300 nm for T ≤ 1100 °C)
Xing 2009 ⁸³ Y₂O₂S:Yb, Ho Pang 2010 ⁸⁶ Y₂O₂S:Yb, Ho@SiO₂-APTES Bakhtiari 2015 ⁸⁸ Y₂O₂S:Eu	Y(NO ₃) ₃ Yb(NO ₃) ₃ Ho(NO ₃) ₃	<u>1/</u> Urea 82 °C <u>2/</u> Aging r.t., 48 h	<u>3/</u> Air, 600 °C, 1 h <u>4/</u> S vapor (S ₈ at 400 °C) Ar, 800 °C, 1 h	<u>2/</u> Y(OH)CO ₃ :Yb, Ho [a] <u>3/</u> Y ₂ O ₃ :Yb, Ho (after annealing in air)	Nanospheres (Ø ≈ 70 nm)
Luo 2009 ⁸⁵ Y₂O₂S:Yb, Ho	Y(NO ₃) ₃ Yb(NO ₃) ₃ Ho(NO ₃) ₃	<u>1/</u> Urea (oleic acid) 82 °C <u>2/</u> Aging r.t., 48 h	<u>3/</u> Air, 600 °C, 1 h <u>4/</u> S vapor (S ₈ at 400 °C) Ar, 550 - 600 °C, 1 h	<u>2/</u> Y(OH)CO ₃ :Yb, Ho [a] <u>3/</u> Y ₂ O ₃ :Yb, Ho	Nanospheres (Ø ≈ 50 nm)
Ai 2010 ⁹¹ Y₂O₂S:Eu, Mg, Ti	Y(NO ₃) ₃ Eu(NO ₃) ₃	<u>1/</u> Urea 90 °C, 3 h	<u>2/</u> Air, 700 °C, 2 h <u>3/</u> S ₈ in graphite (CS ₂) 800 °C, 4 h <u>4/</u> TiO ₂ , Mg(OH) ₂ ·4Mg(CO ₃)·6H ₂ O 1100 °C, 4 h	<u>2/</u> Y ₂ O ₃ :Eu	Hollow submicrospheres (Ø = 350 - 400 nm)
Ai 2010 ⁸⁹ Y₂O₂S:Eu, Mg, Ti	Y(NO ₃) ₃ Eu(NO ₃) ₃	<u>1/</u> Urea 90 °C, 2 h	<u>2/</u> S ₈ in graphite (CS ₂) 800 °C, 4 h <u>3/</u> TiO ₂ , Mg(OH) ₂ ·4Mg(CO ₃)·6H ₂ O 1100 °C, 4 h	<u>1/</u> Y(OH)CO ₃ :Eu	Nanospheres (Ø = 100 - 150 nm)
Fu 2010 ⁹⁸ Y₂O₂S:Yb, Ho	Y(NO ₃) ₃ Yb(NO ₃) ₃ Ho(NO ₃) ₃	<u>1/</u> Na ₂ CO ₃ PEG 4000	<u>2/</u> Air, 600 °C, 1 h <u>3/</u> S vapor (S ₈ at 400 °C) Ar, 800 °C, 1 h	<u>1/</u> Y(OH)CO ₃ :Yb, Ho [a] <u>2/</u> Y ₂ O ₃ :Yb, Ho	Nanocrystals (30 - 100 nm)
Osseni 2011 ⁸⁷ Gd₂O₂S:Eu@mSiO₂ Gd₂O₂S:Eu@SiO₂-APTMS	Gd(NO ₃) ₃ Eu(NO ₃) ₃	<u>1/</u> Urea EtOH 85 °C	<u>2/</u> Ar/H ₂ S (83/17 v/v) 750 °C, 90 min <u>3/</u> Ar, 850 °C, 4 h	<u>1/</u> Gd(OH)CO ₃ ·H ₂ O:Eu	Nanospheres, tunable diameter with EtOH volume (Ø = 100 - 250 nm) Silica coating: 10 nm
Yan 2013 ⁹² Ln₂O₂S:Tb (Ln = Gd, Y) Yan 2013 ⁹³ Y₂O₂S:Tb, Er	Ln(NO ₃) ₃ Tb(NO ₃) ₃ (Er(NO ₃) ₃)	<u>1/</u> Urea ~ 100 °C, 1 h	<u>2/</u> Na ₂ CO ₃ , S ₈ , Ln ₂ O ₃ 900 °C, 1 h	<u>1/</u> Ln(OH)CO ₃ ·H ₂ O:Tb or Y(OH)CO ₃ ·H ₂ O:Tb, Er	Nanocrystals (50 - 200 nm)

<i>Hernández-Adame 2014</i> ⁸⁵ Gd₂O₂S:Tb	Gd(NO ₃) ₃ Tb(NO ₃) ₃	<u>1/</u> Urea	<u>2/</u> Air, 800 °C, 2 h <u>3/</u> S vapor (S ₈ at 900 °C) N ₂ , 900 °C, 3 h	<u>1/</u> Gd(OH)CO ₃ ·H ₂ O:Tb <u>2/</u> Gd ₂ O ₃ :Tb	Good conditions give nanospheres (Ø = 100 nm)
<i>Tian 2015</i> ⁹⁷ Y₂O₂S:Yb,Er	Y(NO ₃) ₃ Yb(NO ₃) ₃ Er(NO ₃) ₃	<u>1/</u> NH ₄ HCO ₃ NH ₃ ·H ₂ O r. t.	<u>2/</u> S vapor (S ₈ at 400 °C) N ₂ , 900 °C, 1 h	<u>1/</u> Y(OH) _x (CO ₃) _y :Yb,Er	Aggregated nanocrystals (30 nm)
<i>Cichos 2016</i> ⁹⁶ Gd₂O₂S:Eu	Gd(NO ₃) ₃ Eu(NO ₃) ₃	<u>1/</u> Urea ~ 100 °C (a) 2 h, (b) 24 h	<u>2/</u> S ₈ , Ar 950 °C, 1 h	<u>1/</u> (a) amorphous (b) Gd(OH)CO ₃ :Eu	(a) Nanospheres (Ø ≈ 130 nm) (b) Microcrystals (≈ 1 µm)
<i>Bagheri 2016</i> ⁹⁴ Gd₂O₂S:Pr	Gd(NO ₃) ₃ Pr(NO ₃) ₃	<u>1/</u> Urea ~ 100 °C, 1 h	<u>2/</u> Air, 600 °C, 1 h <u>3/</u> S ₈ , 900 °C, 1 h	<u>1/</u> Gd(OH)CO ₃ ·H ₂ O:Pr [a]	Nanospheres (Ø = 25 - 80 nm)
<i>Tian 2017</i> ⁸⁴ Y₂O₂S:Er@Y₂O₂S:Yb,Tm	Y(NO ₃) ₃ Er(NO ₃) ₃ Yb(NO ₃) ₃ Tm(NO ₃) ₃	<u>1/</u> Urea 82 °C <u>2/</u> Aging r.t., 48 h	<u>3/</u> S vapor (S ₈ at 800 °C) Ar, 800 °C, 40 min	<u>2/</u> Y ₂ O ₃ :Er <u>2/</u> Y ₂ O ₃ Er@Y ₂ O ₃ :Yb,Tm	Aggregated crystals (50 - 150 nm)

[a] Intermediary phase deduced from later works.

Table 2: Precipitation from aqueous solutions at atmospheric pressure.

I.2.3.4. Aqueous reactions under autogenic pressure

This section is dedicated synthesis in aqueous solution under pressure, in autoclave. We already mentioned the low boiling point of water as a strong limitation if we consider the temperatures commonly required for crystalline nanoparticles synthesis. Synthesis under pressure might be a way to overcome this limitation. Unfortunately, like the precipitation reactions at atmospheric pressure, the reported syntheses in hydrothermal conditions mainly focus on producing an intermediate solid that requires sulfidation in a second step (Table 3). Nevertheless, these syntheses expanded the range of available morphologies for the final oxysulfide nanoparticles.

In the late 2000's, Thirumalai *et al.* reported the hydrothermal synthesis of $\text{Gd}_2\text{O}_2\text{S}:\text{Eu}$ (Table 3, entries 1 and 2).^{99,100} Starting with an amorphous precipitate (obtained by adjusting the pH of an aqueous solution of $\text{Gd}(\text{NO}_3)_3$ with NaOH), they obtained $\text{Gd}(\text{OH})_3$ nanoscaled materials (hexagonal nanocrystals, nanotubes, nanobelts,...) after the hydrothermal treatment. The influence of the pH of precipitation and the temperature and duration of the hydrothermal define the morphology of the material. After impregnation of the solid with Eu^{3+} ions in an aqueous solution, sulfidation was performed using a CS_2 atmosphere generated by reaction of sulfur and carbon. The morphology of $\text{Gd}(\text{OH})_3$ was retained in the final $\text{Gd}_2\text{O}_2\text{S}:\text{Eu}$ nanopowder, with only slight size decreases. The nanomaterials are well-crystallized and the morphology was finely adjustable varying the reaction conditions. Unfortunately, an undescribed sulfidation process was performed before the annealing step. It is probably similar to the one mentioned before for the composite hydroxide method conducted by the same group.⁶⁸ Moreover, an original study on the photo-induced impedance was presented. Interestingly, the morphology was retained also with other lanthanides, as similar results were obtained by Thirumalai *et al.* on $\text{Y}_2\text{O}_2\text{S}:\text{Eu}$ (Table 3, entry 3).¹⁰¹

The oxysulfides nanoparticles obtained by hydrothermal syntheses were also extensively studied by Li, Ai, Liu *et al.* who obtained $\text{Y}_2\text{O}_2\text{S}:\text{Eu}, \text{Mg}, \text{Ti}$ nanoparticles (Table 3, entries 4, 5 and 6).^{90,102,103} This combination of doping ions is typical for persistent luminescence. Aqueous ammonia $\text{NH}_3 \cdot \text{H}_2\text{O}$ was used as a base for precipitation of hydroxides. The authors then inserted the dopants by solid-solid reaction in the annealing step with Eu_2O_3 , $\text{Mg}(\text{OH})_2 \cdot 4\text{Mg}(\text{CO}_3) \cdot 6\text{H}_2\text{O}$ and TiO_2 . Moreover, they noticed that using CS_2 formed *in situ*, rather than solid S_8 , was crucial to keep the morphology. With S_8 , the $\text{Y}(\text{OH})_3$ nanotubes turned into hexagonal nanoparticles after the annealing step.

The group of Cui and Liu also put great efforts on the characterization of such nanoparticles (Table 3, entries 7 and 8).^{104–108} Soluble sources ($\text{Eu}(\text{NO}_3)_3$, $\text{Mg}(\text{NO}_3)_2$ and $\text{Ti}(\text{O}i\text{Bu})_4$) were employed as reactants rather than solids for doping. Thus, a moderated sulfidation annealing temperature ($\leq 800\text{ }^\circ\text{C}$) was employed to yield $\text{Y}_2\text{O}_2\text{S}:\text{Eu},\text{Mg},\text{Ti}$ nanotubes. The synthesis,¹⁰⁴ the influence of earth-alkaline or metal M^{II} ion,^{105,108} the effect of the relative concentration of Mg^{II} and Ti^{IV} ,¹⁰⁶ and the Eu^{III} concentration were separately studied.¹⁰⁷ Later, Yuan *et al.* also reported mild conditions to synthesize composite $\text{Y}_2\text{O}_3:\text{Eu}/\text{Y}_2\text{O}_2\text{S}:\text{Eu}$ nanoparticles starting from soluble nitrate precursors (Table 3, entry 12).¹⁰⁹ The particles were crystalline but presented an irregular morphology. They were incorporated in dye-sensitized solar cells that were fabricated by the group. An enhancement of the cell efficiency was measured thanks to the light scattering properties of the nanocomposite.

A rare example of $\text{Lu}_2\text{O}_2\text{S}:\text{Eu}$ nanocrystals was reported in 2015 by Wang *et al.* (Table 3, entry 9). PVP K30 followed by a solution of thiourea in ethanol were added to lutetium nitrate dissolved in a mixture of water and ethylene glycol. Perfectly regular nanorods were obtained after a thermal treatment with a sulfidizing atmosphere. Here again, the sulfidizing step mechanism was not studied in detail.

In 2016, Cichos *et al.* tested an hydrothermal synthesis (Table 3, entry 10) to yield doped $\text{Gd}_2(\text{CO}_3)_3:\text{Eu}$ particles in comparison with reactions at atmospheric pressure.⁹⁶ The authors noticed that this method was rather not adapted to the synthesis of nanoparticles: several populations were obtained, including micrometric irregular crystals (Figure 13C).

The synthesis reported by Rosticher *et al.* is a promising exception (Table 3, entry 11).¹¹⁰ The crucial difference lies in the sulfidation method. An excess of water-soluble thioacetamide was incorporated before the hydrothermal heating after precipitation of amorphous $\text{Gd}(\text{OH})_3:\text{Eu},\text{Mg},\text{Ti}$ with NaOH . This allowed incorporation of sulfur before the annealing step, which could conveniently be performed under inert atmosphere. Its role was only to improve the crystallinity and the luminescence performances of the powder.

Author – Year Phase	Metal sources	Additives	Hydrothermal step	Annealing step	Morphology (Size)
<i>Thirumalai 2008</i> ⁸⁹ Gd₂O₃S:Eu	Gd(NO ₃) ₃ Eu(NO ₃) ₃	NaOH (pH ≈ 11)	130 - 150 °C 24 - 48 h	Ar/CS ₂ /S/C, 700 °C, 2-3 h	Nanotubes (50 nm x few μm)
<i>Thirumalai 2009</i> ¹⁰⁰ Gd₂O₃S:Eu	Gd(NO ₃) ₃ Eu(NO ₃) ₃	NaOH (7 ≤ pH ≤ 13)	100 - 180 °C 12 - 48 h	Ar/CS ₂ /S/C, 700 °C, 2-3 h	<u>Tunable</u> : Spheres (Ø 15 nm) + hexagonal crystals (20 - 30 nm) Nanosheets (15 x 80 nm ²), Nanobelts (25 nm x few μm) Nanotubes (15 x 200 nm ²), Nanorods (15 x 100 nm ²) Nanowires (15 x 250 nm ²)
<i>Thirumalai 2009</i> ¹⁰¹ Y₂O₃S:Eu	Y(NO ₃) ₃ Eu(NO ₃) ₃	NaOH (7 ≤ pH ≤ 13)	100 - 180 °C 12 - 48 h	Ar/CS ₂ /S/C, 600 °C, 2 h	<u>Tunable</u> : Spherical (15 nm) + hexagonal crystals (20 - 40 nm) Nanosheets (15 x 70 nm ²), Nanobelts (25 nm x few μm) Nanotubes (10 x 200 nm ²), Nanorods (10 x 70 nm ²) Nanowires (15 x 250 nm ²)
<i>Li 2009</i> ⁹⁰ Y₂O₃S:Eu,Mg,Ti	Y(NO ₃) ₃	NH ₃ ·H ₂ O	260 °C 5 h	1/ S ₈ in graphite (CS ₂), 800 °C, 4 h 2/ Eu ₂ O ₃ , TiO ₂ , Mg(OH) ₂ ·4Mg(CO ₃)·6H ₂ O, 1100 °C, 4 h	Nanorods (50 x 400 nm ²)
<i>Li 2010</i> ¹⁰² Y₂O₃S:Eu,Mg,Ti	Y(NO ₃) ₃	NaOH (pH ≈ 14)	180 °C 12 h	H ₂ , S ₈ , Na ₂ CO ₃ , Eu ₂ O ₃ , TiO ₂ , Mg(OH) ₂ ·4Mg(CO ₃)·6H ₂ O 600-800 °C, 4 h	Hexagonal nanoparticles (30 - 50 nm)
<i>Ai 2010</i> ¹⁰³ Y₂O₃S:Eu,Mg,Ti	Y(NO ₃) ₃	NaOH (pH ≈ 13)	180 °C 12 h	1/ S ₈ in graphite (CS ₂), 800 °C, 4 h 2/ Eu ₂ O ₃ , TiO ₂ , Mg(OH) ₂ ·4Mg(CO ₃)·6H ₂ O, 1100 °C, 4 h	Nanotubes (100 - 200 nm x 1 - 3 μm)
<i>Cui 2014</i> , ¹⁰⁴ <i>Liu 2014</i> , ¹⁰⁵ <i>Liu 2014</i> , ¹⁰⁶ <i>Cui 2014</i> ¹⁰⁷ Y₂O₃S:Eu,Mg,Ti	Y(NO ₃) ₃ Eu(NO ₃) ₃ Mg(NO ₃) ₂ Ti(OBu) ₄	NaOH (pH ≈ 13)	180 °C 12 h	S ₈ /C (CS ₂), 600-800 °C, 6 h	Nanotubes (200 nm x 3 μm)
<i>Huang 2014</i> ¹⁰⁸ Y₂O₃S:Eu,Zn,Ti	Y(NO ₃) ₃ Eu(NO ₃) ₃ Zn(NO ₃) ₂ Ti(OBu) ₄	NaOH (pH ≈ 13)	180 °C 12 h	S ₈ /C (CS ₂), 600-800 °C, 6 h	Nanotubes (200 nm x 3 μm)
<i>Wang 2015</i> Lu₂O₃S:Eu	Lu(NO ₃) ₃ Eu(NO ₃) ₃	NaOH (pH ≈ 11) Thiourea, PVP K30	200 °C 24 h	S/N ₂ , 600 °C, 2 h	Nanorods (20 x 500 nm ²)

<i>Cichos 2016</i> ⁹⁶ Gd₂O₂S:Eu	Gd(NO ₃) ₃ Eu(NO ₃) ₃	Urea	120 °C 12 h	S ₈ , Ar, 950 °C, 1 h	Irregular microcrystals (≥ 1 µm) + submicrospheres (300 - 500 nm)
<i>Rosticher 2016</i> ¹¹⁰ Gd₂O₂S:Eu,Mg,Ti	Gd(NO ₃) ₃ Eu(NO ₃) ₃ Mg(NO ₃) ₂ TiCl ₄	NaOH (pH ≈ 8) Thioacetamide	200 °C 2 h	Ar, 700 °C, 2 h	Nanospheres (Ø 20 nm) + faceted crystals (50 - 100 nm)
<i>Yuan 2016</i> ¹⁰⁹ Y₂O₃:Eu/Y₂O₂S:Eu	Y(NO ₃) ₃ Eu(NO ₃) ₃	NaOH	100 °C 5 h	S ₈ , N ₂ , 600 °C, 1 h	Irregular morphology (≤ 150 nm)

Table 3: Hydrothermal syntheses of Ln₂O₂S nanomaterials.

I.2.3.5. Conclusion

The formation of oxysulfide nanoparticles in water encounters several limits. Because of the aqueous solvent, excess oxygen favors the formation of intermediary phases such as hydroxides, hydroxycarbonates or oxides. Only an adequate sulfidation annealing step at high temperatures enables the formation of the oxysulfide nanoparticles. Nevertheless, it can affect the morphology of the nanoparticles with aggregation and sintering.

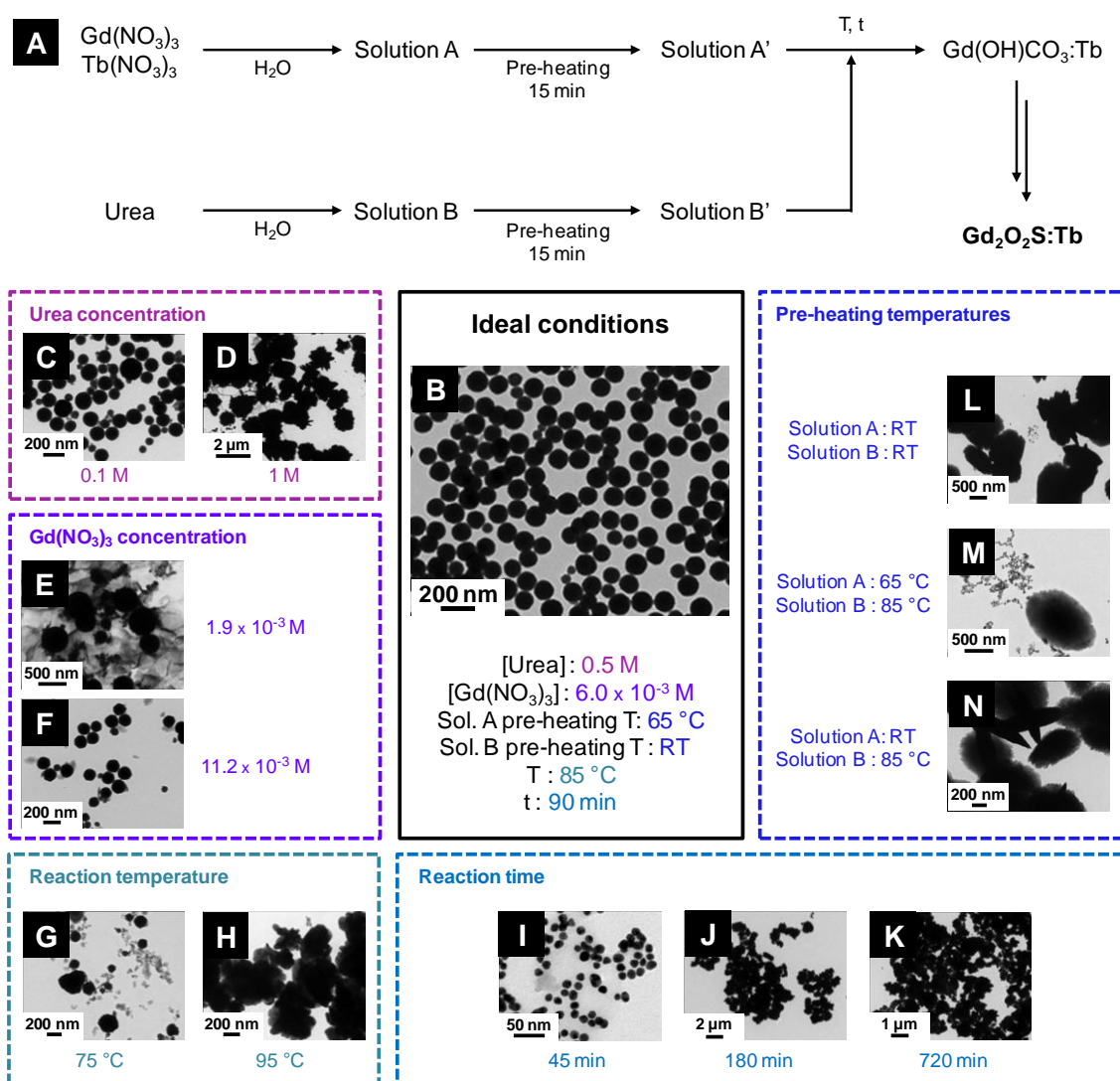


Figure 12: Optimized synthesis of $\text{Gd}_2\text{O}_2\text{S:Tb}$ nanoparticles by Hernández-Adame *et al.*⁹⁵ (A) Synthetic strategy: the authors first synthesized from nitrates and urea a doped hydroxycarbonate precursor that was later converted to the oxysulfide. TEM micrographs of the final $\text{Gd}_2\text{O}_2\text{S:Tb}$ nanoparticles in the optimized conditions (B) and of the different $\text{Gd}(\text{OH})(\text{CO}_3)$ particles obtained with through the optimization (C to N). Only one parameter is changed at once, the others being identical to the optimal conditions.

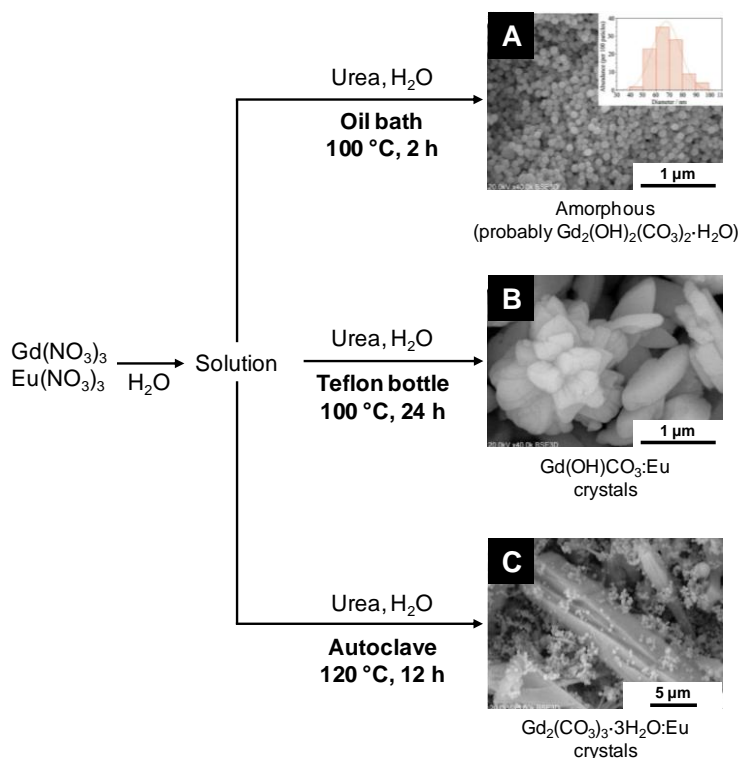


Figure 13: Structural and morphological variations of $\text{Gd}_2\text{O}_2\text{S}$ precursors obtained by Cichos *et al.*⁹⁶ Depending on the heating process, strong variations are observed: amorphous spherical nanoparticles (A with the size distribution in inset), hydroxycarbonate microcrystals (B) or carbonate microcrystals (C) can be obtained.

Moreover, the synthesis of the intermediary phases is also challenging. Precise reaction parameters have to be employed, with long optimization processes. In Figure 12 and Figure 13, we reminded for instance the works of Hernández-Adame *et al.* and Cichos *et al.* on the synthesis of doped gadolinium oxysulfide nanoparticles with urea. Not only the reaction temperature and time had a great effect on the final morphology of the intermediates: concentrations of the reactants, pre-heating temperatures, heating techniques are also crucial to obtain the desired product.

Working in organic medium then seems to be a suitable solution to overcome the excess available oxygen.

I.2.4. Syntheses in organic medium

The following section is dedicated to the reactions mainly performed in organic medium. Thanks to the availability of high boiling-point solvents, the temperature of the reaction medium can reach 200 - 300 °C much easier than in water. Moreover, the control of the nanoparticles size and morphology in organic solvents is easily attainable using surfactants.

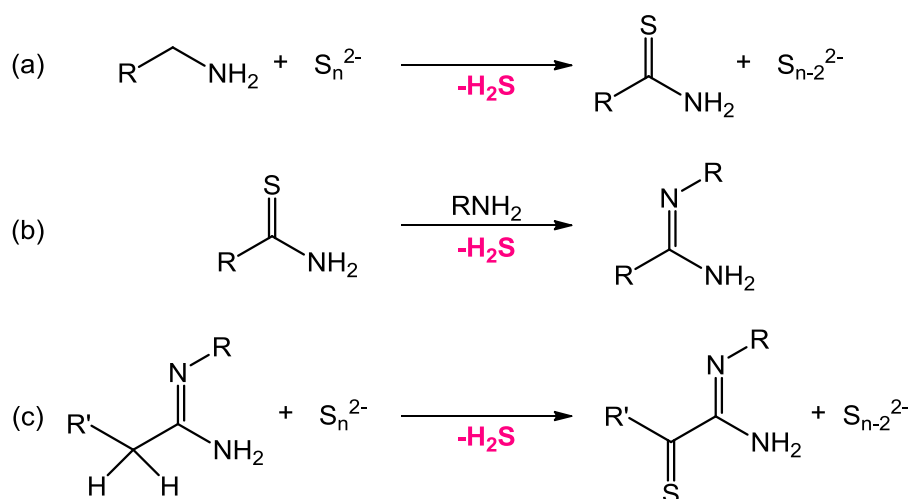


Figure 14: Reaction pathways releasing H₂S in a primary amine/elemental sulfur medium at 130 °C as proposed by Thomson *et al.*¹¹¹ Water traces can also react with the thioamide to form the corresponding amide and H₂S similarly to reaction (b).

In the case of lanthanide oxysulfide nanoparticles, we also note several benefits of organic medium for the stoichiometry:

the control of the oxygen concentration that is assured by the absence of excess reactive oxygen brought by water and reactions under inert atmosphere,

the use of molecular sulfur sources with for instance the possibility of decomposing hydrophobic single-source precursors (typically, lanthanide complexes with sulfur-containing ligands) or the dissolution and activation of elemental sulfur in primary amines, as they react to form reactive alkylammonium polysulfides which release *in situ* H₂S (Figure 14).¹¹¹

In both cases, the amount of reactive anions can be set to the desired value by playing on the concentration and the nature of the reactants. In water-based reactions, an excess of water in the precipitation step was followed by an excess of sulfur during the annealing step. Thus, organic medium brings the possibility to finely control the stoichiometry of the anions and one could expect that it leads to different oxysulfide compositions apart from thermodynamics considerations.

I.2.4.1. Decomposition of sulfur-containing single-source precursors

The decomposition of lanthanide complexes bearing ligands with sulfur in the presence of dioxygen can lead to oxysulfide nanoparticles. It was shown for the first time in 2006 in a communication by Zhao *et al.* who developed the synthesis of thin monodisperse hexagonal nanoplates of Eu₂O₂S, Sm₂O₂S and Gd₂O₂S.¹¹² In a mixture of organic solvents and surfactants typical for colloidal synthesis (1-octadecene, oleic acid and oleylamine),

$[\text{Eu}(\text{phen})(\text{ddtc})_3]$ (phen = 1,10-phenanthroline, ddtc = diethyldithiocarbamate; Figure 15) was decomposed under air at 290 °C in 45 minutes, forming anisotropic nanocrystals ($15 \times 1.7 \text{ nm}^2$, Figure 16). For the first time, the observation of self-assembled oxysulfide nanoplates to nanowires was made (Figure 16A, B and C). The nanoplates were piled one above each other, because of the hydrophobic interaction between the surface surfactant chains of oleic acid (oleylamine-metal bonds are weaker than oleic acid-metal bonds).¹¹³

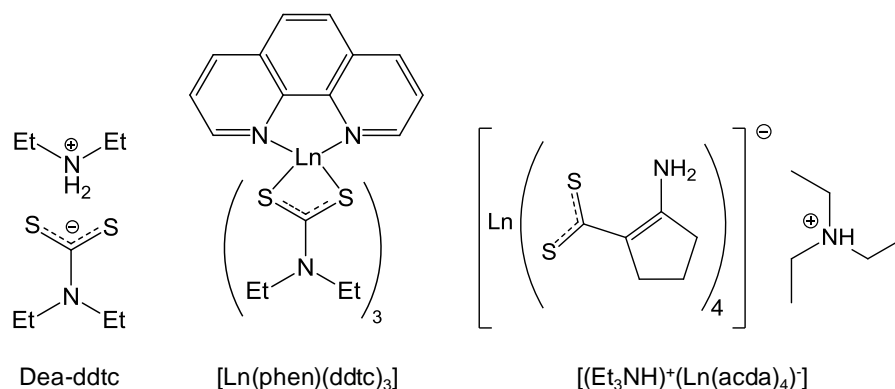


Figure 15: Chemical formulas of diethylammonium diethyldithiocarbamate (dea-ddtc), $[\text{Ln}(\text{1,10-phenanthroline})(\text{diethyldithiocarbamate})_3]$ complex ($[\text{Ln}(\text{phen})(\text{ddtc})_3]$), and Triethylammonium of tetra(2-aminocyclopentenedithiocarbamate) lanthanide ($[(\text{Et}_3\text{NH})^+(\text{Ln}(\text{acda})_4)^-]$)

Interestingly, EuS (Eu^{II}) nanocrystals were obtained with the same synthesis but under inert atmosphere with oleylamine alone (which played the role of reducing agent).¹¹⁴ A more detailed study on the pyrolysis of the $[\text{Ln}(\text{phen})(\text{ddtc})_3]$ precursor and the nanoparticles properties was also reported. A noticeable work using the same strategy was conducted by Tan *et al.* in 2016.⁵⁸ In comparison with europium, the decomposition of $[\text{La}(\text{phen})(\text{ddtc})_3]$ and $[\text{Pr}(\text{phen})(\text{ddtc})_3]$ only yielded LaS and PrS. From oxidation of the sulfides, oxysulfates nanoparticles of $\text{La}_2\text{O}_2\text{SO}_4$ and $\text{Pr}_2\text{O}_2\text{SO}_4$ were obtained. The nanoparticles of $\text{Eu}_2\text{O}_2\text{S}$, $\text{La}_2\text{O}_2\text{SO}_4$ and $\text{Pr}_2\text{O}_2\text{SO}_4$ were then tested for the water-gas-shift reaction.

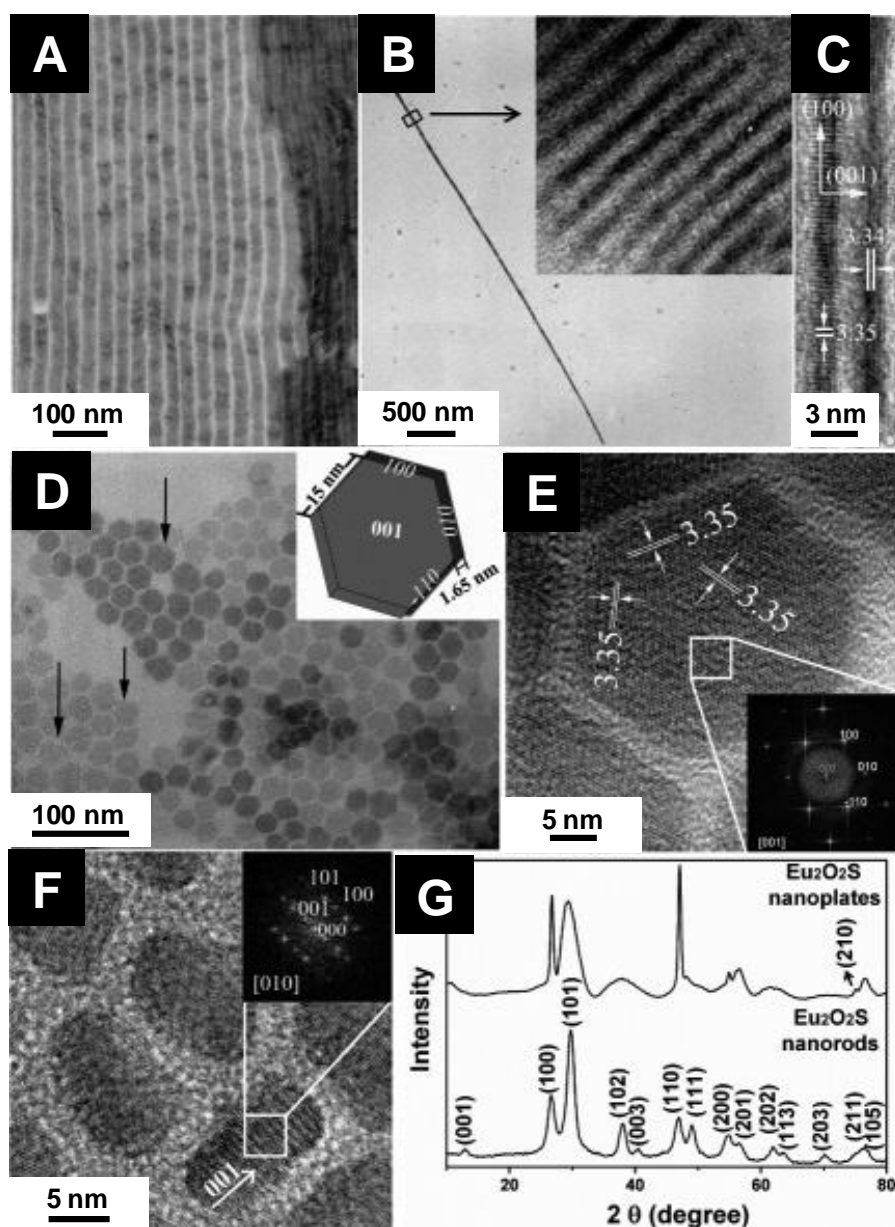


Figure 16: Characterization of $\text{Eu}_2\text{O}_2\text{S}$ nanoparticles obtained by decomposition of $[\text{Eu}(\text{phen})(\text{ddtc})_3]$ by Zhao *et al.*¹¹² TEM micrographs of self-assemblies formed by the hexagonal nanoplates (A), of a single nanowire (B) with a zoom in inset and HRTEM micrograph of two nanowires (C). (D) TEM micrographs of hexagonal nanoplates lying on their flat surface. Inset: representation of a single nanoplate. HRTEM images of $\text{Eu}_2\text{O}_2\text{S}$ nanoplates lying on their flat surface (E) and of short nanorods (F). Insets are FFT of the indicated regions. (G) Powder XRD pattern of the $\text{Eu}_2\text{O}_2\text{S}$ nanoparticles.

Lin *et al.* obtained europium- and terbium-doped $\text{Gd}_2\text{O}_2\text{S}$ and europium-doped $\text{Tb}_2\text{O}_2\text{S}$ by decomposition of the same precursor. Although the morphology of the nanoparticles was not perfectly regular, and the crystallinity not optimal, an extensive luminescence study was performed and biologic tests (*in vivo* imaging, cell viability) were conducted. The latter required a coating with 3-aminopropyltriethoxysilane (Figure 10) and grafting of methoxy-

polyethyleneglycol and Alexa Fluor 660 (photostable red dye which emits photons in the wavelength range of 630 - 650 nm).

In 2012, He *et al.* described a similar decomposition of a precursor formed *in situ*. The reaction yielded europium oxysulfide nanorods. In this synthesis, europium oleate, oleylamine, 1,10-phenanthroline and dodecanethiol were heated at 320 °C under inert atmosphere before hot injection of diethylammonium diethyldithiocarbamate (dea-ddtc, Figure 15) dissolved in oleylamine. Nanorods were isolated after 1 hour of reaction. The oxygen source was not explicitly discussed, but it was likely the oleate ions in the europium-oleate complex. Even if dea-ddtc is the most probable sulfur source, the introduction of dodecanethiol was not discussed. Nevertheless, this report showed that forming the single-source precursor *in situ* was a viable strategy. The non-stoichiometric character of the $\text{Eu}_{2+x}\text{O}_2\text{S}$ nanoparticles was evidenced by the Eu:S ratio measured by EDS. Non-stoichiometry is attributed to Eu^{II} in the solid and was already observed for the bulk phase in the 1960's by Ballestracci and Quezel who estimated that 1 % of the europium atoms were divalent thanks to neutron diffraction and magnetic measurements.^{48,49} He *et al.* also described magnetic properties of europium oxysulfide nanoparticles and confirm the $\text{Eu}^{\text{II}}/\text{Eu}^{\text{III}}$ ratio, even if the average composition $\text{Eu}_{2.11}\text{O}_2\text{S}$ corresponds to about 15 % of Eu^{II} . Moreover, an electrophoretic deposition of the nanorods was proposed.

Ghosh *et al.* reported another precursor to obtain $\text{Eu}_2\text{O}_2\text{S}$ nanoparticles.⁵⁹ According to the authors, $\text{La}_2\text{O}_2\text{S}$ and $\text{Nd}_2\text{O}_2\text{S}$ can also be prepared with a similar procedure. Synthesized from europium nitrate, triethylamine (Et_3N) and 2-aminocyclopentene-1-dithiocarboxylic acid (Hacda), $[(\text{Et}_3\text{NH})^+(\text{Eu}(\text{acda})_4)^-]$ was decomposed via three different methods (Figure 17).

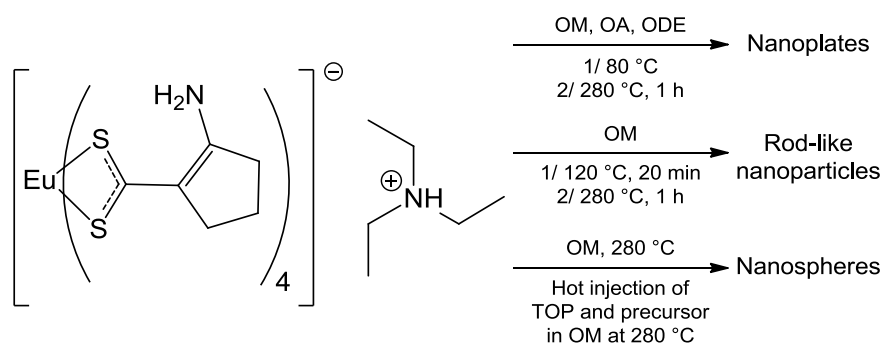


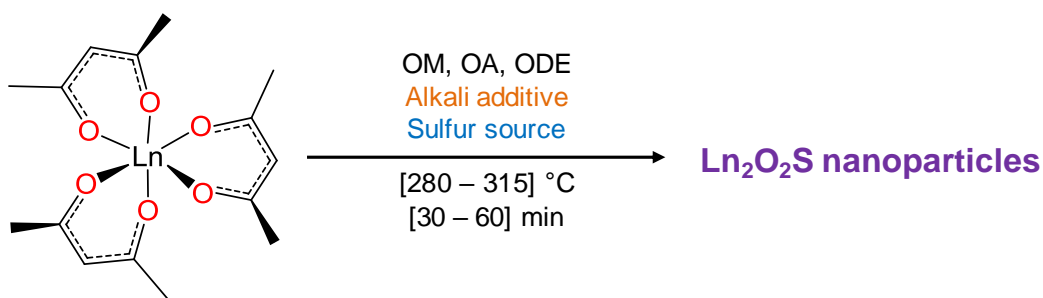
Figure 17: Triethylammonium of tetra(2-aminocyclopentenedithiocarbamate) europium ($[(\text{Et}_3\text{NH})^+(\text{Eu}(\text{acda})_4)^-]$) decomposition in organic solvents by Ghosh *et al.*

By heating the precursor in an OM/OA/ODE mixture, ultrathin nanoplates of $\text{Eu}_2\text{O}_2\text{S}$ were obtained. However, the 0.3 nm reported thickness is quite surprising, as it would represent a

single monolayer of the solid, and there is no correlated peak extinction in the corresponding XRD pattern. Using similar conditions with oleylamine only led to rod-like nanoparticles ($7 \times 3 \text{ nm}^2$). Finally, hot injection of $[(\text{Et}_3\text{NH})^+(\text{Eu}(\text{acda})_4)^-]$ and trioctylphosphine (TOP) led to polydisperse nanospheres with an average diameter of 13 nm. The catalytic activity of $\text{Eu}_2\text{O}_2\text{S}$, and especially its activity as a peroxidase mimic, was deeply investigated. Because $\text{Eu}_2\text{O}_2\text{S}$ catalyzed the oxidation of 3,3',5,5'-tetramethylbenzidine (TMB) in presence of H_2O_2 and neither $\text{La}_2\text{O}_2\text{S}$ nor $\text{Nd}_2\text{O}_2\text{S}$ succeeded in it, the authors concluded to a mechanism involving the $\text{Eu}^{\text{III}}/\text{Eu}^{\text{II}}$ redox couple.

I.2.4.2. Syntheses with high boiling-point organic solvents at atmospheric pressure

Although colloidal synthesis in organic solvents have been used for years in the synthesis of metal and metal oxide nanoparticles, the first report for metal oxysulfides was published by Ding *et al.* in 2011.¹¹⁵ Lanthanide acetylacetonate $\text{Ln}(\text{acac})_3$ (1 equiv.), elemental sulfur (1 equiv.) and sodium acetylacetonate (1 equiv.) were added in an OM/OA/ODE mixture and heated for 45 min. at 310 °C under inert atmosphere after degassing under vacuum at 120 °C. Size-monodisperse hexagonal nanoplates of $\text{Ln}_2\text{O}_2\text{S}$ were obtained. They were thin (a few monolayers) and 5 - 40 nm wide depending on the lanthanide. The composition of the powder showed a lack of sulfur ($\text{Na}_{0.4}\text{La}_{1.6}\text{O}_2\text{S}_{0.6}$), which was attributed to terminal $[\text{Ln}_2\text{O}_2]^{2+}$ layers. The crucial advantage of this method is its versatility: $\text{La}_2\text{O}_2\text{S}$, $\text{Pr}_2\text{O}_2\text{S}$, $\text{Nd}_2\text{O}_2\text{S}$, $\text{Sm}_2\text{O}_2\text{S}$, $\text{Eu}_2\text{O}_2\text{S}$, $\text{Gd}_2\text{O}_2\text{S}$, $\text{Tb}_2\text{O}_2\text{S}$ were prepared. The sodium ions, added in stoichiometric amounts, were proposed to help the crystallization and favor the oxysulfide formation. The hypothesis of the authors is that the close ionic radii of sodium ($r(\text{Na}^{\text{I}}(\text{VII})) = 1.26 \text{ \AA}$) and larger lanthanide ions ($r(\text{La}^{\text{III}}(\text{VII})) = 1.24 \text{ \AA}$ to $r(\text{Tb}^{\text{III}}(\text{VII})) = 1.12 \text{ \AA}$) enable cation exchanges in the solid and favors the oxysulfide crystallization. Lithium ions were tested and were efficient for $\text{Y}_2\text{O}_2\text{S}$ synthesis. In 2013, a more complete study (experimental study and calculations based on density functional theory) on the alkaline additives on the formation and morphology of the obtained nanocrystals also showed the possible use of potassium to synthesize oxysulfide nanoparticles ($\text{La}_2\text{O}_2\text{S}$, $\text{Eu}_2\text{O}_2\text{S}$, $\text{Gd}_2\text{O}_2\text{S}$, and $\text{Yb}_2\text{O}_2\text{S}$).¹¹⁶ In 2017, Lei *et al.* investigated the roles of yttrium and sodium in the formation and growth of $\text{Gd}_2\text{O}_2\text{S}$, by using them separately or combined. They also demonstrated that a large excess of sulfur allows forming gadolinium oxysulfide nanoplates without adding sodium ions.¹¹⁷



Author Year	Sulfur source	Additives	Reaction conditions	Obtained phases (morphology)
Ding 2011 ¹¹⁵	Elemental sulfur 2 equiv.	Na(acac) (1 equiv.)	310 °C 45 min	Hex. nanoplates La ₂ O ₂ S (Ø = 22 nm) Pr ₂ O ₂ S (Ø = 20 - 40 nm) Nd ₂ O ₂ S (Ø = 15 - 30 nm) Sm ₂ O ₂ S (Ø = 20 - 40 nm) Eu ₂ O ₂ S (Ø = 10 - 30 nm) Gd ₂ O ₂ S (Ø = 5 - 10 nm) Tb ₂ O ₂ S (Ø = 15 - 25 nm)
	Elemental sulfur 2 equiv.	Li(acac) (1 equiv.)	310 °C 45 min	Y ₂ O ₂ S (nanoparticles, Ø < 5 nm)
Zhang 2013 ¹¹⁶	Elemental sulfur 2 equiv.	Li(acac) (1 equiv.)	310 °C 30 min	La ₂ O ₂ S (hex. nanoplates, Ø = 9 nm)
	Elemental sulfur 2 equiv.	K(acac) (1 equiv.)	310 °C 30 min	La ₂ O ₂ S (hex. nanoplates, Ø = 40 - 50 nm) Eu ₂ O ₂ S (irreg. nanoplates, Ø = 10 - 15 nm) Gd ₂ O ₂ S (irreg. nanoplates, Ø = 11 nm) Yb ₂ O ₂ S (nanoparticles, Ø = 1 nm)
Gu 2013 ¹¹⁸	H ₂ S	/	280 °C 1 h	Y ₂ O ₂ S (irreg. nanoplates, Ø < 10 nm) Eu ₂ O ₂ S (hex. nanoplates, Ø ≈ 10 nm) Gd ₂ O ₂ S (irreg. nanoplates, Ø < 10 nm) Er ₂ O ₂ S (irreg. nanoplates, Ø < 20 nm) Yb ₂ O ₂ S (flower-like assemblies)
Lei 2017 ¹¹⁷	Elemental sulfur 20 equiv.	/	315 °C 1 h	Gd ₂ O ₂ S (nanoplates, Ø = 7 nm)
	Elemental sulfur 2 equiv.	Na(acac) (1 equiv.) Y(acac) ₃ (0.2 equiv.)	315 °C 1 h	Gd ₂ O ₂ S (nanoplates, Ø = 40 nm)
	Elemental sulfur 20 equiv.	Na(acac) (1 equiv.) Y(acac) ₃ (0.2 equiv.)	315 °C 1 h	Gd ₂ O ₂ S (flower-like assemblies)

Figure 18: Ding's alkali-based synthesis of lanthanide oxysulfide and its derivatives. The number of equivalent ("equiv." in the table) is the molar ratio between the reactant and metal. The term "hex." stands for "hexagonal" and "irreg." for "irregular".

In 2017, Tan *et al.* announced the formation iron/sodium co-doped lanthanum oxysulfide nanoparticles $(\text{Na,L a})_2\text{O}_2\text{S:Fe}$.¹¹⁹ Such doping with light transition metal is very rare due to ionic radii mismatch. Thus, according to the authors, only a limited amount of iron would have been able to substitute lanthanum, and surprisingly, no contraction of the lattice was observed despite the ionic radii difference ($r(\text{La}^{\text{III}}(\text{VII})) = 1.24 \text{ \AA}$; $r(\text{Fe}^{\text{III}}) \approx 0.85 \text{ \AA}$). Even though such iron doping would be very interesting for catalytic features, it is quite unclear that iron was well inserted in the $\text{La}_2\text{O}_2\text{S}$ phase. In 2015, Jiang *et al.* employed Ding's synthesis and demonstrated the possible use of $\text{La}_2\text{O}_2\text{S:Eu}$ nanoparticles as optical temperature sensors ("nanothermometer").¹²⁰

Gu *et al.* managed to obtain yttrium, gadolinium, erbium and ytterbium oxysulfide nanoplates using oleylamine as only solvent and H_2S as sulfurating agent. $\text{Ln}(\text{acac})_3$ and oleylamine were degassed at 120°C and then heated at 280°C for 1 hour under a $\text{H}_2\text{S}/\text{N}_2$ flow (20/80 v/v, 60 mL/min) to yield $\text{Ln}_2\text{O}_2\text{S}$ nanoplates.¹¹⁸ Again, sodium ions were shown to help the crystallization of the nanoplates but were not necessary in this case. $\text{Y}_2\text{O}_2\text{S}$, $\text{Eu}_2\text{O}_2\text{S}$, $\text{Gd}_2\text{O}_2\text{S}$, $\text{Er}_2\text{O}_2\text{S}$ and $\text{Yb}_2\text{O}_2\text{S}$ were prepared by this route.

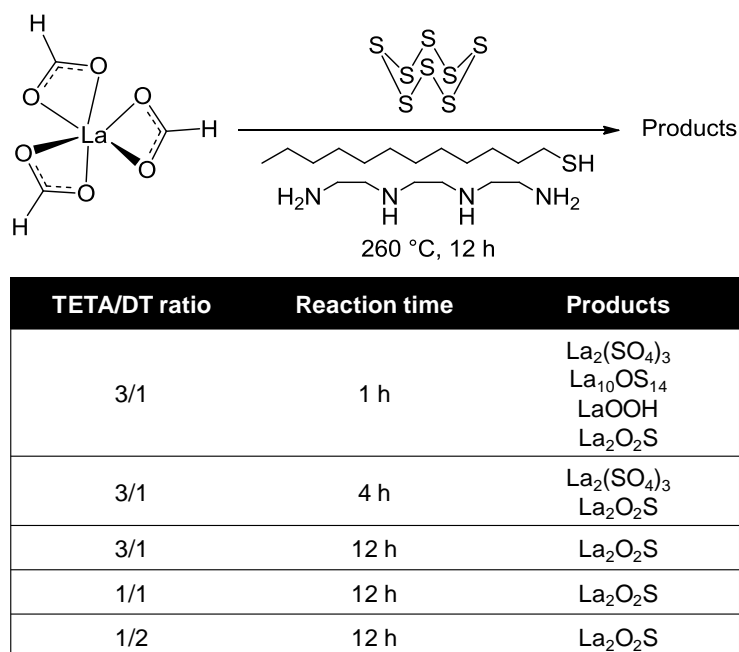


Figure 19: Reaction of Ma *et al.* to yield $\text{La}_2\text{O}_2\text{S}$ nanoparticles.

Another method was reported in 2013 by Ma *et al.* to synthesize europium-doped lanthanum oxysulfide $\text{La}_2\text{O}_2\text{S:Eu}$. Lanthanide formates $\text{La}(\text{HCOO})_3$ and $\text{Eu}(\text{HCOO})_3$ were heated at 260°C in the presence of elemental sulfur (2 equiv. of S) in triethylenetetramine (TETA) and dodecanethiol (DT) (Figure 19). After 12 hours, $\text{La}_2\text{O}_2\text{S:Eu}$ nanocrystals were obtained with

triethylenetetramine/dodecanethiol ratio being 1:2 and the nanospheres diameter was around 100 nm. Without dodecanethiol, 100 nm in width and 10 nm in thickness $\text{La}_2\text{O}_2\text{S:Eu}$ nanoplates were obtained.

The amine/thiol ratio influenced the morphology. When the TETA/DT ratio was 3:1 or 1:1, micronic structures were obtained. Interestingly, other precursors ($\text{La}(\text{NO}_3)_3$, LaCl_3 , La_2O_3 , and $\text{La}(\text{OH})_3$) were not selective enough or did not completely react (impurities of $\text{La}(\text{OH})_3$ or La_2O_3 based on XRD). Also, shorter reaction times with TETA/DT = 3:1 for the exhibited the rare $\text{La}_{10}\text{OS}_{14}$ intermediary phase with LaOOH and $\text{La}_2(\text{SO}_4)_3$. Although the crystals are large and the selectivity can be improved, it is to the best of our knowledge the only occurrence of a promising protocol for nanoscaled $\text{Ln}_{10}\text{OS}_{14}$.

I.2.4.3. Solvothermal syntheses in autoclave

In 2000, Li *et al.* tested a direct and simple solvothermal sulfidation process for numerous lanthanide oxides. Ln_xO_y powders ($\text{Ln} = \text{Y}, \text{Sc}, \text{La}, \text{Pr}, \text{Nd}, \text{Eu}, \text{Sm}, \text{Gd}, \text{Ho}, \text{Er}, \text{Yb}$ or Lu) and S_8 were suspended in ethylenediamine and heated in autoclave at 150 °C for 8 hours.¹²¹ Aggregated and irregularly-shaped crystalline spherical nanoparticles of $\text{Pr}_2\text{O}_2\text{S}$, $\text{Eu}_2\text{O}_2\text{S}$ and $\text{Gd}_2\text{O}_2\text{S}$ were obtained with this method (< 50 nm). The authors suggested an anion-exchange mechanism between the O^{II} in the Ln_xO_y crystal and the S^{II} available in polyanions when S_8 reacts with TETA. They supposed next that oxysulfide nuclei could leave the surface of the oxide to grow apart.

For $\text{Ln} = \text{La}, \text{Nd}, \text{Sm}, \text{Ho}$ and Er , the conversion was incomplete ($\text{Ln}_2\text{O}_2\text{S}$ and Ln_xO_y on the XRD pattern) and no change was observed with longer reaction times. Only the starting oxide was observed for $\text{Ln} = \text{Y}, \text{Sc}, \text{Yb}$ and Lu . In 2012, $\text{Gd}_2\text{O}_2\text{S:Eu}$ and $\text{Gd}_2\text{O}_2\text{S:Er,Yb}$ nanoplates were also obtained by Liu *et al.* in ethylenediamine using gadolinium nitrate and elemental sulfur.¹²² PVP (K29-32) or OM was added to a solution of the lanthanide nitrate in ethanol. The resulting solution was added dropwise into ethylenediamine and sulfur. The autoclave was heated at 220 °C for at least 4 hours to form crystalline hexagonal nanoplates. With OM, subsequent aggregation in flower-like structures was observed. Separated nanocrystals of irregular shape were obtained with PVP. $\text{Y}_2\text{O}_2\text{S:Eu}$ and $\text{Y}_2\text{O}_2\text{S:Er,Yb}$ were obtained from yttrium acetate by the same group with PVP and a thermal treatment at 250 °C for 24 hours.¹²³ Various self-assemblies of the nanoparticles were formed, depending on the presence of PVP, sulfur concentration, and so on.

Song *et al.* obtained $\text{Gd}_2\text{O}_2\text{S}:\text{Eu}$ and $\text{Gd}_2\text{O}_2\text{S}:\text{Tb}$ nanospheres from the solvothermal treatment of lanthanide nitrates in a mixture of ethanol and ethylene glycol, containing polyvinylpyrrolidone (PVP K30, $M = 40000 \text{ g/mol}$) and thiourea. The autoclave was heated at 200°C for 24 hours and the isolated solid was then sulfidized in a N_2/S atmosphere at $600\text{--}800^\circ\text{C}$ to form doped gadolinium oxysulfide nanoparticles. PVP is believed to be responsible for the spherical morphology, and polymer residues were evidenced on the rough surface of the nanoparticles. They presented a good crystallinity and a good monodispersity in diameter. Their size was tunable between 150 nm and $1.25 \mu\text{m}$ by varying the PVP content and the ethanol/ethylene glycol ratio. A similar strategy was used by Deng *et al.* to yield $\text{Y}_2\text{O}_2\text{S}:\text{Sm}$ hollow nanospheres ($\varnothing = 140 - 200 \text{ nm}$).¹²⁴ The thermal treatment was based on Li's work ($\text{Y}_2\text{O}_2\text{S}$ nanoparticles hydrothermal synthesis, Table 3, entry 4).⁹⁰ The authors first proposed a mechanism involving $\text{H}_2\text{S}/\text{CO}_2$ bubbles to explain the holes, but finally declared in a second paper on $\text{Y}_2\text{O}_2\text{S}:\text{Eu},\text{Mg},\text{Ti}$ nanoparticles that NH_3/CO_2 bubbles were more likely the templating agents.¹²⁵ Similarly to Song's spheres, the surface was rough and the nanoparticles seemed to be constituted with smaller units.

Thirumalai *et al.* have mainly focused their work on water-based syntheses, but also prepared various morphologies of $\text{Gd}_2\text{O}_2\text{S}:\text{Eu}$ nanoparticles in oleylamine.¹²⁶ $\text{GdCl}_3 \cdot 6\text{H}_2\text{O}$ and $\text{EuCl}_3 \cdot 6\text{H}_2\text{O}$ were introduced in hot oleylamine and various amounts of thioacetamide were added. The resulting solution was heated in an autoclave at $120 - 240^\circ\text{C}$ for $12 - 24$ hours. Flower-like nanocrystals ($\approx 10 \text{ nm}$), nanospheres ($\varnothing = 5 - 10 \text{ nm}$) and nanorods of various lengths ($\varnothing = 6 \text{ nm}$) were obtained depending on the reaction conditions and the thioacetamide amount. An excess of sulfur was proposed to be mandatory to ensure a high chemical potential, which promoted the formation of nanorods. Despite the good morphology control, the XRD patterns of the nanoparticles showed a poor crystallinity of the materials: only broad peaks were observed. It is intriguing because nanorods presented big crystal domains, and HRTEM images showed large and regular lattices.

I.2.3. Conclusion: selecting the best synthetic strategy

Many synthetic conditions are available for the synthesis of lanthanide oxysulfide nanoparticles. Yttrium, lanthanum and gadolinium oxysulfide nanoparticles are more commonly achieved. Both aqueous and organic media are suitable for the synthesis, but obviously require different compounds and conditions to obtain the targeted oxysulfide phase. In light of the results obtained for the synthesis of lanthanide oxysulfide nanoparticles, the synthesis of Ding *et al.* seemed to be the most appropriate for future developments in catalysis and/or photocatalysis. The nanoparticles obtained are very small (below 25 nm) and thus exhibit a high surface-to-volume ratio. The use of dissolved elemental sulfur and the well-controlled oxygen amount are desirable: they enable us to obtain the crystalline oxysulfide nanoparticles at reasonable temperatures without annealing under sulfidating toxic atmospheres which can also sinter the nanocrystals. Thanks to the organic ligands, the nanoparticles can be redispersed in organic solvents. Also, the synthesis is versatile and is adapted to the synthesis of at least eight lanthanides already, meaning that we will be able to play on the magnetic and optical properties of the objects if necessary *via* the number of *4f* electrons. However, one can notice that Ce₂O₂S nanoparticles were not achieved this way, despite the possibility to use the promising redox couple Ce^{III}/Ce^{IV} for catalytic applications. The following chapter is thus dedicated to the synthesis of cerium-containing Ln₂O₂S nanoparticles in organic medium and the study of their reactivity, which happened to be more complex than expected.

References

- (1) Eastman, E. D.; Brewer, L.; Bromley, L. A.; Gilles, P. W.; Lofgren, N. L. *J. Am. Chem. Soc.* **1951**, 73 (8), 3896.
- (2) Flahaut, J.; Guittard, M.; Patrie, M. *Bull. Soc. Chim. Fr.* **1958**, 7, 990.
- (3) Sterba, J. *Ann. Chim. Phys.* **1904**, 2, 193.
- (4) Biltz, W. *Berichte der Dtsch. Chem. Gesellschaft* **1908**, 41 (3), 3341.
- (5) Klemm, W.; Meisel, K.; v. Vogel, H. U. *Zeitschrift für Anorg. und Allg. Chemie* **1930**, 190 (1), 123.
- (6) Pitha, J. J.; Smith, A. L.; Ward, R. *J. Am. Chem. Soc.* **1947**, 69 (8), 1870.
- (7) Zachariasen, W. H. *Acta Crystallogr.* **1949**, 2 (1), 60.
- (8) Marcon, J.-P. *Comptes Rendus Hebd. l'Académie des Sci. - Série C* **1967**, 265, 235.
- (9) Haire, R. G.; Fahey, J. A. *J. Inorg. Nucl. Chem.* **1977**, 39 (5), 837.
- (10) Baybarz, R. D.; Fahey, J. A.; Haire, R. G. *J. Inorg. Nucl. Chem.* **1974**, 36 (9), 2023.
- (11) Julien-Pouzol, M.; Jaulmes, S.; Guittard, M.; Laruelle, P. *J. Solid State Chem.* **1978**, 26 (2), 185.
- (12) Khodadad, P.; Tek, T.; Flahaut, J.; Domange, L. *Comptes Rendus Hebd. l'Académie des Sci.* **1965**, 260 (8), 2235.
- (13) Ballestracci, R. *Mater. Res. Bull.* **1967**, 2 (7), 473.
- (14) Wichelhaus, W. *Naturwissenschaften* **1978**, 65 (11), 593.
- (15) Lissner, F.; Schleid, T. *Zeitschrift für Naturforsch. B* **1992**, 47 (11), 1614.
- (16) Wontcheu, J.; Schleid, T. *Zeitschrift für Krist. - New Cryst. Struct.* **2003**, 218 (3), 285.
- (17) Schleid, T. *Eur. J. Solid State Inorg. Chem.* **1991**, 28, 557.
- (18) Schleid, T. *Zeitschrift für Anorg. und Allg. Chemie* **1991**, 602 (1), 39.
- (19) Range, K.-J.; Lange, K. G.; Gietl, A. *J. Less Common Met.* **1990**, 158 (1), 137.
- (20) Schleid, T. *Eur. J. Solid State Inorg. Chem.* **1992**, 29 (6), 1015.
- (21) Carré, D.; Laruelle, P.; Besançon, P. *Comptes Rendus Hebd. l'Académie des Sci. - Série C* **1970**, 270 (6), 537.
- (22) Besançon, P. *J. Solid State Chem.* **1973**, 7 (2), 232.
- (23) Besançon, P.; Carré, D.; Guittard, M.; Flahaut, J. *Comptes Rendus Hebd. l'Académie des Sci. - Série C* **1970**, 271 (12), 679.
- (24) Besançon, P.; Carré, D.; Laruelle, P. *Acta Crystallogr. Sect. B Struct. Crystallogr. Cryst. Chem.* **1973**, 29 (5), 1064.
- (25) Schleid, T.; Weber, F. A. *Zeitschrift für Krist. - New Cryst. Struct.* **1998**, 213 (1–4), 1998.
- (26) Marcon, J.-P. *Comptes Rendus Hebd. l'Académie des Sci. - Série C* **1967**, 264 (17), 1475.
- (27) Dugué, J.; Carré, D.; Guittard, M. *Acta Crystallogr.* **1978**, B34, 3564.
- (28) Wichelhaus, W. *Angew. Chemie Int. Ed. English* **1978**, 17 (6), 451.
- (29) Dugué, J.; Carré, D.; Guittard, M. *Acta Crystallogr.* **1979**, B35, 1550.
- (30) Royce, M. R. U.S. Patent N°3418246, 1968.
- (31) Jüstel, T.; Nikol, H.; Ronda, C. *Angew. Chemie Int. Ed.* **1998**, 37 (22), 3084.
- (32) Ronda, C. ; Jüstel, T.; Nikol, H. *J. Alloys Compd.* **1998**, 275–277, 669.
- (33) Resende, L. V.; Morais, C. A. *Miner. Eng.* **2015**, 70, 217.

- (34) Alves, R. V.; Buchanan, R. A.; Wickersheim, K. A.; Yates, E. A. C. *J. Appl. Phys.* **1971**, *42* (8), 3043.
- (35) Markushev, V. M.; Ter-Gabriélyan, N. É.; Briskina, C. M.; Belan, V. R.; Zolin, V. F. *Sov. J. Quantum Electron.* **1990**, *20* (7), 773.
- (36) Iparraguirre, I.; Azkargorta, J.; Merdrignac-Conanec, O.; Al-Saleh, M.; Chlique, C.; Zhang, X.; Balda, R.; Fernández, J. *Opt. Express* **2012**, *20* (21), 23690.
- (37) Zhu, K.; Ding, W.; Sun, W.; Han, P.; Wang, L.; Zhang, Q. *J. Mater. Sci. Mater. Electron.* **2016**, *27* (3), 2379.
- (38) He, W.; Zhang, J.; Wang, L.; Zhang, Q. *J. Rare Earths* **2009**, *27* (2), 231.
- (39) Sun, W.; Zhu, K.; Xu, H.; Yang, X.; Yu, M.; Li, X.; Wang, L.; Zhang, Q. *J. Mater. Sci. Mater. Electron.* **2017**, *28* (1), 697.
- (40) Rossner, W.; Grabmaier, B. C. *J. Lumin.* **1991**, *48–49* (1), 29.
- (41) Brixner, L. H. *Mater. Chem. Phys.* **1987**, *16* (3–4), 253.
- (42) Michail, C. M.; Fountos, G. P.; Liaparinos, P. F.; Kalyvas, N. E.; Valais, I.; Kandarakis, I. S.; Panayiotakis, G. S. *Med. Phys.* **2010**, *37*, 3694.
- (43) Auzel, F. *Chem. Rev.* **2004**, *104* (1), 139.
- (44) Ajithkumar, G.; Yoo, B.; Goral, D. E.; Hornsby, P. J.; Lin, A.-L.; Ladiwala, U.; Dravid, V. P.; Sardar, D. K. *J. Mater. Chem. B* **2013**, *1* (11), 1561.
- (45) Jain, A.; Kumar, A.; Dhoble, S. J.; Peshwe, D. R. *Renew. Sustain. Energy Rev.* **2016**, *65*, 135.
- (46) Leverenz, H. W. *Science* **1949**, *109* (2826), 183.
- (47) Zhang, P.; Hong, Z.; Wang, M.; Fang, X.; Qian, G.; Wang, Z. *J. Lumin.* **2005**, *113* (1–2), 89.
- (48) Ballestracci, R.; Bertaut, E. F.; Quezel, G. *J. Phys. Chem. Solids* **1968**, *29* (6), 1001.
- (49) Quezel, G.; Ballestracci, R.; Rossat-Mignod, J. *J. Phys. Chem. Solids* **1970**, *31* (4), 669.
- (50) Biondo, V.; Sarvezuk, P. W. C.; Ivashita, F. F.; Silva, K. L.; Paesano, A.; Isnard, O. *Mater. Res. Bull.* **2014**, *54*, 41.
- (51) Tóth, É.; Helm, L.; Merbach, A. E. *Relaxivity of MRI Contrast Agents*; Krause, W., Ed.; Topics in Current Chemistry; Springer Berlin Heidelberg: Berlin, Heidelberg, 2002; Vol. 221.
- (52) Bulte, J. W. M.; Kraitchman, D. L. *NMR Biomed.* **2004**, *17* (7), 484.
- (53) Engström, M.; Klasson, A.; Pedersen, H.; Vahlberg, C.; Käll, P.-O.; Uvdal, K. *Magn. Reson. Mater. Physics, Biol. Med.* **2006**, *19* (4), 180.
- (54) Petoral, R. M.; Söderlind, F.; Klasson, A.; Suska, A.; Fortin, M. A.; Abrikossova, N.; Selegård, L.; Käll, P.-O.; Engström, M.; Uvdal, K. *J. Phys. Chem. C* **2009**, *113* (17), 6913.
- (55) Kryza, D.; Taleb, J.; Janier, M.; Marmuse, L.; Miladi, I.; Bonazza, P.; Louis, C.; Perriat, P.; Roux, S.; Tillement, O.; Billotey, C. *Bioconjug. Chem.* **2011**, *22* (6), 1145.
- (56) Cherry, S. R. *Annu. Rev. Biomed. Eng.* **2006**, *8* (1), 35.
- (57) Yang, L.; Cai, Z.; Hao, L.; Xing, Z.; Dai, Y.; Xu, X.; Pan, S.; Duan, Y.; Zou, J. *ACS Appl. Mater. Interfaces* **2017**, *9* (27), 22518.
- (58) Tan, S.; Paglieri, S. N.; Li, D. *Catal. Commun.* **2016**, *73*, 16.
- (59) Ghosh, A. B.; Saha, N.; Sarkar, A.; Dutta, A. K.; Biswas, P.; Nag, K.; Adhikary, B. *New J. Chem.* **2016**, *40* (2), 1595.
- (60) Park, J.; Zheng, H.; Jun, Y.; Alivisatos, A. P. *J. Am. Chem. Soc.* **2009**, *131* (39), 13943.
- (61) Huang, Y.-Z.; Chen, L.; Wu, L.-M. *Cryst. Growth Des.* **2008**, *8* (2), 739.
- (62) Hakmeh, N.; Chlique, C.; Merdrignac-Conanec, O.; Fan, B.; Chevire, F.; Zhang, X.; Fan, X.; Qiao, X. *J. Solid State Chem.* **2015**, *226*, 255.

- (63) Hirai, T.; Orikoshi, T.; Komasaawa, I. *Chem. Mater.* **2002**, *14* (8), 3576.
- (64) Hirai, T.; Orikoshi, T. *J. Colloid Interface Sci.* **2004**, *273* (2), 470.
- (65) Portehault, D.; Devi, S.; Beaunier, P.; Gervais, C.; Giordano, C.; Sanchez, C.; Antonietti, M. *Angew. Chemie Int. Ed.* **2011**, *50* (14), 3262.
- (66) Gouget, G.; Debecker, D. P.; Kim, A.; Olivieri, G.; Gallet, J.-J.; Bournel, F.; Thomas, C.; Ersen, O.; Moldovan, S.; Sanchez, C.; Carenco, S.; Portehault, D. *Inorg. Chem.* **2017**, *56* (15), 9225.
- (67) Wang, Z.; Cheng, P.; He, P.; Hu, F.; Luo, L.; Zhou, Q. *Nanosci. Nanotechnol. Lett.* **2014**, *6* (12), 1053.
- (68) Thirumalai, J.; Chandramohan, R.; Valanarasu, S.; Vijayan, T. A.; Ezhilvizhian, S. *Micro Nano Lett.* **2011**, *6* (8), 614.
- (69) Han, L.; Hu, Y.; Pan, M.; Xie, Y.; Liu, Y.; Li, D.; Dong, X. *CrystEngComm* **2015**, *17* (12), 2529.
- (70) Han, L.; Pan, M.; Hu, Y.; Xie, Y.; Liu, Y.; Li, D.; Dong, X. *J. Am. Ceram. Soc.* **2015**, *98* (9), 2817.
- (71) Lu, X.; Yang, M.; Yang, L.; Ma, Q.; Dong, X.; Tian, J. *J. Mater. Sci. Mater. Electron.* **2015**, *26* (6), 4078.
- (72) Cui, C. E.; Lei, X.; Huang, P.; Wang, L.; Yang, F. *J. Lumin.* **2013**, *138*, 138.
- (73) Cui, C. E.; Liu, H.; Huang, P.; Wang, L. *Opt. Mater.* **2013**, *36* (2), 495.
- (74) Liu, Z.; Sun, X.; Xu, S.; Lian, J.; Li, X.; Xiu, Z.; Li, Q.; Huo, D.; Li, J. G. *J. Phys. Chem. C* **2008**, *112* (7), 2353.
- (75) Pechini, M. P. Method of preparing lead and alkaline earth titanates and niobates and coating method using the same to form a capacitor, 1967.
- (76) Dhanaraj, J.; Jagannathan, R.; Trivedi, D. C. *J. Mater. Chem.* **2003**, *13* (7), 1778.
- (77) Dai, Q.; Song, H.; Wang, M.; Bai, X.; Dong, B.; Qin, R.; Qu, X.; Zhang, H. *J. Phys. Chem. C* **2008**, *112* (49), 19399.
- (78) Dhanaraj, J.; Geethalakshmi, M.; Jagannathan, R.; Kutty, T. R. . *Chem. Phys. Lett.* **2004**, *387* (1–3), 23.
- (79) Thirumalai, J.; Jagannathan, R.; Trivedi, D. C. *J. Lumin.* **2007**, *126* (2), 353.
- (80) Thirumalai, J.; Chandramohan, R.; Sekar, M.; Rajachandrasekar, R. *J. Nanoparticle Res.* **2008**, *10* (3), 455.
- (81) Nakkiran, A.; Thirumalai, J.; Jagannathan, R. *Chem. Phys. Lett.* **2007**, *436* (1–3), 155.
- (82) Kawahara, Y.; Petrykin, V.; Ichihara, T.; Kijima, N.; Kakihana, M. *Chem. Mater.* **2006**, *18* (26), 6303.
- (83) Xing, M.; Cao, W.; Pang, T.; Ling, X. *Solid State Commun.* **2009**, *149* (23–24), 911.
- (84) Tian, Y.; Lu, F.; Xing, M.; Ran, J.; Fu, Y.; Peng, Y.; Luo, X. *Opt. Mater.* **2017**, *64*, 58.
- (85) Luo, X.; Cao, W.; Xing, M. *J. Mater. Res.* **2009**, *24* (05), 1756.
- (86) Pang, T.; Cao, W.; Xing, M.; Feng, W.; Xu, S.; Luo, X. *J. Rare Earths* **2010**, *28* (4), 509.
- (87) Osseni, S. A.; Lechevallier, S.; Verelst, M.; Dujardin, C.; Dexpert-Ghys, J.; Neumeyer, D.; Leclercq, M.; Baaziz, H.; Cussac, D.; Santran, V.; Mauricot, R. *J. Mater. Chem.* **2011**, *21* (45), 18365.
- (88) Bakhtiari, H.; Ghasemi, M. R.; Hashemizadeh Aghda, A.; Noorkojouri, H.; Sarabadani, P.; Zeeb, M. *J. Clust. Sci.* **2015**, *26* (5), 1671.
- (89) Ai, P. F.; Li, W. Y.; Xiao, L. Y.; Li, Y. D.; Wang, H. J.; Liu, Y. L. *Ceram. Int.* **2010**, *36* (7), 2169.

- (90) Li, W.; Liu, Y.; Ai, P.; Chen, X. *J. Rare Earths* **2009**, 27 (6), 895.
- (91) Ai, P.-F.; Liu, Y.-L.; Xiao, L.-Y.; Wang, H.-J.; Meng, J.-X. *Sci. Technol. Adv. Mater.* **2010**, 11 (3), 035002.
- (92) Yan, X.; Fern, G. R.; Withnall, R.; Silver, J. *Nanoscale* **2013**, 5 (18), 8640.
- (93) Yan, X.; Fern, G. R.; Withnall, R.; Silver, J. *Nanoscale* **2013**, 5 (3), 1091.
- (94) Bagheri, A.; Rezaee Ebrahim Saraee, K.; Shakur, H. R.; Zamani Zeinali, H. *Appl. Phys. A Mater. Sci. Process.* **2016**, 122 (5), 1.
- (95) Hernández-Adame, L.; Méndez-Blas, A.; Ruiz-García, J.; Vega-Acosta, J. R.; Medellín-Rodríguez, F. J.; Palestino, G. *Chem. Eng. J.* **2014**, 258 (6), 136.
- (96) Cichos, J.; Karbowiak, M.; Hreniak, D.; Stręk, W. *J. Rare Earths* **2016**, 34 (8), 850.
- (97) Tian, Y.; Fu, Y.; Xing, M.; Luo, X. *J. Nanomater.* **2015**, 2015, 1.
- (98) Fu, Y.; Cao, W.; Peng, Y.; Luo, X.; Xing, M. *J. Mater. Sci.* **2010**, 45 (23), 6556.
- (99) Thirumalai, J.; Chandramohan, R.; Divakar, R.; Mohandas, E.; Sekar, M.; Parameswaran, P. *Nanotechnology* **2008**, 19 (39), 395703.
- (100) Thirumalai, J.; Chandramohan, R.; Valanarasu, S.; Vijayan, T. a.; Somasundaram, R. M.; Mahalingam, T.; Srikumar, S. R. *J. Mater. Sci.* **2009**, 44 (14), 3889.
- (101) Thirumalai, J.; Chandramohan, R.; Auluck, S.; Mahalingam, T.; Srikumar, S. R. *J. Colloid Interface Sci.* **2009**, 336 (2), 889.
- (102) Li, W.; Liu, Y.; Ai, P. *Mater. Chem. Phys.* **2010**, 119 (1–2), 52.
- (103) Ai, P. F.; Liu, Y. L.; Li, W. Y.; Xiao, L. Y. *Phys. B Condens. Matter* **2010**, 405 (16), 3360.
- (104) Cui, C.; Jiang, G.; Huang, P.; Wang, L.; Liu, D. *J. Lumin.* **2014**, 145, 665.
- (105) Liu, D.; Cui, C.; Huang, P.; Wang, L.; Jiang, G. *J. Alloys Compd.* **2014**, 583 (3), 530.
- (106) Liu, D.; Huang, P.; Cui, C.; Wang, L.; Jiang, G. *Ceram. Int.* **2014**, 40 (1), 117.
- (107) Cui, C.; Jiang, G.; Huang, P.; Wang, L.; Liu, D. *Ceram. Int.* **2014**, 40 (3), 4725.
- (108) Huang, P.; Liu, D.; Cui, C. E.; Wang, L.; Jiang, G. *Appl. Phys. A* **2014**, 116 (2), 759.
- (109) Yuan, G.; Li, M.; Yu, M.; Tian, C.; Wang, G.; Fu, H. *Sci. Rep.* **2016**, 6 (1), 37133.
- (110) Rosticher, C.; Viana, B.; Fortin, M.-A.; Lagueux, J.; Faucher, L.; Chanéac, C. *RSC Adv.* **2016**, 6 (60), 55472.
- (111) Thomson, J. W.; Nagashima, K.; Macdonald, P. M.; Ozin, G. a. *J. Am. Chem. Soc.* **2011**, 133 (13), 5036.
- (112) Zhao, F.; Yuan, M.; Zhang, W.; Gao, S. *J. Am. Chem. Soc.* **2006**, 128 (36), 11758.
- (113) Cheon, J.; Kang, N.-J.; Lee, S.-M.; Lee, J.-H.; Yoon, J.-H.; Oh, S. J. *J. Am. Chem. Soc.* **2004**, 126 (7), 1950.
- (114) Zhao, F.; Sun, H.-L.; Su, G.; Gao, S. *Small* **2006**, 2 (2), 244.
- (115) Ding, Y.; Gu, J.; Ke, J.; Zhang, Y.-W.; Yan, C.-H. *Angew. Chemie Int. Ed.* **2011**, 50 (51), 12330.
- (116) Zhang, T.; Gu, J.; Ding, Y.; Zhang, Y.-W.; Yan, C.-H. *Chempluschem* **2013**, 78 (6), 515.
- (117) Lei, L.; Zhang, S.; Xia, H.; Tian, Y.; Zhang, J.; Xu, S. *Nanoscale* **2017**, 9 (17), 5718.
- (118) Gu, J.; Ding, Y.; Ke, J.; Zhang, Y.; Yan, C. *Acta Chim. Sin.* **2013**, 71 (3), 360.
- (119) Tan, S.; Li, D. *ChemCatChem* **2017**, 82071, 1.
- (120) Jiang, G.; Wei, X.; Chen, Y.; Duan, C.; Yin, M.; Yang, B.; Cao, W. *Mater. Lett.* **2015**, 143, 98.
- (121) Li, Y.; Huang, Y.; Bai, T.; Li, L. *Inorg. Chem.* **2000**, 39 (15), 3418.

- (122) Liu, J.; Luo, H.; Liu, P.; Han, L.; Zheng, X.; Xu, B.; Yu, X. *Dalt. Trans.* **2012**, 41 (45), 13984.
- (123) Liu, H.; Liu, P.; Su, X.; Liu, J.; Li, X.; Luo, H.; Yao, Z.; Yu, X.; Zhan, M. *RSC Adv.* **2014**, 4 (100), 57048.
- (124) Deng, S. Q.; Xue, Z. P.; Yang, Y. H.; Yang, Q.; Liu, Y. L. *J. Mater. Sci. Technol.* **2012**, 28 (7), 666.
- (125) Deng, S.; Xue, Z.; Liu, Y.; Lei, B.; Xiao, Y.; Zheng, M. *J. Alloys Compd.* **2012**, 542, 207.
- (126) Thirumalai, J.; Chandramohan, R.; Vijayan, T. A. *J. Mater. Sci. Mater. Electron.* **2011**, 22 (8), 936.

Chapter II

Synthesizing and storing $\text{Ln}_2\text{O}_2\text{S}$

nanoparticles: from $\text{Gd}_2\text{O}_2\text{S}$ to $\text{Ce}_2\text{O}_2\text{S}$

Table of content

II.1. From $\text{Gd}_2\text{O}_2\text{S}$ to $\text{Ce}_2\text{O}_2\text{S}$	65
II.1.1. $\text{Gd}_2\text{O}_2\text{S}$ nanoparticles synthesis.....	65
II.1.1.1. Why $\text{Gd}_2\text{O}_2\text{S}$ nanoparticles?.....	65
II.1.1.2. Synthesis optimization.....	66
II.1.1.2.1. Initial synthesis	66
II.1.1.2.2. Reaction time	67
II.1.1.2.3. Sodium source	67
II.1.1.2.4. Role of sulfur concentration	68
II.1.1.2.5. Optimized synthesis conditions	69
II.1.2. Preliminary characterization of the $\text{Gd}_2\text{O}_2\text{S}$ nanoparticles.....	69
II.1.2.1. Composition of the $\text{Gd}_2\text{O}_2\text{S}$ nanoplates.....	69
II.1.2.2. Crystal structure.....	70
II.1.2.3. Conclusion	72
II.1.3.1. Cerium: an exception in the $\text{Ln}_2\text{O}_2\text{S}$ series	73
II.1.3.2. $\text{Ce}_2\text{O}_2\text{S}$ synthesis, isolation and storage	73
II.2. $\text{Ln}_2\text{O}_2\text{S}$ ($\text{Ln} = \text{Gd}, \text{Ce}$) behavior in air and water	76
II.3. Bimetallic $(\text{Gd,Ce})_2\text{O}_2\text{S}$ nanoparticles.....	80
II.3.1. Synthesis and composition of the compounds.....	80
II.3.2. Structural analysis of compounds exposed to air	81

II.3.3. Structural analysis of compound with $y = 70$ % under inert atmosphere	83
II.3.4. Transmission electron microscopy on the $y = 0, 37.5, 50$ and 75 % compounds.....	83
II.4. Reactivity toward O_2 and H_2O : comparison between $GdCeO_2S$ and Gd_2O_2S	86
II.5. Conclusion	90
References	91

II.1. From Gd₂O₂S to Ce₂O₂S

II.1.1. Gd₂O₂S nanoparticles synthesis

II.1.1.1. Why Gd₂O₂S nanoparticles?

Gadolinium oxysulfide nanoparticles are promising candidates for several applications, such as MRI bimodal contrast agents or X-ray absorbing materials (see previous section). Their synthesis is well documented in water as well as in organic solvents. In our laboratory, Gd₂O₂S:Eu,Mg,Ti nanoparticles were already synthesized in water by Céline Rosticher to achieve persisting luminescence.¹

Among the numerous routes described in Chapter I for the synthesis of Gd₂O₂S nanoparticles, we have chosen the route proposed by Ding *et al.*² The authors used the decomposition of Gd(acac)₃ in presence of elemental sulfur and an alkaline complex in a mixture of oleylamine, oleic acid and octadecene whose roles will be detailed later. Several advantages motivated our choice.

First, the method enables the formation of small 5 - 10 nm long and 2 - 3 nm thick nanoplates. Second, the method guarantees a high surface-to-volume ratio which is helpful for catalytic reactions. Ding's results also indicate that monodispersity in size can be achieved, an advantage for a reliable characterization and use of the nanoparticles.

Finally, the as-prepared nanoparticles are crystalline, which enables a straightforward structural characterization by means of XRD. The detection of amorphous impurity phases and of species at the surface remains a technical challenge.

Element	Y	La	Pr	Nd	Sm	Eu	Gd	Tb
Ln ₂ O ₂ S nanoplates width (nm)	< 5	22	20-40	15-30	20-40	10-30	5-10	15-25

Table 4: Width of the Ln₂O₂S nanoparticles obtained by Ding.²

Ding's synthesis route has proven to be successful for the majority of the first rare-earths (Y and La to Tb, Ce and Pm excluded).² In this work, we have chosen Gd, for which small and regular nanoparticles can be obtained (see Table 4). Gadolinium complexes are also affordable in price (Chapter I, Table 1).

II.1.1.2. Synthesis optimization

II.1.1.2.1. Initial synthesis

The synthesis of $\text{Gd}_2\text{O}_2\text{S}$ nanoparticles requires the employment of six chemicals (Figure 20). The two main reactants are gadolinium acetylacetonate hydrate ($\text{Gd}(\text{acac})_3 \cdot x\text{H}_2\text{O}$) and elemental sulfur (S_8). They are mixed together with organic compounds, namely oleylamine (OM), oleic acid (OA) and 1-octadecene (ODE). The reaction is carried out at 310 °C under inert atmosphere.

Oleylamine plays a crucial role in the synthesis. First, during the decomposition of the gadolinium complex, the oxygen of the acetylacetonate ligands and oleylamine can condensate to form *in situ* water. To evaporate water, a temperature dwell at 120 °C for 20 minutes minimum is performed before further heating. Furthermore, oleylamine can dissolve elemental sulfur at room temperature and activate it at higher temperatures *via* the formation of polyanions that release *in situ* H_2S (Chapter I, Figure 14).

This mixture of organic compounds constitutes the solvent of the reaction. Oleic acid and oleylamine are also surfactants that are susceptible to control the growth of the nanoparticles. After the condensation of acetylacetonate ligands with oleylamine, the lanthanide precursor is surrounded by new ligands with long alkyl chains.

Finally, an alkaline source is added to the reaction for reasons that remain unclear, which will be extensively discussed later in Chapter III. Ding *et al.* employed sodium acetylacetonate $\text{Na}(\text{acac})$.

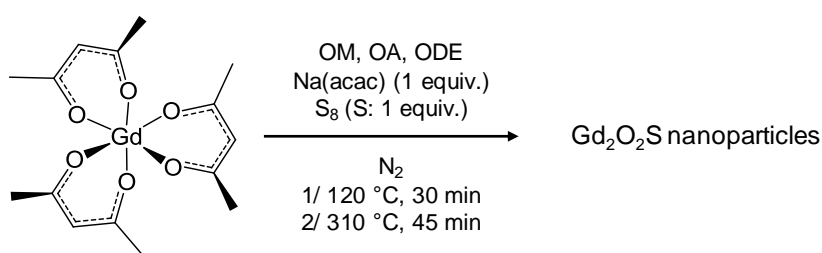


Figure 20: The route proposed by Ding *et al.* for the synthesis of $\text{Gd}_2\text{O}_2\text{S}$ nanoparticles.²

The synthesis route proposed by Ding *et al.*, schematically described in Figure 20, has been recently optimized in our laboratory. The work was initiated by Mario Ávila Gutiérrez during his Master degree's internship (2015), under the supervision of Sophie Carencó. Some of his results have been used as a starting point for the present PhD thesis with reference numbers [MA...], where the initials indicate the author and the number is the reaction number recorded in the logbooks of the laboratory.

II.1.1.2.2. Reaction time

The synthesis route is described in detail in the experimental section. In summary, the mixture is heated at 120 °C under vacuum for 20 minutes minimum to evaporate water and other low-boiling-point impurities. Subsequently, the mixture is submitted to a flow of inert gas (N₂ or Ar) and is heated up to 310 °C. The mixture starts to become turbid around 280 °C. The turbidity is total after 305 °C.

Since we noted neither visual nor structural changes as measured by XRD in the mixture, we decided and subsequently confirmed that the thermal treatment at 310 °C for 45 minutes was not necessary, so we reduced to 30 minutes the dwell time.

II.1.1.2.3. Sodium source

Ding *et al.* mentioned that a sodium source is necessary to obtain Ln₂O₂S nanocrystals.² This result was confirmed in our group, since very small amorphous nanoparticles are obtained when the reaction was performed without additive (Figure 21A) while crystalline aggregated hexagonal nanoplates are obtained by using Na(acac) (Figure 21B).

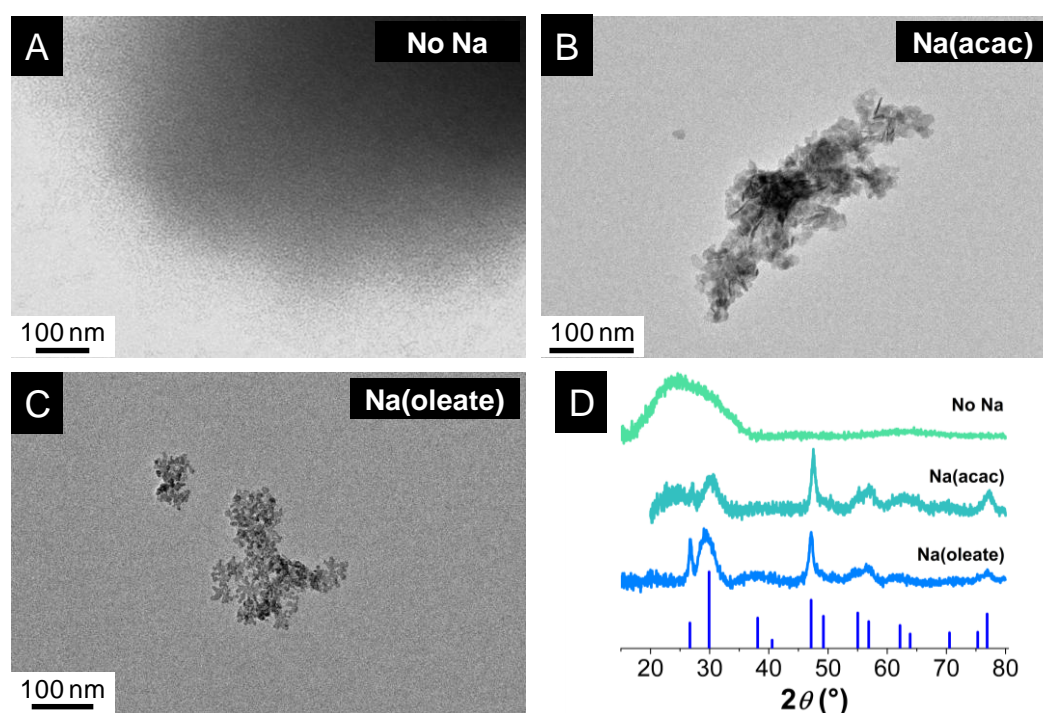


Figure 21: Influence of sodium additives on the formation of Gd₂O₂S nanoparticles. TEM images of final nanoparticles using no source of sodium (A, [MA005]), Na(acac) (B, [MA006]) and Na(oleate) (C) and the corresponding powder XRD patterns (D). Blue vertical lines correspond to the Gd₂O₂S phase (JCPDS 26-1422).

During the early stage of the reaction, Na(acac) can react with oleic acid (in excess) to form Na(oleate). We then also tried to use Na(oleate) [CL001], which also enabled the formation of

similar anisotropic nanocrystals (Figure 21C). The difference is that the viscosity of the medium is slightly higher by using Na(oleate). To prevent its *in situ* formation, Na(oleate) was directly chosen as reactant in the following syntheses.

II.1.1.2.4. Role of sulfur concentration

Another interesting aspect of the synthesis route followed by Ding *et al.* is the concentration of sulfur used.² In spite of the fact that the authors used a nominal Gd:S ratio of 1, whereas the final Gd:S composition in the solid is 2 ($\text{Gd}_2\text{O}_2\text{S}$), they found that the sulfur concentration in the final $\text{La}_2\text{O}_2\text{S}$ product is lower than expected, especially because of defective terminal layers and sodium insertion. This possibility will be discussed in detail later in Chapter III. Anyway, this observation indicates that the initial sulfur concentration used by Ding *et al.* is more than twice higher than in the nanoparticles.

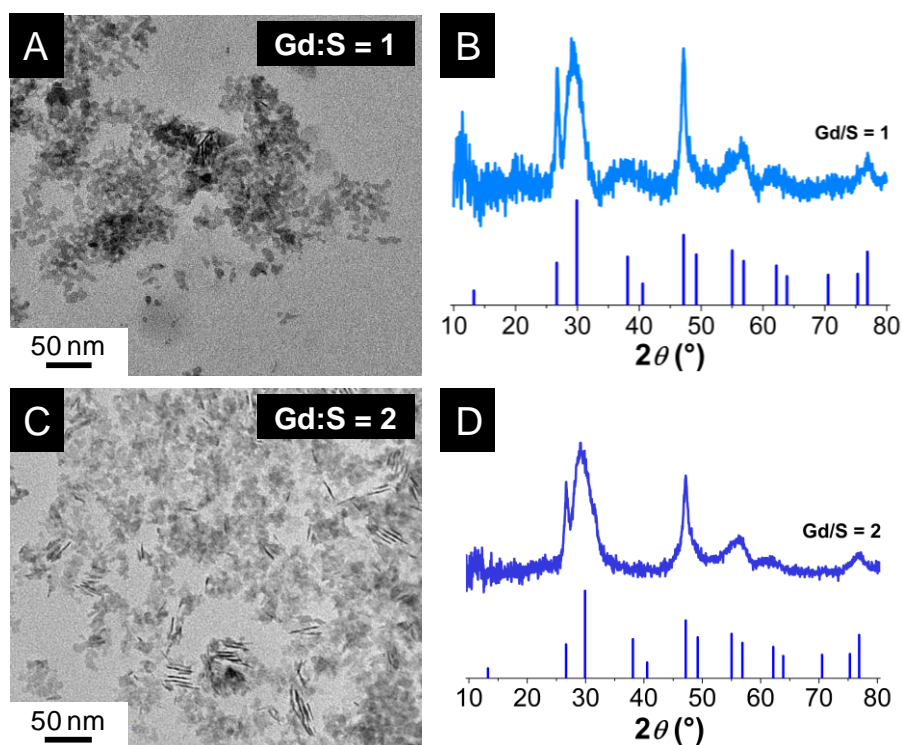


Figure 22: Influence of the sulfur amount on the $\text{Gd}_2\text{O}_2\text{S}$ nanoparticles synthesis. TEM micrograph (A) and powder XRD pattern (0.5 h analysis, B) for a nominal ratio Gd:S = 1. TEM micrograph (C) and powder XRD pattern (2.5 h analysis, D) for a nominal ratio Gd:S = 2 (stoichiometric amount). XRD pattern references is JCPDS files 26-1422.

We thus tried to synthesize $\text{Gd}_2\text{O}_2\text{S}$ nanoparticles using a Gd:S ratio of 0.5 [CL079, CL204]. Remarkably, neither morphological nor structural differences were observed with respect to the case where Gd:S = 1.

As we found that the initial sulfur composition does not affect the synthesis of the nanoparticles, we decided to use the lowest possible ratio $\text{Gd:S} = 2$.

II.1.1.2.5. Optimized synthesis conditions

We tried to optimize the synthesis conditions starting from those proposed by Ding *et al.* (see Figure 23).

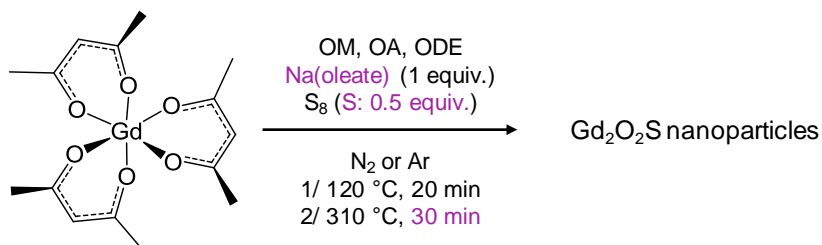


Figure 23: Optimized synthesis conditions for the synthesis of $\text{Gd}_2\text{O}_2\text{S}$ nanoparticles.

This synthesis was reproduced under exactly the same conditions more than twenty times in the laboratory. The experiments include those carried out by Anh-Minh Nguyen and Thi Kim-Chi Lê (PhD students). We established that the synthesis is reproducible as to the size, morphology and crystallinity of the nanoparticles.

II.1.2. Preliminary characterization of the $\text{Gd}_2\text{O}_2\text{S}$ nanoparticles

II.1.2.1. Composition of the $\text{Gd}_2\text{O}_2\text{S}$ nanoplates

In Figure 24 we report the average EDS composition of the $\text{Gd}_2\text{O}_2\text{S}$ nanoparticles obtained by measuring 15 different samples synthesized under the same conditions.

While in a single sample the variation of sodium and sulfur composition is limited to 2 - 3 mol%, the variations in the table reflect the difference from sample to sample.

The variation of sodium concentration is larger, which is attributed to the fact that sodium is mainly found onto the surface of the nanoparticle, so its final amount may depend on the washing processes that partly remove it (see Chapter III). In any case, sodium could not be removed completely and the minimum Na:Gd ratio was 0.05.

The sulfur concentration can also vary from sample to sample, but its quantity is significantly lower than that in the $\text{La}_2\text{O}_2\text{S}$ nanoparticles synthesized by Ding *et al.*² The composition of our samples is better described by the formula $\text{Gd}_2\text{O}_2\text{S}_{0.5}$. We will discuss in Chapter III about how the excess of positive charges created by sulfur deficiency can be compensated.

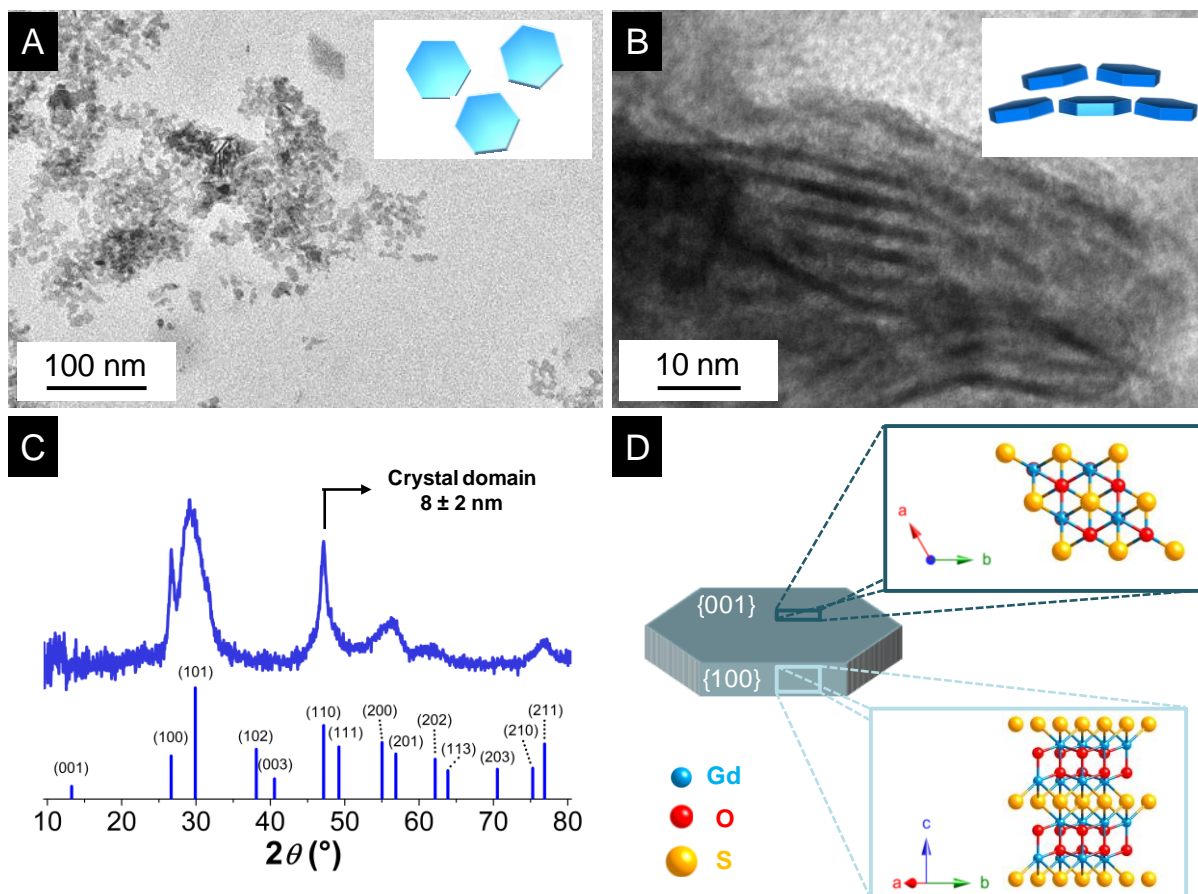


Figure 25: TEM micrographs of $\text{Gd}_2\text{O}_2\text{S}$ nanoparticles majorly seen on their $\{001\}$ facets (A) or $\{100\}$ facets (B). Insets: schematic representations of the nanoparticles assemblies. (C) Powder XRD pattern of $\text{Gd}_2\text{O}_2\text{S}$ nanoparticles with reference JCPDS 26-1422. (D) Schematic view of the nanoplate inner structure seen from different angles.

Because of such broad peaks, (110) is the only Bragg peak that can be used to estimate the crystallite size from a measure of the full width at half maximum (FWHM). In the fit of the peak, the smaller (111) peak, which appears as a shoulder of the former peak, is also included. By using Pseudo-Voigt functions for the fit of the two peaks, the FWHM of the (110) peak yields a crystallite size of 8 ± 2 nm. This indicates that the nanocrystals are single crystals, for the lateral (110) dimension of the nanoparticles is also 8 nm. The single crystalline nature of the nanoparticles is confirmed by HRTEM (Figure 26). Under the electron beam, the surface ligands burn, which blurs somehow the image. Still, 6 - 8 nm hexagonal-like single crystals can be observed.

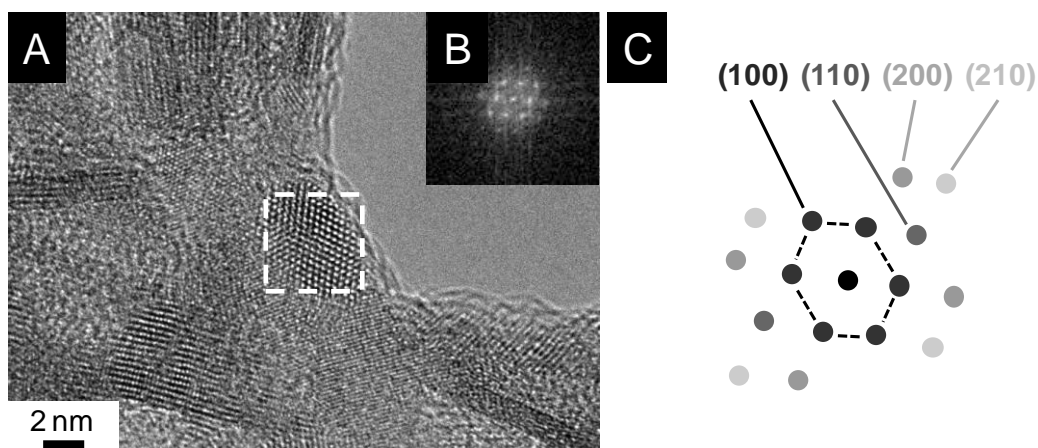


Figure 26: (A) HRTEM micrograph of Gd₂O₂S nanoparticles [CL079]. (B) FFT obtained from the image in the square region indicated by a dashed white line (B). (C) Schematics of the corresponding lattice.

II.1.2.3. Conclusion

At this point, our conclusion regarding the synthesis and preliminary characterization of the Gd₂O₂S nanoparticles is as follows:

- whitish powder stable in air,
- anisotropic nanoparticles (hexagonal nanoplates),
- Gd₂O₂S single crystals
- sulfur deficiency,
- presence of sodium.

A further characterization of the nanoparticles is needed to answer to the following open questions.

1. Why are pure Gd₂O₂S crystals obtained in spite of the fact that half of the sulfur is missing?
2. Where is the sodium which is always present in our nanoparticles located?
3. How does the surface affect the structure and reactivity of such small nanoparticles?

We suspected that the surface played a preponderant role in such small particles even though Ln₂O₂S nanoplates surface structure and reactivity had never been deeply investigated. We realized this point even more through the study of cerium oxysulfide nanoparticles.

II.1.3.1. Cerium: an exception in the Ln₂O₂S series

While most lanthanides are trivalent only, cerium can be either trivalent or tetravalent because the [Xe] 5d⁰ 4f¹ electronic configuration of Ce^{III} favors the loss of the last *f* electron. In the case of oxysulfides, oxidation of Ce^{III} into Ce^{IV} was evidenced by Flahaut *et al.* who already noticed that bulk Ce₂O₂S is air-sensitive even at ambient temperature.³ They explained that the initial brown color turned progressively into dark green in a few weeks. Mixed-valence compounds were also obtained, namely Ce₄O₄S₃ and Ce₆O₆S₄, that can be described as Ce^{III}₂Ce^{IV}₂O₄S₃ and Ce^{III}₄Ce^{IV}₂O₆S₄ respectively.^{4–6}

This instability may explain why Ding *et al.* did not report on the synthesis of Ce₂O₂S nanoparticles, even though they synthesized other lanthanide oxysulfides from La to Tb (Pm was excluded because of its nuclear instability).² We envisage that the difficulty associated with the synthesis of pure Ce₂O₂S is twofold: (i) the intrinsic reactivity of the precursor; (ii) the nanoparticles are air-sensitive and are swiftly degraded by the isolation and washing processes performed in air.

II.1.3.2. Ce₂O₂S synthesis, isolation and storage

Note: This whole section (down to “End of quote”) is a quote adapted from “*Synthesis of Ce₂O₂S and Gd_{2(1-y)Ce_{2y}O₂S Nanoparticles and Reactivity from In situ X-ray Absorption Spectroscopy and X-ray Photoelectron Spectroscopy}*” from Larquet, C.; Nguyen, A.-M.; Ávila-Gutiérrez, M.; Tinat, L.; Lassalle-Kaiser, B.; Gallet, J.-J.; Bournel, F.; Gauzzi, A.; Sanchez, C.; Carenco, S. *Inorg. Chem.* **2017**, 56 (22), 14227–14236.⁷

Ce(acac)₃ hydrate was reacted at 310 °C for 30 min with a stoichiometric amount of sulfur (0.5 equiv. *vs.* Ce) in a mixture of oleylamine, oleic acid and 1-octadecene, in the presence of Na(oleate) hydrate. The reaction was performed under inert atmosphere. In a first attempt, the particles were isolated and washed under ambient air [CL053, CL061]. The product was dark brown at first but turned greenish after a few hours and light brown after a few weeks (Figure 27A), suggesting product decomposition in air. Consistent with this observation, the X-ray diffraction pattern matched the pattern of Ce₂O₂S a few hours after the synthesis and evolved into another pattern similar to that of CeO₂ in a time span of two weeks (Figure 27B).

A similar observation was previously reported in bulk samples as well but in a time span of months³ and the final product was identified by Sourisseau *et al.*^{8,9} to be Ce₂O_{2.5}S with an insertion of oxygen in the layer of cerium oxide owing to a partial oxidation of Ce^{III} in Ce^{IV}. This suggests that washing and handling of the nanoparticles in air was inappropriate, although the synthetic route itself was efficient.

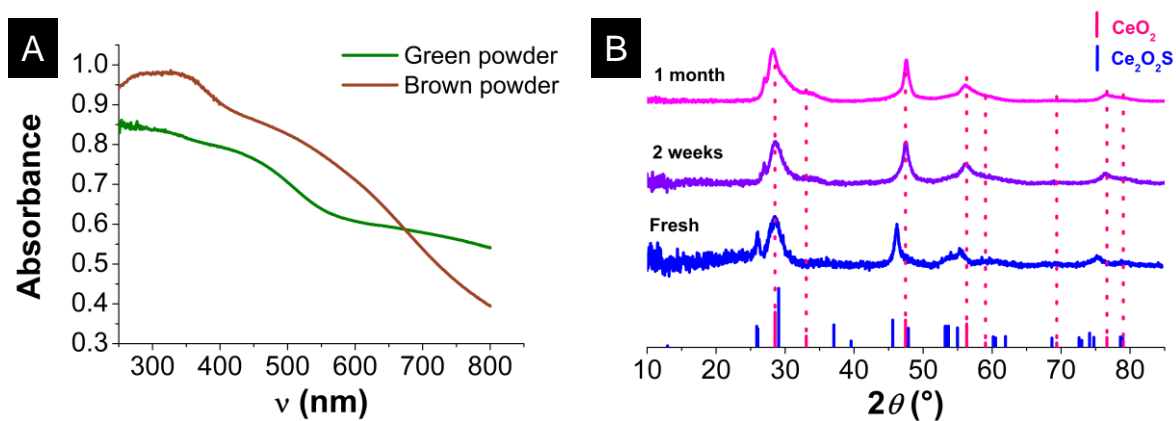


Figure 27: Degradation of $\text{Ce}_2\text{O}_2\text{S}$ nanoparticles as seen from diffuse UV-visible reflectance (A) and powder XRD (B). CeO_2 and $\text{Ce}_2\text{O}_2\text{S}$ references are respectively based on JCPDS files 16-1410 and 26-1085.

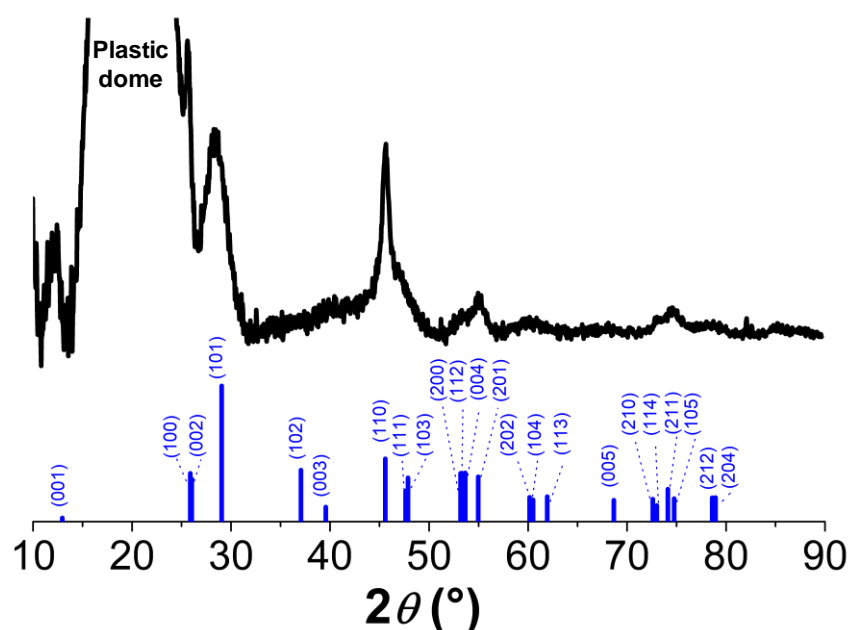


Figure 28: Powder XRD pattern of $\text{Ce}_2\text{O}_2\text{S}$ kept under inert atmosphere. Reference data is bulk $\text{Ce}_2\text{O}_2\text{S}$ based on JCPDS file 26-1085.

To overcome this issue, we isolated the nanoparticles from the crude product and washed them with anhydrous solvents in the inert atmosphere of a glovebox ($\text{H}_2\text{O} < 0.5$ ppm, $\text{O}_2 < 0.5$ ppm; [CL243]). Transmission Electron Microscopy (TEM) carried out on these nanoparticles confirmed the formation of nanoplates whose dimensions vary between 10 to 20 nm in length and 1.5 to 2.5 nm in thickness (Figure 29A). Because of the high amount of remaining ligands on the nanoparticles (washing them in the glovebox is a hard process), we were not able to perform High Resolution Transmission Electron Microscopy (HRTEM).

Despite their small size, X-ray diffraction pattern (XRD) confirmed the crystalline structure of $\text{Ce}_2\text{O}_2\text{S}$ nanoparticles (Figure 28).

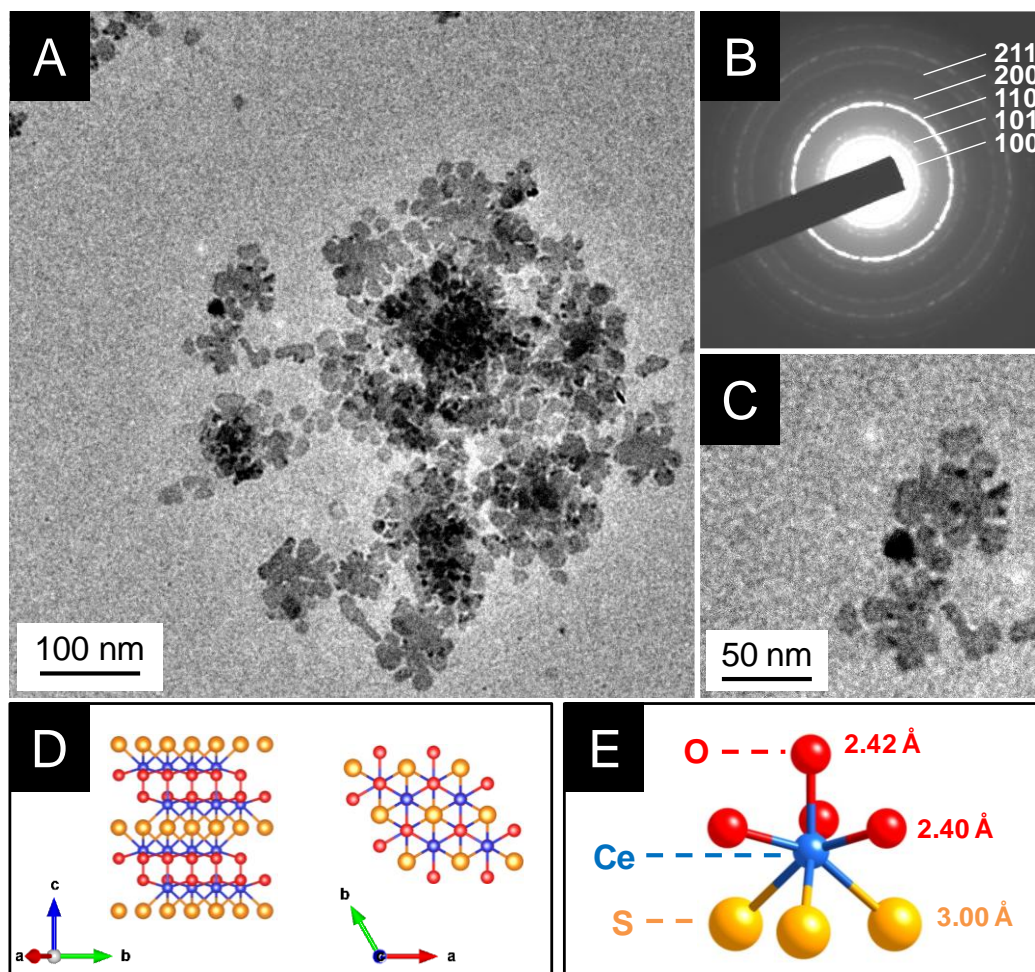


Figure 29: TEM image (A) and the corresponding diffraction pattern (B) of representative $\text{Ce}_2\text{O}_2\text{S}$ nanoparticles. (C) Zoom on the $\text{Ce}_2\text{O}_2\text{S}$ nanoplates. (D) Representation of the lamellar and hexagonal structure of $\text{Ce}_2\text{O}_2\text{S}$ (JCPDS 02-2554) and (E) cerium environment in the structure.

The pattern matches the reference pattern of hexagonal $\text{Ce}_2\text{O}_2\text{S}$. Diffraction peaks have different widths, which are related to the anisotropy of the nanoparticles shape. Scherrer's formula applied to the (110) diffraction peak gives an average crystal domain size in the range of 8 - 14 nm, consistent with the observed width of the nanoplates. Hence, each nanoplate is made of a single nanocrystal. Selected-area electronic diffraction (SAED) performed on a few nanoparticles confirmed their good crystalline properties, as the d -spacings of the diffraction rings (Figure 29B) match well those of the $\text{Ce}_2\text{O}_2\text{S}$ reference structure.

Energy-dispersive X-Ray spectroscopy (EDS) was performed on the nanoparticles. Consistent with the previous work by Ding *et al.*,² the data indicate the presence of significant amounts of sodium in the nanoparticles powders. Due to its sensitivity, only a limited washing was

performed on the $\text{Ce}_2\text{O}_2\text{S}$ sample. As a result, a high quantity of sodium oleate remained ($\text{Na}:\text{Ce} \approx 2.7$). According to these authors, the role of sodium is critical on the crystallization of all $\text{Ln}_2\text{O}_2\text{S}$ nanoplates prepared by this route, although recently Lei *et al.* reported on a sodium-free synthesis.¹⁰

End of quote.

Thus, $\text{Ce}_2\text{O}_2\text{S}$ nanoparticles can be synthesized under the aforementioned optimized conditions. The inert conditions of their isolation, washing and storage are essential to preserve the oxysulfide structure. Because of a large surface to volume ratio, the diffusion processes in the present small nanoparticles are quicker than in bulk samples. This causes a fast and irreversible degradation in air. At present, we merely observed that ambient conditions can oxidize the nanoparticles but the degradation mechanism is not known yet, except XRD analysis indicates that CeO_2 nanoparticles are one of the degradation products.

II.2. $\text{Ln}_2\text{O}_2\text{S}$ ($\text{Ln} = \text{Gd}, \text{Ce}$) behavior in air and water

Adapted from Larquet, C. *et al. Inorg. Chem.* **2017**, 56 (22), 14227–14236.⁷

As mentioned above, brown-colored $\text{Ce}_2\text{O}_2\text{S}$ becomes green after exposure in air. Isolation and storage of the nanoparticles under controlled inert atmosphere is thus critical. As discussed above, the degradation in air, seen as a loss of the $\text{Ln}_2\text{O}_2\text{S}$ crystalline structure, occurs faster for nanoparticles than for bulk samples, which is attributed to the higher surface to volume ratio of the former. Generally, there is a lack of information regarding the surface reactivity of lanthanide oxysulfide nanoparticles that may be responsible for their degradation. In this work, we employed X-ray Absorption Near Edge Spectroscopy (XANES) at the sulfur K-edge was used to evaluate the sulfur oxidation state in the nanoparticles (Figure 31). Our spectra can be directly compared with those previously obtained on various sulfide, sulfite, sulfonate and sulfate materials which constitute a set of standard spectra.^{11–14} From these spectra, one notes that the features of reduced sulfur species are found at low energy while those of oxidized species appear at higher energy. Remarkably, oxidation state of sulfur is often linearly related to the edge energy.^{11,15,16}

As reference material, we first measured $\text{Gd}_2\text{O}_2\text{S}$ nanoparticles ($\text{Gd}_2\text{O}_2\text{S-air}$) synthesized following the same route (described in the experimental section). These nanoparticles are stable upon storage in air, during washing steps and storage (see XRD pattern in Figure 25C), because Gd only accepts oxidation state (III) under ambient conditions. Second, we prepared $\text{Gd}_2\text{O}_2\text{S}$ nanoparticles, stored and transferred them to the beamline chamber under controlled

inert conditions (Gd_2O_2S -Inert, Figure 30B; [CL242]). The corresponding XANES spectra are presented in Figure 31.

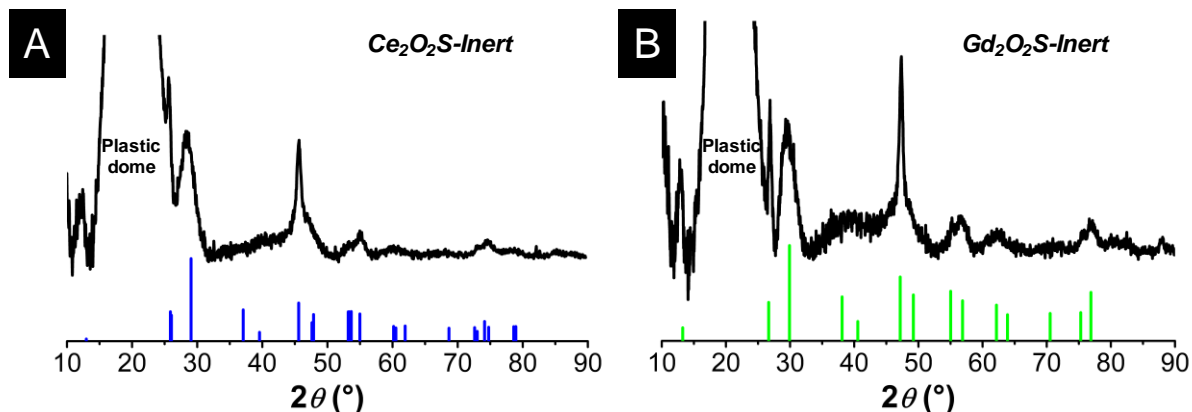


Figure 30: Powder XRD patterns of Ce_2O_2S nanoparticles (A) and Gd_2O_2S nanoparticles (B) both isolated, washed and stored under inert atmosphere.

Gd_2O_2S -Inert (Figure 31, green) does not show the broad peak near 2480 eV characteristic of oxidized sulfur (S^{IV} to S^{VI}). On the other hand, this feature is present in the Gd_2O_2S -air spectrum (Figure 31, light green). Accordingly, in the 2470-2475 eV region, the peaks corresponding to reduced sulfur are less pronounced, suggesting that the fully reduced sulfur in as-prepared Gd_2O_2S -Inert was partially converted into oxidized sulfur upon exposure to air.

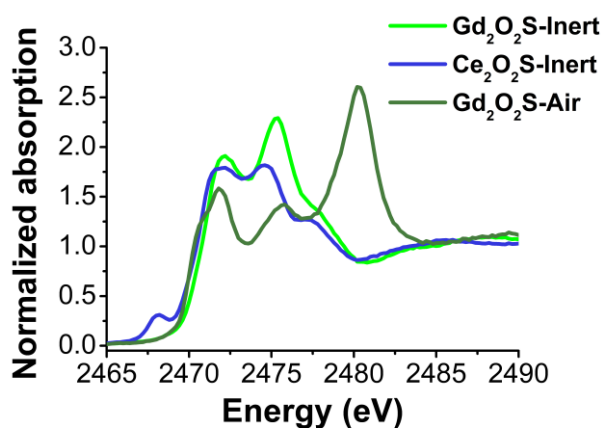


Figure 31: XANES spectra at sulfur K-edge of Gd_2O_2S (Gd_2O_2S -Inert) and Ce_2O_2S (Ce_2O_2S -Inert) nanoparticles treated and stored under controlled inert atmosphere and Gd_2O_2S (Gd_2O_2S -air) treated and stored for five weeks in air.

Since the XANES spectra were collected in fluorescence mode, they reflect both the surface and the core of the samples; sulfur oxides could in principle be either on the surface of the nanoparticles or inside the inorganic core. XRD patterns of both samples are, however, identical, which confirms the crystalline structure of Gd_2O_2S . TEM also confirmed that the size and shape of the nanoparticles is preserved (data not shown). Oxidation of sulfur due to

exposure in air is then likely a surface phenomenon. Also, Fourier transform infrared spectra exhibit specific peaks corresponding to sulfate functions (Chapter III). To the best of our knowledge, this is the first observation of surface reactivity of $\text{Gd}_2\text{O}_2\text{S}$, which is usually considered a stable phase in air. $\text{Ce}_2\text{O}_2\text{S-Inert}$ (XRD in Figure 30A) did not show any sign of surface oxidation, as expected from the care taken to avoid air exposure. Its spectrum features an additional contribution at low energy (2468 eV) whose origin is not known at this stage. The small feature at 2468 eV was found to be linked to the presence of cerium and is under investigation.

When the nanoparticles react with air (i.e. with water vapor and/or dioxygen), swift oxidation from Ce^{III} to Ce^{IV} may occur in addition to sulfur oxidation. XANES spectra were then taken at the Ce L_{III} -edge, using an environmental cell in flowing water. The sample was taken out of the glovebox and quickly placed in the cell. Prior exposure to water, the spectrum presented the characteristic peak of Ce^{III} at 5719.2 eV and two small contributions characteristic of Ce^{IV} , at around 5723 and 5729.5 eV (Figure 32, dark blue spectrum). Due to the brief exposure of the sample to air, the S K-edge spectra presented a small peak in the energy region corresponding to oxidized sulfur (inset of Figure 32, dark blue spectrum), but most of the sulfur was still reduced, as expected from the *ex situ* spectrum presented above. Following the introduction of water into the cell for a few minutes, the Ce L_{III} -edge spectrum exhibited a strong peak of Ce^{IV} and a small one of Ce^{III} (Figure 32, light blue spectrum). The S K-edge spectrum also exhibits the characteristic features of more oxidized species, namely an intense peak near 2480 eV and minor ones in the 2470-2475 eV range (see inset of Figure 32, light blue spectrum).

At this stage, we cannot conclude on the different roles of H_2O and of O_2 on the surface oxidation of $\text{Gd}_2\text{O}_2\text{S}$ and on the oxidation of $\text{Ce}_2\text{O}_2\text{S}$ in the core of the nanoparticles, because the water used in the cell contained dissolved O_2 . Nevertheless, the *in situ* XANES experiment shows that oxidation is a swift process for the $\text{Ce}_2\text{O}_2\text{S}$ nanoparticles and that both sulfur and cerium are affected.

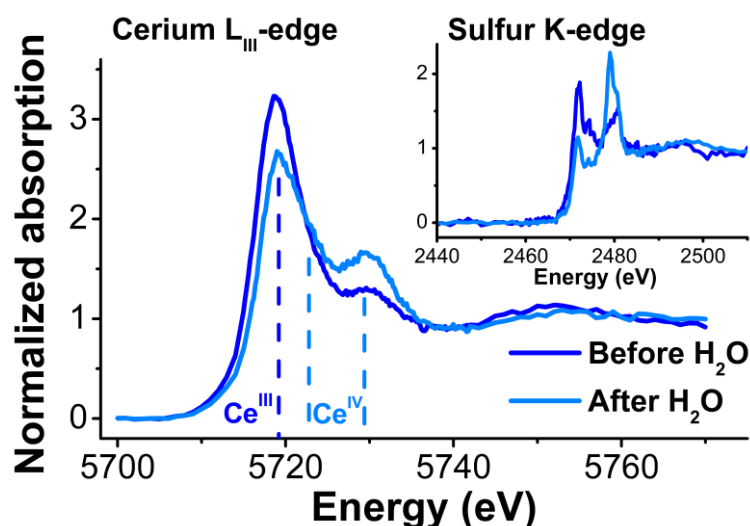


Figure 32: *In situ* cerium L_{III}-edge and sulfur K-edge XANES spectra of Ce₂O₂S nanoparticles before and after exposure to water. The position of the peaks attributed to Ce^{III} and Ce^{IV} are consistent with previously published XANES Ce L_{III}-edge spectra.^{17,18}

We presume that the oxidation of sulfur and of cerium may be related to two distinct mechanisms: (i) cerium oxidation leads to the formation of a mixed-valence phase such as Ce₂O_{2.5}S; (ii) the oxidation of the sulfides leads to the formation of S^V and of S^{VI} species (e.g. sulfates). We argue that the first mechanism is specific to nanoparticles containing cerium while the second one should occur in any Ln₂O₂S phase, including Gd₂O₂S.

Experimentally, we have observed that *Ce₂O₂S-Inert* turns from dark brown to dark green after exposure to air. Dark green is the color of Ce₂O_{2.5}S, suggesting a fast oxidation of Ce^{III}. The color of the nanoparticles fades only after several days. Oxysulfate phases¹⁹ were not detected by XRD during ageing under air (Figure 27B). At this stage, in the case of Ce₂O₂S, it is unclear whether the oxidized sulfur species are solely at the surface of the nanoparticles or present as amorphous phases. In any case, degradation eventually led to CeO₂ and amorphous species. These amorphous compounds may contain oxidized sulfur, as the XANES experiments (Figure 31 and Figure 32) show the formation of S^V and S^{VI} species when the lanthanide oxysulfide nanoparticles are exposed to air and/or water.

End of quote

The instability of cerium oxysulfide may hinder applications as the crystal and electronic properties are modified. The modification of color is the most dramatic indication of these changes.

At this point, we considered two solutions to protect cerium oxysulfide nanoparticles from their degradation. The first and most logical is to cover the surface with a smart coating, such

as a stable crystalline or amorphous shell. The choice of this shell is not obvious, especially if we consider a further use of our nanoparticles as a photocatalyst for instance. We can imagine that the shell must be permeable to light and electrons but not to water or oxygen that would degrade the internal $\text{Ce}_2\text{O}_2\text{S}$ phase. A second possibility is to synthesize bimetallic nanoparticles i.e. to partially substitute cerium with another lanthanide which may stabilize the phase. A solid solution of two phases can be envisaged owing to the comparable ionic radii of lanthanides. However, the stability of the resulting compound is not guaranteed because the cerium oxysulfide structure is exposed to air locally.

Both solutions were explored. The former solution was adopted by using $\text{Gd}_2\text{O}_2\text{S}$ as coating shell. At present, our experiments are not conclusive as to the realization of a core-shell type of $\text{Ce}_2\text{O}_2\text{S}@ \text{Gd}_2\text{O}_2\text{S}$ nanoparticles, even if our preliminary results are interesting. The second solution gave excellent results and constitutes an essential part of the present PhD thesis.

II.3. Bimetallic $(\text{Gd,Ce})_2\text{O}_2\text{S}$ nanoparticles

Adapted from Larquet, C. *et al. Inorg. Chem.* **2017**, 56 (22), 14227–14236.⁷

Different strategies may be used to obtain bimetallic nanoparticles. Most of the synthetic routes hitherto reported consist of the reaction between small amounts (usually $\leq 1\%$) of a dopant and the lanthanide (see experimental section). This approach is justified by the very similar ionic radii of the lanthanides ranging from $r_{\text{La(III)}} = 1.03 \text{ \AA}$ to $r_{\text{Lu(III)}} = 0.86 \text{ \AA}$ which favors the formation of a crystalline phase with randomly distributed ions.

II.3.1. Synthesis and composition of the compounds

Following the above considerations, in the present case we simply mixed the precursors of Gd and Ce in appropriate stoichiometry since the radii of Gd and Ce were close enough ($r(\text{Gd}^{\text{III}}(\text{VII})) = 1.14 \text{ \AA}$; $r(\text{Ce}^{\text{III}}(\text{VII})) = 1.21 \text{ \AA}$). This straightforward route enabled us to obtain bimetallic powders in a wide range of composition from $y = 0\%$ to $y = 90\%$ [CL204 to CL213]. In the nanoparticles, the Gd:Ce ratio measured by energy dispersive X-ray spectroscopy (EDS) was found to be consistent with the nominal composition (Figure 33).

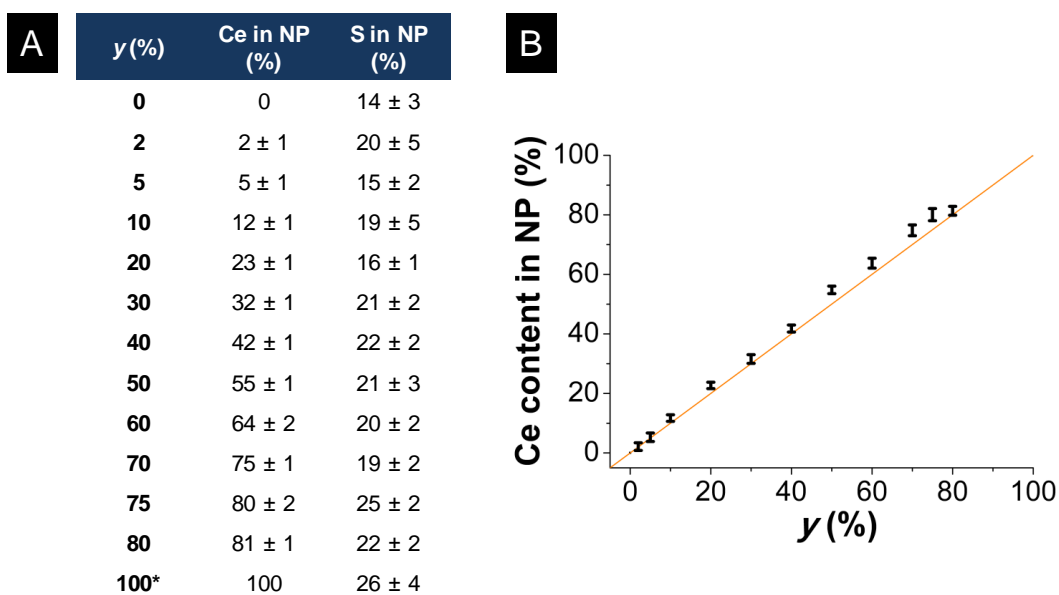


Figure 33: Cerium and sulfur content in the $\text{Gd}_{2(1-y)}\text{Ce}_{2y}\text{O}_2\text{S}$ nanoparticles (A). Schematic representation of the cerium content vs. the nominal ratio (B).

From $y = 0\%$ to $y = 80\%$, the color of these nanoparticles samples does not change over time. For $y = 90\%$, the powder was initially deep brown, but became light brown within two weeks in air at room temperature, suggesting a degradation of the structure.

II.3.2. Structural analysis of compounds exposed to air

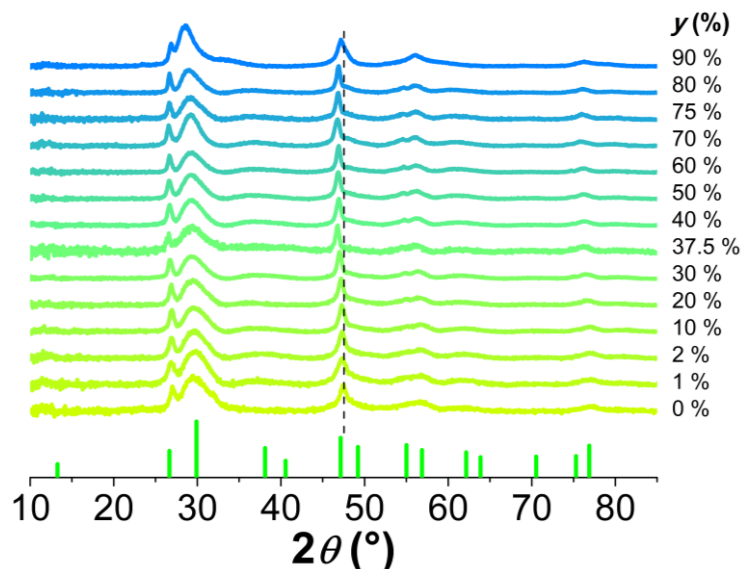


Figure 34: Powder XRD patterns of $\text{Gd}_{2(1-y)}\text{Ce}_{2y}\text{O}_2\text{S}$ nanoparticles.

XRD patterns of nanoparticles isolated in air were systematically performed (Figure 34). Below 90 %, the patterns were consistent with $\text{Ln}_2\text{O}_2\text{S}$ but a small shift of the peaks is observed. For 90 % of cerium, the pattern was not consistent with the reference pattern of

$\text{Ln}_2\text{O}_2\text{S}$, in agreement with the observation mentioned above. XRD pattern shows diffraction peaks of CeO_2 in addition to $\text{Ln}_2\text{O}_2\text{S}$, as observed for $\text{Ce}_2\text{O}_2\text{S}$ nanoparticles (Figure 35).

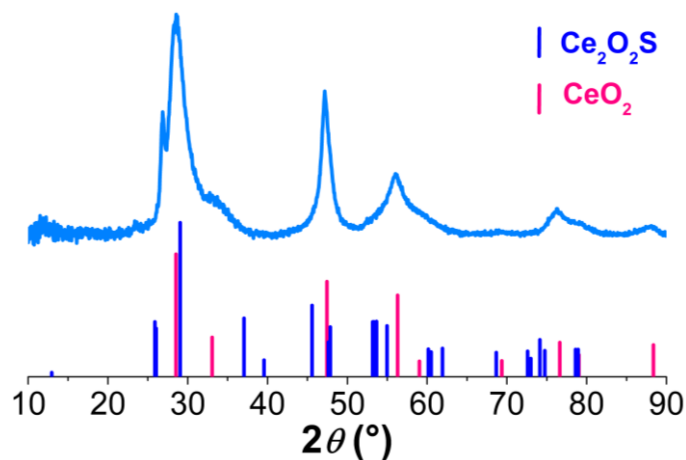


Figure 35: Powder XRD pattern of $\text{Gd}_{1.8}\text{Ce}_{0.2}\text{O}_2\text{S}$ nanoparticles [CL213].

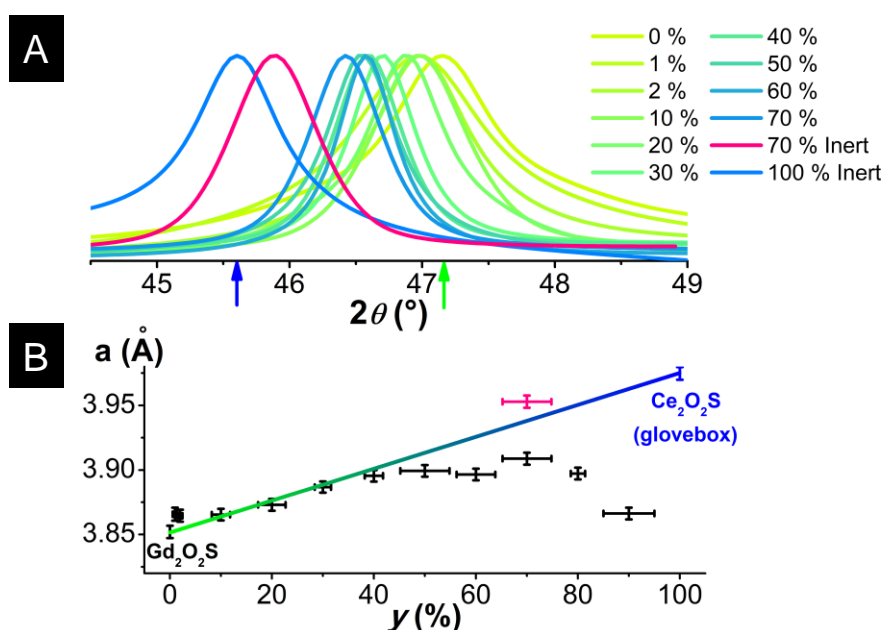


Figure 36: (A) X-ray diffraction normalized (110) peaks fitted using pseudo-Voigt functions for $\text{Gd}_{2(1-y)}\text{Ce}_{2y}\text{O}_2\text{S}$ nanoparticles isolated in air and under inert atmosphere for two $\text{Gd}_{0.6}\text{Ce}_{1.4}\text{O}_2\text{S}$ and $\text{Ce}_2\text{O}_2\text{S}$ samples (see experimental section). Vertical arrows indicate the (110) reflection position of $\text{Ce}_2\text{O}_2\text{S}$ (blue, JCPDS 26-1085) and $\text{Gd}_2\text{O}_2\text{S}$ (green, JCPDS 26-1422). (B) Lattice parameter a as a function of the cerium fraction y . The straight colored line is a linear fit to the data. The data concern bimetallic $\text{Gd}_{2(1-y)}\text{Ce}_{2y}\text{O}_2\text{S}$ nanoparticles isolated in air (black dots with error bars) or under inert atmosphere (pink and blue dots with error bars). The lattice parameters of the samples kept under inert atmosphere correspond to the ones expected by the Vegard's law.

The lattice parameter $a = 2d_{(110)}$ was determined by fitting the position of the (110) and (111) diffraction peaks using pseudo-Voigt curves (Figure 36A). Two regimes are observed. From 0

to 40 %, the lattice parameter follows the Vegard's law expected using the lattice parameters of $\text{Gd}_2\text{O}_2\text{S}$ and $\text{Ce}_2\text{O}_2\text{S}$ (Figure 36B).^{20,21} This indicates that both cerium and gadolinium ions partially occupy the same site in the unit cell. From $y = 40$ % to $y = 80$ % the lattice parameter a levels off. To explain this behavior, we envisage the following two scenarios: (i) 40 % is the solubility limit of cerium, or (ii) there is no solubility limit but the phase is not stable in air.

II.3.3. Structural analysis of compound with $y = 70$ % under inert atmosphere

In order to clarify the above point, in a complementary experiment, the as-prepared $y = 70$ % compound ($\text{Gd}_{0.6}\text{Ce}_{1.4}\text{O}_2\text{S}$) was isolated and washed under inert conditions. The value of the lattice parameter of this sample is larger than that of the sample isolated in air and nicely follows Vegard's law (Figure 36B, pink dot), which supports scenario (ii).

It is interesting to analyze the compounds after air exposure. As discussed above and according to Figure 33, the EDS data show that the ratio of lanthanide present in the powder is equal to the nominal ratio. This fact, in addition to the leveling off of the a parameter for $y = 40$ %, suggests that secondary Ce-containing species are formed on the surface of the $\text{Ln}_2\text{O}_2\text{S}$ bimetallic structure as a consequence of air exposure. In order to investigate this question, an additional TEM was carried out.

II.3.4. Transmission electron microscopy on the $y = 0, 37.5, 50$ and 75 % compounds

Similar to the case of the $\text{Gd}_2\text{O}_2\text{S}$ and $\text{Ce}_2\text{O}_2\text{S}$ nanoparticles, bimetallic Gd-Ce oxysulfide nanoparticles crystallize in the form of hexagonal nanoplates (Figure 38). Transmission Electron Microscopy images typically display the $\{001\}$ or $\{100\}$ facets of the nanoplates. Their width and thickness are 10 - 20 nm and 2 nm, respectively, somehow larger than the $y = 0$ $\text{Gd}_2\text{O}_2\text{S}$ nanoparticles (7.8 ± 1.3 nm in width and 1.5 ± 0.2 nm in thickness). The width of the nanoparticles are in agreement with Scherrer's crystalline domain size calculated from the (110) reflection peak (Table 5).

y (%)	0	1	2	10	20	30	40	50	60	70	80	100*
Crystal domain size (nm)	8 ± 2	7 ± 2	9 ± 2	10 ± 2	11 ± 3	14 ± 3	14 ± 3	13 ± 3	16 ± 4	13 ± 3	16 ± 4	11 ± 3

Table 5: Crystal domain size obtained via Scherrer's equation on (110) diffraction peak of $\text{Gd}_{2(1-y)}\text{Ce}_{2y}\text{O}_2\text{S}$ nanoparticles.

High-resolution transmission electron microscopy (HRTEM) confirmed that both $\text{Gd}_2\text{O}_2\text{S}$ and bimetallic nanoparticles are single crystals of $\text{Gd}_{2(1-y)}\text{Ce}_{2y}\text{O}_2\text{S}$. The analysis of the Fourier

transforms of the HRTEM images (Figure 26 and Figure 37) agrees with the crystal system and with the lattice parameters obtained by means of XRD.

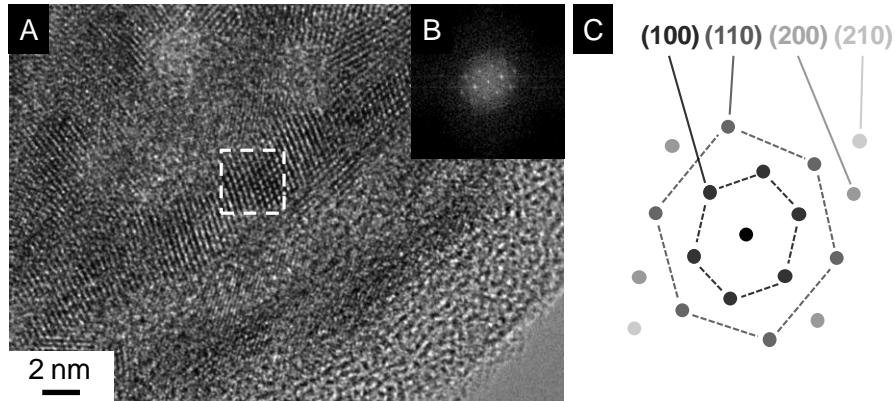


Figure 37: (A) HRTEM micrograph of Gd_{1.8}Ce_{0.2}O₂S nanoparticles [CL026]. (B) FFT associated with the monocrystal delimited zone (B) and the corresponding crystallographic attribution (C).

For $y > 70$ %, we find some smaller and shapeless nanoparticles that may consist of cerium-containing species that nucleate in the solution during the synthesis or of degraded Gd-Ce oxysulfide nanoparticles exposed to air, as indicated by the smaller a lattice parameter of these particles.

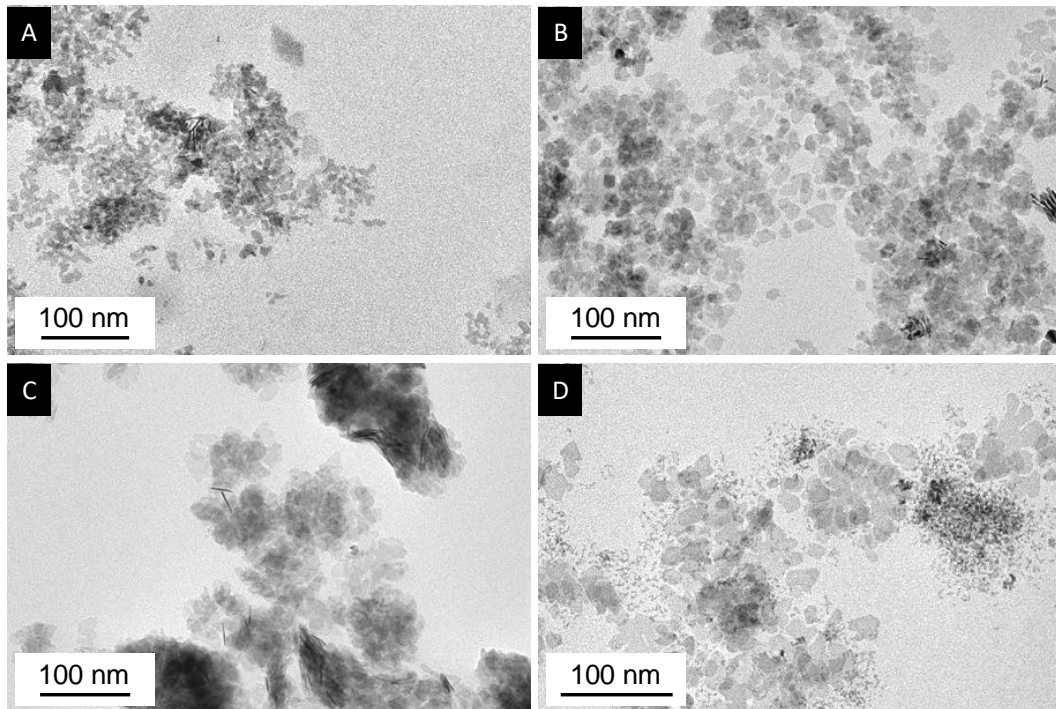


Figure 38: TEM micrographs of Gd_{2(1-y)}Ce_{2y}O₂S nanoparticles containing the following cerium fractions: (A) $y = 0$ %, (B) 37.5 %, (C) 50 % and (D) 75 %.

Altogether, the substitution of Gd by Ce in Gd₂O₂S slightly affects the oxysulfide nanoparticles morphology, and nanoplates of dimension 30 nm or smaller are obtained. For

$y < 80 \%$, the reactivity of cerium in $\text{Gd}_{2(1-y)}\text{Ce}_{2y}\text{O}_2\text{S}$ is found to be lower than in pure $\text{Ce}_2\text{O}_2\text{S}$ nanoparticles but it is still sufficient to destabilize the structure for $y > 40 \%$.

End of quote

Although the formation of a solid solution between $\text{Gd}_2\text{O}_2\text{S}$ and $\text{Ce}_2\text{O}_2\text{S}$ is expected for the reasons mentioned above, the stability of the compounds even for high cerium concentration may be surprising. The phase becomes unstable in air only when the Ce concentration is as large as $y = 50 \%$ samples. In these samples, a significant departure from Vegard's law has been found in the samples exposed to air, while the samples kept under inert atmosphere display no degradation. These observations prompt us to investigate the effects of air or water exposure on the bimetallic nanoparticles to compare their reactivity with that of $\text{Gd}_2\text{O}_2\text{S}$ and $\text{Ce}_2\text{O}_2\text{S}$. A first clue was given by XANES experiments at S K-edge (Figure 39).

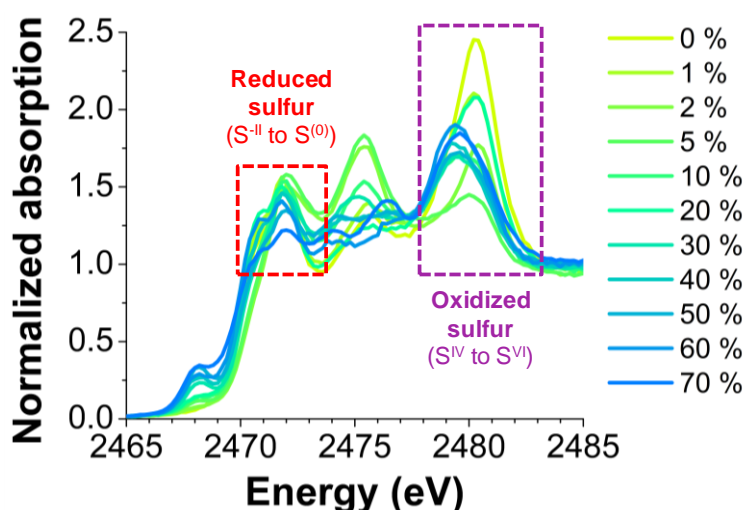


Figure 39: XANES spectra at sulfur K-edge of $\text{Gd}_{2(1-y)}\text{Ce}_{2y}\text{O}_2\text{S}$ nanoparticles for $y = 0 - 70 \%$.

As expected, sulfur in bimetallic nanoparticles is partially oxidized, showing a similar reactivity than that of $\text{Gd}_2\text{O}_2\text{S}$. One notes that the mechanism of sulfur oxidation processes seems to depend on cerium concentration (oxidation peak centered at ~ 2480 eV for low amounts of cerium or ~ 2478 eV when $y > 10 \%$).

Due to limited beamtime, we could not perform XANES at Ce L_{III} -edge on these samples, but one would expect that cerium is mainly trivalent (Ce^{III}) for structures with $y < 50 \%$, while it is significantly oxidized for $y \geq 50 \%$, thus leading to degradation for $y \geq 80 \%$.

In order to investigate the species formed during the process of nanoparticle oxidation, we performed *in situ* X-ray photoelectron spectroscopy on samples with or without cerium.

II.4. Reactivity toward O₂ and H₂O: comparison between GdCeO₂S and Gd₂O₂S

Adapted from Larquet, C. *et al. Inorg. Chem.* **2017**, 56 (22), 14227–14236.⁷

So far, we have discussed the effect of air as an oxidizing medium, without differentiating the roles of water and of dioxygen. In order to address this question, a Near-Ambient-Pressure X-Ray Photoelectron Spectroscopy (NAP-XPS) facility installed at the TEMPO beamline of SOLEIL was used as a surface analysis technique. In our case, almost the whole nanoparticle can be probed because of the reduced thickness of our nanoparticles (≈ 1.5 -2.0 nm).

We considered the following two scenarios for the oxidation of sulfur and of cerium: (i) the oxidation of both elements occurs independently; (ii) one of the two ions (Ce^{III} and S^{-II}) delays the oxidation of the other ion. In case (i), sulfur in GdCeO₂S and in Gd₂O₂S should oxidize at the same rate. In case (ii), the sequential oxidation of cerium and of sulfur, or vice-versa, should be observed by XPS. In order to verify these two scenarios, fresh Gd₂O₂S and GdCeO₂S ($y = 50\%$) nanoparticles were synthesized, isolated in air, and drop-casted on gold-covered silicon wafer. Exposure to air was limited and the samples were stored under inert atmosphere and introduced in the setup *via* a glove bag connected to the load lock of the NAP-XPS.

The nanoparticles were analyzed at room temperature under vacuum, and then under water pressure, a mixture of water and oxygen, and back under vacuum. For information, standard electrode potentials of several couples of our system are listed here: $E^0(\text{O}_2/\text{H}_2\text{O}) = 1.23\text{ V}$; $E^0(\text{H}^+/\text{H}_2) = 0\text{ V}$; $E^0(\text{S}^{\text{VI}}/\text{S}^{-\text{II}}) = 0.33\text{ V}$; $E^0(\text{S}^{\text{IV}}/\text{S}^{-\text{II}}) = 0.38\text{ V}$; $E^0(\text{Ce}^{\text{IV}}/\text{Ce}^{\text{III}}) = 1.61\text{ V}$.

The two samples were deposited on a single sample-holder and subsequently exposed to exactly the same atmospheres. Thoroughly degassed water vapor was introduced before introducing the O₂ gas, for the former gas is less oxidizing than the latter. O₂ was then introduced along with water, because obtaining ultra-high-vacuum conditions after having introduced water would require baking the vacuum chamber for a long time not compatible with the constraints set by synchrotron runs. For the same reason, the last measurements under vacuum conditions were actually carried out under a residual background pressure of water.

Binding energies (B.E.) were calibrated using the Au 4f doublet, as described in Experimental section. S 2p and Gd 4d photoemission spectra were collected in a single sweep in the 135 - 175 eV region of B.E. (Figure 40). The Ce 3d_{3/2} and Ce 3d_{5/2} B.E. were also monitored

in the 870 - 920 eV region for the GdCeO₂S nanoparticles (Figure 41A). As shown in Figure 41C, we successfully determined the Ce^{III} fraction by using a careful fitting procedure of the intensity which takes into account the overlap of the spin-orbit split peak (Figure 41B).

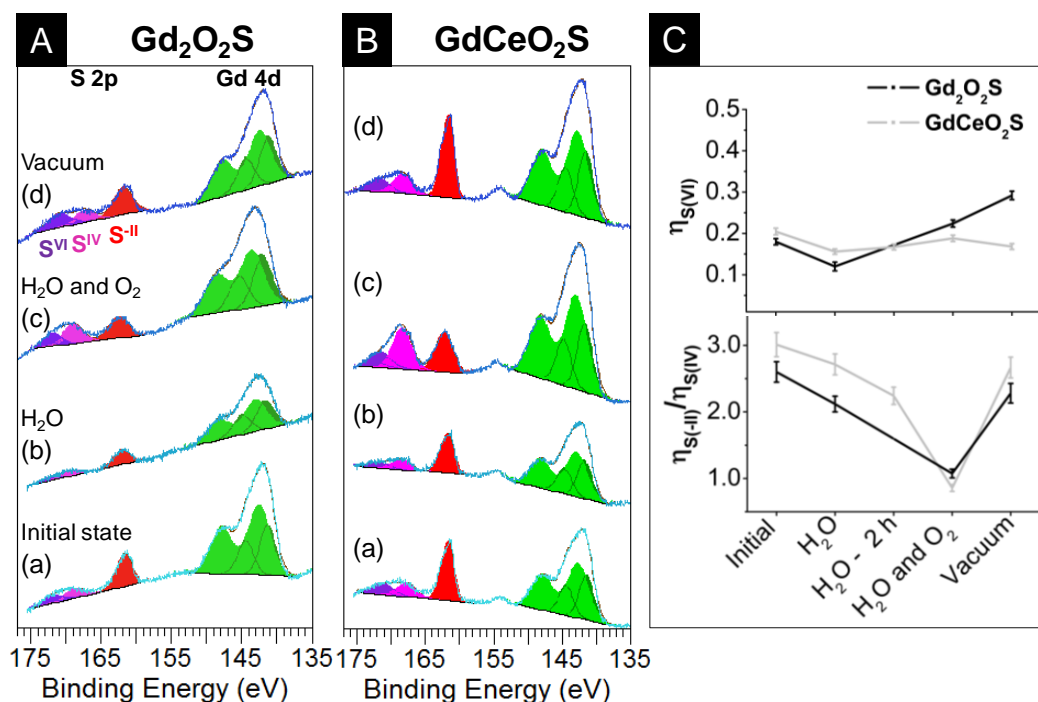


Figure 40: Room temperature NAP-XPS spectra of air-exposed samples of (A) Gd₂O₂S and (B) GdCeO₂S nanoparticles collected using an incident photon energy of 735 eV at the following conditions: (a) ultra-high vacuum (10⁻⁹ mbar); (b) H₂O pressure of 0.2 mbar; (c) Mixture of H₂O (0.2 mbar) and O₂ (0.2 mbar) partial pressures; (d) Vacuum obtained upon pumping down the chamber after (c). (B) For GdCeO₂S, an additional spectrum was also collected after exposing the sample to water vapor for two hours without beam to avoid radiation damage. Color code: S 2*p* doublet in red (S^{-II}), pink (S^{IV}) and purple (S^{VI}); Gd 4*d* doublets in light green and deep green (shake-down satellite peaks).²² The fitting curves (in brown) are mostly superimposed with the experimental curves. (C) Top: S^{VI} fraction ($\eta_{S(VI)}$); Bottom: S^{-II}/S^{IV} fraction ratio ($\eta_{S(-II)} / \eta_{S(IV)}$).

In all spectra, the sulfide species are identified by a S 2*p*_{3/2} doublet at 161.6 ± 0.3 eV (Figure 40A).²³ Oxidized sulfur is also always present and confirms the XANES result that samples whose work-up was carried out under air are already partially oxidized. Here, oxidized sulfur is composed of two major oxidation species that we identify as S^{IV} and S^{VI}. Each S 2*p*_{3/2} spectrum was fitted by a double peak; the B.E. of the lower-energy component was 168.1 ± 0.7 eV for S^{IV} (in pink) and 171.3 ± 0.5 eV for S^{VI} (in purple). The relative area of each contribution allowed us to plot the ratios of the species for different atmospheres (Figure 40C). For both nanoparticles samples, the Gd spectrum showed no significant evolution, as expected. The exposure of both Gd₂O₂S and GdCeO₂S samples to water vapor led to a partial S^{-II} - S^{IV} conversion within 2 hours (Figure 40C); the S^{-II} species correspond to the oxysulfide,

while S^{IV} is attributed to sulfites ions $(SO_3)^{2-}$ forming an step during the sulfide to sulfate transformation.²⁴ The addition of O_2 in the chamber led to an increase of S^{IV} concentration within a few minutes, suggesting that O_2 is a stronger oxidizing agent than water.

The evolution of the S^{VI} fraction is more complex. Initially, the S^{VI} species are attributed to sulfates formed during the short exposure of the nanoparticles to air. For both samples, this fraction does not significantly decrease during subsequent treatments, suggesting that the S^{VI} formed in the room atmosphere prior to the XPS measurement is irreversible. In Gd_2O_2S , the quantity of S^{VI} species increases during the last steps of exposure to O_2 and of pumping. However, in $GdCeO_2S$, this quantity remains almost constant over the course of the further treatments (Figure 40C). It is possible that Ce^{III} was playing a sacrificial role, thus preventing sulfur from further oxidation (Figure 41).

During exposure to water vapor and then to O_2 , sulfur oxidation is accompanied by an oxidation of Ce^{III} into Ce^{IV} especially during the early stage of exposure to air (Figure 41C). However, this oxidation is limited and the $Ce^{III}:Ce^{IV}$ ratio remains significant, consistent with the fact that the bulk crystal structure, which contains Ce^{III} , is preserved, as observed *ex situ* in the $y = 50$ % samples.

Restoring the high vacuum conditions almost restored the initial S^{-II} fraction and affected the Ce^{III} fraction. Flahaut *et al.* previously observed a similar reversibility by heating bulk Ce_2O_2S up to 1300 °C under vacuum.³ Ikeue *et al.* also reported that oxysulfate sheets can be reduced to oxysulfide ones in H_2S atmosphere.¹⁹ Here, the process occurs at room temperature but the ultra-high vacuum conditions play a reducing role; furthermore, the effect is enhanced in nanoparticles owing to the high surface/volume ratio. Having said this, the reversibility of the reduction under vacuum conditions is different from the oxysulfide/oxysulfate transition, since the XRD patterns of our samples did not show any structural modification even after several months. This further supports the argument that the oxido-reduction process is favored at the surface of the nanoparticles. Water desorption can be at the origin of the reduction of the metal, that later reduces the sulfur. Such metal reduction by water desorption was for instance observed on amorphous vanadium oxide.²⁵ However, the whole reduction mechanism was not investigated.

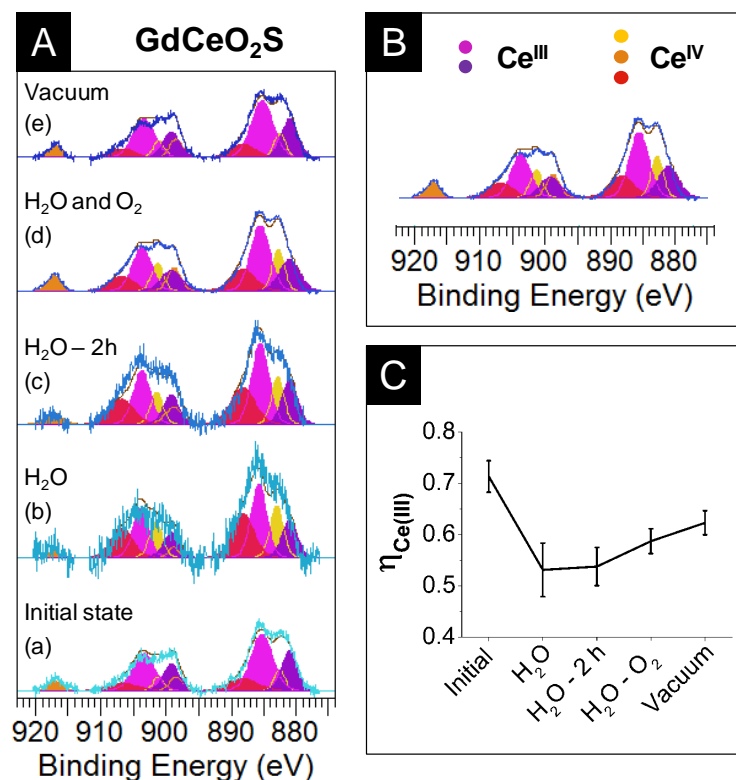


Figure 41: (A) Ce 3d NAP-XPS spectra of GdCeO₂S nanoparticles measured with an incident photon energy of 1100 eV and after background subtraction. The Ce^{III} species are represented by the pink and violet peaks. Yellow, orange and red peaks are specific to Ce^{IV} species. (a) Ultra-high vacuum (10⁻⁹ mbar); (b) H₂O partial pressure of 0.2 mbar; (c) after two hours of exposure to a H₂O partial pressure of 0.2 mbar; (d) H₂O partial pressure of 0.2 mbar and O₂ partial pressure of 0.2 mbar; (e) Back to vacuum. (B) Typical deconvolution of the Ce^{III} and Ce^{IV} peaks. (C) Evolution of the fraction of Ce^{III} (η_{Ce(III)}) during the NAP-XPS experiment. See the experimental section for the details of the fitting procedure.

End of quote

II.5. Conclusion

By means of an optimized colloidal synthesis route, we were able to synthesize single-crystal $\text{Gd}_2\text{O}_2\text{S}$ nanoparticles. We established that the oxydo-reductive properties of cerium affect the stability of the $\text{Ce}_2\text{O}_2\text{S}$ nanoparticles and showed that their synthesis can be realized with similar reaction conditions and isolation/washing under inert atmosphere. A solid solution of $\text{Gd}_{2(1-y)}\text{Ce}_{2y}\text{O}_2\text{S}$ nanoparticles is obtained by using a mixture of $\text{Gd}(\text{acac})_3$ and $\text{Ce}(\text{acac})_3$. The as-prepared nanoparticles remain stable in air up to $y = 80\%$, but slight structures changes occur in air for $y > 40\%$.

The reactivity of the nanoparticles was investigated in detail. We found that air and water partially oxidize sulfur in $\text{Gd}_2\text{O}_2\text{S}$ nanoparticles, unveiling their unexpected reactivity. Since XRD indicates that the $\text{Gd}_2\text{O}_2\text{S}$ structure remains stable, this reactivity is attributed to the surface of the nanoparticles. The oxidized species are likely to be SO_3^{2-} (S^{IV}) and SO_4^{2-} (S^{VI}). $\text{Ce}_2\text{O}_2\text{S}$ degradation under air or water is the consequence of the concomitant oxidations of cerium and sulfur and leads to the formation of CeO_2 nanocrystallites, as indicated by our XRD analysis. This suggests that the sulfur resulting from phase decomposition may form amorphous sulfates. The two oxidation processes are also present in GdCeO_2S ($y = 50\%$), which accounts for the unit cell volume found in $y > 40\%$ compounds.

References

- (1) Rosticher, C.; Viana, B.; Fortin, M.-A.; Lagueux, J.; Faucher, L.; Chanéac, C. Gadolinium Oxysulfide Nanoprobes with Both Persistent Luminescent and Magnetic Properties for Multimodal Imaging. *RSC Adv.* **2016**, *6* (60), 55472–55478.
- (2) Ding, Y.; Gu, J.; Ke, J.; Zhang, Y.-W.; Yan, C.-H. Sodium Doping Controlled Synthesis of Monodisperse Lanthanide Oxysulfide Ultrathin Nanoplates Guided by Density Functional Calculations. *Angew. Chemie Int. Ed.* **2011**, *50* (51), 12330–12334.
- (3) Flahaut, J.; Guittard, M.; Patrie, M. Les Oxysulfures $\text{Me}_2\text{O}_2\text{S}$ Des Éléments Du Groupe Des Terres Rares. *Bull. Soc. Chim. Fr.* **1958**, *7*, 990–994.
- (4) Dugué, J.; Carré, D.; Guittard, M. Etude Structurale Des Oxysulfures de Cérium(III) et Cérium(IV). I. Structure Cristalline de l'Oxysulfure de Cérium $\text{Ce}_4\text{O}_4\text{S}_3$. *Acta Crystallogr.* **1978**, *B34*, 3564–3568.
- (5) Wichelhaus, W. $\text{Ce}_4\text{O}_4\text{S}_3$: A Mixed-Valence Cerium Oxide Sulfide. *Angew. Chemie Int. Ed. English* **1978**, *17* (6), 451–452.
- (6) Dugué, J.; Carré, D.; Guittard, M. Etude Structurale Des Oxysulfures de Cérium(III) et Cérium(IV). II. Structure Cristalline de l'Oxysulfure de Cérium $\text{Ce}_6\text{O}_6\text{S}_4$. *Acta Crystallogr.* **1979**, *B35*, 1550–1554.
- (7) Larquet, C.; Nguyen, A.-M.; Ávila-Gutiérrez, M.; Tinat, L.; Lassalle-Kaiser, B.; Gallet, J.-J.; Bournel, F.; Gauzzi, A.; Sanchez, C.; Carenco, S. Synthesis of $\text{Ce}_2\text{O}_2\text{S}$ and $\text{Gd}_2(1-y)\text{Ce}_2y\text{O}_2\text{S}$ Nanoparticles and Reactivity from in Situ X-Ray Absorption Spectroscopy and X-Ray Photoelectron Spectroscopy. *Inorg. Chem.* **2017**, *56* (22), 14227–14236.
- (8) Sourisseau, C.; Cavagnat, R.; Mauricot, R.; Boucher, F.; Evain, M. Structure and Bondings in Cerium Oxysulfide Compounds I - Electronic, Infrared and Resonance Raman Spectra of $\text{Ce}_2.00\text{O}_2.5\text{S}$. *J. Raman Spectrosc.* **1997**, *28* (12), 965–971.
- (9) Sourisseau, C.; Fouassier, M.; Mauricot, R.; Boucher, F.; Evain, M. Structure and Bonding in Cerium Oxysulfide Compounds. II—Comparative Lattice Dynamics Calculations on $\text{Ce}_2\text{O}_2\text{S}$ and $\text{Ce}_2.00\text{O}_2.5\text{S}$. *J. Raman Spectrosc.* **1997**, *28* (12), 973–978.
- (10) Lei, L.; Zhang, S.; Xia, H.; Tian, Y.; Zhang, J.; Xu, S. Controlled Synthesis of Lanthanide-Doped $\text{Gd}_2\text{O}_2\text{S}$ Nanocrystals with Novel Excitation-Dependent Multicolor Emissions. *Nanoscale* **2017**, *9* (17), 5718–5724.
- (11) Frank, P.; Hedman, B.; Carlson, R. M. K.; Tyson, T. A.; Roe, A. L.; Hodgson, K. A Large Reservoir of Sulfate and Sulfonate Resides within Plasma Cells From. *Biochemistry* **1987**, *26*, 4975–4979.
- (12) Vairavamurthy, A.; Manowitz, B.; Luther, G. W.; Jeon, Y. Oxidation State of Sulfur in Thiosulfate and Implications for Anaerobic Energy Metabolism. *Geochim. Cosmochim. Acta* **1993**, *57* (7), 1619–1623.
- (13) Prietzel, J.; Thieme, J.; Tyufekchieva, N.; Paterson, D.; McNulty, I.; Kögel-knabner, I. Sulfur Speciation in Well-Aerated and Wetland Soils in a Forested Catchment Assessed by Sulfur K - Edge X-Ray Absorption near-Edge Spectroscopy (XANES). *J. Plant Nutr. Soil Sci.* **2009**, *172*, 393–409.
- (14) Morgan, B.; Burton, E. D.; Rate, A. W. Iron Monosulfide Enrichment and the Presence of Organosulfur in Eutrophic Estuarine Sediments. *Chem. Geol.* **2012**, *296–297*, 119–130.
- (15) Rodriguez, J. A.; Chaturvedi, S.; Hanson, J. C.; Brito, J. L. Reaction of H_2 and H_2S with CoMoO_4 and NiMoO_4 : TPR, XANES, Time-Resolved XRD, and Molecular-Orbital Studies. *J. Phys. Chem. B* **1999**, *103*, 770–781.
- (16) Rodriguez, J. A.; Jirsak, T.; Freitag, A.; Hanson, J. C.; Larese, J. Z.; Chaturvedi, S. Interaction of SO_2 with CeO_2 and Cu/CeO_2 Catalysts: Photoemission, XANES and TPD Studies. *Catal. Letters* **1999**, *62* (2), 113–119.

- (17) Cui, D.; Zhang, P.; Ma, Y.; He, X.; Li, Y.; Zhang, J.; Zhao, Y.; Zhang, Z. Effect of Cerium Oxide Nanoparticles on Asparagus Lettuce Cultured in an Agar Medium. *Environ. Sci. Nano* **2014**, *1* (5), 459–465.
- (18) Gregson, M.; Lu, E.; Tuna, F.; McInnes, E. J. L.; Hennig, C.; Scheinost, A. C.; McMaster, J.; Lewis, W.; Blake, A. J.; Kerridge, A.; Liddle, S. T. Emergence of Comparable Covalency in Isostructural Cerium(IV)– and Uranium(IV)–carbon Multiple Bonds. *Chem. Sci.* **2016**, *7* (5), 3286–3297.
- (19) Ikeue, K.; Kawano, T.; Eto, M.; Zhang, D.; Machida, M. X-Ray Structural Study on the Different Redox Behavior of La and Pr Oxysulfates/Oxysulfides. *J. Alloys Compd.* **2008**, *451* (1–2), 338–340.
- (20) Vegard, L. Die Konstitution Der Mischkristalle Und Die Raumfüllung Der Atome. *Zeitschrift für Phys.* **1921**, *5* (1), 17–26.
- (21) Denton, A. R.; Ashcroft, N. W. Vegard’s Law. *Phys. Rev. A* **1991**, *43* (6), 3161–3164.
- (22) Uwamino, Y.; Ishizuka, T.; Yamatera, H. X-Ray Photoelectron Spectroscopy of Rare-Earth Compounds. *J. Electron Spectros. Relat. Phenomena* **1984**, *34* (1), 67–78.
- (23) Smart, R. S. C.; Skinner, W. M.; Gerson, A. R. XPS of Sulphide Mineral Surfaces: Metal-Deficient, Polysulphides, Defects and Elemental Sulphur. *Surf. Interface Anal.* **1999**, *28* (1), 101–105.
- (24) Manocha, A. S.; Park, R. L. Flotation Related ESCA Studies on PbS Surfaces. *Appl. Surf. Sci.* **1977**, *1* (1), 129–141.
- (25) Araki, B.; Audières, J.-P.; Michaud, M.; Livage, J. Action de La Vapeur d’eau Sur V₂O₅ Amorphe. *Bull. Soc. Chim. Fr.* **1981**, No. 9–10, 366–370.

Chapter III

Unveiling the structure of $\text{Ln}_2\text{O}_2\text{S}$

nanoplates synthesized in high boiling

point organic solvents with an alkali

source: $\text{Gd}_2\text{O}_2\text{S}$ as a case study

Table of content

Foreword 95

III.1. Non stoichiometric $\text{Ln}_2\text{O}_2\text{S}$ nanoparticles 96

III.1.1. Sulfur amount in $\text{Ln}_2\text{O}_2\text{S}$ nanoplates 96

III.1.2. Charge equilibrium: the role of surface ligands 100

III.1.2.1. Ligands nature and amount 100

III.1.2.2. Coordination mode of oleates around Gd^{III} cations..... 105

III.1.3. Conclusion and perspectives on ligands removal 107

III.2. Role and localization of the alkali ion 110

III.2.1. State of the art: an ongoing controversy..... 110

III.2.2. Localization of the alkali in the final product 112

III.2.3. Role of the alkali complex..... 116

III.2.3.1. Influence of the alkali nature..... 116

III.2.3.2. Influence of the alkali stoichiometry..... 118

III.2.3.3. New hypothesis: sodium stabilizes sulfur radicals..... 120

III.2.4. Conclusion about the role of sodium.....	122
III.3. First insights in the formation mechanism of Gd ₂ O ₂ S nanoplates	123
III.3.1. Investigating the synthesis unfolding: why and how?	123
III.3.2. SAXS and WAXS of colloidal solutions of Gd ₂ O ₂ S nanoplates (final state).....	124
III.3.3. Mechanism of formation of the Gd ₂ O ₂ S nanoplates	127
III.3.3.1. Sampling method.....	127
III.3.3.2. From the complex to the nuclei (T < 300 °C)	127
III.3.3.3. Nuclei, nanoplates and aggregates (T > 300 °C).....	129
III.3.3.4. Conclusion: a new view on the role played by alkali.....	131
III.4. Conclusion	133
References	135

Foreword

Our first studies on $\text{Ln}_2\text{O}_2\text{S}$ nanoparticles raised questions about three major issues:

- **Sulfur** - Why is there a sulfur lack in the $\text{Ln}_2\text{O}_2\text{S}$ nanoparticles?
- **Sodium** - Where is the sodium and what is its role in the synthesis?
- **Formation** - How do the particles nucleate and grow in solution?

We will demonstrate that these questions are intimately connected. That is why they are dealt with in the same chapter.

III.1. Non stoichiometric $\text{Ln}_2\text{O}_2\text{S}$ nanoparticles

III.1.1. Sulfur amount in $\text{Ln}_2\text{O}_2\text{S}$ nanoplates

When Ding *et al.* presented their synthesis of $\text{Ln}_2\text{O}_2\text{S}$ nanoparticles, they also indicated that these were sulfur-defective with a molar ratio $\text{S}:\text{La} = 0.38 \pm 0.05$ ($\text{S}:(\text{La} + \text{Na}) = 0.30 \pm 0.05$) instead of the expected value $\text{S}:\text{La} = 0.5$.¹ The authors then concluded that the nanoplates were terminated by two $[\text{La}_2\text{O}_2]^{2+}$ layers (doped with Na) as represented in Figure 42. The charge balance should be ensured by negatively charged ligands that they supposed to be oleate ligands.

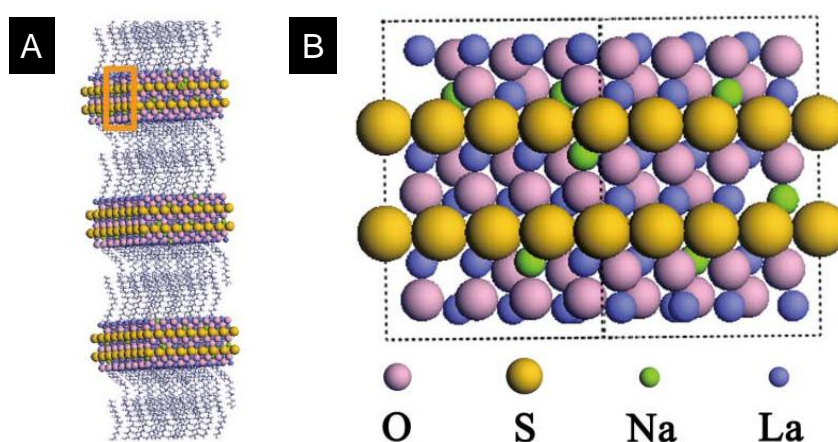


Figure 42: From Ding *et al.*¹: Schematic representation of self-assembled Na-doped $\text{Ln}_2\text{O}_2\text{S}$ nanoparticles (A) with a zoom on a nanoplate thickness terminated by $[\text{Ln}_2\text{O}_2]^{2+}$ layers in (B).

Our syntheses with gadolinium led to the same observation on the sulfur final amount in the nanoparticles. Despite the powder XRD pattern attesting the $\text{Gd}_2\text{O}_2\text{S}$ structure (Chapter II, Figure 6), the sulfur amount probed by EDS (Table 6) was far lower than expected and gives non stoichiometric nanoparticles with the formula $\text{Gd}_2\text{O}_2\text{S}_x$, with $x = 0.3 - 0.6$ (0.15 - 0.30 equiv. vs. Gd).

Gd (equiv.)	S (equiv.)	Na (equiv.)
1.00	0.15 - 0.30	0.05 - 0.40

Table 6: Range chemical composition obtained on several $\text{Gd}_2\text{O}_2\text{S}$ nanoparticles syntheses. There is no correlation between the sulfur amount and the sodium amount.

The sulfur amount in our case (Table 6) is lower than the one reported by Ding *et al.* for $\text{La}_2\text{O}_2\text{S}$ nanoparticles. This lower S:Gd ratio may be due to the width difference of the nanocrystals: 22 nm for $\text{La}_2\text{O}_2\text{S}$ nanoplates¹ vs. 7 - 8 nm for $\text{Gd}_2\text{O}_2\text{S}$ nanoplates.^{1,2} We thus

calculated the expected stoichiometry for $\text{Gd}_2\text{O}_2\text{S}_x$ nanoparticles when they are terminated by two $[\text{Ln}_2\text{O}_2]^{2+}$ layers (Figure 43).

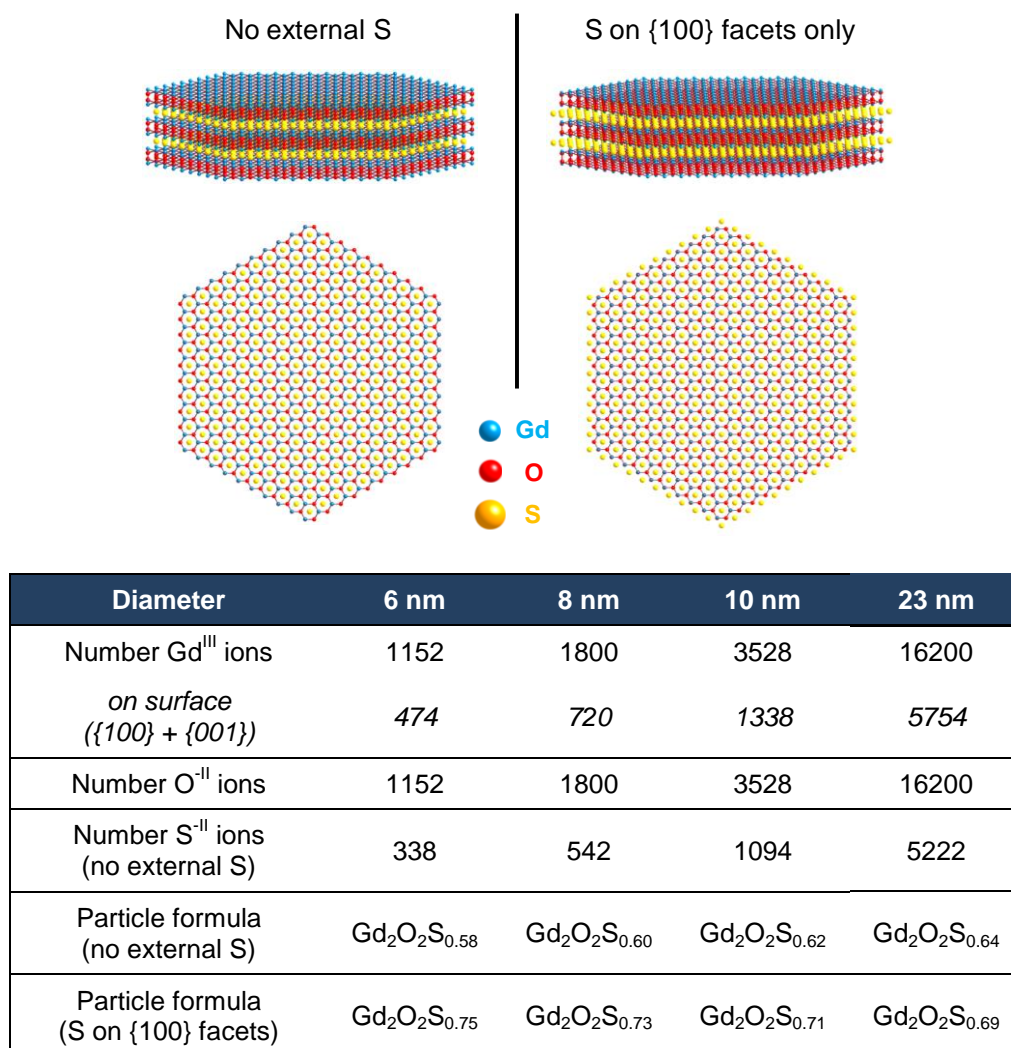


Figure 43: Expected stoichiometry of sulfur defective $\text{Gd}_2\text{O}_2\text{S}_x$ nanoparticles with no external sulfur and in the case of external sulfur only on $\{100\}$ facets.

Obviously, the sulfur stoichiometry is more sensitive to the surface when the nanoparticles dimensions get smaller. In comparison, a 23 nm wide nanoparticle stoichiometry would be close to $\text{La}_2\text{O}_2\text{S}_{0.64}$ without external sulfur and $\text{La}_2\text{O}_2\text{S}_{0.69}$ with external sulfur on the $\{100\}$ facets ($\text{La}_2\text{O}_2\text{S}$ and $\text{Gd}_2\text{O}_2\text{S}$ lattice parameters are close to each other). Both results are in agreement with the sulfur amount measured by Ding *et al.*¹ For us, the $\text{Gd}_2\text{O}_2\text{S}_{\sim 0.6}$ stoichiometry in the case of no external sulfur is in agreement with our EDS measurements. Nevertheless, some syntheses gave a significant lower amount and we demonstrated in the previous chapter that the sulfur at the surface got oxidized. To reconcile these results, we imagined the $\text{Gd}_2\text{O}_2\text{S}_x$ nanoparticles similar to a core-shell structure in which the core is a $\text{Gd}_2\text{O}_2\text{S}$ perfect crystal terminated by $[\text{Gd}_2\text{O}_2]^{2+}$ layers and the shell is a structurally

disorganized reactive layer. In terms of chemical synthesis, the shell could correspond to incomplete crystalline external layers.

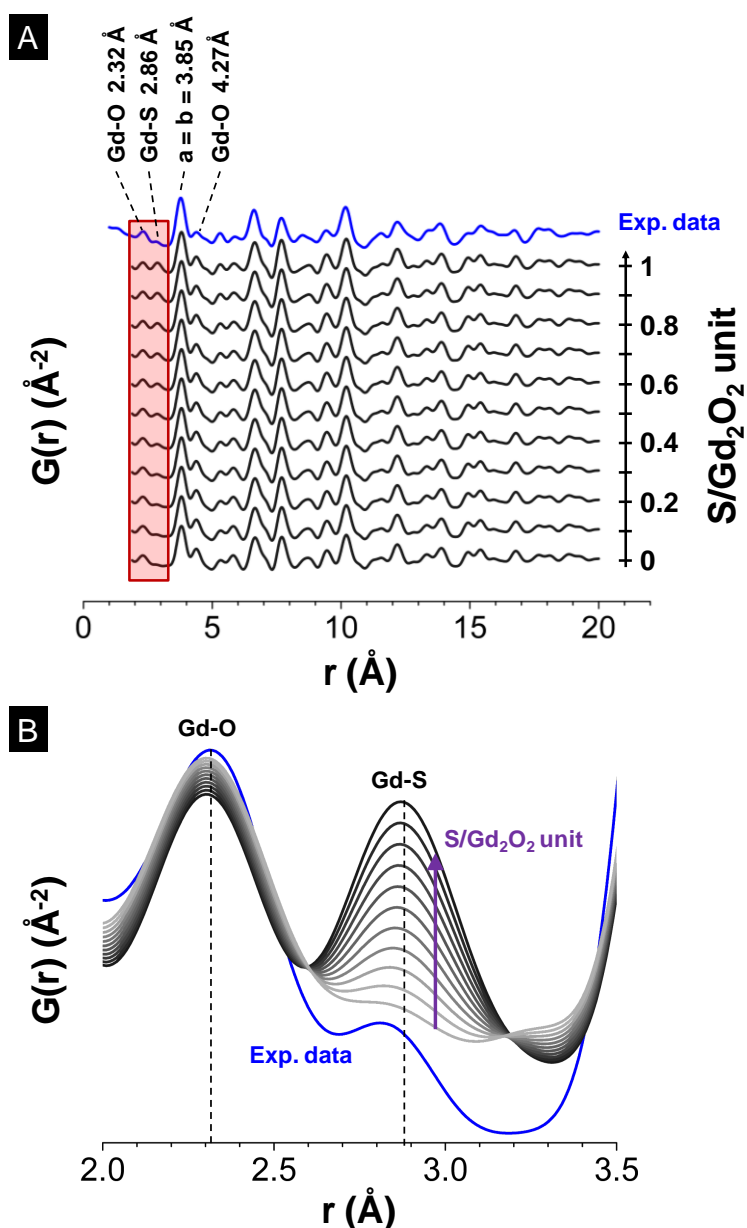


Figure 44: (A) PDF analysis of synthesized $\text{Gd}_2\text{O}_2\text{S}$ nanoplates (in blue) and comparison with calculated PDF from bulk reference data with different sulfur amounts (black). (B) Range 2.0-3.5 \AA , which contains the (Gd-O) and (Gd-S) bonds (gray scale for the calculated PDF).

To get a structural analysis of the whole sample, and not only what we thought to be the “core” crystal $\text{Gd}_2\text{O}_2\text{S}$, we used the pair distribution function (PDF) analysis of the X-ray diffraction pattern. The PDF measurements and analysis were made with the help of Capucine Sassoie, Mohamed Selmane and Pierre Lecante. We compared the experimental PDF of the $\text{Gd}_2\text{O}_2\text{S}$ nanoparticles with the PDF calculated from referenced crystalline structural data.³

The pair distribution function $G(r)$ is directly correlated to the probability to find a distance whose length is r between 2 atoms. Thus, this analysis does not require an extended crystal and is also suitable for amorphous and defective compounds.

Two conclusions arise. First, the good agreement between the experimental and calculated PDFs confirmed that our sample is mainly composed by $\text{Gd}_2\text{O}_2\text{S}$ crystals. Second, the peak intensity ratio (Gd-O)/(Gd-S) (Figure 44B) showed that our sample is non-stoichiometric with a composition close to $\text{Gd}_2\text{O}_2\text{S}_{0.5}$.

PDF gives a direct proof that there is a lack of (Gd-S) bonds in the crystal, while a traditional composition analysis such as EDS only indicates a ratio between two elements. Moreover, we were able with PDF to probe the (Gd-O) bonds in the crystal and thus get a comparison with the (Gd-S) bonds. It confirms that we approximately have the correct oxygen content (based on the $\text{Gd}_2\text{O}_2\text{S}$ reference), which cannot be estimated with EDS.

Once again, the PDF estimated sulfur amount is still lower than the expected value even if we consider terminal $[\text{Gd}_2\text{O}_2]^{2+}$ layers. We could imagine that there are also sulfur vacancies in the internal sulfur layers of the crystal. Nevertheless, the distances obtained with the PDF analysis are so close to the reference data that such vacancies are unlikely, as they would create a noticeable distortion of the lattice. That is why we propose to keep the hypothesis of an imperfect shell surrounding a perfect crystal.

The dimensions of the $\text{Ln}_2\text{O}_2\text{S}$ nanoparticles are crucial for the sulfur deficiency. We saw that Ding's $\text{La}_2\text{O}_2\text{S}$ nanoparticles are bigger and that their composition was predictable with a simple geometric model. It is reasonable to believe that gadolinium oxysulfide is a particularly interesting case, as it results in very small and thin nanoplates and its stoichiometry is consequently highly sensitive to the sulfur repartition at the surface.

Another reason that could explain why Ding's $\text{La}_2\text{O}_2\text{S}$ nanoplates are closer to the composition they measured is also the use of 1 equiv. of sulfur vs. gadolinium, twice the stoichiometric amount. It can compensate the loss of small quantities of sulfur under the forms of unreacted gaseous H_2S or polyanions in solutions.

So far, we were able to give an advanced view of the sulfur-defective structure of the $\text{Ln}_2\text{O}_2\text{S}$ nanoplates. Now, it is time to investigate the species that are able to compensate the positively charged inorganic $\text{Gd}_2\text{O}_2\text{S}_x$ inorganic nanocrystals. In the following sections, we will use the notations $\text{Gd}_2\text{O}_2\text{S}$ as well as $\text{Gd}_2\text{O}_2\text{S}_x$, depending on the context.

III.1.2. Charge equilibrium: the role of surface ligands

III.1.2.1. Ligands nature and amount

We are now sure that the inorganic crystal which composes the core of the nanoparticle is not neutral. The sulfur-defective structure makes it positively charged, as sulfur is at the $-II$ oxidation state in the structure.

In the reacting mixture, oleate ligands can be negatively charged and represent the ideal candidates for charge compensation. Oleates are already present in the starting medium and are good ligands for Ln^{III} species.⁴ Nevertheless, we can also imagine that balance can be brought with oleylamine chains by bonding to gadolinium cations *via* their lone pair or the formation of amides. Fourier transform infrared spectroscopy (FTIR) was conducted on Gd_2O_2S nanoparticles (Figure 45).

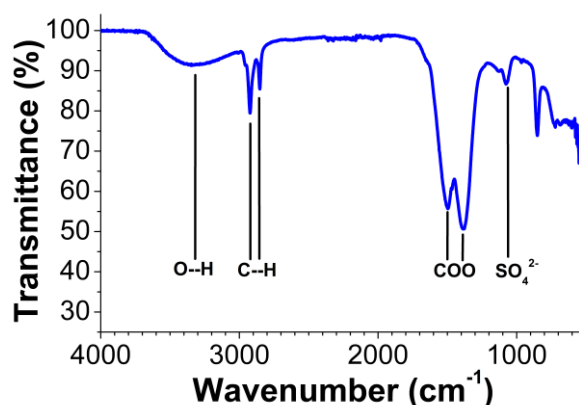


Figure 45: FTIR spectrum of Gd_2O_2S nanoplates collected in ATR mode.

We can confirm the presence of oxidized sulfur *via* the $S=O$ band at 1070 cm^{-1} .⁵ Organic chains are observed through $C-H$ stretching bands at around 2900 cm^{-1} and come from the ligands.⁴ Also, two important bands characteristic of the COO group (asymmetric stretching at 1497 cm^{-1} and symmetric stretching at 1385 cm^{-1}) are present, and are attributed to oleate ligands at the surface of the nanocrystals. There is likely a negligible amount of free oleic acid remaining in the final product (no significant signal around 1700 cm^{-1}): the species bound to the surface are oleates. Thus, the broad signal centered around 3300 cm^{-1} can be attributed to the $O-H$ stretching band of water. The water likely comes from the washing process where non-analytical grade solvents are used in ambient atmosphere. The $N-H$ stretching bands of possible oleylamine are at around 3300 cm^{-1} and thus would not be discerned from the $O-H$ broad signal of water. Nevertheless, the FTIR spectrum confirmed a significant amount of oleate ligands.

To get a more accurate qualitative and quantitative description of the surface ligands, we performed thermogravimetric analysis couples with mass spectrometry (TGA-MS). We expected to measure the amount of ligands stabilizing the nanoparticles and their nature. Indeed, oleic acid and oleylamine will provide different fragments in mass spectrometry.

The measurements were performed by Dr. Djamilia HOURLIER at the *Institute of Electronics, Microelectronics and Nanotechnology* (IEMN) in Lille.

Samples of $\text{Gd}_2\text{O}_2\text{S}$ nanoplates were tested in different conditions: inert atmosphere (He), air-like mixture (O_2/He with 20/80 v/v) and reductive atmosphere (H_2/He with 5/95 v/v). We will focus on the thermal behavior under inert atmosphere, and the oxidizing atmosphere will be treated afterwards in conclusion. Helium was preferred to N_2 to avoid the confusion with the CO fraction ($m/z = 28$). The results of the TGA in inert atmosphere are presented in Figure 46.

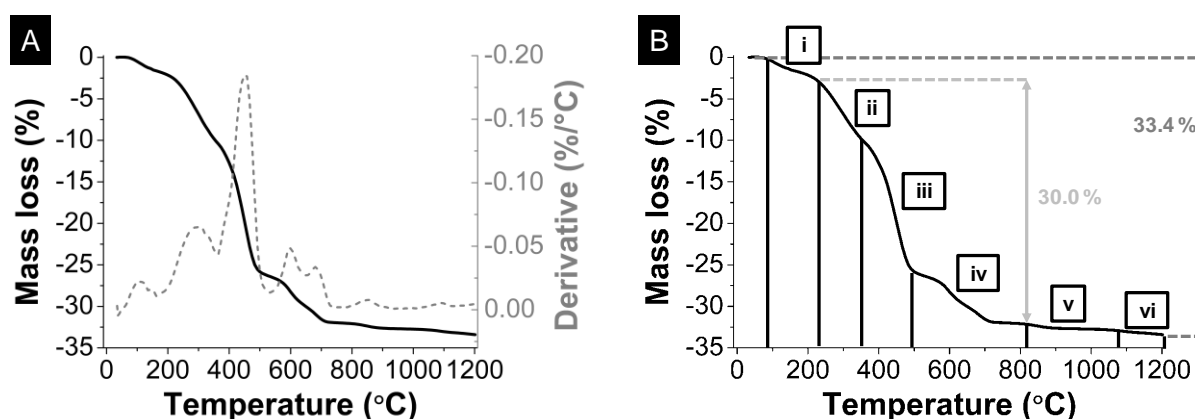


Figure 46: (A) Thermogravimetric analysis of $\text{Gd}_2\text{O}_2\text{S}$ nanoplates in inert atmosphere. The curve is divided in six phases corresponding to six distinguishable mass losses (B).

The total mass loss between 25 °C and 1200 °C is 33.4 %, corresponding to one third of the sample that has been removed as volatile substances during the heating process. The thermogramm can be divided in at least six distinct phases that are presented in Figure 46B. From the mass spectrometry results, we were able to identify the main volatile products in each phase (Figure 47).

Remarkably, the processes are well separated. The major volatile products detected are:

- (i) H_2O ($m/z = 18, 17, 16$)
- (ii) CO_2 ($m/z = 44, 28, 16, 12$)
- (iii) Carbonated fractions (ligands chains) with CH_4 ($m/z = 16, 15, 14, 12$) + CO + H_2O
- (iv) 2 substeps: CO_2 + CO ($m/z = 28, 16, 12$) first, then only CO

- (v) $\text{H}_2\text{O} + \text{CO}$
 (vi) H_2S ($m/z = 34, 33$)

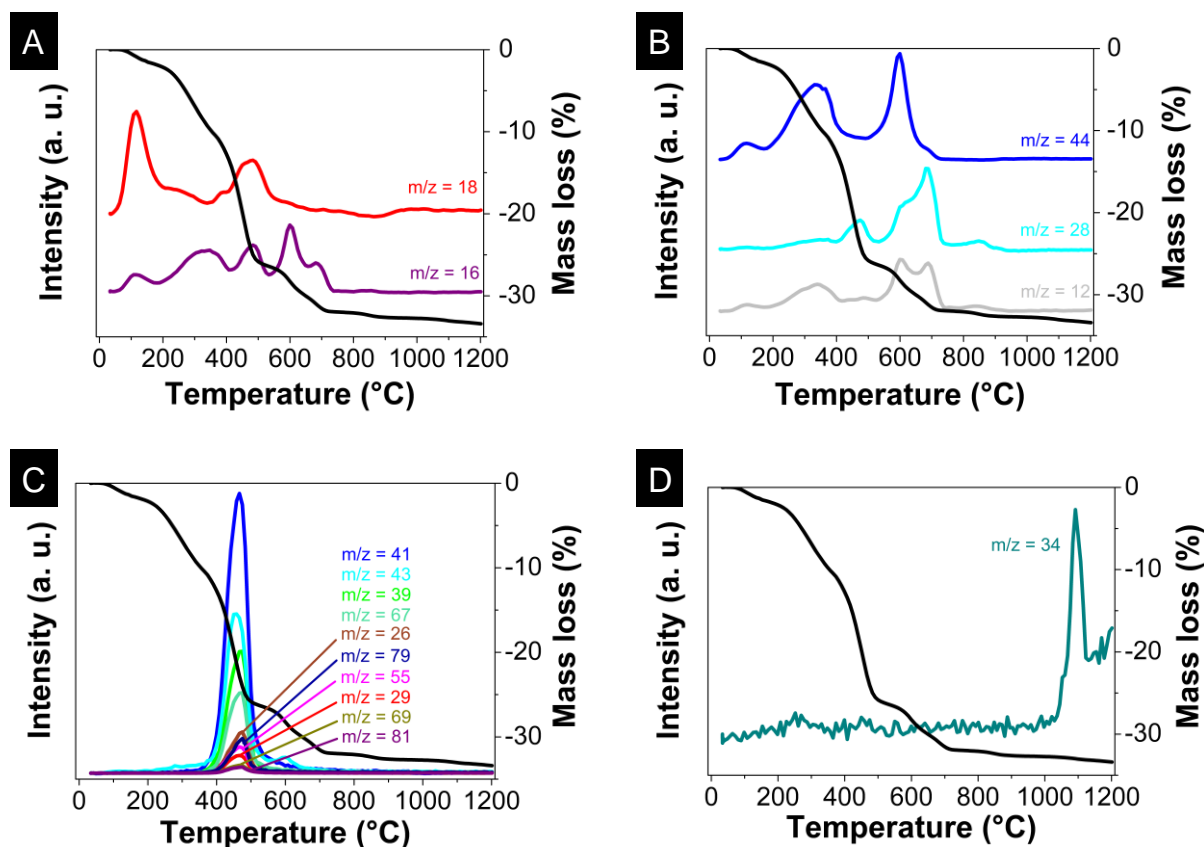


Figure 47: Thermal evolution of the fragments obtained from mass spectrometry. (A) H_2O ($m/z = 18, m/z = 16$); (B) CO ($m/z = 28, m/z = 12$) and CO_2 ($m/z = 44, m/z = 12$); (C) carbonated species from ligands chains; (D) H_2S ($m/z = 34$).

The loss of water around 100 °C was expected as mentioned before considering that our organic solvents did contain a small amount of water and that the samples were isolated and washed in ambient air (Figure 46B step i). In step (ii), the decarboxylation of oleate groups is likely to occur. In step (iii), decomposition of the major part of organic-based ligands occurs, resulting in the detection of numerous fractions related to long carbon chains. Evidence for this is given by the release of oleate at $m/z = 41, 55, 43, 69, 81$ shown in Figure 48, resulting from the scission of the oleate ligands followed by hydrogen radical recombination. The $m/z = 30$ fragment of the oleylamine mass spectrum⁶ is absent: consequently, there is no oleylamine on our nanoparticles, or at least a negligible amount compared to oleates. As with many organic compounds when they are heated, the ligands decomposition here leads not only to volatile molecules, but also left a carbonized char residue on the condensed phase called free carbon. The formation of free carbon results from cracking of the organic chains and recombination of radicals. This degradation step causes the most important mass loss. CO

and H₂O are also formed in step (iii). It can correspond to the decarbonylation of formic acid formed *in situ* during the ligand decomposition.

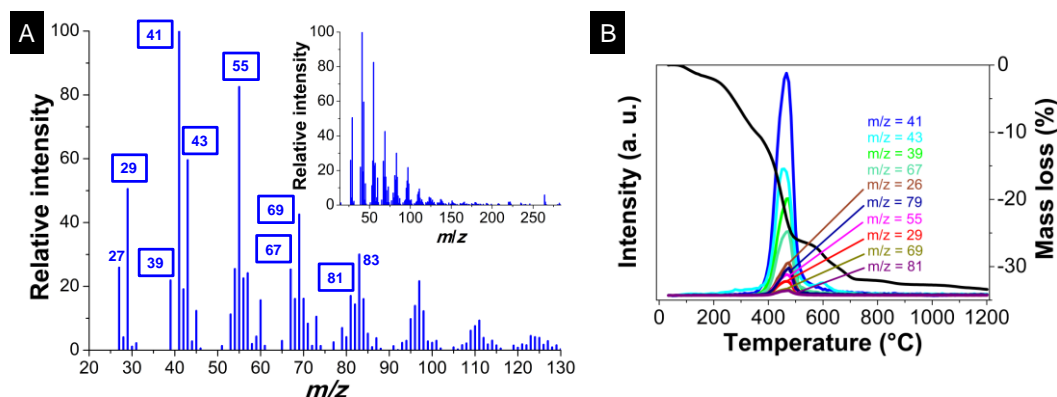


Figure 48: (A) Oleic acid mass spectrum with $m/z = 20-130$ from the NIST database.⁷ The inset displays the total spectrum. (B) Thermogram of Gd₂O₂S nanoplates and detected fractions of carbonated species of ligands (framed on A).

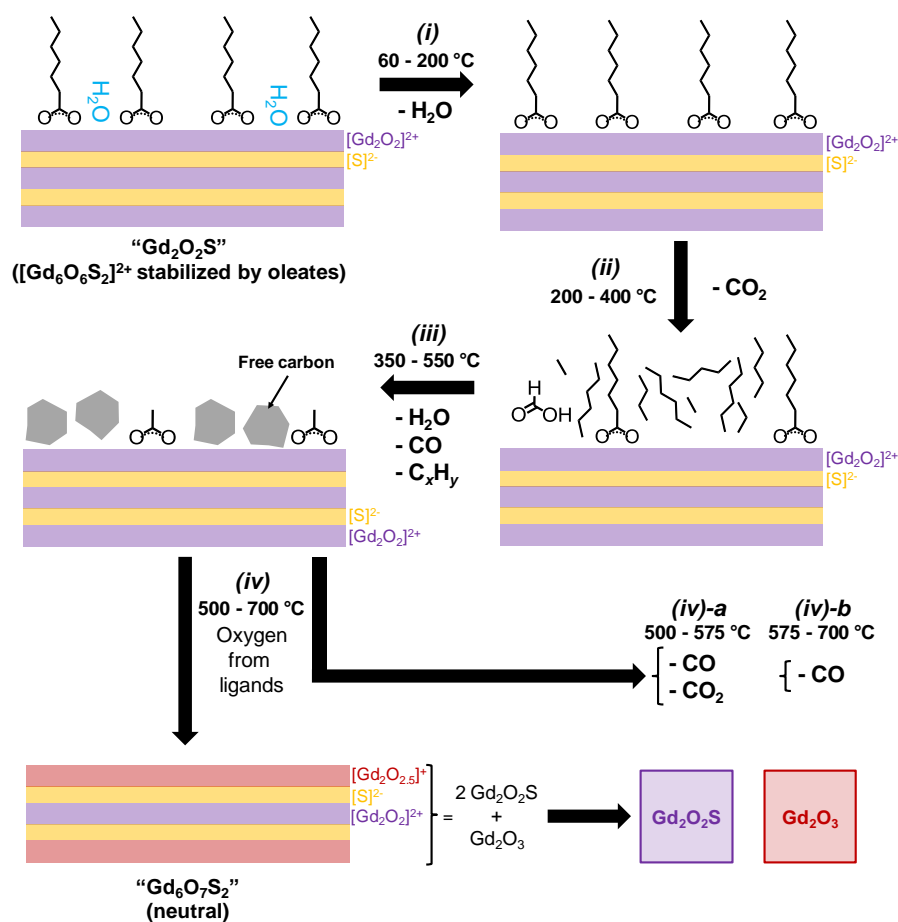


Figure 49: Schematic representation of the supposed mechanisms involved during the annealing of Gd₂O₂S nanoplates (steps i to iv).

We indicated that the step (iv) can be divided in two steps regarding the evolution of the fragments corresponding to CO₂ and CO (Figure 47). Nevertheless, we propose that they were

both the products of the reaction between the free carbon (formed by the decomposition of the ligands carbon chains) and excess oxygen that could come from the thermal decomposition of the $\text{Gd}_2\text{O}_2\text{S}$ nanocrystal itself (see below).

There are two crucial points here. First, during steps (ii) and (iii), ligands are partially destroyed: the charge balance can still be ensured by carboxylates groups but sintering becomes easier (Figure 49). Second, as the crystals grow and sinter, the neat lack of sulfur of the powder makes the formation of pure $\text{Gd}_2\text{O}_2\text{S}$ impossible. Also, the formation of large crystals of $\text{Gd}_2\text{O}_2\text{S}_{\sim 0.5}$ is prohibited as charge balance would not be respected in this case (no more ligands to compensate the charge). Oxygen insertion is proposed to neutralize the particles. Thus, at high temperatures ($> 900\text{ }^\circ\text{C}$), the coexistence of growing crystals of $\text{Gd}_2\text{O}_2\text{S}$ with allotropes of Gd_2O_3 was observed on the XRD patterns of the annealed powders (Figure 50).

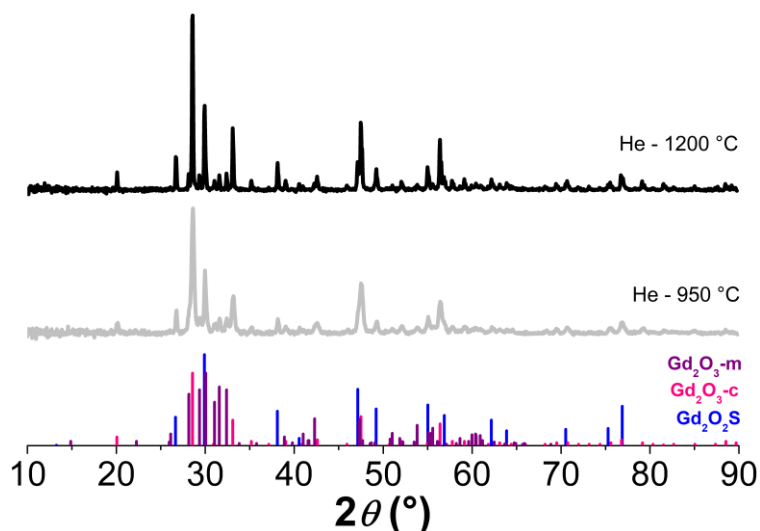


Figure 50: Powder XRD patterns of annealed products obtained from $\text{Gd}_2\text{O}_2\text{S}$ nanoplates. The nanoplates were heated under helium in the ATG crucible up to $950\text{ }^\circ\text{C}$ (gray line) or $1200\text{ }^\circ\text{C}$ (black line). XRD pattern references are JCPDS files 26-1422 ($\text{Gd}_2\text{O}_2\text{S}$, blue), 12-0797 (Gd_2O_3 -cubic, pink) and 42-1465 (Gd_2O_3 -monoclinic, purple).

How can we explain the CO and CO_2 release in step (iv)? Oxygen can be provided by the sulfonate and sulfate groups already present at ambient temperature, as the fractions $m/z = 80$ (SO_3^{2-}) and $m/z = 96$ (SO_4^{2-}) are very weakly represented (data not shown).

Moreover, oleates coordinated on the surface form $\text{C}-\text{O}-\text{Gd}$ bonds. Upon heating, a number of the $\text{C}-\text{O}$ bonds break, leaving excess oxygen on the surface (Figure 49). $[\text{Gd}_2\text{O}_2]^{2+}$ terminal layers become $[\text{Gd}_2\text{O}_{2.5}]^+$ (red layers in Figure 49) while the ligands decompose, and the resulting nanoplate formula progressively evolve from $[\text{Gd}_6\text{O}_6\text{S}_2]^{2+}$ ($[\text{Gd}_2\text{O}_2\text{S}_{0.67}]^{(2/3)+}$) to

neutral $\text{Gd}_6\text{O}_7\text{S}_2$. Then, the phase separation and growth leads to large crystals of $\text{Gd}_2\text{O}_2\text{S}$ and Gd_2O_3 . We think that there is an excess of oxygen coming from the decomposing carboxylate ligands which feed the surface layers. This excess oxygen can also be at the origin of the oxygen release mentioned earlier that leads to CO and CO_2 . Moreover, we propose that CO_2 is formed first by reaction of oxygen with the free carbon, and that CO_2 can also react with the free carbon to form CO following the Boudouard reaction: $\text{CO}_2 + \text{C} = 2 \text{CO}$. The equilibrium favors the CO formation at high temperatures, which could explain that CO becomes the major product in (iv)-b (Figure 47B).

The step (v) is unclear for us, as it only presents a low mass loss induced by CO. On the other hand, step (vi) is easier to interpret: it corresponds to a loss of a small quantity of H_2S . It may come from a limited degradation of the oxysulfide phase: the mass stabilized after treatment at 1200 °C and the fractions of the different products ($\text{Gd}_2\text{O}_2\text{S}$, $\text{Gd}_2\text{O}_3\text{-c}$ and $\text{Gd}_2\text{O}_3\text{-m}$) in the XRD pattern did not change significantly between the end of (v) and the end of (vi), as seen in Figure 50.

Interestingly, we noted in this section that only oleate ligands surround our $\text{Ln}_2\text{O}_2\text{S}$ nanoparticles. Their amount was estimated to be around 30 wt% of the powder of $\text{Gd}_2\text{O}_2\text{S}$ nanoplates. Furthermore, the $\text{Gd}_2\text{O}_2\text{S}$ structure survives up to 1200 °C even if the sulfur-defective structure necessarily causes the growth of a significant amount of Gd_2O_3 . We were also able to propose a mechanism that includes the different steps of the thermal evolution of the $\text{Gd}_2\text{O}_2\text{S}$ nanoplates under inert atmosphere.

III.1.2.2. Coordination mode of oleates around Gd^{III} cations

The previous section shows that oleates are the most significant ligands (if not the only ones) around the nanoparticles. In infrared spectroscopy, the frequency difference between the asymmetric and symmetric stretching bands of the COO group is indicative of the bonding type of the carboxylate ligand. In particular, Deacon and Phillips indexed more than eighty acetate or trifluoroacetate compounds whose crystalline structures and infrared spectra were available, according to the acetate coordination type: unidentate ligand, chelating ligand, bridging bidentate ligand and monoatomic bridging ligand (Figure 51).⁸

In our case (Figure 45), the difference between the two modes is $\Delta\nu = 112 \text{ cm}^{-1}$ ($\nu_{\text{asym}} = 1497 \text{ cm}^{-1}$ and $\nu_{\text{sym}} = 1385 \text{ cm}^{-1}$). In comparison, the values measured on sodium oleate are $\Delta\nu = 100, 118$ and 139 cm^{-1} (separation of the symmetric band in three contributions, data not shown). The low value of $\Delta\nu$ ($< 150 \text{ cm}^{-1}$) close to the value of the

corresponding sodium carboxylate is typical of chelating or bridging carboxylate ligands, and eliminates the monodentate ligand configuration (Figure 51I). Moreover, in comparison with the numerous structures presented by Deacon and Phillips, this value is one of the lowest, and suggests that chelation is favored in our case (Figure 51II).

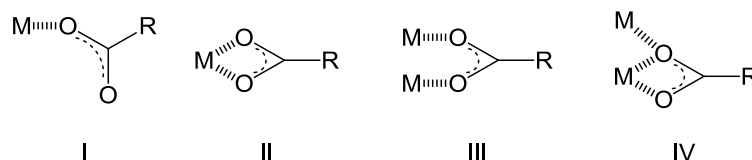


Figure 51: Four coordination modes between a carboxylate ligand and a metal as references by Deacon and Phillips: monodentate (I), chelating (II), bridging bidentate (III) and monoatomic bridging (IV).⁸ Geometric derivatives mixing different bonding types also exist and are not presented.

Interestingly, thanks to the thermogravimetric analysis, we have an estimation of the ligands amount: around 30 wt% of a $\text{Gd}_2\text{O}_2\text{S}$ nanoparticles sample. It is thus possible to estimate the ratio between the quantity of oxygen coming from the oleate ligands and the exposed gadolinium of our nanoplates, considering the nanoplate geometry.

We based this estimation on the average amount of $\text{Gd}_2\text{O}_2\text{S}$ nanoplates obtained per synthesis: 100 mg, fractioned between 67 mg of $\text{Gd}_2\text{O}_2\text{S}_x$ nanocrystal, 30 mg of oleate ligands and 3 mg of byproducts (mainly water). With these quantities and the fact that only 40 % of the gadolinium of the nanoplates was exposed to the surface (both $\{100\}$ and $\{001\}$ facets), we calculated that each gadolinium atom monopolized 1.43 oxygen atoms from the oleate ligands (Figure 52). For such a value, a mix between chelation (two oxygen atoms per metallic cation) and bridging (1 O per M) can be envisaged. This result is in agreement with the structures of lanthanide carboxylates (from samarium to lutetium⁹ and yttrium¹⁰) for which the IR signals evidenced a ratio 2 chelating ligands for 1 bridging ligand (total: 1.6 O/Ln).

However, with the ligand quantity, the charge compensation is not reached. If we suppose that we got $\text{Gd}_2\text{O}_2\text{S}_{0.5}$ nanoparticles (+1 total charge), they should be surrounded by 1 equiv. of oleate ligands (-1 charge per molecule) to obtain the charge balance. Here, 0.72 oleate ligand per $\text{Gd}_2\text{O}_2\text{S}$ approximately surrounds the nanocrystals, which is not enough. Nevertheless, one should remember that the oleate ligands are mainly bonded to gadolinium atoms by chelation. It means that there is not much remaining space for a ligand to bond a metal. Actually, the number of oleate ions represents a spatial occupation of 4.5 ligands/nm^2 , which is already a high value for such ligands (0.2 nm^2 for a single $-\text{COO}^-$ group).^{11,12} Accordingly, Anderson *et*

al. reminded that the steric hindrance between the alkyl chains of the oleate will limit the coverage to the density of crystalline alkyl chains (4.9 chains/nm²).^{13,14}

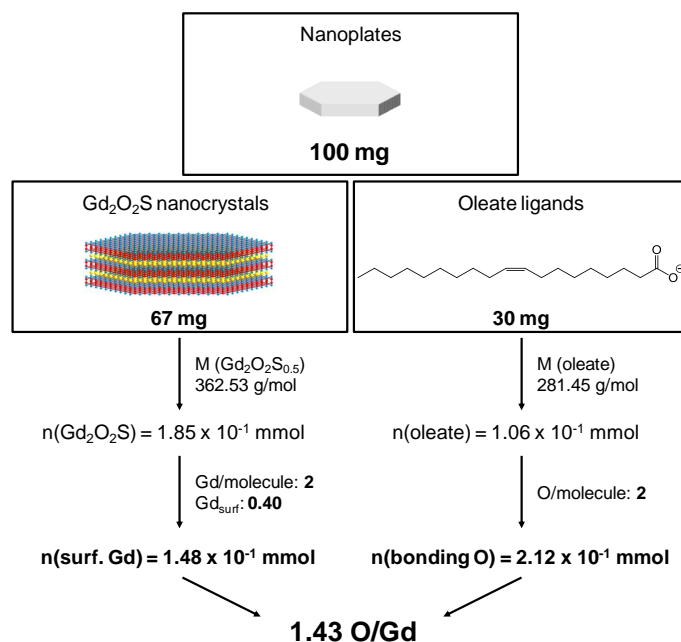


Figure 52: Estimation of the number of oleate oxygen atoms bonded per surface gadolinium of the Gd₂O₂S nanoplates.

We can conclude that the coordination mode is a mix of chelation and bridging modes. The hypothesis of chelation is likely if we admit that Gd(oleate)_x complexes form as intermediates (Chapter II) with oleate in chelating mode. One should also remember that the shell of the particles also contains sulfonates and sulfates that may help for charge balance.

III.1.3. Conclusion and perspectives on ligands removal

Several crucial features of the final products were determined in this first section. The non-stoichiometric character of the nanoplates was proven by EDS and PDF analysis, where the Gd-S bond was under-represented in comparison with a theoretical Gd₂O₂S crystal. The thermal behavior of the nanoparticles was investigated and led to the conclusion that only oleate ligands were coordinating the surface gadolinium atoms (around 1.4 oleates/Gd_{surf}). Also, carboxylate ligands turned out to be bonded to the cations by chelating and bridging bidentate modes.

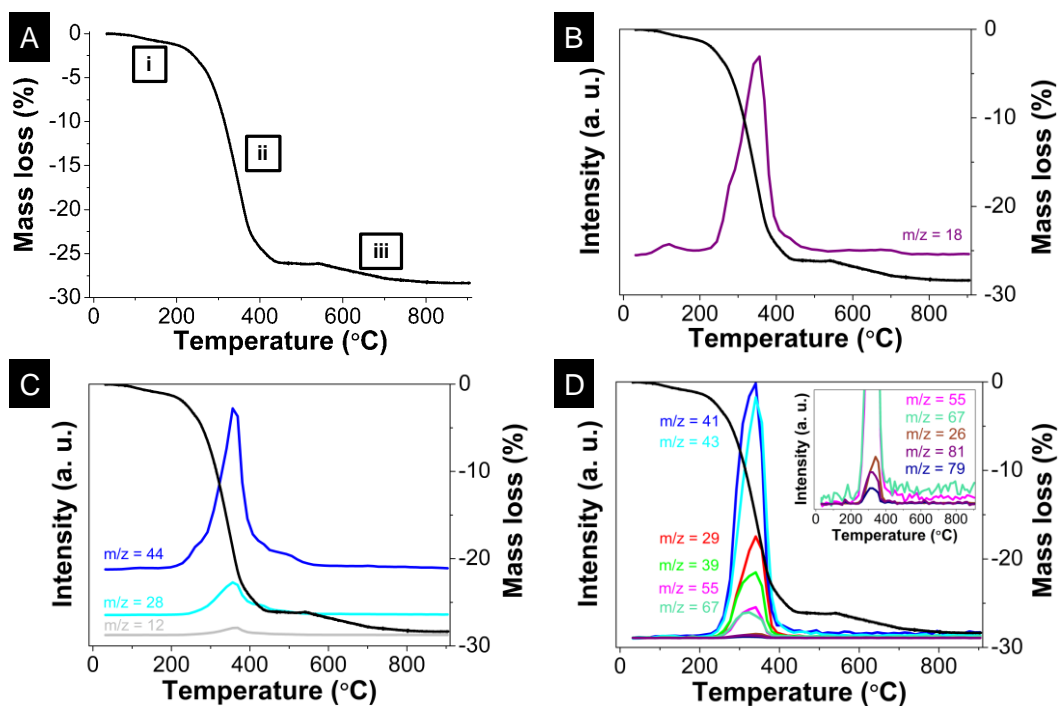


Figure 53: Thermal behavior of $\text{Gd}_2\text{O}_2\text{S}$ nanoplates under oxidizing atmosphere. Evolution of the mass (A) and fragments from mass spectrometry: (B) H_2O ($m/z = 18$); (C) CO ($m/z = 28$, $m/z = 12$) and CO_2 ($m/z = 44$, $m/z = 12$); (D) carbonated species from ligands chains.

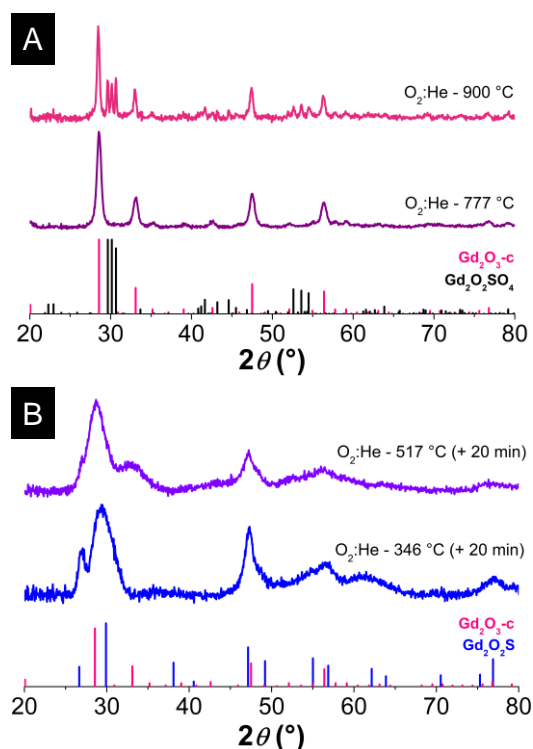


Figure 54: Powder XRD patterns of annealed $\text{Gd}_2\text{O}_2\text{S}$ nanoplates under $\text{O}_2:\text{He}$ (20/80 v/v). (A) Powder obtained at 900 $^{\circ}\text{C}$. (B) Powders obtained at 517 $^{\circ}\text{C}$ (violet) and 346 $^{\circ}\text{C}$ (blue), both being let at their final temperature for 20 minutes. XRD pattern references are JCPDS files 26-1422 ($\text{Gd}_2\text{O}_2\text{S}$, blue), 12-0797 (Gd_2O_3 -cubic, pink) and 77-9842 ($\text{Gd}_2\text{O}_2\text{SO}_4$, black).

The thermal behavior of $\text{Gd}_2\text{O}_2\text{S}$ nanoplates was investigated under other atmospheres and at intermediate reaction temperatures, in order to identify the nature of the solid formed at the most relevant steps. In particular, under O_2/He (20/80 v/v), the final mass loss is lower than in inert atmosphere (Figure 53). This is due to the formation of gadolinium oxysulfate $\text{Gd}_2\text{O}_2\text{SO}_4$. These compounds are known to form in oxidizing medium starting from oxysulfides.¹⁵ Here, we can suppose that the oxysulfide phase (that completely disappears) turns amorphous in a first step, letting only gadolinium oxide to crystallize (Gd_2O_3 -cubic). Then this amorphous product recrystallizes under the form of oxysulfate (Figure 54A).

It is worth noting that the thermal decomposition in oxygen observed in the TGA curve (Figure 53) occurs in two different steps. The first mass loss located between 250 °C and 400 °C is the most important (25 %) and is followed by a second mass loss of about 4 % above 500 °C. We thus tried to apply different thermal treatments: a first at 350 °C (end of phase (ii) in Figure 53A) and 517 °C (after the end of phase (ii)). Interestingly, when heated around 350 °C for 20 minutes, the ligands are majorly destructed but the product still corresponds to $\text{Gd}_2\text{O}_2\text{S}$ nanocrystals (Figure 54B)! In comparison, the same thermal treatment at 517 °C majorly led to nanoscaled gadolinium oxide.

In this section, we demonstrate that the inner crystal of $\text{Gd}_2\text{O}_2\text{S}$ is stable up to around 350 °C under oxidizing atmosphere. The nanoscale is also conserved at this temperature. If the decomposition of the ligands is the critical step and is the starting point of nanoparticles sintering, we can expect that $\text{Gd}_2\text{O}_2\text{S}$ nanoplates are stable up to around 450 – 500 °C under inert atmosphere. A thermal treatment at the adapted temperature (under oxidizing atmosphere around 350 °C, likely higher under inert atmosphere) could represent a smooth way to remove the ligands in case of the long carbonated species are undesirable or for replacement with water-soluble ligands.

At this stage, only one reactant of the synthesis was not properly investigated: sodium. Yet, various syntheses reported in the literature with elemental sulfur were shown to work more efficiently in the presence of an alkali (Na, K or Li). The next section is thus dedicated to the analysis of sodium in the final products and its hypothetical role during the synthesis.

III.2. Role and localization of the alkali ion

This section may be summarized with the following question: where is the sodium?

III.2.1. State of the art: an ongoing controversy

In the syntheses conducted by Ding *et al.* of $\text{Ln}_2\text{O}_2\text{S}$ nanoparticles in 2011, a source of sodium was systematically added in the initial reaction medium.¹ They noticed that the insertion of the alkali was helpful for the crystallization of the nanoplates. The explanation advanced by the authors is that Na^{I} introduction in Ln^{III} host lattices create oxygen vacancies more easily than sulfur vacancies. Moreover, $\text{Ln}_2\text{O}_2\text{S}$ formation competes with Ln_2O_3 rather than Ln_2S_3 , because of the strong affinity of lanthanides with oxygen (very few sesquisulfide syntheses were reported below 400 °C). Therefore, the oxygen vacancies thermodynamically enhanced the stability domain of $\text{Ln}_2\text{O}_2\text{S}$ and make it easier to obtain. Ding *et al.* named their product “Na-doped $\text{Ln}_2\text{O}_2\text{S}$ nanoplates”, and described the structure as a defective $\text{Ln}_2\text{O}_2\text{S}$, containing significant of sodium ($\approx 25\%$ vs. La). Because of the measured composition and their hypotheses for the $\text{Ln}_2\text{O}_2\text{S}$ formation, they estimated that a non negligible amount of sodium remained in the nanoparticles with only little influence on the $\text{Ln}_2\text{O}_2\text{S}$ structure (no visible shift for the XRD pattern). Note that Ding *et al.* managed to synthesize very small $\text{Y}_2\text{O}_2\text{S}$ nanoparticles ($\varnothing < 5\text{ nm}$) using $\text{Li}(\text{acac})$.¹

In 2013, in the same group, Zhang *et al.* added some complementary results.¹⁶ The formation of $\text{La}_2\text{O}_2\text{S}$ was conducted using lithium, sodium and potassium doping. Remarkably, the three alkaline salts were effective for the crystallization, with unequal results. Whereas Ding *et al.* sodium doping gave well crystallized nanoplates with a width of around 23 nm, lithium doping led to 9 nm wide badly crystallized thin nanoplates. Potassium doping, on the contrary, enabled the formation of larger well-crystallized nanoparticles (45 nm wide). In addition, potassium was effective for the crystallization of europium, gadolinium and ytterbium oxysulfide nanoparticles. Again, thanks to *ab initio* calculations, the authors explain that alkali ions in the structure tend to form oxygen vacancies more easily than sulfur vacancies and therefore facilitate the formation of $\text{Ln}_2\text{O}_2\text{S}$ nanoparticles. They thus explain that potassium doping is less and less effective in the formation of heavier lanthanide oxysulfide because of the lanthanide contraction that makes the lanthanide substitution by potassium harder and harder (Figure 55). Finally, they also noticed that the sulfur amount in the nanoparticles doped with lithium and potassium was lower than with the sodium doping.

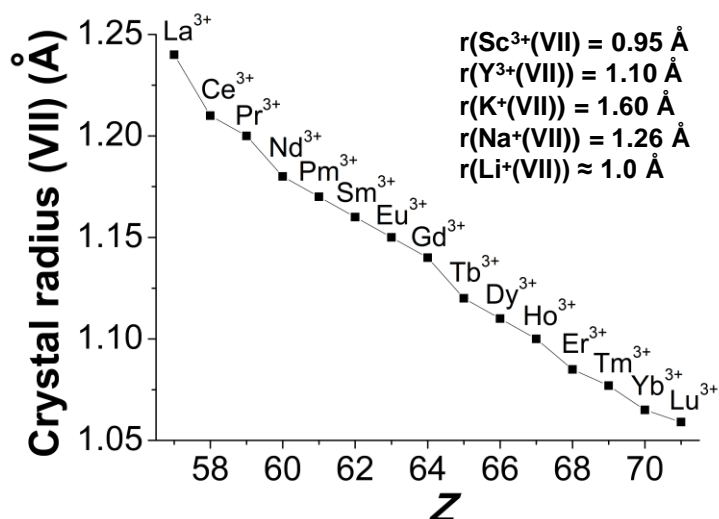


Figure 55: Ionic radii of the lanthanide trivalent cations with a coordination number of seven. Scandium, yttrium, sodium and lithium ionic radii values are also indicated.

In this article, the argumentation is contestable. First, the authors keep considering that the different alkali cations substitute the trivalent lanthanide ions during and after the reaction in the oxysulfide structure with no expected impact on the lattice parameters (6 - 7 % of alkali at least in the final product, up to 25 % in the case of sodium; lithium amount could not be measured with EDS). Yet, with a coordination number of seven (if they were substituting the lanthanide atoms in $\text{Ln}_2\text{O}_2\text{S}$ as proposed by Ding and Zhang), the ionic radii of potassium $r(\text{K}^{\text{I}}(\text{VII})) = 1.60 \text{ \AA}$ and lithium $r(\text{Li}^{\text{I}}(\text{VII})) \approx 1 \text{ \AA}$ make the substitution reactions highly unfavorable ($r(\text{La}(\text{VII})) = 1.24 \text{ \AA}$) and must result in a significant contraction or dilatation of the final lattice that is not discussed by the authors (observed in the case of Ce^{III} - Gd^{III} substitution, Chapter II). It is all the more surprising as the substitution is, according to the authors, the driving force for the crystallization. One would then expect that potassium-doped oxysulfide nanoparticles would be less crystallized than sodium-doped ones ($r(\text{Na}(\text{VII})) = 1.26 \text{ \AA}$), as observed for lithium. Yet, the nanoparticles are as well crystallized.

Second, the explanation for the decrease of sulfur content in the final products is not fully convincing. In the case of lithium, the authors reminded that the nanoplates are smaller, and that the sulfur-free surface contribution becomes more important. We agree with this hypothesis. On the other hand, potassium-doped nanoparticles are bigger. The authors explained that potassium has a better affinity with oxygen than sodium because of its stronger Lewis acidity, and thus create more sulfur vacancies which led to a lower sulfur amount in the final product. This argument is invalid and lead to other contradictions. Potassium cations are monovalent and bigger than sodium cations: there is no reason to believe that K^{I} Lewis acidity

is somehow stronger than Na^+ ; the opposite would even be more probable ($\chi_{\text{Na}} = 0.93$ and $\chi_{\text{K}} = 0.82$ with Pauling's scale). Even if a similar substitution was possible for the three alkali cations, the alkali with the strongest affinity with oxygen (K^+ according to Zhang) should be the worst for the oxysulfide crystallization, driven by formation of oxygen vacancies. But the nanoparticles obtained with potassium were well-crystallized.

However, due to the lanthanide contraction, the increasing affinity for oxygen along the lanthanide series is likely (for the cation, the smaller the harder according to HSAB theory). It could explain why the authors did not get lutetium oxysulfide but only lutetium oxide nanoparticles. Although they obtained ytterbium oxysulfide nanoparticles and proposed this interpretation, successful tests on dysprosium, holmium or erbium would have been even more convincing.

In conclusion, the role of the alkali ion in the formation of $\text{Ln}_2\text{O}_2\text{S}$ nanoplates is particularly unclear. There is an effect of the alkaline complex on the crystallization of the nanoplates and the nature of the alkali influences the final morphology. However, the precise role of the cation during the synthesis can still be debated. Also, the current hypothesis that the alkali ions remain in the nanoplates is unlikely: this should at least be observed when the difference between the radii of the doping ion and the lanthanide is high enough (0.1 Å for instance).

III.2.2. Localization of the alkali in the final product

In agreement to Ding *et al.*, we always observed that sodium remained on our final $\text{Gd}_{2(1-y)}\text{Ce}_{2y}\text{O}_2\text{S}$ nanoparticles. The EDS results are presented in Figure 56. The sodium amount never decreases lower than 0.05 equiv. vs. $\text{Gd} + \text{Ce}$. However, no other significant trend could be extracted from the several experiments conducted with Anh-Minh Nguyen and Thi Kim-Chi Lê. In fact, the sodium content is reproducibly non-consistent through samples and through experimentalists, which can be taken as good news for each of the latter. The most sensitive part of our nanoparticles is the surface, and we hypothesized that sodium was mainly located at the surface of the nanoparticles. This way, its amount is mainly dependent on the isolation and washing steps, hence on the quality of the colloidal dispersion during these steps, and may significantly vary.

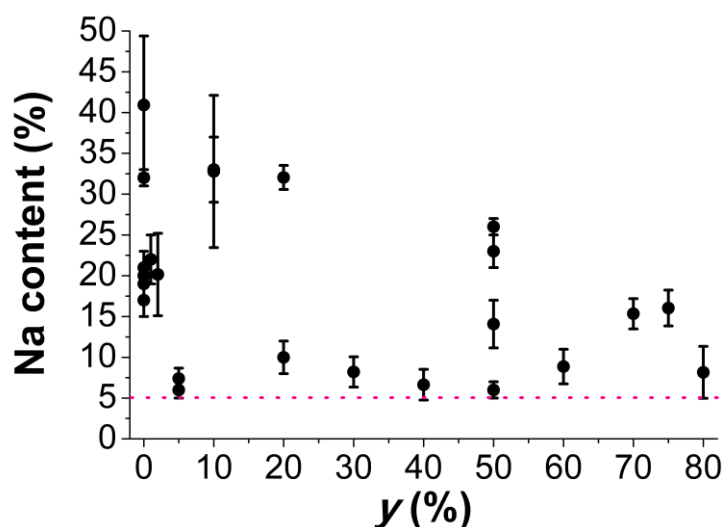


Figure 56: Sodium content for $\text{Gd}_{2(1-y)}\text{Ce}_{2y}\text{O}_2\text{S}$ nanoparticles isolated and washed in similar conditions. The sodium content is: $\text{Na}(\%) = n_{\text{Na}} / (n_{\text{Gd}} + n_{\text{Ce}})$.

How to prove that sodium remains only on the surface? To address this question, two solutions can be envisaged. The first one is to directly characterize the surface of our objects. XPS could have been suitable, but in our case, the particles are so thin that XPS almost probes the entire particle (sodium is present on the spectra). Mapping sodium using EFTEM would also require great efforts to isolate single nanoparticles as they tend to aggregate and keep clean images with high magnifications as the ligands burn under the beam and make the image blur. The second solution is indirect. It consists in proving that sodium is NOT inside the inner $\text{Ln}_2\text{O}_2\text{S}$ crystal. In particular, we noticed for $\text{Gd}_2\text{O}_2\text{S}$ that the lattice distances were matching the reference bulk data (Figure 57A).

Previously, we discussed the pair distribution function to evaluate the occurrence of Gd–S bonds in the powder. Additional information can be extracted from the whole pattern (2 - 14 Å). Real space calculated PDF are here compared without any further structure refinement (neither cell parameters nor atomic positions). Because all the distances match with the bulk reference data to the precision of the measurement with no shift larger than 0.02 Å, including long range ones, sodium is absent as mentioned in Chapter II.

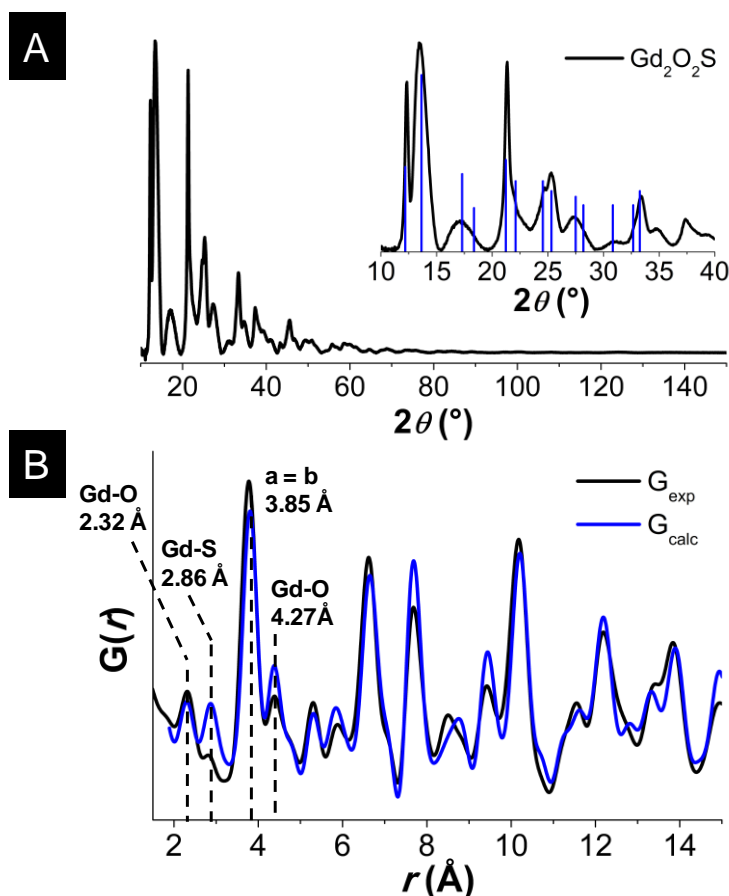


Figure 57: (A) Powder XRD pattern obtained for $2\theta = 10^\circ - 150^\circ$ and zoom on the region $10^\circ - 40^\circ$ (inset) with $\text{Gd}_2\text{O}_2\text{S}$ reference data Bragg peaks (JCPDS 26-1422). (B) Comparison between the experimental and calculated from $\text{Gd}_2\text{O}_2\text{S}$ structure data (JCPDS 08-6593) pair distribution functions.

Eventually, we checked if the sodium amount decreased along the washing process. Typically, the particles are isolated with ethanol and then washed three times with a mixture THF-ethanol 1/5 v/v (or hexane/ethanol). The amount of sodium was measured by EDS on samples obtained in the different washing steps (Figure 58).

The separation step eliminated most of the nominal sodium amount with a decrease from 1 equiv. to 0.21 equiv. vs. Gd. Nevertheless, the first washing also removed an additional 0.08 equiv. vs. Gd. Then, sodium amount regularly decreased from 0.13 equiv. to 0.08 equiv. vs. Gd along the whole washing process. The easy removal of most of the sodium is in agreement with our hypothesis that sodium is not inside the nanocrystals.

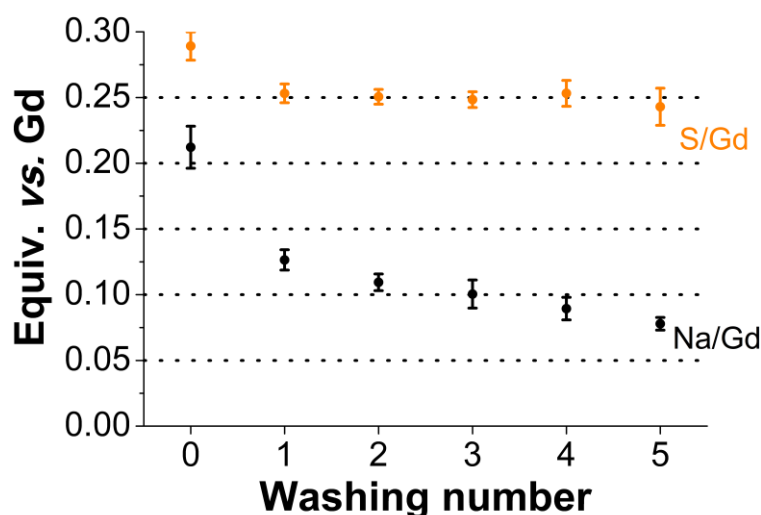


Figure 58: Sodium and sulfur amounts evolution during the washing process of $\text{Gd}_2\text{O}_2\text{S}$ nanoplates. EDS was performed on 5 different sites of each sample. Washing “0” refers to the powder centrifuged from the crude solution, with ethanol only (separation step).

So, where is sodium on the surface? We propose in the vicinity of the only negatively charged species outside the crystal: the carboxylate groups of oleate ligands. Another plausible idea is that sodium oleate remains in the final product, for instance with the hydrophobic carbon chain interpenetrated with another oleate molecule bonded to a nanocrystal. The slow and incomplete decrease of the sodium quantity in the washing process can be attributed to the low solubility of sodium cations in the THF-ethanol mixture and a minimum fraction (around 5 equiv. vs. Gd, Figure 56) of sodium cations strongly attached to carboxylate groups. In comparison, sulfur quantity does not change upon washing and guarantees that sulfur is an inseparable element of the nanoparticle.

Considering the results of this section, we can question the conclusions of the previous authors on the supposed reaction driving force. As the measured distances in our $\text{Gd}_2\text{O}_2\text{S}$ nanocrystals are in accordance with bulk gadolinium oxysulfide, it seems that sodium did not substitute the lanthanide atoms in the oxysulfide final structure, even if the cations radii would have been suitable for such a mechanism. Thus, the role of the alkali ion is still mysterious: no Na-Gd substitution means no formation of oxygen vacancies and consequently no driving force for the oxysulfide crystallization.

III.2.3. Role of the alkali complex

III.2.3.1. Influence of the alkali nature

Based on the idea that the alkali cation can reversibly substitute lanthanide cations, we first undertook a series of tests with sodium oleate and lithium acetylacetonate for small and heavy lanthanides (starting from gadolinium). As mentioned in Chapter II, the choice of the alkali acetylacetonate or oleate complex has no significant influence on the $\text{Ln}_2\text{O}_2\text{S}$ nanoparticles synthesis, because oleic acid in the reaction medium tends to substitute the acetylacetonate ligands which react with oleylamine. Besides, both acetate and acetylacetonate complexes can be used for the lanthanide precursor.

Lithium ionic radius should be more adapted to make substitution reactions with lanthanides than potassium or sodium with the small lanthanides (Figure 55). Gadolinium, dysprosium, erbium, ytterbium, lutetium and scandium precursors were employed in a protocol similar to these producing $\text{Gd}_2\text{O}_2\text{S}$. If the acetylacetonate complex was not commercially available, the $\text{Ln}(\text{ac})_3$ complex was used instead. For ytterbium, lutetium and scandium, only lithium was tested because Na^{I} radius is at least 0.2 Å larger than the lanthanide cations.

The yields were contrasted (they were all calculated with the hypotheses that the $\text{Ln}_2\text{O}_2\text{S}$ phase is formed and that 30 % of the final mass is composed of oleates). For the reactions with $\text{Gd}(\text{acac})_3$ and $\text{Er}(\text{acac})_3$, lithium and sodium complexes gave a significant amount of powder ($\eta \approx 55$ % for Er and $\eta = 60 - 90$ % for Gd). Interestingly, in the case of erbium, a first difference was noticed in the color of the final reaction medium: orange as usually observed for gadolinium with $\text{Na}(\text{oleate})$, pinkish with $\text{Li}(\text{acac})$. $\text{Yb}(\text{acac})_3$ and $\text{Lu}(\text{ac})_3$ reactions with lithium gave around 100 mg of powder ($\eta \approx 70$ %). Reactions of $\text{Sc}(\text{acac})_3$ with lithium and $\text{Dy}(\text{acac})_3$ with both the alkali resulted in very small amounts of powder ($\eta < 5$ %).

The powder XRD patterns of some of these samples are presented in Figure 59. A first important observation is that lithium promotes the crystallization of gadolinium oxysulfide nanoparticles as well as sodium oleate (Chapter II, Figure 2 and Figure 59A in this chapter). For dysprosium, the reaction with sodium oleate seemingly gave a mixture of $\text{Dy}_2\text{O}_2\text{S}$ and Dy_2O_3 (Figure 59B). However, the yield was poor, preventing any final conclusion. Erbium is a Manichean case: sodium oleate as an additive led to erbium oxide whereas lithium acetylacetonate led to erbium oxysulfide (Figure 59C). The powder obtained from $\text{Lu}(\text{ac})_3$ seemed to be an oxide-oxysulfide mixture (Figure 59D).

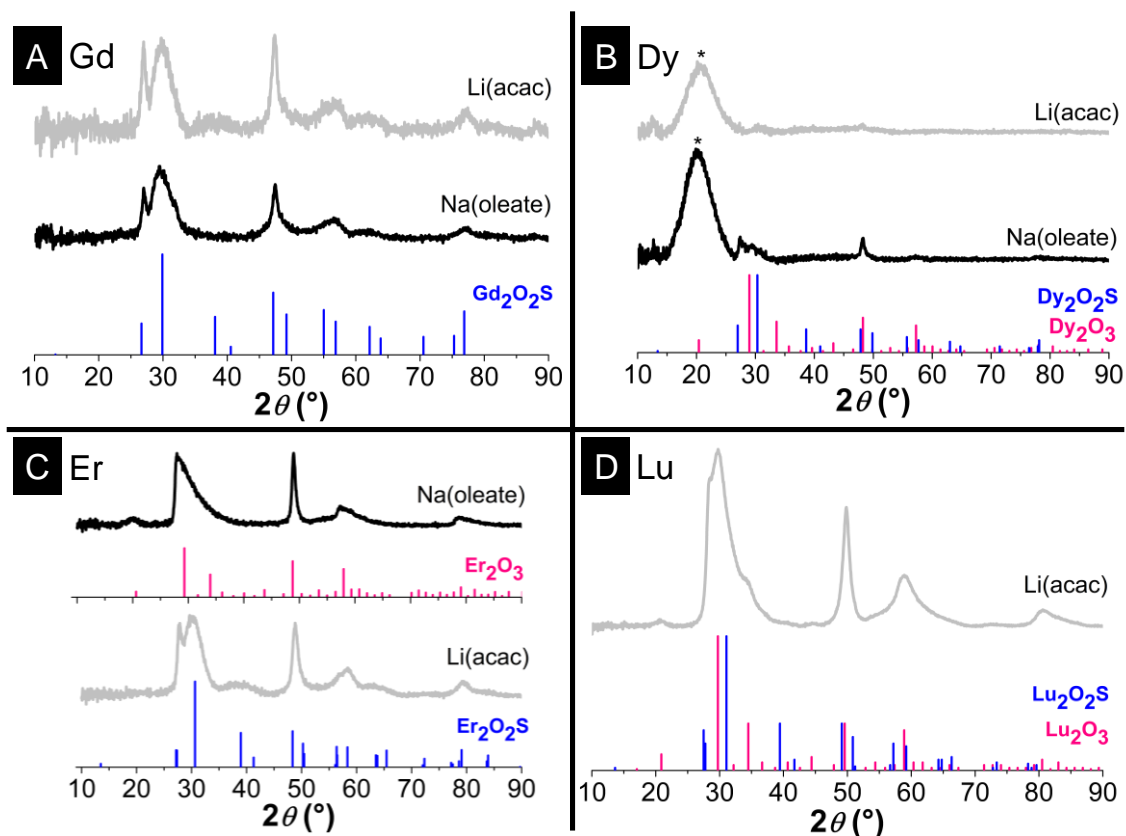


Figure 59: Powder XRD patterns of lanthanide-based nanoparticles whose syntheses were conducted with an alkali complex. Gadolinium (A), dysprosium (B), erbium (C) and lutetium (D) oxysulfide nanoparticles were targeted. Stars indicate the contribution of the plastic dome used for keeping the nanoparticles under inert atmosphere. XRD pattern references are JCPDS files 26-1422 ($\text{Gd}_2\text{O}_2\text{S}$), 26-0592 ($\text{Dy}_2\text{O}_2\text{S}$), 22-0612 (Dy_2O_3), 65-3445 ($\text{Er}_2\text{O}_2\text{S}$), 08-0050 (Er_2O_3), 26-1445 ($\text{Lu}_2\text{O}_2\text{S}$), 12-0728 (Lu_2O_3).

We summarized the results of the different works on alkali complexes in Figure 60.

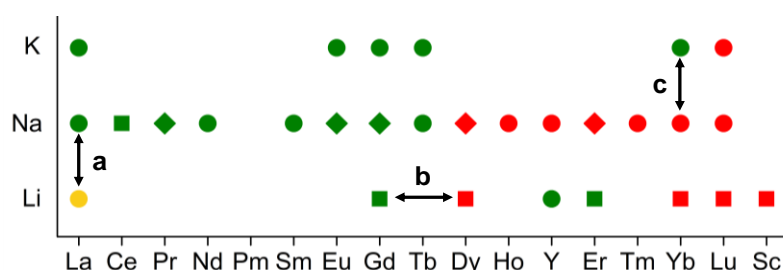


Figure 60: Influence of the alkali nature on the crystallization of $\text{Ln}_2\text{O}_2\text{S}$ nanoparticles from Ding *et al.*¹ or Zhang *et al.*¹⁶ (circles), our work (squares) and both works (diamonds). Light green: crystalline nanoparticles; yellow: poorly crystallized nanoparticles; red: no nanoparticles, oxide nanoparticles, mixture.

The works with sodium can suggest that a substitution occurs. But the results of lithium and potassium additives contradict the previous conclusion, especially because lithium is able to

provide crystalline lanthanum oxysulfide nanoparticles (Figure 60a) and potassium ytterbium oxysulfide nanoparticles (Figure 60c).

Some results are also intriguing. For instance, gadolinium, yttrium and erbium oxysulfide nanoparticles could crystallize with lithium. Dysprosium, whose cation radius is comprised in between Gd and Y, could not (Figure 60b).

At this stage, it is impossible for us to formulate a hypothesis on the role of the alkali complex. We could only confirm that the insertion process is unlikely.

III.2.3.2. Influence of the alkali stoichiometry

In the works of Ding *et al.*¹ and Zhang *et al.*,¹⁶ the alkali stoichiometry was maintained at 1 equivalent *vs.* the lanthanide for all the syntheses. Because our tests without sodium led to an amorphous product composed of very small objects, we thought that either sodium was mandatory for the crystallization of the nanoplates, as suggested by Ding and Zhang, or the crystallization was kinetically enhanced by the alkali complex.

In 2013, Gu *et al.* crystallized $\text{Ln}_2\text{O}_2\text{S}$ nanoplates without alkali using gaseous H_2S as sulfidating agent.¹⁷ More recently, in 2017, Lei *et al.* managed to crystallize $\text{Gd}_2\text{O}_2\text{S}$ nanoparticles without alkali source with a modified procedure involving a large excess of elemental sulfur (20 equiv. *vs.* Gd).¹⁸ Sodium and yttrium doping were tested in these conditions. The authors noticed that the size of the nanoparticles grew with increasing sodium stoichiometry (0 equiv.; 1 equiv.; 4 equiv. *vs.* Gd), and that yttrium could influence the final morphology. Thus, the alkali in this case of sulfur excess is **not mandatory**, but seems to facilitate the crystallization process in a large extent.

We tried to reproduce Lei *et al.* synthesis without sodium (20 equiv. S *vs.* Gd, 315 °C, 1 h), and failed to do so.¹⁸ A few milligrams of solid were finally obtained after changing our washing procedure (on the advice of Lei himself, contacted by email). Furthermore, he confirmed that the yield is very low without sodium. This key point, not indicated in the paper, underlines the preponderant effect of the alkali additive in the crystallization process and speed. Moreover, in Lei's synthesis,¹⁸ nanoplates crystallization without sodium is already encouraging but is tarnished by the modified kinetics brought by the sulfur excess. Similar study was missing for reaction conducted with a stoichiometric amount of sulfur.

To investigate the role of sodium in the crystallization of $\text{Gd}_2\text{O}_2\text{S}$ nanoplates with a stoichiometric amount of sulfur, we carried out our optimized reaction with different sodium loadings, remembering that 1 equiv. *vs.* Gd gave 7 nm long crystalline nanoplates and 0 equiv.

vs. Gd gave a low amount of small amorphous nanoparticles (Chapter II, Figure 2). In particular, we wondered if it would be possible to crystallize $\text{Gd}_2\text{O}_2\text{S}$ with small sodium amounts. The results are presented in Table 7 and Figure 61.

Na:Gd nominal ratio (equiv. vs. Gd)	Na concentration (mol.L^{-1})	Na in the final product (equiv. vs. Gd)	S in the final product (equiv. vs. Gd)
0	0	0	/
0.01	3×10^{-4}	0	0.06 ± 0.01
0.10	3.0×10^{-3}	0.06 ± 0.02	0.13 ± 0.02
0.50	1.49×10^{-2}	0.03 ± 0.01	0.22 ± 0.02
1.00	2.98×10^{-2}	0.20 ± 0.03	0.19 ± 0.02

Table 7: Na:Gd and S:Gd ratio in $\text{Gd}_2\text{O}_2\text{S}$ nanoparticles samples depending on the nominal Na/Gd ratio.

0.01 equiv. of sodium gave small nanoplates, but the EDS analysis indicated a S:Gd ratio of 6 % (Table 7). Accordingly, the XRD pattern showed a broad peak between 25° and 35° that indicated the presence of gadolinium oxide nanoparticles, with probably a low amount of gadolinium oxysulfide nanoparticles (Figure 61F). With 0.50 equiv., the nanoparticles obtained are well crystallized and similar to the product obtained with 1 equiv., even if the aggregation of the nanoplates was less pronounced (Figure 61D and F). At 0.10 equiv. the XRD pattern already showed the pure oxysulfide phase even if it was not perfectly crystallized when compared to higher sodium amounts (broader peaks and background signal due to an amorphous component, Figure 61F). Interestingly, the final sodium amount was decreased around 0.05 equiv. vs. Gd when the nominal Na:Gd ratio was 0.1 and 0.5. Our washing process with organic solvents seems to be unable to remove the last 5 % sodium. It is still coherent with the hypothesis that sodium cations are trapped around the carboxylate groups of oleate ligands so that a minimum sodium quantity remains on the final nanoparticles.

The fact that only 0.10 equiv. of sodium is both required and sufficient to crystallize the oxysulfide structure in our conditions is a key factor. Based on Lei's synthesis without sodium, we propose that Na^{I} is not mandatory for the crystallization of the $\text{Ln}_2\text{O}_2\text{S}$ nanoparticles, as concluded by Ding *et al.* with the model of sodium insertion inside the crystal. However, Na^{I} empirically catalyzes the crystallization or at least, it kinetically helps the reaction.

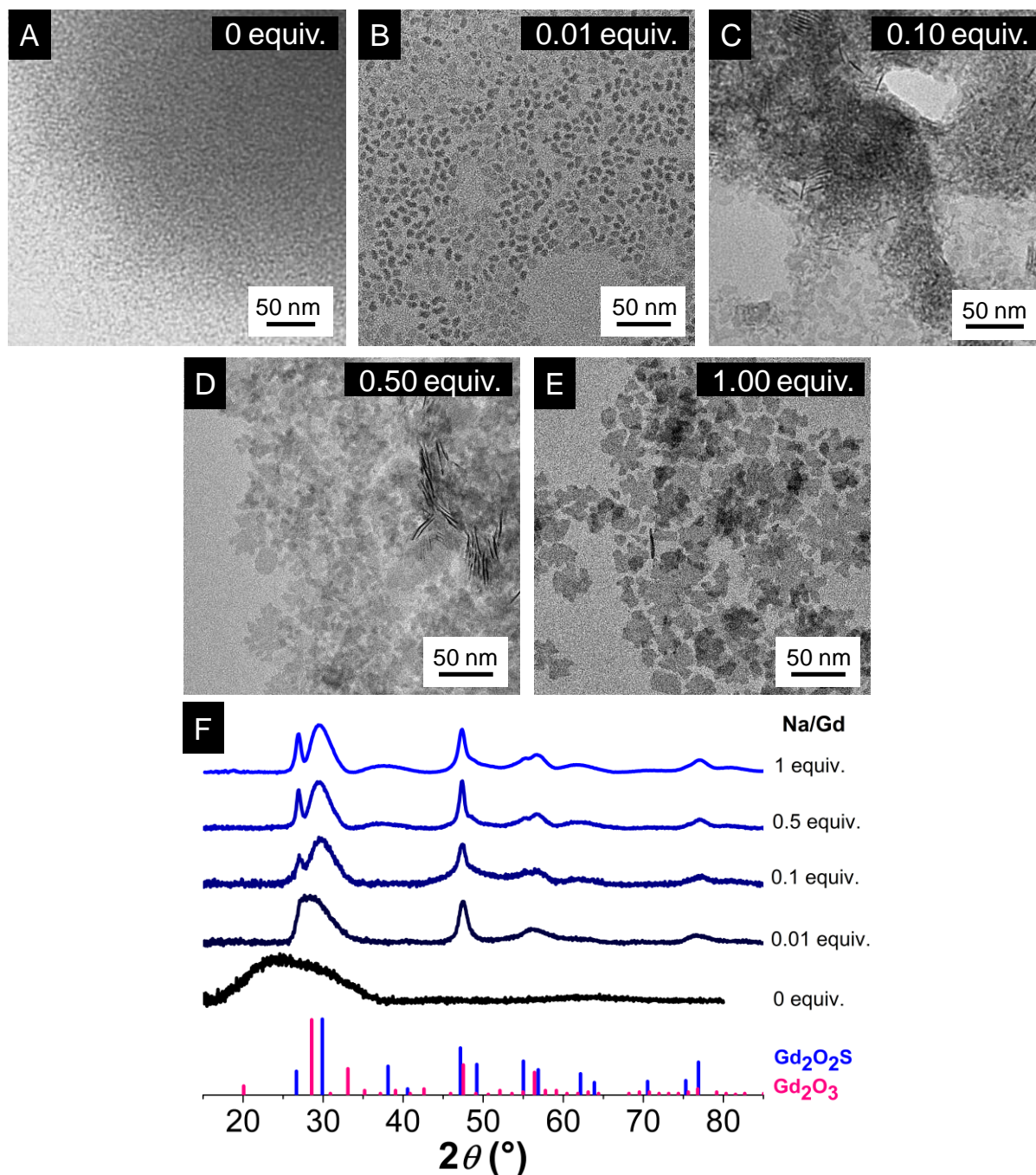


Figure 61: Influence of the sodium oleate concentration in the crystallization of $\text{Gd}_2\text{O}_2\text{S}$ nanoparticles. TEM micrographs of final particles obtained with 0 (A), 0.01 (B), 0.5 (C) and 1 equivalent of Na(oleate) vs. Gd(acac)_3 and their corresponding powder XRD patterns (E).

III.2.3.3. New hypothesis: sodium stabilizes sulfur radicals

If the sodium does not insert the gadolinium oxysulfide structure, how does it influence the crystallization of the nanoplates? In our opinion, the answer could be in the very beginning of the sulfidating process. In the first chapter, we have already described the formation of H_2S obtained by the reactions of polysulfides S_n^{2-} with aliphatic amines as described by Thomson

*et al.*¹⁹ H₂S formed *in situ* in the amine can then act as the source of sulfur in inorganic crystals such as sulfides and oxysulfides. The thioamide species also formed *in situ* can play the role of sulfidating agent as well.¹⁹

At the beginning of the process, the polysulfide anions are formed by the opening of the S₈ ring. At room temperature as well as upon heating, the opening of the S₈ ring can be triggered by radical species of sulfur. They instantly form when elemental sulfur is in solution in amines and their amount strongly depends on the amine (typically between 10⁻⁴ and 10⁻⁶ radical per sulfur atom).²⁰

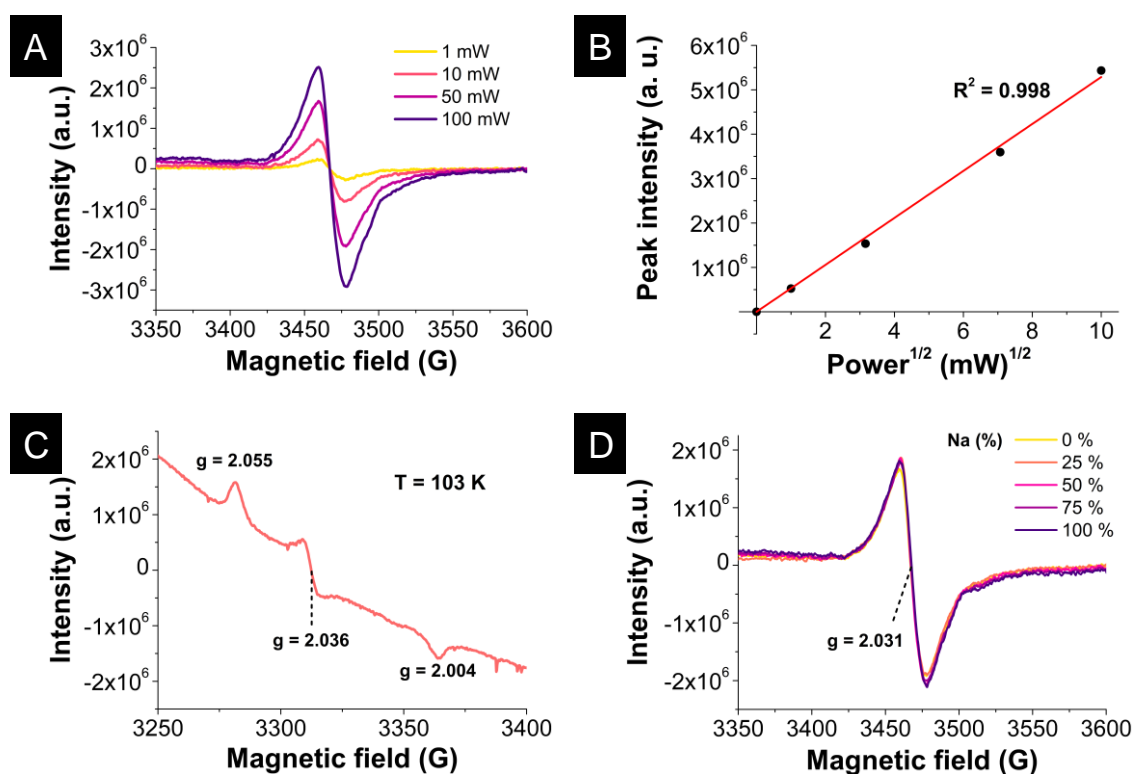


Figure 62: (A) ESR spectra of a S₈ in oleylamine solution at different microwave powers at room temperature, and (B) relation between the peak intensity and the microwave power square root. The linear trend guarantees that the signal does not saturate. (C) ESR spectra of the oleylamine/S₈ solution performed at 103 K and 10 mW. (D) ESR spectra of oleylamine/S₈/Na(oleate) solutions performed at room temperature and 50 mW. 0 % Na indicates the absence of Na(oleate) and 100 % is the nominal concentration in the reaction medium.

The formation of sulfur polyanions could be facilitated by the presence of alkali cations for charge balance. The intermediate radical formation is supposed to go through the homolytic cleavage of S–S bonds and consequently does not create localized charges on the sulfur atoms.²⁰ Can the presence of alkali cations in a sulfur/amine mixture stabilize the final polyanions, thus increase the reactivity of S₈ in the solution? If yes, more intermediate radicals should be observed in the presence of alkali cations.

Electron spin resonance was thus used to determine the influence of sodium concentration on free radical concentration in the medium. This experiment was conducted by Dr. Thierry Allard at IMPMC (Paris). The system was simplified to a mixture oleylamine/S₈/Na(oleate), where the S₈ concentration was fixed to the same value than in the reaction medium. We observed at ambient temperature a signal around $g = 2.0$ (free radicals zone) and verified first that there was no saturation of the signal in the microwave power range we used (Figure 62A and B). Also, we performed an ESR spectrum at a low temperature (103 K) on the sample without sodium and confirmed that the radicals we observed (Figure 62C with characteristics signals at $g = 2.004$, $g = 2.036$ and $g = 2.055$) were identical to those reported by Hodgson *et al.* (same shape and respective g values are 2.003, 2.035 and 2.055).²⁰

Different sodium concentrations were then used (Figure 62D). On the ESR spectra, there is no significant difference either in the shape of the spectra or in the intensity of the peak. Because the spectra were obtained in the exact same conditions, we can conclude that the free radicals concentration does not change in the presence of sodium, and that our hypothesis about the stabilization of sulfur radicals is consequently wrong.

III.2.4. Conclusion about the role of sodium

In this section, we were yet unable to determine the role of the sodium cation, or the alkali in general. However, several hypotheses were eliminated. The insertion of the alkali in the Ln₂O₂S structure does not occur. Its absence inside the final nanocrystals was also confirmed by fine structural analysis: it should only be coordinated on the oleate groups of the surface ligands or remaining oleate chains. Besides, sodium was shown not to influence the sulfur free radical concentration and should not activate this reactant in our reaction conditions. To formulate new (and hopefully better) hypotheses, we decided to investigate the mechanism of the reaction from a larger viewpoint.

III.3. First insights in the formation mechanism of Gd₂O₂S nanoplates

III.3.1. Investigating the synthesis unfolding: why and how?

The numerous syntheses of Ln₂O₂S nanoparticles described in Chapter I propose a description of the final state with more or less details. One can easily imagine that it is essential to get the most accurate description of the synthesized nano-objects to use them properly for further synthetic steps (functionalization, annealing, doping) or for direct applications.

It is harder, but equally worthwhile, to understand the formation mechanism of the nanoparticles. By “formation mechanism”, we mean the elementary (physico)chemical steps from the molecular precursor in solution to the nanocrystals described by TEM, XRD, etc. in the previous sections. In our opinion, the knowledge on the formation mechanism is more than a mere curiosity. It provides valuable information, which can be reused and compiled to optimize the existing syntheses and lead to new compositions and structures.

Ln₂O₂S nanoparticles literature suffers from a shortfall of information on the formation mechanisms both in aqueous and organic media. The first step in water-based syntheses, which is the formation of the so-called “oxygenated precursor” (hydroxycarbonate, oxide, hydroxide...) is poorly described. Sometimes, the product of this reaction is not even characterized. The description of the sulfidation step (generally performed by solid-solid or solid-gas reaction with S₈ or *in situ* produced CS₂) is often limited to few experimental details. In organic media, the discussions on the mechanism of Ln₂O₂S formation are found in the articles of Ding *et al.* and their successors,^{1,17,18} and were mainly reviewed in this chapter. Again, none of them were supported by experimental data obtained during the synthesis.

Monitoring nanoparticles formation is a challenging work. In the stages of a typical nanoparticles synthesis, the nature of the objects considerably evolves: molecules, clusters, nuclei, nanoparticles, each one with their own specificities and detection methods. Generally, two or three techniques must be combined to collect enough clues and unveil the formation mechanism.

We selected small and wide angle X-ray scattering (SAXS and WAXS) to analyze the synthesis of Gd₂O₂S nanoplates.

III.3.2. SAXS and WAXS of colloidal solutions of $\text{Gd}_2\text{O}_2\text{S}$ nanoplates (final state)

The SAXS-WAXS experiments were carried out at the *Center of Atomic Energy* (CEA) in Saclay (France) under the direction of Dr. David CARRIERE with the help of Dr. Xavier Frogneux.

SAXS-WAXS *ex situ* experiments were conducted to study the formation of $\text{Gd}_2\text{O}_2\text{S}$ nanoparticles. These techniques allowed us to investigate a large size range, typically between 1 nm and 100 nm. We thus expected to monitor the formation of the inorganic crystals and at least determine the typical temperature ranges for their nucleation and growth.

In our SAXS-WAXS experiments, the samples are colloidal solutions placed in thin glass capillaries. Fortunately, the concentrations of the typical synthesis of $\text{Gd}_2\text{O}_2\text{S}$ nanoparticles were optimal for the signal detection. Thus, no dilution or concentration step was required and the solution was directly injected in a capillary.

As a first approach, colloidal solutions representing the final states of different syntheses were studied. Some samples were prepared in advance. Others were synthesized at the CEA, right before the analyses (ca one hour before). The results of the scattering experiments are presented in Figure 63.

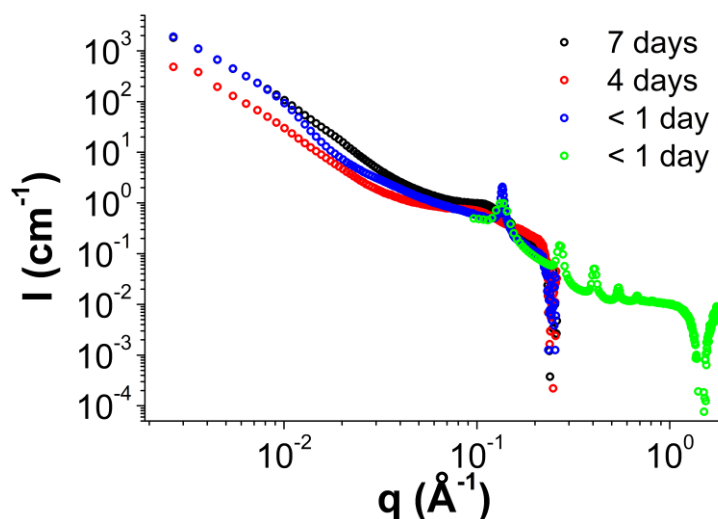


Figure 63: SAXS-WAXS experiments on colloidal solutions obtained after synthesis. SAXS experiments were obtained on samples prepared 7 days earlier (black circles, [CL516]), 4 days earlier (red circles, [CL518]) and right before (blue circles, [CL519]) analysis. WAXS was performed on a sample prepared right before analysis (green circles, [CL520]).

Remarkably, the samples correspond to the same synthesis but do not present the same SAXS signal. It is a sign that the solutions aged with time, and that only the fresh samples can be properly analyzed.

The high q range of SAXS properly overlaps with the low q range of WAXS for samples prepared at the CEA (Figure 64).

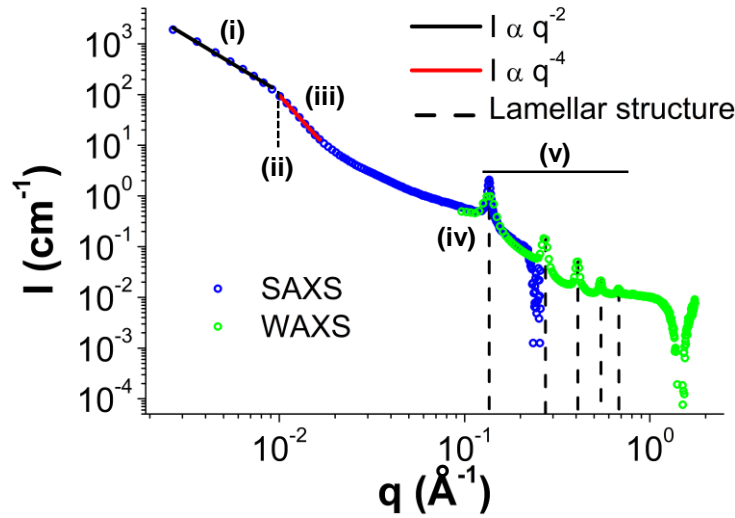


Figure 64: Analysis of the SAXS (in blue) and WAXS (in green) experiments of the final colloidal solution of a synthesis of $\text{Gd}_2\text{O}_2\text{S}$ nanoparticles.

On the X-ray scattering experiments, we observed several features which can be interpreted with the following relations:

- (i) A power law $I = Bq^{-p}$ with $p \approx 2$ ($p = 2.2$, violet line).
- (ii) A correlation signal for $q \approx 10^{-2} \text{ \AA}^{-1}$ characteristic of a gyration radius $R_{g1} \approx 20 \text{ nm}$.
- (iii) A power law $I = Bq^{-p}$ with $p = 4$ (red line).
- (iv) A correlation signal for $q \approx 10^{-1} \text{ \AA}^{-1}$ characteristic of a gyration radius $R_{g2} \approx 1.5 \text{ nm}$.
- (v) A series of peaks $k\Delta q = 0.14 \text{ \AA}^{-1}$ (dashed black lines).

The $p = 2$ and $p = 4$ power laws (Figure 64, violet and red lines) are respectively characteristic of planar objects and smooth objects. Because of previous TEM observations and the R_{g1} gyration radius value, we deduced that R_{g1} is correlated to aggregates of $\text{Gd}_2\text{O}_2\text{S}$ nanoplates (Figure 65A). The peaks observed by WAXS (pointed by dashed black lines) indicated that the nanoplates are stacked in lamellar superstructures with typical spacing of 4.5 nm. Besides, the analysis of the peaks width gave a typical length of 60 nm for the aggregates. Taking the model of a cylinder composed of nanoplates ($R = 3.5 \text{ nm}$, $L = 60 \text{ nm}$), the calculated gyration radius would be 17.5 nm and corroborates this hypothesis on the geometry based on R_{g1} value (Equation 1, Figure 65B).

$$R_{g,cylinder}^2 = \frac{R^2}{2} + \frac{L^2}{12}$$

Equation 1: Expression of the gyration radius for a dense cylinder with a length L and a section radius R .

The second correlation signal with R_{g2} was attributed to the thickness of the nanoplates that is around 1.5 nm itself based on TEM. The final drop in the high q range of SAXS (blue circles) may be correlated to strong interactions between the constituting objects (the nanoplates) and the solvent. This could be due to the presence of the oleate ligands at the surface of the nanoparticles, which can interact with the other hydrophobic chains that constitute the solvent (oleylamine, octadecene, oleic acid).

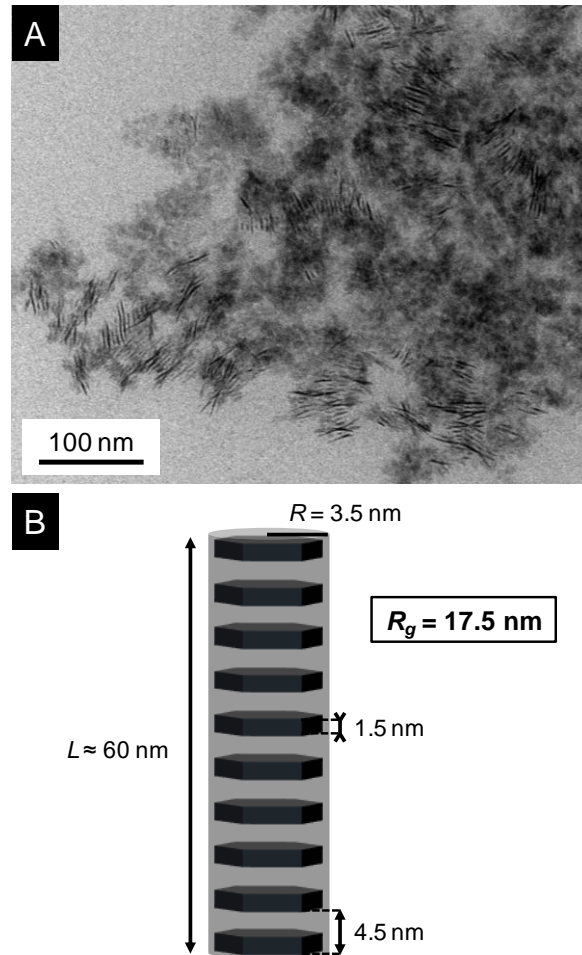


Figure 65: Typical aggregates of Gd₂O₂S nanoplates observed by TEM (A) and their description using the SAXS-WAXS interpretation (B).

The SAXS-WAXS experiments on the final solutions were in accordance with our previous observations and gave a more accurate view of the aggregates. Now that the final state has been investigated, it is time to take a closer look to the synthesis progress.

III.3.3. Mechanism of formation of the Gd₂O₂S nanoplates

III.3.3.1. Sampling method

For the SAXS-WAXS experiments, the reaction medium was sampled at different temperatures as detailed in Figure 66 (see the details in experimental section). To be representative of the whole reaction, the medium was sampled during the temperature increase, the temperature plateau and the cooling. The samples (≈ 0.4 mL) are immediately cooled down in a quasi-inert atmosphere thanks to a water bath.

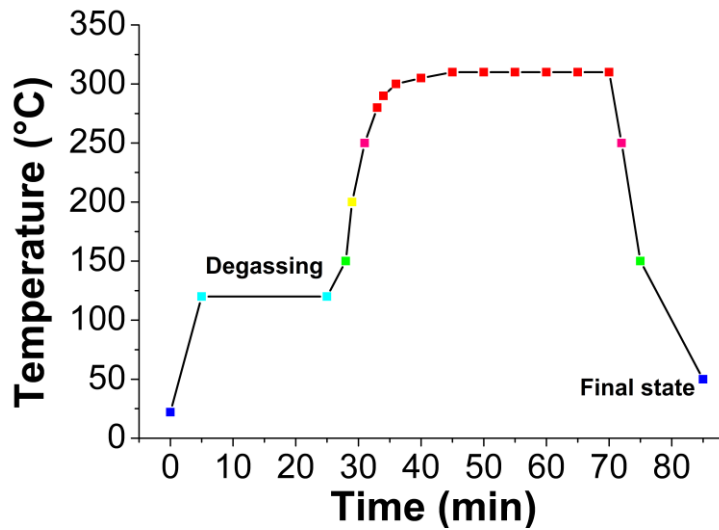


Figure 66: Temperature evolution as a function of time. Each colored point represents a relevant sampling point. The plateau at 120 °C is the degassing step under vacuum (evaporation of water and other low boiling points compounds).

We will discuss the mechanism in two main phases, corresponding to two temperature ranges and two different processes: from the complex to the nuclei (up to 300 °C), and then the aggregation of the colloids (> 300 °C)

III.3.3.2. From the complex to the nuclei ($T < 300$ °C)

Below 300 °C, the SAXS-WAXS curves are similar (Figure 67) and distinct from the final state:

- (i) At small angles ($q < 2.10^{-2} \text{ \AA}^{-1}$), there is a strong diffusion with a power law $I = Bq^{-p}$ with $p \approx 3.4 - 3.8$ (p decreases with temperature).
- (ii) For $q > 2.10^{-2} \text{ \AA}^{-1}$, a very clear $I = Bq^{-1}$ power law is observed.
- (iii) A correlation signal is obtained for $q \approx 10^{-1} \text{ \AA}^{-1}$ characteristic of a gyration radius $R_{g2} \approx 1.5 \text{ nm}$.

- (iv) The (001) peaks of lamellar structures are present with a characteristic step of 4.3 nm, close to value (4.5 nm) observed at the final state.

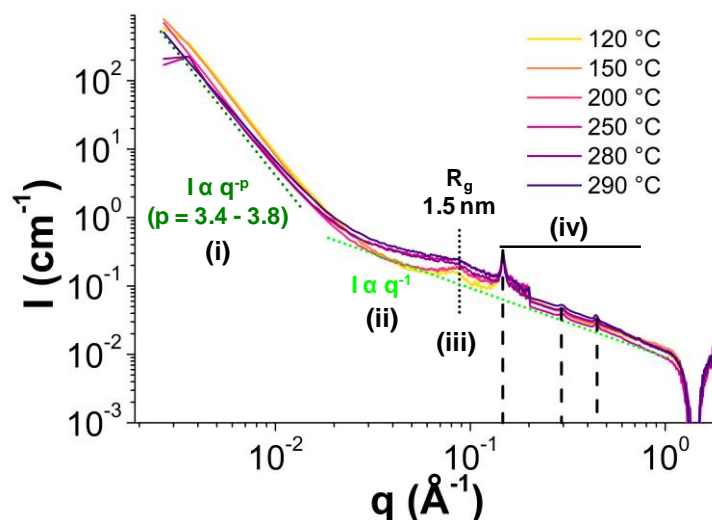


Figure 67: SAXS-WAXS obtained from samples taken during the temperature increase. The SAXS and WAXS data were merged at 0.20 \AA^{-1} (small gap).

Interestingly, the lamellar phase and the correlation signal are **already observable at 120 °C!** It indicated that at the earliest stages of the synthesis, the solvent and/or the complexes were already structured. This structure is likely possibly organized by the surfactants that composed the solvent (Figure 68), possibly with inorganic species within the lamellar structure.

This result is particularly satisfying: such an organization is possible only in the presence of cations in the system. The solvent itself is not structured at ambient temperature (data not shown). According to the literature, oleic acid is an isotropic liquid in the range 15-130 °C.²¹ However, in a oleic acid/sodium oleate mixture all the oleic acid is liquid above 32 °C but a fraction of sodium oleate remains solid-like with a lamellar organization, with a characteristic spacing of 4.5 nm.²¹ Moreover, the power law $I = Bq^{-p}$ with $p \approx 3.4 - 3.8$ indicated the presence of big assemblies whose roughness increased with temperature. This feature is likely related to the lamellar organization.

Because the typical sizes obtained from R_{g1} and R_{g2} were very similar to these of the final state, the geometry of the lamellar assembly must only slightly vary. Cations under the form of clusters or complexes must thus occupy a 1.5 nm thick space between the surfactants. Moreover, the $I = Bq^{-1}$ power law demonstrated the presence of rod-shaped objects. We thus suspected that the clusters were organized in cylinders in plane with the lamellar structure.

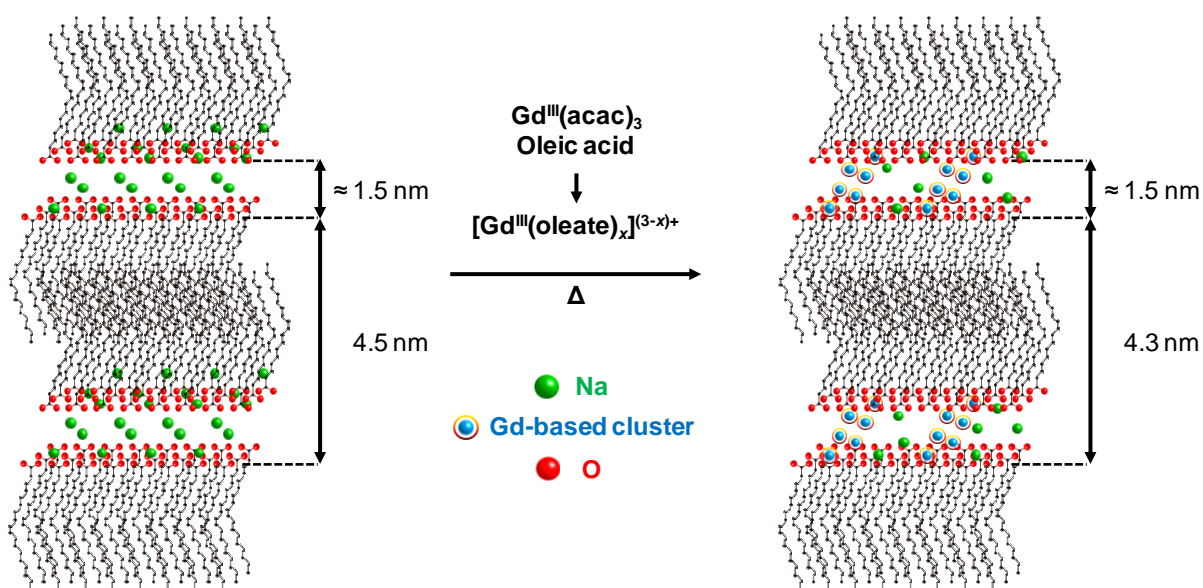


Figure 68: Proposed organization of sodium oleate without and with gadolinium clusters in the lamellar structure.

At 250 °C, a first change occurred. The bump at $q = 8.10^{-2} \text{ \AA}^{-1}$ started to fade, and progressively disappeared (nothing was observed at 310 °C). This modification could be related to the destruction of the cylinders made of clusters, and thus represent the first step of the nucleation: the clusters were consumed to form small objects whose thickness is still 1.5 nm. The width of these nuclei is limited and there is still no sign of the big aggregates of the final state (nanoplates assemblies, see Figure 65).

III.3.3.3. Nuclei, nanoplates and aggregates ($T > 300 \text{ °C}$)

At high temperature, the X-ray scattering profiles significantly changed. At 310 °C, the nanoplates were formed, and we retrieved all the features observed in the final state. First, the intensity at low q values increased. It showed that the crystalline fraction grew (Figure 69). Because the reaction is quantitative (vs. Gd) at 310 °C after 25 min, we will be able to estimate the advancement of the reaction depending on the temperature using the crystalline fraction (ongoing work). At higher q values, the peaks characteristic of the lamellar structure were more and more distinct and slightly shifted towards small angles (Figure 69).

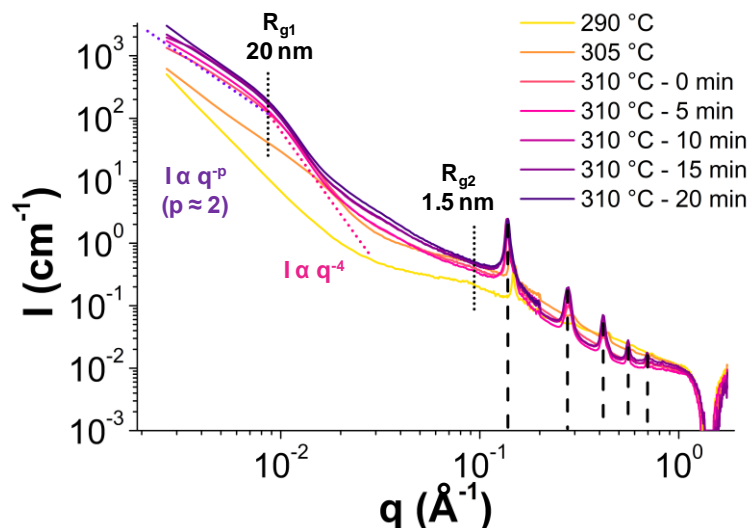


Figure 69: SAXS-WAXS on samples obtained in the high temperature region ($T > 300$ °C). The SAXS and WAXS data were merged at 0.20 \AA^{-1} (small gap).

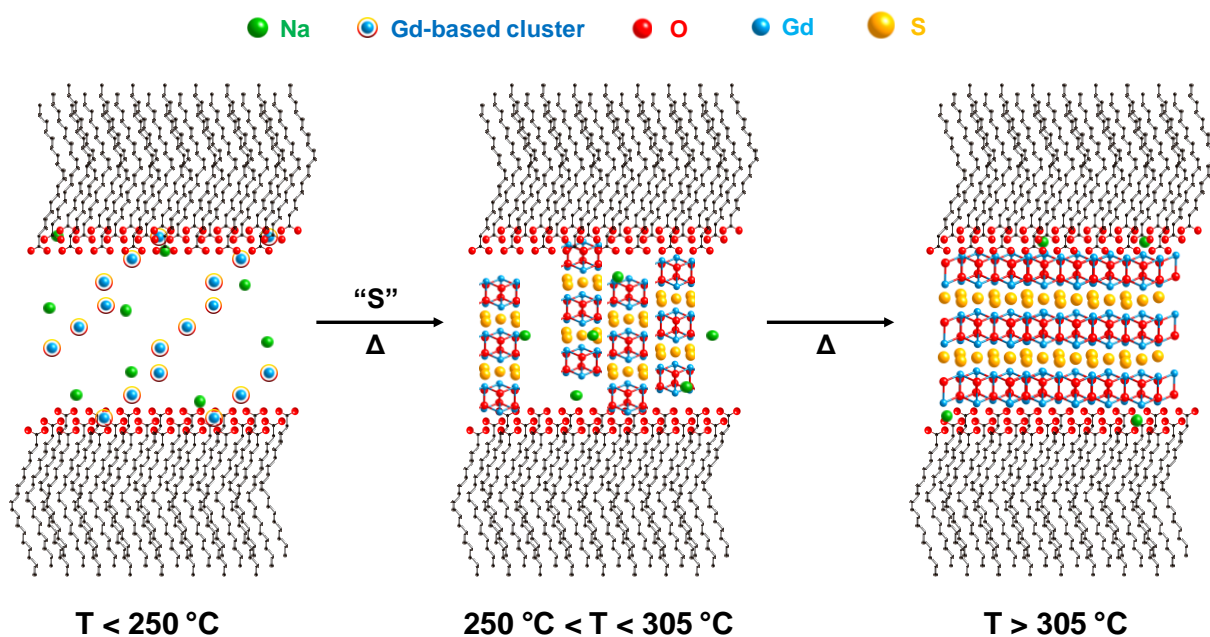


Figure 70: Proposed mechanism of the $\text{Gd}_2\text{O}_2\text{S}$ nanoparticles formation from the organized clusters. At 305 °C, the nanoparticles are in an intermediate phase: the nuclei started to assemble, but the length of the formed nanoparticles is still below the final state. Moreover, an increased intensity in the low q values and an inflexion around $2 \cdot 10^{-2} \text{ \AA}^{-1}$ (lower gyration radius than the final state) are the first signs of nanoplates aggregation in large assemblies appear. The plateau at 310 °C finalized the growth of the nanoplates in lateral extension and their organization in large aggregates whose gyration radii are close to R_{g1} . This proposed formation mechanism is illustrated in Figure 70.

III.3.3.4. Conclusion: a new view on the role played by alkali

A new hypothesis on the sodium role emerged with the analysis of the formation mechanism. In our conditions (OA:Na(oleate) = 5/1), a lamellar phase of Na(oleate) exists in solution with an interlamellar distance of 4.3 nm (just below the 4.5 nm reported in the literature for a 1/1 mixture).²¹ This difference can be explained by the insertion of gadolinium complexes or clusters inside the layers of the lamellar phase as demonstrated by SAXS. The reaction of Gd(acac)₃ and oleic acid forms Gd(oleate)_x species that may interact more easily with the lamellar phase to get the gadolinium clusters insertion.

The layer between the polar heads of oleate chains remains close to 1.5 nm during the whole reaction. It is a good clue that the nanoplates growth is templated by the lamellar oleate phase, and only a small swelling is observed at the end of the reaction when the nanoplates tend to get their final width and thickness. Moreover, the lamellar organization of the Ln₂O₂S phase itself (isomorphism) is probably an entropic advantage for the crystallization of this phase inside the lamellar oleate phase.

The proposed mechanism also explains why the Ln₂O₂S nanoplates always present a sulfur-defective structure. Necessarily, the nanoplates must be ended on {001} facets by positively charge layers to face the oleate ligands.

Without sodium, the nanoparticles growth is no more templated and facilitated by the lamellar phase. With our sulfur amount (1 equiv. vs. Gd), it was thus impossible to crystallize Ln₂O₂S or another phase. Lei *et al.* favored the crystallization by putting a very large excess of sulfur.¹⁸ However, only a very small fraction of the gadolinium precursor was able to react probably because of a random organization in solution.

The selectivity of lanthanides towards one or several alkali can also be envisaged this way. The alkali oleate phase must change depending on the alkali (thickness of the cationic layer, cations repartition).²² Thus, the cluster insertion in the M(oleate) phase strongly depends on the interlayer distance and the affinity of the clusters for the interlayer in general. Besides, the affinity and repartition of the lanthanide-based clusters in the M(oleate) lamellar phase is probably at the origin of the possible crystallization of the Ln₂O₂S phase and the variable growth of the nanoplates (La₂O₂S = 23 nm, Gd₂O₂S = 7 nm). Ongoing work on EXAFS at Gd L_{III}-edge spectra (Figure 71) may be promising to collect the missing information on the chemical environment of the gadolinium cations during the synthesis (in collaboration with Andrea Zitolo and with the help of Thi Kim-Chi Lê, Anh-Minh Nguyen and Lionel Tinat).

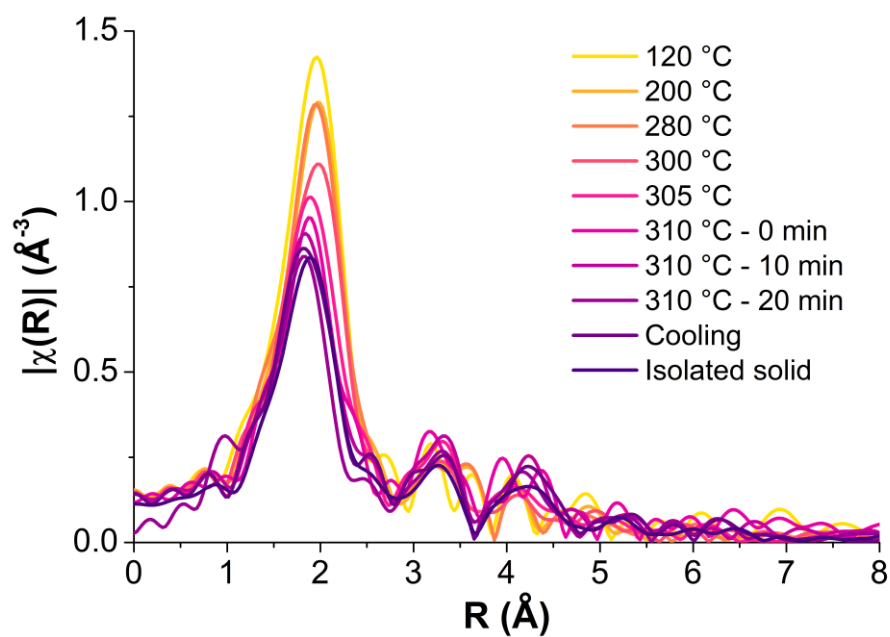


Figure 71: EXAFS spectra at Gd L_{III}-edge of the reaction medium of the Gd₂O₂S nanoplates synthesis. The medium was sampled similarly to the protocol of SAXS experiments (see Experimental section).

If we have no evidence for now of the clusters nature, we can hypothesize that they contain oleate groups as well as bridging oxo or hydroxo groups between the metal centers: Gd(O)_x(Oleate)_y or Gd(OH)_x(oleate)_y.

III.4. Conclusion

At the end of this chapter, our vision of the nanoparticle has changed. We summarized our conclusions in the scheme of Figure 72.

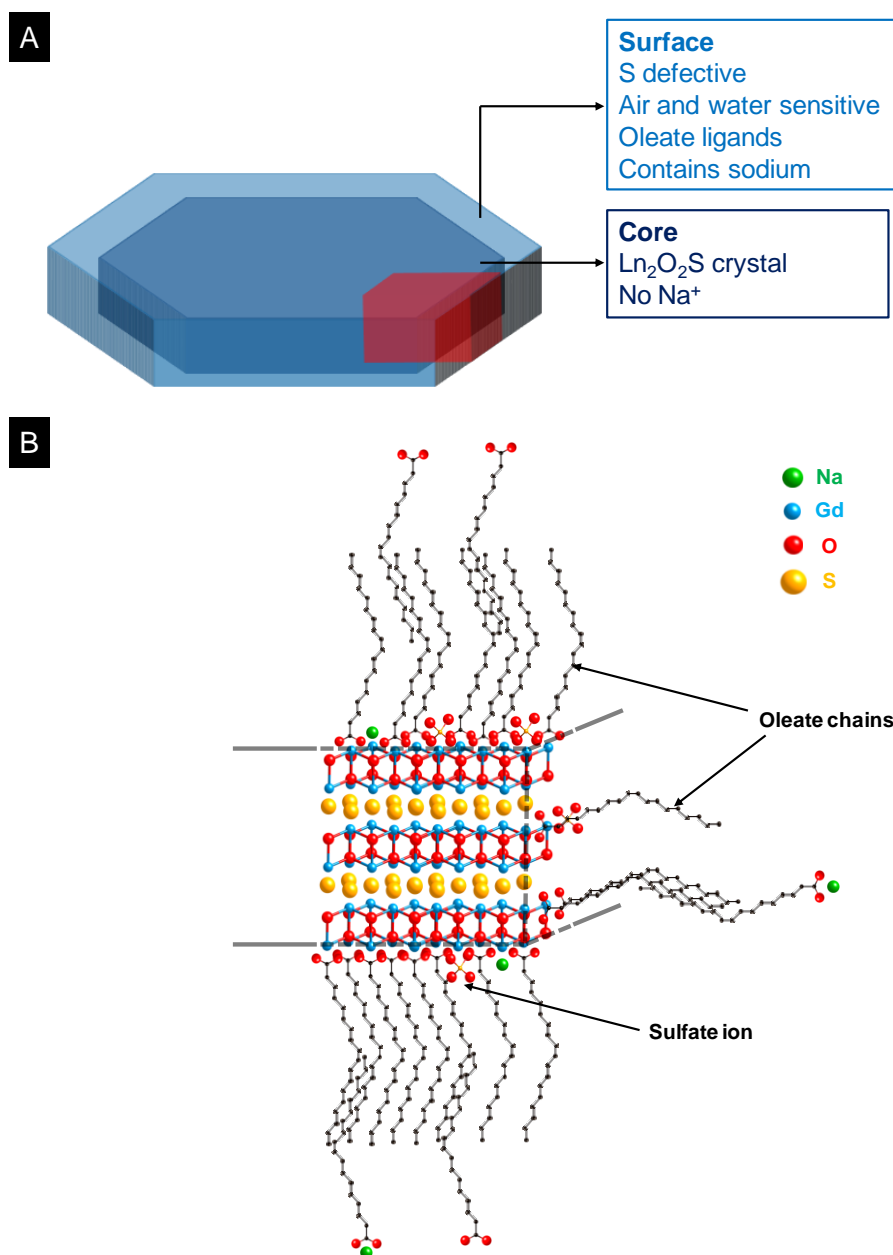


Figure 72: Schematic view of an $\text{Ln}_2\text{O}_2\text{S}$ nanoplate (A) and zoom on the red zone with the details of the structure at the interface between the $\text{Ln}_2\text{O}_2\text{S}$ crystal and the oleate ligands (B).

In particular, we underline the $[\text{Ln}_2\text{O}_2]^{2+}$ terminating layers on $\{001\}$ facets and the presence of external sulfur under the form of sulfate ions (or sulfonate). Sodium ions are located at the end of oleate chain, whether close to the surface of the particle or on “free” chains bonded to the ligands by the Van der Waals interactions between the hydrophobic chains.

The research and discussion about sodium localization was challenging but of great importance. It appeared to us that the traditional model proposed by Ding *et al* to justify the sodium insertion in the structure, although intuitive, was not fitting all the available data: consequently, it needed to be challenged. By investigating the whole reaction mechanism, we finally revealed the role of the sodium cation. It enables the formation of a lamellar phase in the reaction medium that contains inorganic gadolinium-based clusters and promotes the formation of the lamellar $\text{Ln}_2\text{O}_2\text{S}$ phase.

Our conclusions ensure that the sodium cation has no reason to be inside the $\text{Ln}_2\text{O}_2\text{S}$ nanocrystal. Consequently, the optical and magnetic properties that we probed on the $\text{Ln}_2\text{O}_2\text{S}$ nanoparticles and that are discussed in the next chapter majorly depend on the inner crystalline core and its electronic properties. They will not be influenced by the sodium amount that we measure in the sample. Otherwise, it would have been a study of the properties of $\text{Na}_w\text{Ln}_2\text{O}_2\text{S}_x$ nanoparticles.

References

- (1) Ding, Y.; Gu, J.; Ke, J.; Zhang, Y.-W.; Yan, C.-H. Sodium Doping Controlled Synthesis of Monodisperse Lanthanide Oxysulfide Ultrathin Nanoplates Guided by Density Functional Calculations. *Angew. Chemie Int. Ed.* **2011**, *50* (51), 12330–12334.
- (2) Larquet, C.; Nguyen, A.-M.; Ávila-Gutiérrez, M.; Tinat, L.; Lassalle-Kaiser, B.; Gallet, J.-J.; Bournel, F.; Gauzzi, A.; Sanchez, C.; Carenco, S. Synthesis of Ce₂O₂S and Gd₂(1-y)Ce_{2y}O₂S Nanoparticles and Reactivity from in Situ X-Ray Absorption Spectroscopy and X-Ray Photoelectron Spectroscopy. *Inorg. Chem.* **2017**, *56* (22), 14227–14236.
- (3) Leskelä, M.; Niinistö, L. Solid Solutions in the Rare-Earth Oxysulfide Series. *J. Solid State Chem.* **1976**, *19* (3), 245–250.
- (4) Liu, G.; Conn, C. E.; Drummond, C. J. Lanthanide Oleates: Chelation, Self-Assembly, and Exemplification of Ordered Nanostructured Colloidal Contrast Agents for Medical Imaging. *J. Phys. Chem. B* **2009**, *113* (49), 15949–15959.
- (5) Miller, F. A.; Wilkins, C. H. Infrared Spectra and Characteristic Frequencies of Inorganic Ions. *Anal. Chem.* **1952**, *24* (8), 1253–1294.
- (6) Sopoušek, J.; Pinkas, J.; Brož, P.; Buršík, J.; Vykoukal, V.; Škoda, D.; Stýskalík, A.; Zobač, O.; Vřešťál, J.; Hrdlička, A.; Šimbera, J. Ag-Cu Colloid Synthesis: Bimetallic Nanoparticle Characterisation and Thermal Treatment. *J. Nanomater.* **2014**, *2014*, 1–13.
- (7) NIST. Oleic acid mass spectrum (CAS: 112-80-1) <https://webbook.nist.gov/cgi/cbook.cgi?ID=C112801&Units=SI&Mask=200#Mass-Spec>.
- (8) Deacon, G. B.; Phillips, R. J. Relationships between the Carbon-Oxygen Stretching Frequencies of Carboxylato Complexes and the Type of Carboxylate Coordination. *Coord. Chem. Rev.* **1980**, *33* (3), 227–250.
- (9) Vaďura, R.; Kvapil, J. Growth and Lattice Parameters of the Lanthanide Carboxylates I. Tetrahydrated Lanthanide Acetates. *Mater. Res. Bull.* **1971**, *6* (9), 865–873.
- (10) Ribot, F.; Toledano, P.; Sanchez, C. X-Ray and Spectroscopic Investigations of the Structure of Yttrium Acetate Tetrahydrate. *Inorganica Chim. Acta* **1991**, *185* (2), 239–245.
- (11) Tong, L.; Lu, E.; Pichaandi, J.; Cao, P.; Nitz, M.; Winnik, M. A. Quantification of Surface Ligands on NaYF₄ Nanoparticles by Three Independent Analytical Techniques. *Chem. Mater.* **2015**, *27* (13), 4899–4910.
- (12) Hauser, H.; Darke, A.; Phillips, M. C. Ion-Binding to Phospholipids. Interaction of Calcium with Phosphatidylserine. *Eur. J. Biochem.* **1976**, *62* (2), 335–344.
- (13) Anderson, N. C.; Hendricks, M. P.; Choi, J. J.; Owen, J. S. Ligand Exchange and the Stoichiometry of Metal Chalcogenide Nanocrystals: Spectroscopic Observation of Facile Metal-Carboxylate Displacement and Binding. *J. Am. Chem. Soc.* **2013**, *135* (49), 18536–18548.
- (14) Lüth, H.; Nyburg, S. C.; Robinson, P. M.; Scott, H. G. Crystallographic and Calorimetric Phase Studies of the N-Eicosane, C₂₀H₄₂: N-Docosane, C₂₂H₄₆ System. *Mol. Cryst. Liq. Cryst.* **1974**, *27* (3–4), 337–357.
- (15) Ikeue, K.; Kawano, T.; Eto, M.; Zhang, D.; Machida, M. X-Ray Structural Study on the Different Redox Behavior of La and Pr Oxysulfates/Oxysulfides. *J. Alloys Compd.* **2008**, *451* (1–2), 338–340.
- (16) Zhang, T.; Gu, J.; Ding, Y.; Zhang, Y.-W.; Yan, C.-H. Experimental and Theoretical Studies on the Controlled Synthesis of Alkali-Metal-Doped Rare-Earth Oxysulfide Nanocrystals. *Chempluschem* **2013**, *78* (6), 515–521.
- (17) Gu, J.; Ding, Y.; Ke, J.; Zhang, Y.; Yan, C. Controllable Synthesis of Monodispersed Middle and Heavy Rare Earth Oxysulfide Nanoplates Based on the Principles of HSAB Theory. *Acta Chim. Sin.* **2013**, *71* (3), 360.

- (18) Lei, L.; Zhang, S.; Xia, H.; Tian, Y.; Zhang, J.; Xu, S. Controlled Synthesis of Lanthanide-Doped Gd₂O₂S Nanocrystals with Novel Excitation-Dependent Multicolor Emissions. *Nanoscale* **2017**, *9* (17), 5718–5724.
- (19) Thomson, J. W.; Nagashima, K.; Macdonald, P. M.; Ozin, G. a. From Sulfur–Amine Solutions to Metal Sulfide Nanocrystals: Peering into the Oleylamine–Sulfur Black Box. *J. Am. Chem. Soc.* **2011**, *133* (13), 5036–5041.
- (20) Hodgson, W. G.; Buckler, S. A.; Peters, G. Free Radicals in Amine Solutions of Elemental Sulfur. *J. Am. Chem. Soc.* **1963**, *85* (5), 543–546.
- (21) Tandon, P.; Raudenkolb, S.; Neubert, R. H. .; Rettig, W.; Wartewig, S. X-Ray Diffraction and Spectroscopic Studies of Oleic Acid–sodium Oleate. *Chem. Phys. Lipids* **2001**, *109* (1), 37–45.
- (22) Sugahara, T.; Takamatsu, Y.; Akamatsu, M.; Sakai, K.; Abe, M.; Sakai, H. Effect of Inorganic and Organic Counterions on Interfacial Properties of Oleic Acid-Based Gemini Surfactants. *Colloids Surfaces A Physicochem. Eng. Asp.* **2018**, *538* (August 2017), 73–78.

Chapter IV

Benefits of bimetallic composition: the tunable optical and magnetic properties of $\text{Gd}_{2(1-y)}\text{Ce}_{2y}\text{O}_2\text{S}$ nanoparticles

Table of contents

IV.1. Magnetic properties of $(\text{Gd,Ce})_2\text{O}_2\text{S}$ bimetallic nanoparticles	139
IV.1.1. Introduction	139
IV.1.2. Controllable magnetization of $\text{Gd}_{2(1-y)}\text{Ce}_{2y}\text{O}_2\text{S}$ nanoparticles.....	139
IV.1.3. Size effects in lanthanide oxysulfide: the case of $\text{Gd}_2\text{O}_2\text{S}$	143
IV.1.3.1. Geometric magnetic frustration of $\text{Gd}_2\text{O}_2\text{S}$	143
IV.1.3.2. Comparison of bulk and nanoscaled $\text{Gd}_2\text{O}_2\text{S}$	145
IV.1.3.2.1. Bulk $\text{Gd}_2\text{O}_2\text{S}$ (with an impurity of Gd_2O_3)	145
IV.1.3.2.2. Size effect in $\text{Gd}_2\text{O}_2\text{S}$ magnetic transition	146
IV.1.4. Conclusion	148
IV.2. Optical properties of $(\text{Gd,Ce})_2\text{O}_2\text{S}$ bimetallic nanoparticles	149
IV.2.1 Optical properties – Ln/Ce substitution and bandgap evolution.....	149
IV.2.1.1. Absorption of $\text{Gd}_{2(1-y)}\text{Ce}_{2y}\text{O}_2\text{S}$ nanoparticles	149
IV.2.1.2. Bandgap of $\text{Gd}_{2(1-y)}\text{Ce}_{2y}\text{O}_2\text{S}$ nanoparticles	150
IV.2.1.3. Comparison with other class of compounds	151
IV.2.1.4. Comparison with Pr and Eu cation balance	152
IV.2.2 Investigation of the bandgap nature using density functional calculations	154
IV.2.3. Conclusion	155

References	157
------------------	-----

IV.1. Magnetic properties of (Gd,Ce)₂O₂S bimetallic nanoparticles

IV.1.1. Introduction

In the present chapter devoted to the magnetic and optical properties of the nanoparticles, we shall discuss the prominent role played by the electronic properties of the metal ion. We should focus on the inner portion of the Ln₂O₂S nanocrystal, whose structure is the same as in bulk crystals. Nevertheless, the surface represents a significant part of the nanoparticle. Thus, surface oleate ligands and oxidized sulfur and cerium present on the surface are expected to exert a non-negligible influence.

The magnetic properties in the lanthanide-based compounds depend on the $4f$ electrons. In the specific case of (Gd,Ce)₂O₂S compounds, gadolinium and cerium are quite different: the electronic configuration of gadolinium ions (Gd^{III}) is $4f^7$, which corresponds to a half-full f -multiplet. The spin is thus maximal ($S = 7/2$) because all of the f electrons are unpaired, leading to a large magnetic moment. Consequently, gadolinium-based compounds generally present strong paramagnetic properties.

	Ce ^{III}	Gd ^{III}
Ground state	$^2F_{5/2}$	$^8S_{7/2}$
Magnetic moment μ_{eff} [μ_B]	2.54	7.94
Curie constant C [emu Oe ⁻¹ mol ⁻¹ K]	0.80 (45/56)	7.88 (63/8)

Table 8: Magnetic constants of trivalent cerium and gadolinium cations.

On the contrary, trivalent cerium (Ce^{III}) possesses only one f electron, so its magnetic moment is much smaller (Table 8). In some cases, Ce^{III} is oxidized into Ce^{IV} which is nonmagnetic.

IV.1.2. Controllable magnetization of Gd_{2(1-y)}Ce_{2y}O₂S nanoparticles

Bulk lanthanide oxysulfides Ln₂O₂S are paramagnetic at ambient temperature. At low temperatures (< 10 K), the compounds with Ln = Gd, Tb, Dy, Ho and Yb order antiferromagnetically at Néel temperatures between 2.5 K (for Ho) and 7.7 K (for Tb) and Weiss constants between - 8 K (for Ho) and - 18 K (for Gd). The other compounds remain paramagnetic down to 2 K.¹

In view of the above results, we expect similar paramagnetic properties for the Gd_{2(1-y)}Ce_{2y}O₂S nanoparticles. Specifically, the paramagnetic response of the powders should

decrease with y . Nevertheless, the coupling between gadolinium and cerium ions is possible because both ions have partially occupied f orbitals. Vibrating sample magnetometry (VSM) was thus performed on the powders to check this possibility, with the kind help of Yannick Klein and David Hrabovsky (IMPMC). The powder sample is placed in a nonmagnetic sample holder and mounted in the magnetometer. A linear motor makes the sample vibrate at 40 Hz thus generating an oscillating magnetic dipole. In Figure 73 we plot both the zero-field cooling (ZFC) curves which give evidence of a conventional paramagnetic response in the whole 5 - 350 K range measured. The field-cooling (FC) curves yield identical results.

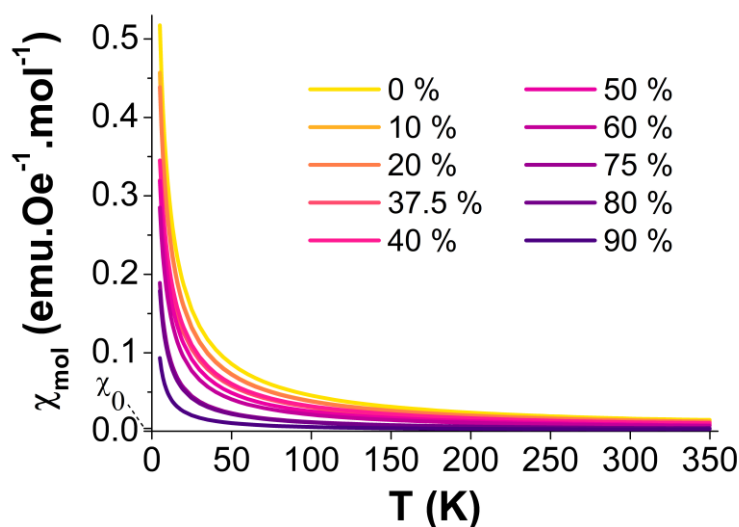


Figure 73: Molar susceptibility χ_{mol} of $\text{Gd}_{2(1-y)}\text{Ce}_{2y}\text{O}_2\text{S}$ powders measured by vibrating sample magnetometry. The average value of χ_0 is indicated. The y value is indicated in % in the legend. The applied field is 50 Oe.

We were able to fit the $\chi_{\text{mol}}(T)$ curves using a generalized Curie's law, as demonstrated in Figure 74. The generalized Curie's law is a Taylor expansion of first order of the Curie's law for isolated paramagnetic ions. The constant contribution χ_0 is orders of magnitude smaller than the total susceptibility at low temperature. In a paramagnetic sample, this term is suitable to describe diamagnetic impurities or Pauli paramagnetism for instance. In the present case, χ_0 takes into account the contribution of the sample holder and of the organic ligands on the surface of the nanoparticles.

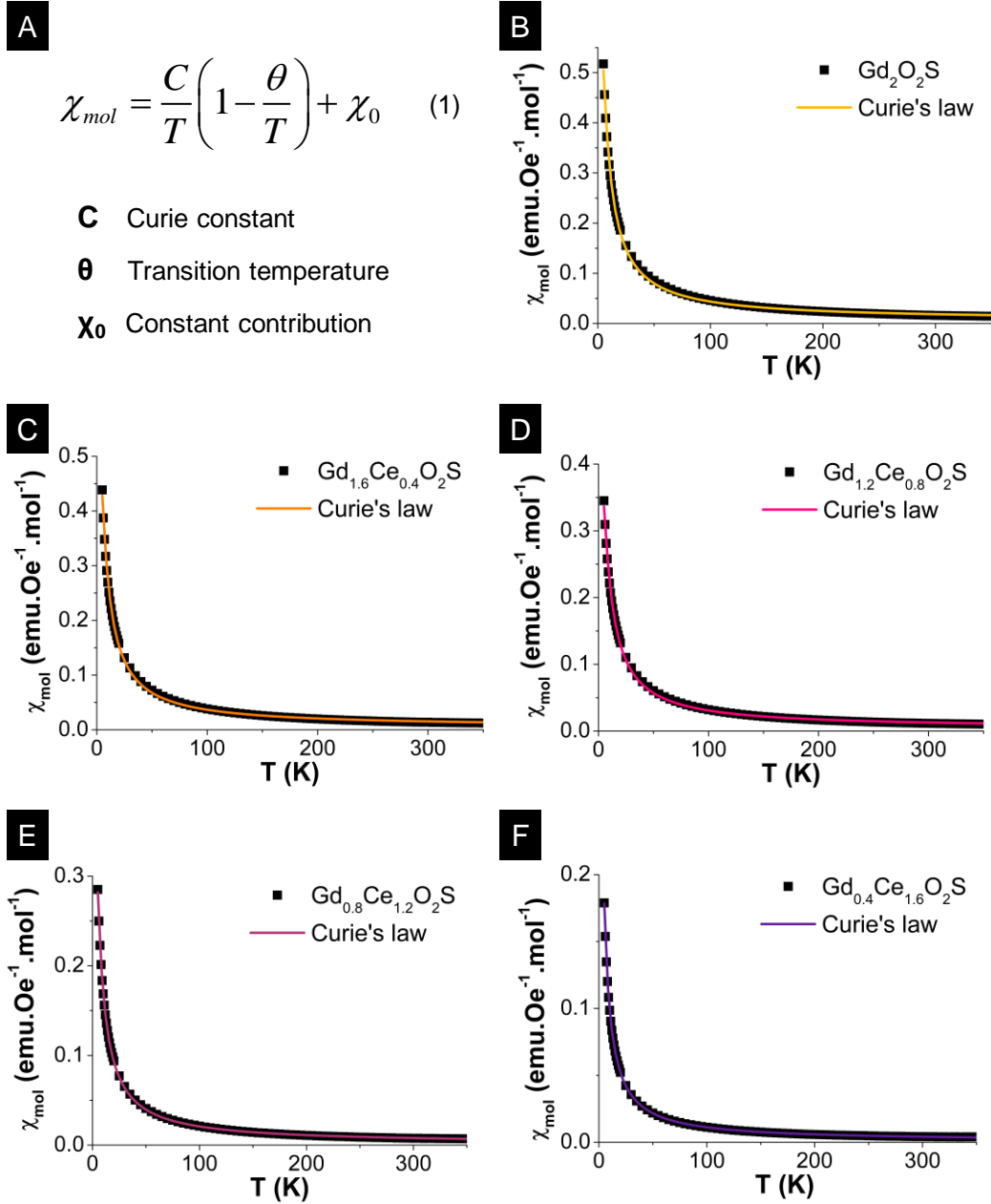


Figure 74: (A) Generalized Curie law. Fit of the ZFC molar susceptibility $\chi_{mol}(T)$ of the Gd_2O_2S (B), $Gd_{1.6}Ce_{0.4}O_2S$ (C), $Gd_{1.2}Ce_{0.8}O_2S$ (D), $Gd_{0.8}Ce_{1.2}O_2S$ (E) and $Gd_{0.4}Ce_{1.6}O_2S$ (F) nanoparticle samples by using the generalized Curie's law. The FC curves (data not shown) are indistinguishable for the ZFC ones.

Note that a good agreement between the Curie's law and the experimental behavior of our samples is found in the whole 5 - 350 K range measured.

The expression of the Curie constant C as defined in Figure 74A is given in Equation 2.

$$C = \frac{N\mu_B^2}{3k_B} g^2 J(J+1)$$

- N** Avogadro constant
 μ_B Bohr magneton
 k_B Boltzmann constant
g Landé factor
J Angular momentum quantum number

Equation 2: Expression of the Curie constant.

$$\mu_{eff} = g\sqrt{J(J+1)}$$

Equation 3: Expression of the effective magnetic moment.

From Equation 2 and Equation 3, the magnetic moment value can be approximated in function of the Curie constant's square root as reported in Equation 4.

$$\mu_{eff} = \sqrt{\frac{3k_B C}{N\mu_B^2}} \approx 2.83\sqrt{C}$$

Equation 4: Approximated expression of the effective magnetic moment, obtained with $N_A = 6.02 \times 10^{23} \text{ mol}^{-1}$, $k_B = 1.38 \times 10^{-16} \text{ erg/K}$ and $\mu_B = 9.27 \times 10^{-21} \text{ erg/G}$.

The above analysis within a simple model of paramagnetic impurities explains well the linear dependence of the square of the magnetic moment on composition (Figure 75).

Indeed, the square magnetic moment is proportional to the Curie constant and to the number of paramagnetic centers. The above linear dependence of $(\mu_{eff})^2$ vs. y is therefore consistent with a picture of solid solution of gadolinium and cerium atoms in the nanoparticles. In order to estimate precisely the magnetic moments, the raw data of susceptibility have been corrected by taking into account that around 30 wt% of the samples is composed of oleate ligands. We finally note that the linear dependence is observed up to $y = 60 \%$. This suggests that, below this concentration, the weight fraction of ligands is constant. This possibility could not be confirmed because of the limited availability of the TGA apparatus, so the above fraction was not measured for all samples. However, the repeatability of the morphology of the synthesized nanoparticles and the preliminary TGA data support this picture.

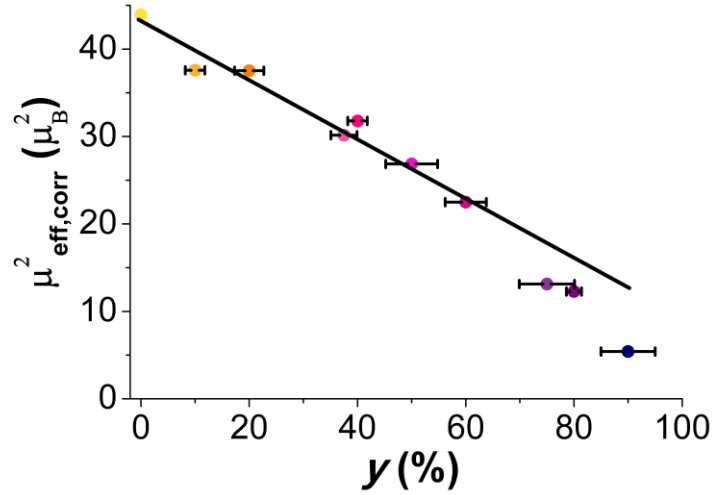


Figure 75: Dependence of the square magnetic moments of $\text{Gd}_{2(1-y)}\text{Ce}_{2y}\text{O}_2\text{S}$ nanoparticles on y . The raw values of magnetic susceptibility have been normalized by assuming that 30 wt% of the samples is made of oleate ligands. The vertical error bars are smaller than the symbols. The black line is a guide to the eye.

For concentrations above 60 %, one observes a sizable downward deviation of the data from the linear dependence. We attribute this deviation to the oxidation of Ce^{III} into Ce^{IV} ; as discussed in Chapter II, this phenomenon becomes increasingly important for $y > 80$ %, leading to the degradation of the nanoparticles. Because the $y = 100$ % sample ($\text{Ce}_2\text{O}_2\text{S}$ nanoparticles) is highly air-sensitive, no magnetic measurement has been conducted.

In conclusion, the $\text{Gd}_{2(1-y)}\text{Ce}_{2y}\text{O}_2\text{S}$ nanoparticles constitute a system with easily tunable magnetic properties *via* the composition and in a wide range ($y = 0 - 80$ %). Nevertheless, for $y > 60$ %, the oxidation of cerium is significant and leads to a decrease of the expected magnetic moment. In addition, the amount of ligands must be taken into account to accurately determine the magnetic properties of the nanocrystals.

IV.1.3. Size effects in lanthanide oxysulfide: the case of $\text{Gd}_2\text{O}_2\text{S}$

IV.1.3.1. Geometric magnetic frustration of $\text{Gd}_2\text{O}_2\text{S}$

In 1968, Ballestracci *et al.* established that gadolinium oxysulfide is paramagnetic with an antiferromagnetic transition at very low temperature.² They studied the $\text{Ln}_2\text{O}_2\text{S}$ bulk compounds by neutron diffraction and estimated the Néel temperature (T_N) of $\text{Gd}_2\text{O}_2\text{S}$ to be 5.7 K. In the paramagnetic domain, its Curie-Weiss temperature (T_{CW}) is -18 K. The magnetic moment of gadolinium atoms ($7.92 \mu_B$) was very close to these of the isolated paramagnetic ion ($7.94 \mu_B$). One notes that even with the correction on the magnetic moment

extracted from the Curie-Weiss fit of the $\text{Gd}_2\text{O}_2\text{S}$ nanoplates, $\mu_{\text{eff,corr}}$ ($6.63 \mu_{\text{B}}$) is still below the expected value for a paramagnetic isolated Gd^{III} cation and ($7.94 \mu_{\text{B}}$). This could be explained by the presence of water and inorganic impurities (sulfates, oxides), which are not crystalline but still alter the mass fraction of $\text{Gd}_2\text{O}_2\text{S}$.

In 2014, Biondo *et al.* revisited the properties of $\text{Ln}_2\text{O}_2\text{S}$ oxysulfides ($\text{Ln} = \text{Sm}, \text{Eu}, \text{Gd}$).³ For $\text{Gd}_2\text{O}_2\text{S}$, their values were close to those of Ballestracci *et al.*, i.e. $T_{\text{N}} = 5.8 \text{ K}$, $T_{\text{C}} = -21.3 \text{ K}$. They came to the conclusion that the compound is geometrically frustrated, for the lanthanide magnetic ions form a regular triangular lattice. To understand the concept of geometric frustration, imagine that the spin of one of the apex of the triangle is up-oriented. The spin of its first neighbor, the B apex, shall then be down-oriented. Because A and B have opposite spin orientations, the spin orientation of the apex C becomes undetermined (Figure 76B).

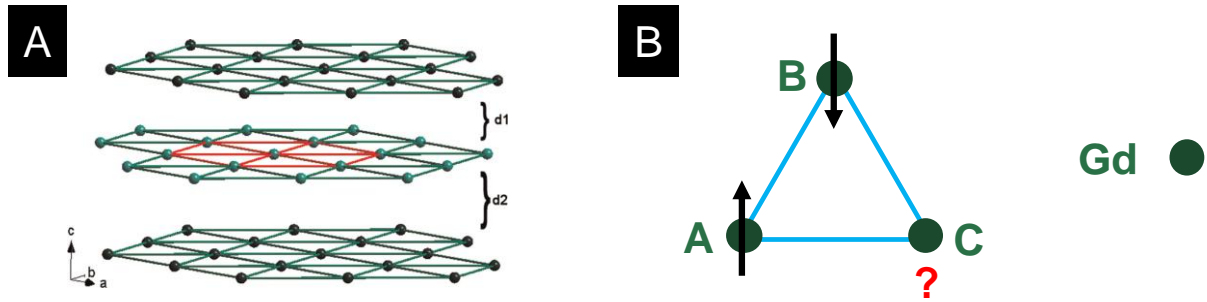


Figure 76: (A) The triangular lattice formed by the lanthanide ions in the $\text{Ln}_2\text{O}_2\text{S}$ $\{001\}$ planes (from Biondo *et al.*³). (B) Schematic illustration of the situation of geometric frustration for a triangular spin lattice with antiferromagnetic coupling.

Geometric magnetic frustration can be seen as individual spin clusters behaving independently and is characterized by the frustration index f defined by Ramirez: $f = |T_{\text{CW}}|/T_{\text{N}}$.⁴ In susceptibility measurements, it means that $\chi^{-1}(T)$ deviates from linearity for $T = T_{\text{N}}$ in a region where there is a free spin in a strongly interacting environment. In a classical antiferromagnet, the ordering (Néel) temperature is very close to the Curie-Weiss temperature and $f \approx 1$ (Figure 77A). If $f \ll 1$ ($T_{\text{N}} \ll |T_{\text{CW}}|$), the antiferromagnetic order is stabilized only at very low temperatures because of geometric frustration (Figure 77B).

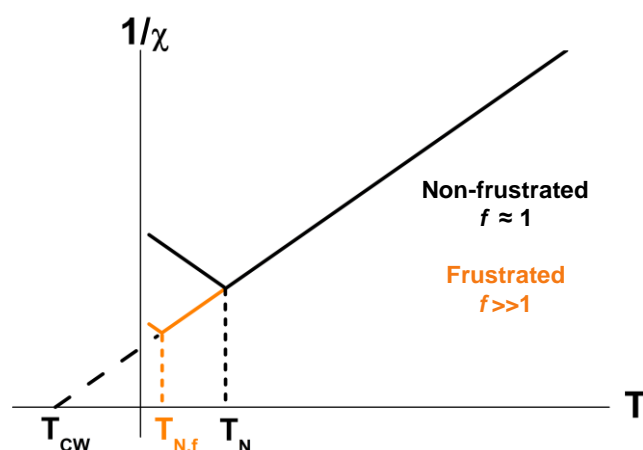


Figure 77: Schematic illustration of the inverse susceptibility curves for antiferromagnetic compounds without (black line) and with (orange line) geometric frustration.

According to this criterion, bulk $\text{Gd}_2\text{O}_2\text{S}$ is a frustrated magnet ($f > 3$). Nevertheless, the antiferromagnetic transition is still observable above around 5.5 K. A major question remains unaddressed: do $\text{Gd}_2\text{O}_2\text{S}$ nanoplates exhibit the same magnetic properties than the bulk phase?

IV.1.3.2. Comparison of bulk and nanoscaled $\text{Gd}_2\text{O}_2\text{S}$

IV.1.3.2.1. Bulk $\text{Gd}_2\text{O}_2\text{S}$ (with an impurity of Gd_2O_3)

In order to single out the effect of nanoscale on the magnetic properties of $\text{Gd}_2\text{O}_2\text{S}$, $\text{Gd}_2\text{O}_2\text{S}$ was synthesized in bulk form.

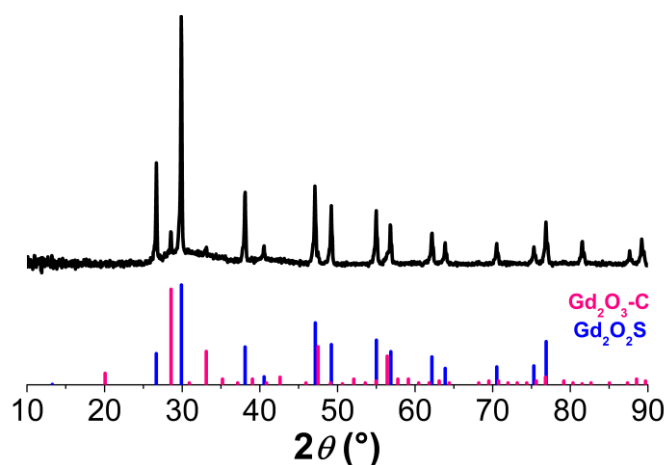


Figure 78: Powder XRD of bulk $\text{Gd}_2\text{O}_2\text{S}$ obtained by reducing $\text{Gd}_2(\text{SO}_4)_3 \cdot 8\text{H}_2\text{O}$ using H_2 . Cubic Gd_2O_3 was also identified as impurity. XRD pattern references are JCPDS files 26-1422 ($\text{Gd}_2\text{O}_2\text{S}$, blue) and 12-0797 (Gd_2O_3 -cubic, pink).

The simplest strategy that could be carried out to synthesize bulk $\text{Gd}_2\text{O}_2\text{S}$ in the laboratory was the reduction of the hydrated sulfate $\text{Gd}_2(\text{SO}_4)_3 \cdot 8\text{H}_2\text{O}$ by H_2 ([CL457], see experimental

section), as suggested by Biondo *et al.*³ The powder XRD pattern confirmed that the main product is Gd₂O₂S, but revealed the presence of the Gd₂O₃ cubic phase as an impurity (Figure 78).

Gd₂O₃ is paramagnetic and does not exhibit any transition above 2 K (complex AFM ordering around 1.6 K).^{5,6} Significant changes of behavior in the present temperature range must then be attributed to Gd₂O₂S. For this reason and considering that it is challenging to synthesize high-purity bulk Gd₂O₂S with any method, we continued the present study on the present sample.

IV.1.3.2.2. Size effect in Gd₂O₂S magnetic transition

Our VSM apparatus cannot easily stabilize temperature near 2 K. This is why the measures presented above were collected down to 5 K. In order to study the possibility of AFM transition at lower temperatures, additional magnetization measurements were carried out in the 2.0 - 100 K region using a commercial SQUID (superconducting quantum interference device) apparatus with the help of David Hrabovsky and Yanling Li.

The results obtained on bulk and nanoplate samples of Gd₂O₂S are presented in Figure 79. As before, the effective mass of the nanoparticles has been corrected by assuming an amount of ligands of 30 wt% and a constant contribution χ_0 estimated from the fit in the paramagnetic region between 20 K and 110 K.

The magnetic response of bulk Gd₂O₂S is consistent with previously reported results.¹⁻³ In particular, we found an AFM transition at 5.5 K, consistent with Biondo *et al.*³ Moreover, the extrapolation of $\chi_{\text{mol}}^{-1}(\text{T})$ from the paramagnetic region yields the Curie-Weiss constant $T_{\text{CW}} = -20.0$ K, which indicates the existence of geometric frustration in our bulk Gd₂O₂S sample, with $f = 20.0/5.5 \approx 3.6$. Besides, the Curie constant and the effective magnetic moment are close to the values of paramagnetic ion: $C = 7.60 \text{ emu Oe}^{-1} \text{ mol}^{-1} \text{ K}$ and $\mu_{\text{eff}} = 7.80 \mu_{\text{B}}$.

The paramagnetic response of the Gd₂O₂S nanoplates between 20 K and 110 K is similar to that of the bulk although slightly different constants ($C = 6.67 \text{ emu Oe}^{-1} \text{ mol}^{-1} \text{ K}$ and $\mu_{\text{eff}} = 7.30 \mu_{\text{B}}$) are obtained. However, **no magnetic transition was observed at low temperature above 2 K**. Accordingly, the Curie-Weiss constant, $T_{\text{CW}} = -4.2$ K, is significantly smaller as compared to that found in the bulk. A fit using the generalized Curie law is less appropriate in this region, which suggests that the behavior of the Gd₂O₂S nanoplates is not rigorously paramagnetic between 2 K and 20 K.

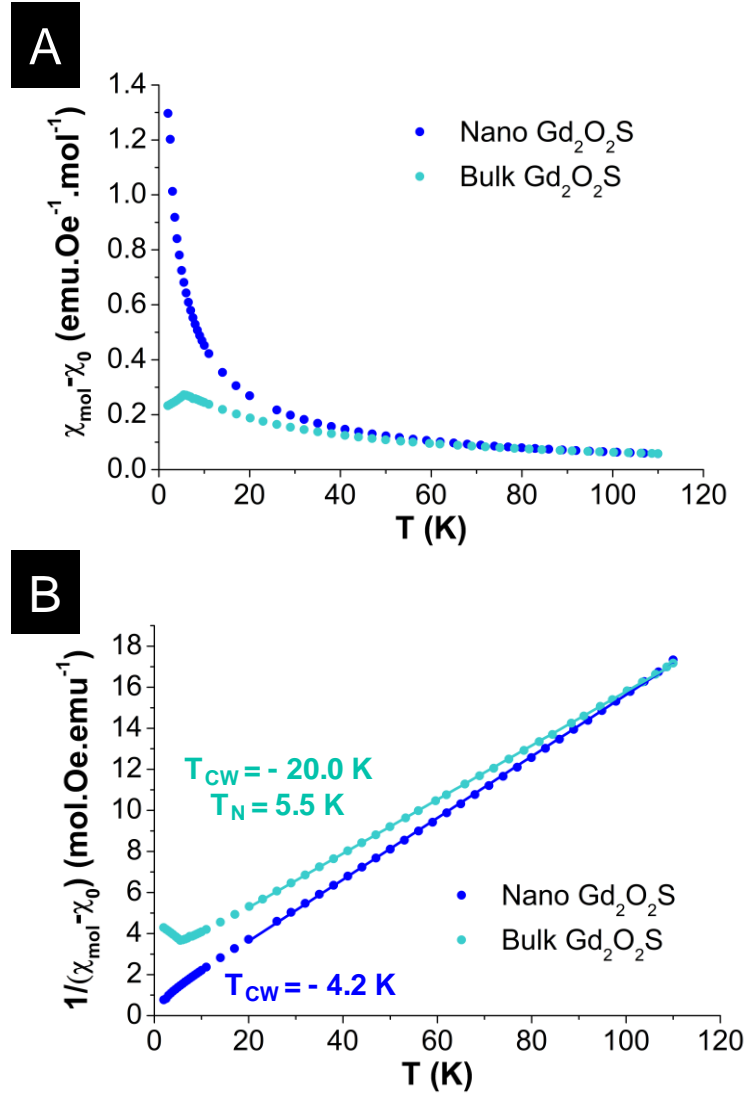


Figure 79: Comparison of the temperature dependence of the molar magnetic susceptibility (A) and of its inverse (B) for bulk and nanoplate [CL529] $\text{Gd}_2\text{O}_2\text{S}$ samples between 2 K and 110 K. The data refer to field-cooling (FC) measurements. ZFC data (not shown) are identical. For the nanoplates, the molar susceptibility was corrected by 30 wt% of ligands and χ_0 as explained in the text. For bulk samples, no correction is needed and $\chi_0 = 0$.

To the best of our knowledge, the size effect observed above was neither reported nor envisaged for oxysulfide nanoparticles. It may constitute a rare illustration of the stability of long-range order in a mesoscopic system. Although, we have no reliable explanation of the suppression of AFM order in the nanoplate, we may attempt to put forward some hypotheses. The electronic and properties of very thin compounds (one to a few layers) are known to differ from bulk compounds. Specifically, the effective reduction of dimensionality is known to destabilize long-range magnetic order due to thermal fluctuations as originally proposed by T. M. Rice.⁷

The surface can also play a crucial role. We estimate that $\sim 20\%$ of the gadolinium atoms are at the $\{100\}$ surfaces, a very large value.

IV.1.4. Conclusion

The present investigation of the magnetic properties of $(\text{Gd,Ce})_2\text{O}_2\text{S}$ nanoparticles confirmed the expectation that the magnetic properties can be tuned by varying the relative proportion of Gd and Ce ions, characterized by high and low magnetic moments, respectively. An unexpected result is the absence of AFM order in the $\text{Gd}_2\text{O}_2\text{S}$ nanoplates above 2 K, while bulk crystals exhibit ordering temperatures at around 5.5 K. We argue that this size effect could be related to geometric frustration but needs further investigation to be quantitatively explained. Owing to the simple crystal structure of the $\text{Gd}_2\text{O}_2\text{S}$ nanoplates, we argue that the present result may foster our current understanding of the fascinating phenomenon of geometric frustration which remains little understood.

IV.2. Optical properties of (Gd,Ce)₂O₂S bimetallic nanoparticles

Note: This whole section (down to “End of quote”) is a quote adapted from “*Bandgap Engineering from Cation Balance: the Case of Lanthanide Oxysulfide Nanoparticles*” from Larquet, C.; Nguyen, A.-M.; Paulatto, L.; Sassoie, C.; Selmane, M.; Lecante, P.; Maheu, C.; Géantet, C.; Cardenas, L.; Chanéac, C.; Gauzzi, A.; Sanchez, C.; Carenco, S. to be submitted soon.

IV.2.1 Optical properties – Ln/Ce substitution and bandgap evolution

IV.2.1.1. Absorption of Gd_{2(1-y)}Ce_{2y}O₂S nanoparticles

In a previous work, we reported the synthesis of Ce₂O₂S nanoparticles that are unstable when exposed to air. However, we showed that it is possible to obtain a large range of cerium-containing Gd_{2(1-y)}Ce_{2y}O₂S nanoparticles that are stable in air.⁸ Here, cerium loading is defined as $y = n_{\text{Ce}} / (n_{\text{Ce}} + n_{\text{Gd}})$ where n refers to the initial metallic precursor quantity in mol. The Gd:Ce ratios of the precursors introduced at the beginning of the reaction and measured by energy dispersive X-ray spectroscopy (EDX) on the isolated product were consistent (Chapter II, Figure 14).

The substitution of Gd^{III} for Ce^{III} strongly affects light absorption of the Gd_{2(1-y)}Ce_{2y}O₂S nanoparticles powders, from white ($y = 0$ %) to brown ($y = 70 - 90$ %). The $F(R)$ spectra of the Gd_{2(1-y)}Ce_{2y}O₂S nanoparticles are plotted in Figure 81A. The $F(R)$ function ($F(R) = (1 - R)^2 / 2R$ where R is the reflectance) is linearly related to the extinction coefficient of the material and thus to its absorption properties. Note that the range of wavelengths where light is absorbed increases with Ce fraction. In agreement with the change of colors observed in the powders (Figure 80), Gd₂O₂S absorbs only in the UV region while Ce-rich nanoparticles absorb a large fraction of the visible light (brown powders).

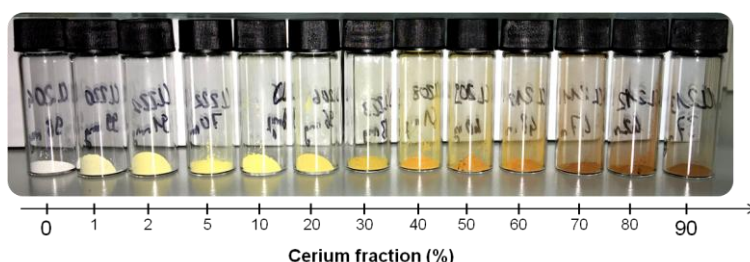


Figure 80: Picture showing the change in color caused by the Gd/Ce substitution for several compositions of Gd_{2(1-y)}Ce_{2y}O₂S nanoparticles stored in air.

Although this evolution is gradual, two regimes can be distinguished. In the doping regime ($0\% < y \leq 2\%$), two inflexion points are observed with a smooth absorption increase before 500 nm and a sharp increase around 270 nm, close to the absorption step of Gd₂O₂S. In the

solid solution regime ($y \geq 5\%$), only the smooth increase of absorption is observed and this feature shifts towards higher wavelengths.

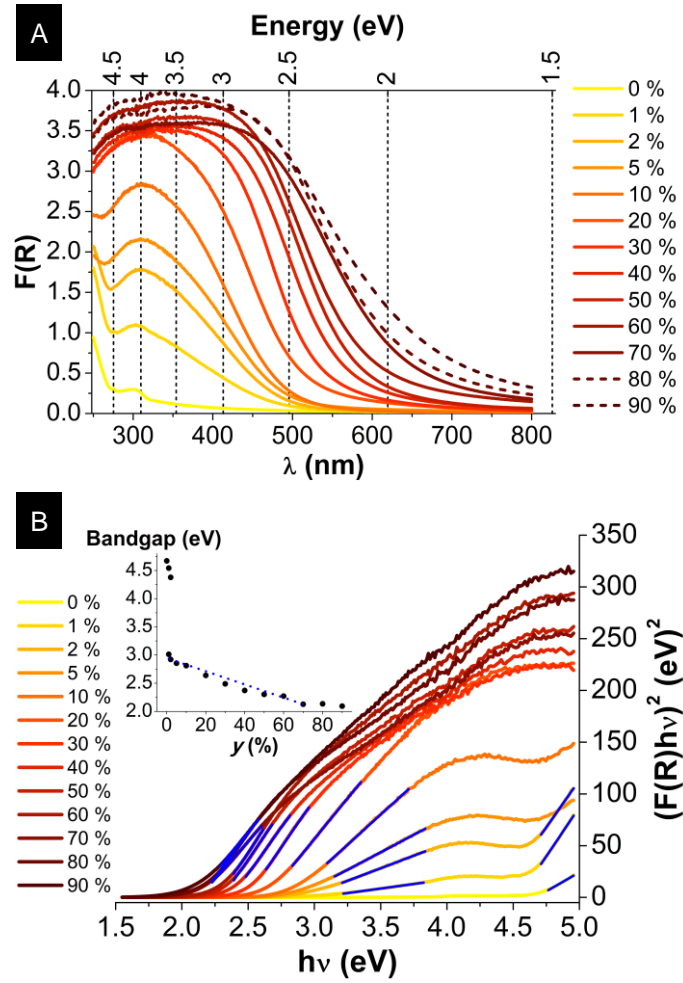


Figure 81: (A) $F(R)$ spectra obtained from UV-visible diffuse reflectance of $\text{Gd}_{2(1-y)}\text{Ce}_{2y}\text{O}_2\text{S}$ nanoparticles for y in the 0 - 90 % range. Samples $y = 80\%$ and $y = 90\%$ are indicated by dashed lines because these samples are unstable in air. (B) Evolution of the $(F(R)h\nu)^2$ vs. $h\nu$ curves as a function of composition. Dark blue lines are a linear extrapolation of the data. Inset: dependence of the optical bandgap extracted from the above curves on Ce-composition, y , for the whole series of $\text{Gd}_{2(1-y)}\text{Ce}_{2y}\text{O}_2\text{S}$ nanoparticles. The blue dashed line is a guide to the eye.

IV.2.1.2. Bandgap of $\text{Gd}_{2(1-y)}\text{Ce}_{2y}\text{O}_2\text{S}$ nanoparticles

Thanks to the work by Kubelka, Munk and later analyzed by Tauc *et al.*,^{9,10} it is possible to extract the value of the bandgap from the reflectance spectra using the $F(R)$ function (Figure 81B). This model is parameterized by a power n which depends on the type of bandgap. Then the extrapolation of the linear portion of the $(F(R)h\nu)^n$ vs. $h\nu$ curves enables to estimate the bandgap.

In a first report, Mikami *et al.* suggested that the bandgap of $\text{Ln}_2\text{O}_2\text{S}$ compounds is indirect.^{11,12} In this case, $n = 1/2$. However, in recent reports on $\text{Ln}_2\text{O}_2\text{S}$ compounds, it was argued that the bandgap is direct, which corresponds to $n = 2$.^{13,14} Here, the colors of the powders are in agreement with the latter picture, as the assumption $n = 1/2$ yielded unphysical values of 1.2 - 4.1 eV. Thus, hereafter we assume a picture of direct bandgap for the $\text{Gd}_{2(1-y)}\text{Ce}_y\text{O}_2\text{S}$ nanoparticles.

The analysis of the $F(R)$ spectra of $\text{Gd}_{2(1-y)}\text{Ce}_y\text{O}_2\text{S}$ nanoparticles is presented in Figure 81B. For $y > 5\%$ (solid solution regime), the linear zone on the $(F(R)h\nu)^2$ curve gives a bandgap below 3 eV. For the two compounds in the range $0\% < y < 5\%$ (doping regime), two values were extracted from the curves: (i) one related to cerium insertion (2.9 – 3.1 eV) and (ii) the other close to the bandgap of $\text{Gd}_2\text{O}_2\text{S}$ nanoparticles (4.3 - 4.7 eV). For these two compounds, the aforementioned does not provide a unique value. However, the strong effect of cerium on the optical properties is evident from our data.

Figure 81B shows the bandgaps extracted from the absorption spectra in the high energy region for $y = 0, 1$ and 2% (doping regime). The dark blue line indicates a linear trend for $y > 2\%$ (solid solution regime), although the reliability of the measurements obtained for $y = 80\%$ and $y = 90\%$ is questionable because of the limited stability of Ce-rich nanoparticles in air.⁸

The shift of bandgap is remarkably large (2.6 eV) considering that the crystal structure is preserved. As shown in a previous work,⁸ the only structural change consists in a 1.5 % reduction of lattice parameter a , as expected from Vegard law's.

The bandgap of the nanocrystals is tunable between 3.0 eV and 2.1 eV by adjusting composition in the solid solution regime. To some extent, in the high energy region, the bandgap high is also tunable in the doping regime (Figure 81B), even if it is much more sensitive to the composition of the nanoparticle, which leads to the appearance of a second absorption phenomenon at higher wavelengths. We can suspect that the mixed valence of cerium⁸ can be at least partially responsible for the strong absorption in the visible range but so far, we have no experimental evidence to support this hypothesis.

IV.2.1.3. Comparison with other class of compounds

Bandgap engineering enabling large changes of absorption properties has been discussed for many materials. However these changes typically require significant structural changes. In composite semi-conductors, the gap energy variation is related to the interatomic distance.

That is why bandgap shifts can be observed as a consequence of anionic or cationic substitution. The more the structure is modified (variation of the interatomic distances), the higher the expected shift. For example, the anionic substitution was investigated in hybrid lead-halide perovskites, extensively studied for their promising properties for solar cells applications.¹⁵ The substitution of bromine by iodine in $(\text{CHA})_2\text{PbBr}_{4(1-x)}\text{I}_{4x}$ (CHA = cyclohexylammonium) is accompanied by a bandgap decrease of ~ 0.7 eV between $(\text{CHA})_2\text{PbBr}_4$ and $(\text{CHA})_2\text{PbI}_4$ but with significant structural modifications.¹⁶ Solid solutions of $\text{CdS}_x\text{Se}_{1-x}$ are also known to exhibit large absorption shifts.¹⁷ In the case of oxysulfides, $\text{Sm}_2\text{Ti}_2\text{O}_7$ and $\text{Sm}_2\text{Ti}_2\text{O}_5\text{S}_2$ show a bandgap variation of $\Delta E_g \approx 1.6$ eV but no solid solution can be formed.¹⁸ The substitution of two cations also significantly changes the bandgap: 3.8 eV for ZnS, 2.5 eV for CdS and 2.1 eV for α -HgS.¹⁹ In addition to strong variations of lattice parameter in isostructural solid solutions, the substitution of zinc by cadmium in $\text{Zn}_{1-x}\text{Cd}_x\text{S}$ drives a cubic blende ZnS to hexagonal CdS structural transition.²⁰

In conclusion, to the best of our knowledge, the present system is unique because the cationic substitution is responsible for an important absorption shift with neither structural nor morphological modifications. In view of this promising result, we investigated whether Ce-substitution constitutes an exception or other substitutions would give similar results.

IV.2.1.4. Comparison with Pr and Eu cation balance

We have chosen $\text{Ce}_2\text{O}_2\text{S}$ among all $\text{Ln}_2\text{O}_2\text{S}$ compounds because it is the only low bandgap semiconductor. The insertion of other lanthanides is expected to have less effect on the absorption. Also, the question arises whether the insertion of Ce in other $\text{Ln}_2\text{O}_2\text{S}$ compounds may lead to absorption shifts similar to those observed in $\text{Gd}_{2(1-y)}\text{Ce}_{2y}\text{O}_2\text{S}$ nanoparticles.

Other bimetallic nanoparticles were synthesized to investigate this effect. We selected Pr and Eu, the former because of its cation size (1.20 Å) close to Ce (1.21 Å), the latter because of its two oxidation states (here, +II and +III). Using $\text{Ce}(\text{acac})_3 \cdot x\text{H}_2\text{O}$, $\text{Pr}(\text{acac})_3 \cdot x\text{H}_2\text{O}$, $\text{Eu}(\text{acetate})_3 \cdot x\text{H}_2\text{O}$ and $\text{Gd}(\text{acac})_3 \cdot x\text{H}_2\text{O}$ as lanthanide precursors, nanoparticles of $\text{Pr}_2\text{O}_2\text{S}$ (light green powder), $\text{Eu}_2\text{O}_2\text{S}$ (white powder), $\text{Gd}_{1.8}\text{Pr}_{0.2}\text{O}_2\text{S}$ (white powder), $\text{Gd}_{1.8}\text{Eu}_{0.2}\text{O}_2\text{S}$ (white powder), $\text{Pr}_{1.8}\text{Ce}_{0.2}\text{O}_2\text{S}$ (orange powder), and $\text{Eu}_{1.8}\text{Ce}_{0.2}\text{O}_2\text{S}$ (yellow powder) were obtained. The $F(R)$ spectra of these bimetallic nanoparticles are presented in Figure 82.

For $\text{Gd}_{1.8}\text{Ln}_{0.2}\text{O}_2\text{S}$ compounds (Ln = Ce, Pr, Eu), the most significant effect on the absorption is obtained with cerium (Figure 82A). For $\text{Gd}_{1.8}\text{Pr}_{0.2}\text{O}_2\text{S}$, two absorption edges are observed at 280 nm close to $\text{Gd}_2\text{O}_2\text{S}$ edge and 320 nm closer to the absorption edge of $\text{Pr}_2\text{O}_2\text{S}$ (around

350 nm, Figure 82B and C). In the case of europium, the edge is shifted to lower wavelengths (below 250 nm) and a broad peak on the curve grows around 340 nm (Figure 82B).

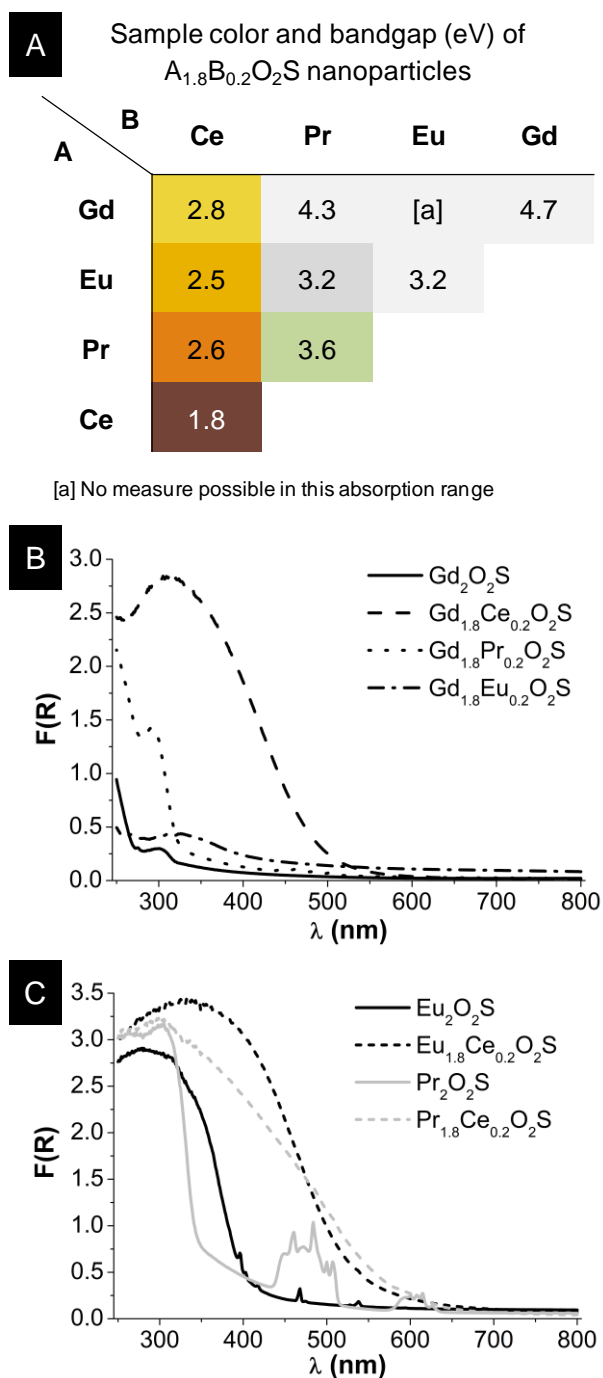


Figure 82: (A) Sample colors and bandgap values estimated using the model proposed by Tauc *et al.* for $A_{1.8}B_{0.2}O_2S$ nanoparticles ($n_B / (n_A + n_B) = 10\%$).¹⁰ $F(R)$ spectra of (B) gadolinium-based bimetallic $Gd_{1.8}Ln_{0.2}O_2S$ oxysulfide nanoparticles, with $Ln = Ce, Pr$ and Eu ; (C) Eu_2O_2S , $Eu_{1.8}Ce_{0.2}O_2S$, Pr_2O_2S and $Pr_{1.8}Ce_{0.2}O_2S$ nanoparticles $F(R)$ spectra.

Inserting cerium in Pr_2O_2S and Eu_2O_2S leads to similar effects on light absorption than Gd_2O_2S ($Ln_{1.8}Ce_{0.2}O_2S$ compounds, Figure 82B). The nanoparticles absorb higher

wavelengths as the bandgap decreases. Moreover, the absorption peaks specific to transitions between $4f$ energy levels of the monometallic compounds are no longer present in the bimetallic compounds whose absorption curves are smooth.

The bandgap shift caused by the insertion of cerium in gadolinium oxysulfide is by far the largest. Cerium also changes the bandgap of $\text{Eu}_2\text{O}_2\text{S}$ and $\text{Pr}_2\text{O}_2\text{S}$ and favors absorption at larger wavelengths. These results demonstrate that the effect of cerium on the bandgap is not specific to gadolinium compounds. Instead, the incorporation of cerium allows tuning the bandgap of at least two other $\text{Ln}_2\text{O}_2\text{S}$ compounds ($\text{Ln} = \text{Pr}$ or Eu).

Cerium appeared to be unique among the lanthanide investigated. To explain the bandgap nature and its huge sensitivity of the optical properties to the Ce concentration, we underwent an in-depth modeling study.

IV.2.2 Investigation of the bandgap nature using density functional calculations

DFT calculations were performed in order to understand the unexpected direct nature of the bandgap. After a series of works, Mikami *et al.* concluded in 2006 from DFT that the bandgaps of $\text{Ln}_2\text{O}_2\text{S}$ (and $\text{Ce}_2\text{O}_2\text{S}$ in particular) were indirect.^{11,12} However, we suggest that the calculations accuracy would be significantly improved by including in valence the $4f$ electrons of the lanthanide metals that are of great importance for their electronic properties. Furthermore, to be as close as possible to nanoplates depicted in Chapter III (S:Gd ratio), we also performed DFT on a specific “slab” geometry. Here, capping agents that stabilize the surfaces of the nanoplate were not considered here because we supposed that only the crystal (core of the nanoplate) was responsible for the optical properties. Yet, the nature of the ligands may slightly influence the band structure.

The calculations were only focused on three layers of the studied $\text{Gd}_2\text{O}_2\text{S}$ or $\text{Ce}_2\text{O}_2\text{S}$ oxysulfide, that can be stabilized by hydrogen atoms instead of sulfur atoms when needed (sulfur-free $\{001\}$ surfaces). This model structure mimics the absence of sulfur in the external layers (replaced by oleate ligands in reality) and avoids dangling electronic states that make the system metallic (see in the experimental section the details on the DFT+U calculations).

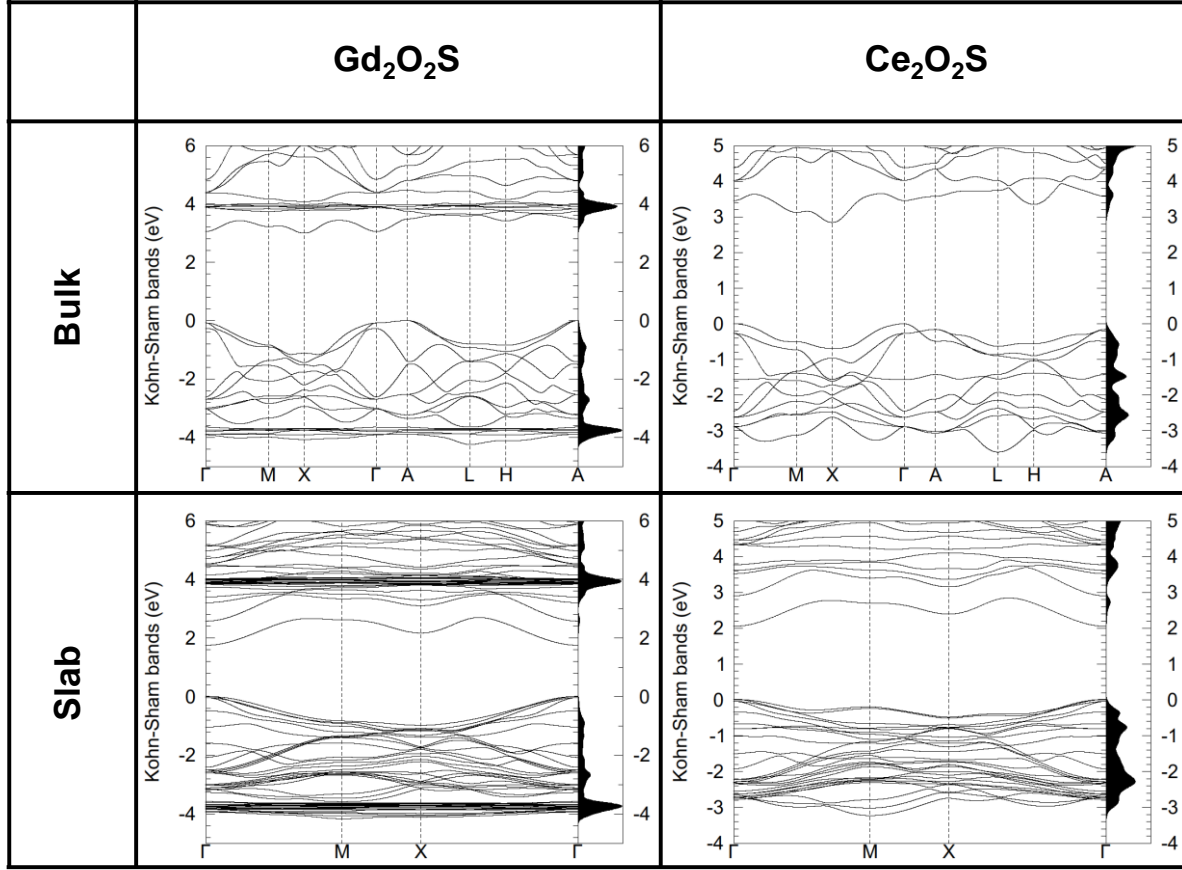


Figure 83: Band structures of $\text{Ln}_2\text{O}_2\text{S}$ ($\text{Ln} = \text{Gd}, \text{Ce}$) in the bulk (top) or for the slab geometry (bottom).

The band structures of the bulk phases of $\text{Gd}_2\text{O}_2\text{S}$ and $\text{Ce}_2\text{O}_2\text{S}$ are presented in Figure 83. Interestingly, we found that the bandgap is indirect even if the $4f$ electrons of the lanthanides are treated as valence electrons. Nevertheless, there are significant differences with the work of Mikami *et al.* on $\text{Ce}_2\text{O}_2\text{S}$ and the bandgap transition is different.¹¹

More importantly, the slab geometry has a great influence on the band structure for both $\text{Gd}_2\text{O}_2\text{S}$ and $\text{Ce}_2\text{O}_2\text{S}$ (Figure 83, bottom) as it reduces the symmetry of the system. Moreover, the bandgap of the slab is direct in both cases. We can thus conclude that the nanoplate morphology (anisotropy, low dimensions) explains the variations of electronic properties. It also reconciles our optical measurements and the DFT calculations on a system composed by $\text{Ln}_2\text{O}_2\text{S}$ nanoparticles.

IV.2.3. Conclusion

$(\text{Gd,Ce})_2\text{O}_2\text{S}$ nanoparticles exhibit colors from white to brown over the whole composition range. Bandgap engineering is thus possible and values varying from 4.7 eV in $\text{Gd}_2\text{O}_2\text{S}$ to 2.1 eV in $\text{Gd}_{0.6}\text{Ce}_{1.4}\text{O}_2\text{S}$ can be obtained without major structural modifications. The above

large changes of bandgap correspond to a slight lattice expansion. Surprisingly, the bandgap of the nanoparticles is direct, as validated by density functional theory, while that of the bulk is indirect. This result may suggest applications of these nanoparticles in solar cells. The fine control of the bandgap over a wide range, solely triggered by the cation ratio, is unique in the field of bandgap engineering. The simple idea of using suitable chemical substitutions producing minor structural changes should inspire the design of other bimetallic nanoscaled compounds which may be promising especially in the field of visible light photocatalysis.

End of quote

References

- (1) Quezel, G.; Ballestracci, R.; Rossat-Mignod, J. Propriétés Magnétiques Des Oxysulfures de Terres Rares. *J. Phys. Chem. Solids* **1970**, *31* (4), 669–684.
- (2) Ballestracci, R.; Bertaut, E. F.; Quezel, G. Étude Par Diffraction Neutronique et Mesures Magnétiques Des Oxysulfures de Terres Rares $\text{RE}_2\text{O}_2\text{S}$. *J. Phys. Chem. Solids* **1968**, *29* (6), 1001–1014.
- (3) Biondo, V.; Sarvezuk, P. W. C.; Ivashita, F. F.; Silva, K. L.; Paesano, A.; Isnard, O. Geometric Magnetic Frustration in $\text{RE}_2\text{O}_2\text{S}$ Oxysulfides (RE=Sm, Eu and Gd). *Mater. Res. Bull.* **2014**, *54*, 41–47.
- (4) Ramirez, A. P. Strongly Geometrically Frustrated Magnets. *Annu. Rev. Mater. Sci.* **1994**, *24* (1), 453–480.
- (5) Giaque, W. F.; Stout, J. W. The Magnetic Flux Distribution When a Cylinder of Constant Permeability Is Placed in a Homogeneous Field. The Magnetic Susceptibility of Gadolinium Oxide at Low Temperatures. *J. Am. Chem. Soc.* **1939**, *61* (6), 1384–1393.
- (6) Child, H. R.; Moon, R. M.; Raubenheimer, L. J.; Koehler, W. C. The Paramagnetic Form Factor of Gadolinium. *J. Appl. Phys.* **1967**, *38* (3), 1381–1383.
- (7) Rice, T. M. Superconductivity in One and Two Dimensions. *Phys. Rev.* **1965**, *140* (6A), A1889–A1891.
- (8) Larquet, C.; Nguyen, A.-M.; Ávila-Gutiérrez, M.; Tinat, L.; Lassalle-Kaiser, B.; Gallet, J.-J.; Bournel, F.; Gauzzi, A.; Sanchez, C.; Carenco, S. Synthesis of $\text{Ce}_2\text{O}_2\text{S}$ and $\text{Gd}_2(1-y)\text{Ce}_2y\text{O}_2\text{S}$ Nanoparticles and Reactivity from in Situ X-Ray Absorption Spectroscopy and X-Ray Photoelectron Spectroscopy. *Inorg. Chem.* **2017**, *56* (22), 14227–14236.
- (9) Kubelka, P.; Munk, F. Ein Beitrag Zur Optik Der Farbanstriche. *Zeitschrift für Tech. Phys.* **1931**, *12*, 593–601.
- (10) Tauc, J.; Grigorovici, R.; Vancu, A. Optical Properties and Electronic Structure of Amorphous Germanium. *Phys. status solidi* **1966**, *15* (2), 627–637.
- (11) Mikami, M.; Nakamura, S. Electronic Structure of Rare-Earth Sesquioxides and Oxysulfides. *J. Alloys Compd.* **2006**, *408–412*, 687–692.
- (12) Mikami, M.; Oshiyama, A. First-Principles Band-Structure Calculation of Yttrium Oxysulfide. *Phys. Rev. B* **1998**, *57* (15), 8939–8944.
- (13) Som, S.; Choubey, A.; Sharma, S. K. Spectral and Trapping Parameters of Eu^{3+} in $\text{Gd}_2\text{O}_2\text{S}$ Nanophosphor. *J. Exp. Nanosci.* **2015**, *10* (5), 350–370.
- (14) Bagheri, A.; Rezaee Ebrahim Saraee, K.; Shakur, H. R.; Zamani Zeinali, H. Synthesis and Characterization of Physical Properties of $\text{Gd}_2\text{O}_2\text{S}:\text{Pr}^{3+}$ Semi-Nanoflower Phosphor. *Appl. Phys. A Mater. Sci. Process.* **2016**, *122* (5), 1–8.
- (15) Jeon, N. J.; Noh, J. H.; Yang, W. S.; Kim, Y. C.; Ryu, S.; Seo, J.; Seok, S. I. Compositional Engineering of Perovskite Materials for High-Performance Solar Cells. *Nature* **2015**, *517* (7535), 476–480.
- (16) Ye, H.-Y.; Liao, W.-Q.; Hu, C.-L.; Zhang, Y.; You, Y.-M.; Mao, J.-G.; Li, P.-F.; Xiong, R.-G. Bandgap Engineering of Lead-Halide Perovskite-Type Ferroelectrics. *Adv. Mater.* **2016**, *28* (13), 2579–2586.
- (17) Zhou, R.; Wan, L.; Niu, H.; Yang, L.; Mao, X.; Zhang, Q.; Miao, S.; Xu, J.; Cao, G. Tailoring Band Structure of Ternary $\text{CdS}_x\text{Se}_{1-x}$ Quantum Dots for Highly Efficient Sensitized Solar Cells. *Sol. Energy Mater. Sol. Cells* **2016**, *155*, 20–29.
- (18) Ishikawa, A.; Takata, T.; Matsumura, T.; Kondo, J. N.; Hara, M.; Kobayashi, H.; Domen, K. Oxysulfides $\text{Sm}_2\text{Ti}_2\text{S}_2\text{O}_5$ as Stable Photocatalysts for Water Oxidation and Reduction under Visible-Light Irradiation. *J. Am. Chem. Soc.* **2002**, *124* (8), 13547.

- (19) Strehlow, W. H.; Cook, E. L. Compilation of Energy Band Gaps in Elemental and Binary Compound Semiconductors and Insulators. *J. Phys. Chem. Ref. Data* **1973**, 2 (1), 163–200.
- (20) Li, Q.; Meng, H.; Zhou, P.; Zheng, Y.; Wang, J.; Yu, J.; Gong, J. Zn_{1-x}Cd_xS Solid Solutions with Controlled Bandgap and Enhanced Visible-Light Photocatalytic H₂-Production Activity. *ACS Catal.* **2013**, 3 (5), 882–889.

Part II

d-Block Transition Metal Oxysulfide Nanoparticles

Chapter V

The synthesis of bulk and nanoscaled transition metal oxysulfides: a burgeoning challenge

Table of content

V.1. Bulk phases and thin films	163
V.1.1. First phases: ZrOS, HfOS, SbOS ₂ and Bi ₂ O ₂ S (1907 – 1990)	163
V.1.2. Recent works on transition metal oxysulfides (1990 – 2018)	164
V.1.2.1. Crystalline transition metal oxysulfides	164
V.1.2.1.1. Copper oxysulfide Cu ₂ O _{1-x} S _x	164
V.1.2.1.2. Zinc oxysulfide ZnO _{1-x} S _x	165
V.1.2.1.3. Molybdenum oxysulfides	165
V.1.2.2. Amorphous titanium, tungsten and molybdenum oxysulfides	165
V.1.2.2.1. Titanium	166
V.1.2.2.2. Tungsten	166
V.1.2.2.3. Molybdenum	167
V.1.2.3. Conclusion: application perspectives and composition limit	168
V.1.3. Toward more complex structures: quaternary oxysulfides and selective bonding..	169
V.1.3.1. Selective and unselective bonding in quaternary structures	169
V.1.3.2. Quaternary oxysulfides: a large catalogue of compositions	170
V.1.3.3. Quinary oxysulfides	174
V.1.4. Conclusion	175

V.2. Transition metal oxysulfides nanoparticles	177
V.2.1. Challenging synthesis, tricky characterization	177
V.2.2. Amorphous and crystalline cobalt oxysulfide	179
V.2.3. Crystalline $\text{ZnO}_{1-x}\text{S}_x$ nanoparticles	180
V.2.4. Other proposed transition metal oxysulfides	182
V.3. Conclusion.....	183
References	185

V.1. Bulk phases and thin films

Note: This chapter I is an excerpt from the following review titled “*Metal Oxysulfides: From Bulk Compounds to Nanomaterials*”, by C. Larquet and S. Carenco, to be submitted soon.

V.1.1. First phases: ZrOS, HfOS, SbOS₂ and Bi₂O₂S (1907 – 1990)

Metal oxysulfides containing one single transition metal are much scarcer than lanthanide and actinide oxysulfides. Until the end of the 1990's, reports of transition metal oxysulfides were isolated occurrences because the oxysulfide phases were regarded as undesirable intermediates in the sulfidation of oxides. Yet, using H₂S on oxides, Hauser had already prepared two oxysulfides of tetravalent metal, namely ZrOS and ThOS based on their composition in 1907.¹ Hauser indicated that the zirconium and thorium oxysulfides were pyrophoric. In 1948, McCullough *et al.* established the structure of cubic ZrOS² prepared similarly to Hauser and in 1962, Jellinek described a new tetragonal form with the same composition.³ Cubic HfOS (isostructural to cubic ZrOS) was first identified by Stocks *et al.* in 1980⁴ and prepared as a pure phase by Eisman *et al.* in 1982.⁵ The latter were also able to prepare solid solutions of zirconium and hafnium oxysulfides Zr_{1-x}Hf_xOS (0 ≤ x ≤ 1) such as Zr_{0.25}Hf_{0.75}OS and Zr_{0.75}Hf_{0.25}OS.

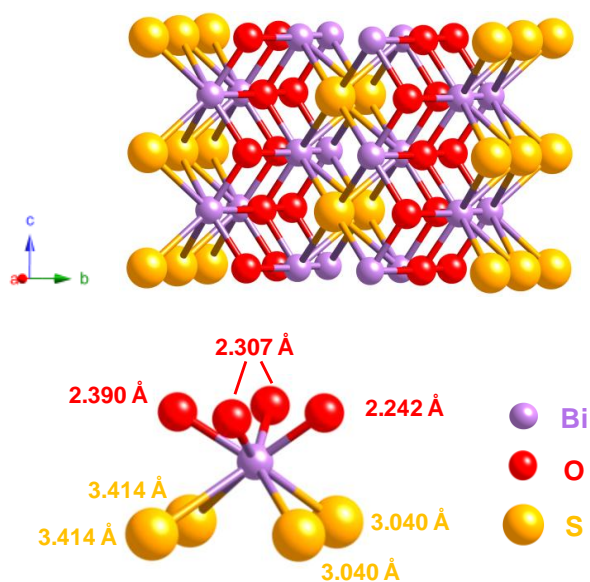


Figure 84: Structure of Bi₂O₂S (JCPDS 10-2907) and bismuth coordination in the solid.

In 1967, Kupčák reported the kermesite's structure.⁶ The antimony-based compound Sb₂OS₂ is a rare crystalline natural oxysulfide mineral, which can form thanks to a partial oxidation of stibnite Sb₂S₃.

A decade after the discovery of $\text{Bi}_2\text{O}_2\text{Se}$,⁷ Koyama *et al.* published in 1984 a study about the combination of bismuth with chalcogens. They obtained the ternary oxysulfide $\text{Bi}_2\text{O}_2\text{S}$ from Bi_2O_3 and Bi_2S_3 via a hydrothermal synthesis.⁸ The $\text{Bi}_2\text{O}_2\text{S}$ structure differs from $\text{Ln}_2\text{O}_2\text{S}$ (Ln = lanthanide), as it crystallizes in the $Pn\bar{n}m$ space group.

The coordination number of the bismuth is eight: bismuth is bound to four atoms of oxygen and four atoms of sulfur (Figure 84). In comparison with $\text{Ln}_2\text{O}_2\text{S}$ in which Ln forms four Ln-O and three Ln-S bonds, bismuth-oxygen bonds are in the same length range (between 2.2 Å and 2.5 Å) but bismuth-sulfur bonds are significantly longer (3.4 Å for $\text{Bi}_2\text{O}_2\text{S}$, < 3 Å for $\text{Ln}_2\text{O}_2\text{S}$). Further works showed that bismuth can form several oxysulfides, leading to superconductive $\text{Bi}_4\text{O}_4\text{S}_3$ ⁹ (containing both sulfide and sulfate ions) and to $\text{Bi}_9\text{O}_{7.5}\text{S}_6$.¹⁰

V.1.2. Recent works on transition metal oxysulfides (1990 – 2018)

For a long time, ternary oxysulfides $\text{M}_x\text{O}_y\text{S}_z$ were limited to lanthanides, actinides and bismuth. Despite the presence of numerous metals in quaternary oxysulfides, the transition metals did not give any crystalline ternary oxysulfide (except ZrOS and HfOS) until the synthesis of $\text{ZnO}_{1-x}\text{S}_x$ in the 1990's. This phase is the most often found as crystalline thin films. It is also the case for titanium, tungsten and molybdenum oxysulfides, except that they are amorphous.

The first-row transition metals ternary oxysulfides represent a challenge, because the coordination of the metal commonly does not exceed six, and consequently cannot bear the $\text{M}_2\text{O}_2\text{S}$ structure of $\text{Ln}_2\text{O}_2\text{S}$ (Ln = lanthanide) where the lanthanide coordination is seven or the $\text{Bi}_2\text{O}_2\text{S}$ structure where the coordination of bismuth is eight. Alternative crystal structures may be obtained in the case of first-row transition metals.

V.1.2.1. Crystalline transition metal oxysulfides

V.1.2.1.1. Copper oxysulfide $\text{Cu}_2\text{O}_{1-x}\text{S}_x$

In 2013, Meyer *et al.* reported the synthesis of ternary compounds $\text{Cu}_2\text{O}_{1-x}\text{S}_x$ with various compositions.¹¹ These were obtained using radio-frequency magnetron sputtering (RFS) with a copper target and a flow of O_2 and H_2S with various gas ratios. The authors showed that for $x > 0.39$, the compounds did not crystallize in the cubic structure of Cu_2O and became amorphous. The lattice constant of cubic $\text{Cu}_2\text{O}_{1-x}\text{S}_x$ evolved with the composition towards bigger values because of sulfur insertion. The variation was linear only up to $x = 0.13$ and did

not follow the Vegard's law. Unfortunately, direct information about the sulfur oxidation state is missing: the oxysulfide nature of the compound remains unsubstantiated.

V.1.2.1.2. Zinc oxysulfide $\text{ZnO}_{1-x}\text{S}_x$

Despite their electronegativity and size differences, sulfur atoms are able to replace the oxygen atoms of the wurtzite structure which progressively turns into the ZnS blende structure. It evidences another challenge of metal oxysulfide identification: they could be isostructural of metal sulfides or metal oxides.

Zinc oxysulfide was first reported as thin films grown by atomic layer deposition (ALD) in 1992 by Sanders *et al.* The oxygen and water traces in the gases were responsible for the oxygen in the resulting film. Since 2010, extensive characterization of $\text{ZnO}_{1-x}\text{S}_x$ thin films were reported, not only involving ALD¹² but also pulsed-laser deposition,¹³ chemical spray pyrolysis^{14–17} or thioacetate-capped ZnO nanocrystals.¹⁸ Because of the active research on bandgap engineering, zinc oxysulfide was envisaged as buffer layer in solar cells.^{19,20} X-Ray photoemission spectroscopy (XPS) showed that the sulfur in these films is reduced and thus in agreement with the announced oxysulfide nature.^{14,18}

V.1.2.1.3. Molybdenum oxysulfides

In 1986, Inoue *et al.* crystallized two $\text{Mo}_x\text{O}_y\text{S}_z$ compounds while studying the $\text{MoS}_2\text{:MoS}_3$ system.²¹ The deep-bluish crystal of $\text{MoO}_{2.74}\text{S}_{0.12}$ (otherwise written as $\text{Mo}_4\text{O}_{10.96}\text{S}_{0.48}$) was isostructural to $\gamma\text{-Mo}_4\text{O}_{11}$ and exhibited charge density wave instabilities similar to these of quasi-2D materials. The similar properties of $\text{MoO}_{2.74}\text{S}_{0.12}$ and $\gamma\text{-Mo}_4\text{O}_{11}$ supported the hypothesis of a true oxysulfide compound. Also, reddish crystals of $\text{MoO}_{1.88}\text{S}_{0.15}$ were obtained and presented structural and electronic similarities with monoclinic MoO_2 .

The decomposition of molybdenum oxodithiocarbamate as a single source precursor also enabled the formation of crystalline thin films.²² Rutherford backscattering spectroscopy (RBS) indicated a pure phase. Unfortunately, the final product shared the XRD patterns of Mo_8O_{23} , Mo_9O_{26} and Mo_2S_3 but the structure was not fully solved.

V.1.2.2. Amorphous titanium, tungsten and molybdenum oxysulfides

In this section are referenced the oxysulfides of three elements: titanium, tungsten and molybdenum. In the 1990's, thin films of these oxysulfides were obtained and studied for their electrochemical properties.

In 1993, Tchangbedji *et al.* announced the formation of a hydrated amorphous phase of vanadium oxysulfide by reacting $\text{Na}_2\text{S}\cdot 9\text{H}_2\text{O}$ and VOCl_2 .²³ The first described formula for

this compound was $V_2O_4S \cdot 2H_2O$, but was adjusted to $V_2O_3S \cdot 3H_2O$ in latter studies (electron paramagnetic resonance and XANES at V K-edge demonstrated the presence of V^{IV} species).^{24,25} Water was believed to stabilize the compounds, as its evaporation was accompanied by the loss of the sulfur in the structure. Unfortunately, the authors did not provide enough convincing arguments to justify the oxysulfide nature and the purity of their phase without ambiguity. In particular, the absence of the IR and XANES at S K-edge spectra, which are discussed in the articles, is detrimental. Because of this lack of information, we did not focus on this phase.

V.1.2.2.1. Titanium

Titanium oxysulfides were obtained under the form of thin films to serve as positive electrode material for solid state batteries. Reported for the first time in 1989 by Meunier *et al.*,^{26,27} they were extensively characterized in the same group by X-ray photoemission spectroscopy (XPS) that was shown well adapted for thin films characterization.²⁸

Titanium oxysulfides (TiO_yS_z) of various compositions were obtained using RFS of hydrolyzed TiS_2 targets. The composition can be adjusted *via* the partial pressure of oxygen during the sputtering process. XPS showed that titanium oxysulfides thin films contain three titanium species (Ti^{IV} as in TiO_2 , Ti^{IV} as in TiS_2 and Ti in mixed environment) and three sulfur species (S^{II} of S^{2-} anions, S^{-I} in disulfide S_2^{2-} ions and undefined S_n^{2-} ions). For high oxygen contents ($TiOS$ for instance), S^{VI} species of sulfate ions attributed to surface species were also observed, although in a lesser extent due to mechanical erosion.^{29–32} Besides, the presence of ordered domains, observed by TEM and XRD, revealed the existence of TiS_2 nanocrystals in the amorphous materials.³³ Lithiated titanium oxysulfides thin films were recently obtained with RFS using $LiTiS_2$ targets.³⁴ Their characterization show similar properties than TiO_yS_z . Their capacities of around $85 \mu Ah \cdot cm^{-2} \cdot \mu m^{-1}$ made them usable in a Li-ion cell.

Aside these thin films, “sulfur-doped TiO_2 ” can be obtained by reacting TiO_2 with thiourea or hexamethyldisilathiane, for instance. However, in this case, the products should not be named “oxysulfides”, because they only contain oxidized sulfur under the form of S^{IV} and S^{VI} species.^{35–37}

V.1.2.2.2. Tungsten

Similarly to titanium oxysulfides, amorphous tungsten oxysulfides thin films with adjustable composition were obtained by RFS on WS_2 targets and mainly characterized by XPS.³⁸ Along with the three species of sulfur described in the titanium section, three different species of

tungsten (W^{VI} as in WO_3 , W^{IV} as in WS_2 and W^V in a mixed environment of O^{2-} , S^{2-} and S_2^{2-}) were observed.^{30,31} TEM and XRD showed the presence of nano-crystallites of WS_2 , but the polymorphs 3R- WS_2 and 2H- WS_2 could not be distinguished.³⁹ The incorporation of lithium in these thin films and their electrochemical properties were studied.^{38,40} It revealed that 1.1 lithium atoms per formula can be incorporated, providing a capacity of $75 \mu A \cdot cm^{-2}$. XPS also demonstrated that the tungsten ions are reduced to $W^{(0)}$ and that sulfide ions participated to the redox process with irreversible behaviours.⁴¹

V.1.2.2.3. Molybdenum

Abraham, Pasquariello *et al.* synthesized various MoO_yS_z amorphous compounds from the thermal decomposition of ammonium dithiomolybdate $(NH_4)_2MoO_2S_2$.^{42,43} This precursor was obtained by bubbling H_2S on ammonium paramolybdate $[(NH_4)_6Mo_7O_{24} \cdot 4H_2O]$ in an ammonia solution. Depending on the thermal treatment (temperature, number of steps), significant amounts of hydrogen and/or nitrogen could be found in the solids. Reacting a mixture of $[(NH_4)_6Mo_7O_{24} \cdot 4H_2O]$ and $(NH_4)_2MoS_4$ also led to a solid precursor whose thermal decomposition yielded MoO_yS_z . Based on the electrochemical properties of these amorphous compounds, the authors suggested different structures for them, with different O/S ratios and involving both S_2^{2-} and S^{2-} anions.⁴⁴ Infrared spectroscopy and XPS supported the presence of Mo–O and Mo–S bonds in the solid, but Mo–Mo bonding could not be evidenced. The solution obtained by reflux of $(NH_4)_2MoO_2S_{12}$ in acetone dispersed in different aqueous electrolyte solutions led to original morphologies of amorphous molybdenum oxysulfides (water/acetone = 1:10 v/v).⁴⁵ For instance, tubular morphologies (with the following electrolyte: 10 % KCl, 10 % NH_4SCN), hollow spheres (with 10 % $(NH_2OH)H_2SO_4$) and fractal sponge-like solids (with 20 % NH_4SCN) were obtained. A solid was collected by evaporation of the solvent. EXAFS at Mo K-edge spectra showed one oxygen atom and four sulfur atoms in the first coordination shell of molybdenum atoms. XPS supported the hypothesis of mainly reduced sulfur, even if a broad peak in the region 167-171 eV indicated oxidized species. In the same group, Genuit *et al.* performed the condensation in acidic medium of $MoO_2S_2^{2-}$ to amorphous $MoOS_2$.⁴⁶ The addition of HCl in a $(NH_4)_2MoO_2S_2$ aqueous solution led to the $MoOS_2$.

Similarly to titanium and tungsten, RFS gave amorphous thin films of molybdenum oxysulfides.^{47,48} The target was a pellet of MoS_2 . Pure oxygen was flowed into the chamber to get oxygen-rich oxysulfides ($MoO_{\sim 1.3}S_{\sim 1.9}$), but the traces of oxygen in the glovebox were originally sufficient to get MoO_yS_z thin films. For oxysulfides with a low content of oxygen

($\text{MoO}_{-0.5}\text{S}_{-2.0}$), TEM showed ordered domains that are isostructural of MoS_2 , based on electronic diffraction. XRD evidenced both MoS_2 and MoO_2 phases when the films were annealed under inert atmosphere. As shown by Buck for contaminated MoS_2 films, substitution of sulfur by oxygen atoms is likely to explain the changes in lattice parameters observed in the MoS_2 -like phase.⁴⁹ Later, XPS provided clues about the oxidation states of molybdenum and sulfur in MoO_yS_z films which strongly varied with the film composition.^{30,50,51} For $y < 0.6$ and $z > 2$ (oxygen-poor oxysulfides), Mo^{IV} cations and $\text{S}^{-\text{II}}$ (as in MoS_2) were dominant. For $y > 3$ and $z < 1$ (oxygen-rich oxysulfides), only Mo^{VI} in octahedral sites (as in MoO_3) was observed. For $0.6 < y < 3$ and $1 < z < 2$, Mo^{V} was observed in addition to Mo^{IV} and Mo^{VI} and was likely surrounded by $\text{O}^{-\text{II}}$ (O^{2-}) and $\text{S}^{-\text{I}}$ (S_2^{2-}) species. Moreover, in $\text{MoO}_{0.6}\text{S}_{1.9}$ thin films, extended X-ray absorption fine structure (EXAFS) at molybdenum K-edge also showed the presence of oxygen atoms in the coordination sphere of molybdenum atoms.⁵¹

During the same decade, useful XPS and IR references for molybdenum oxysulfides were established by Muijsers, Weber *et al.* in the study of MoO_3 films sulfidation.^{52,53} The formation of oxysulfide intermediate species with their corresponding probable structures was detailed.

V.1.2.3. Conclusion: application perspectives and composition limit

The applications of *d*-block transition metal ternary oxysulfides at bulk scale or prepared as thin films are different from their lanthanide homologs. The studies on Ti, Mo and W for instance were focused on the electrochemical properties of the compounds. Transition metals oxysulfides present a larger potential for oxido-reduction processes due to their numerous oxidation states. Nowadays, the limited number of available compositions represents an obstacle to the development of this family of materials.

So far, lithium intercalation and electrochemical properties of bulk metal oxysulfides were discussed because of possible oxido-reduction reactions with transition metals such as titanium or molybdenum. We already mentioned that titanium^{26,32,34} or tungsten^{38,40,41} thin films were studied as cathodes in solid-state lithium-ion batteries. As cathodes, molybdenum oxysulfide thin films were also developed.^{42–44,48,50,54–56} More recently, a $\text{TiO}_2@\text{MoO}_y\text{S}_z$ composite was investigated as anode material.⁵⁷ The external layer of molybdenum oxysulfide was supposed to enhance the conductivity of the hybrid material.

In a patent filed by Stewart *et al.*, Sb_2OS_2 is also mentioned as a catalyst for polycondensation reaction (polyethylene terephthalate preparation).⁵⁸

The limited range of available ternary oxysulfide is frustrating to the chemist, and even more because since the 1970's, the oxysulfide field has been enriched with numerous bimetallic compositions dealing with all the corners of the periodic table.

V.1.3. Toward more complex structures: quaternary oxysulfides and selective bonding

V.1.3.1. Selective and unselective bonding in quaternary structures

We already cited the work of Marcon who isolated actinide oxysulfides $\text{U}_2\text{Pu}_2\text{O}_4\text{S}_3$ and $\text{U}_2\text{Gd}_2\text{O}_4\text{S}_3$.⁵⁹ These structures contain U^{IV} and Ln^{III} . This mixed valence allowed the formation of the $\text{An}^{\text{IV}}_2\text{Ln}^{\text{III}}_2\text{O}_4\text{S}_3$ and $\text{An}^{\text{IV}}_2\text{Ln}^{\text{III}}_4\text{O}_6\text{S}_4$ (of general formula $\text{An}^{\text{IV}}_2\text{Ln}^{\text{III}}_{2n}\text{O}_{2+2n}\text{S}_{2+n}$) structures by a shearing mechanism of the $\text{Ln}_2\text{O}_2\text{S}$ structure when similar mixed-valent uranium-lanthanide oxysulfides were obtained.⁶⁰ With Okabe *et al.*, they also exhibited a series of $\text{U}_2\text{La}_{2n-2}\text{O}_{2n}\text{S}_{n+1}$ compounds.⁶¹

Besides, in the 1980's, a considerable amount of quaternary oxysulfides containing other metals than lanthanides or actinides were synthesized. Firstly, the idea was to insert another metal in the lamellar structure of a lanthanide oxysulfide $\text{Ln}_2\text{O}_2\text{S}$. The easiest way to get a quaternary oxysulfide was to put the other metal in the layer of sulfur anions, and consequently obtain a structure composed by sheets of lanthanide oxide and metal sulfide. This compound, in which oxygen is bound only to the lanthanide and sulfur only to the additional metal, exhibits a particular order that one can call *selective bonding*. As the quaternary oxysulfides can be formed with a large variety of precursors (mainly oxides and sulfides, but also elemental sulfur, H_2S , metals, ...) and not only using lamellar preformed structures such as $\text{Ln}_2\text{O}_2\text{S}$, this selective bonding can be extended to any resulting oxysulfide in which one of the anions is preferentially bound to one of the metals and conversely. It generally led to layered compounds. On the contrary, when no such order is present in the structure (at least one metal site in the structure is bound to the two anions), the compound exhibits *unselective bonding*.

To illustrate this difference, we chose to study a family of quaternary oxysulfides $\text{Ln}_2\text{Ti}_2\text{S}_2\text{O}_5$ (with Ti^{IV}) reported in the late 1990's. These structures turned out to be defective Ruddlesden-Popper phases which alternate $[\text{Ln}_2\text{S}_2]^{2+}$ and $[\text{Ti}_2\text{O}_5]^{2-}$ layers (Figure 85A). However, it is also possible to get compounds where both metals are equally bound to both

oxygen and sulfur without particular arrangement (unselective bonding). It can be illustrated by the previously reported quaternary titanium oxysulfides $\text{La}_4\text{Ti}_3\text{O}_8\text{S}_4$ and $\text{La}_6\text{Ti}_2\text{S}_8\text{O}_5$ that do not show any selective bonding (Figure 85B and Figure 85C).⁶² In the 1980's, the study of the $\text{La}_w\text{Ga}_x\text{O}_y\text{S}_z$ compounds already started the reflexion on the selectivity of the bonds in quaternary oxysulfides (selective bonding for $\text{LaGaOS}_2\text{-}\alpha$, $\text{La}_4\text{Ga}_{1.33}\text{O}_4\text{S}_4$ and La_3GaOS_5 ; unselective bonding for $\text{LaGaOS}_2\text{-}\beta$ and $\text{La}_{3.33}\text{Ga}_6\text{O}_2\text{S}_{12}$, Table 9).⁶³

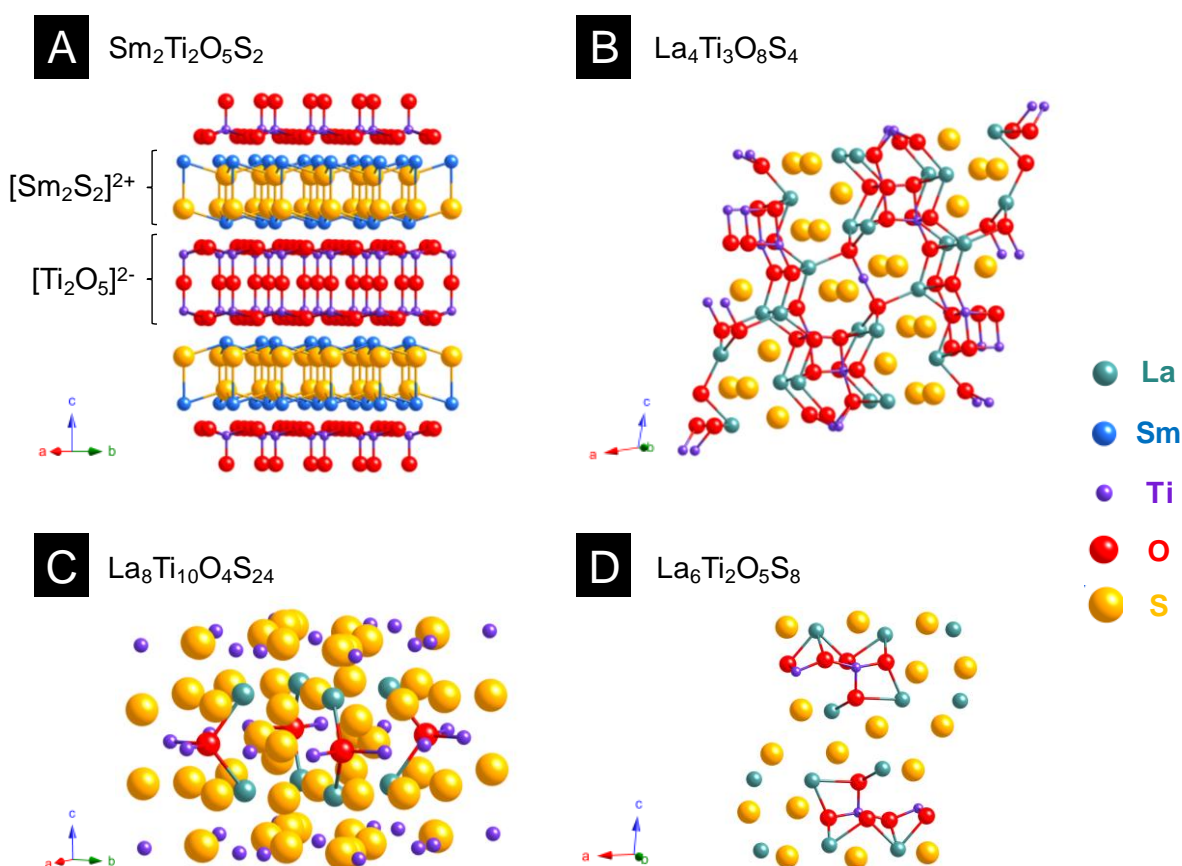


Figure 85: Various quaternary oxysulfide structures containing titanium. (A) $\text{Sm}_2\text{Ti}_2\text{O}_5\text{S}_2$ (JCPDS 13-1325) exhibits selective bonding as sulfur is preferentially bound to titanium and oxygen to samarium. (B) $\text{La}_4\text{Ti}_3\text{O}_8\text{S}_4$ (JCPDS 09-7018), (C) $\text{La}_8\text{Ti}_{10}\text{O}_4\text{S}_{24}$ (JCPDS 09-8085) and (D) $\text{La}_6\text{Ti}_2\text{O}_5\text{S}_8$ (JCPDS 09-7017) show different structures with unselective bonding.

V.1.3.2. Quaternary oxysulfides: a large catalogue of compositions

Using high temperatures and long reaction times, monovalent (Cu^{I} , Ag^{I}), trivalent (Cr^{III} , Ga^{III} , As^{III} , Sb^{III} , Bi^{III}), tetravalent (Sn^{IV}) and pentavalent elements (Nb^{V}) were shown to be able to crystallize along with a lanthanide in various types of oxysulfide compounds (Table 9). In some cases, the second metal can also present mixed oxidation states ($\text{Ti}^{\text{III,IV}}$, $\text{V}^{\text{III,IV}}$).

More recently, lanthanide-free quaternary oxysulfide compounds CaMOS ($\text{M} = \text{Fe}^{64,65}$, Co^{66} , Zn^{67}) and $\text{BaM}'\text{OS}$ (with $\text{M}' = \text{Co}^{66,68}$, Zn^{69}) were synthesized and characterized. This shows

the growing interest in obtaining metal oxysulfides without rare earth (which are strategic resources) in order to explore their magnetic and catalytic properties.

	Phase	Space group	Bonding [a]	References
An_wAn_xO_yS_z and An_wLn_xO_yS_z (An = actinide, Ln = lanthanide)				
	U _{0.5} Pu _{0.5} OS	Tetragonal <i>Pnmm</i>	S	Marcon 1967 ⁵⁹
	U ₂ Pu ₂ O ₄ S ₃	Orthorhombic <i>Pbam</i> [b]	U	Marcon 1967 ⁵⁹
	U ₂ Ln ₂ O ₄ S ₃ (Ln = La, Ce, Pr, Nd, Sm, Gd, Tb)	Orthorhombic <i>Pbam</i>	U	Marcon 1967, ⁵⁹ Tien 1988 ⁶⁰
	U ₂ Ln ₄ O ₆ S ₄ (Ln = La, Ce, Pr, Nd, Sm, Gd, Tb)	Orthorhombic <i>Pnam</i>	U	Tien 1988 ⁶⁰
	U ₂ La ₆ O ₈ S ₅ U ₂ La ₈ O ₁₀ S ₆ U ₂ La ₁₀ O ₁₂ S ₇	Orthorhombic	U	Tien 1988 ⁶⁰
	U ₂ LnO ₂ S ₃ (Ln = Gd, Dy, Ho, Er, Tm, Yb, Lu, Y)	Tetragonal <i>I4/mmm</i>	S	Guittard 1986 ⁷⁰
	U ₄ Lu ₄ O ₄ S ₅	Tetragonal <i>I4/mmm</i>	S	Jaulmes 1990 ⁷¹
Ln_wM_xO_yS_z (Ln = lanthanide or bismuth, M = 1st row transition metal)				
	Ln ₂ Ti ₂ O ₅ S ₂ (Ln = Pr, Nd, Sm)	Tetragonal <i>I4/mmm</i>	S	Goga 1999, ⁷² Boyer 1999 ⁷³
	La ₁₆ Ti ₅ O ₁₇ S _{17+x} (x = 0.75)	Tetragonal <i>I4/m</i>	U	Meignen 2003 ⁷⁴
	La ₄ Ti ₃ O ₈ S ₄	Monoclinic <i>C2/m</i>	U	Cody 1995 ⁶²
	La ₆ Ti ₂ O ₅ S ₈	Monoclinic <i>P2₁/m</i>	U	Cody 1995 ⁶²
	La ₁₄ Ti ₈ O ₄ S ₃₃	Monoclinic <i>C2/m</i>	U	Tranchitella 1996 ⁷⁵
	La ₈ Ti ₁₀ O ₄ S ₂₄	Tetragonal <i>P4/mmm</i>	U	Cario 1998 ⁷⁶
	La _{8.75} Ti _{9.25} O ₄ S ₂₄ La _{8.50} Ti _{9.50} O ₄ S ₂₄ La _{8.10} Ti _{8.05} O ₄ S ₂₄	Tetragonal <i>P4/mmm</i>	U	Tranchitella 1998 ⁷⁷
	La ₂₀ Ti ₁₁ O ₆ S ₄₄	Orthorhombic <i>Pmmn</i>	U	Deudon 1995 ⁷⁸
	Ce ₂₀ Ti ₁₁ O ₆ S ₄₄	Orthorhombic <i>Pmmn</i>	U	Cody 1997 ⁷⁹
	Nd ₁₆ Ti ₅ O ₁₇ S ₁₇	Tetragonal <i>I4/m</i>	U	Boyer-Candalen 2000(3) ⁸⁰
	Gd _{6+x} Ti _{4-x} S _{10-y} O _{6+y}	Orthorhombic <i>Pnma</i>	U	Meignen 2004 ⁸¹
	Ln ₅ V ₃ O ₇ S ₆ (Ln = La, Ce, Pr, Nd)	Orthorhombic <i>Pmmn</i>	U	Vovan 1981, ⁸² Dugué 1985 ⁸³

LaCrOS ₂	Orthorhombic <i>Pbnm</i>	U	Vovan 1978, ⁸⁴ Dugué 1980 ⁸⁵
LnCrOS ₂ (Ln = Ce, Pr, Nd, Sm)	Monoclinic <i>B2/m</i>	U	Vovan 1978, ⁸⁴ Dugué 1980(2) ⁸⁶
La ₄ MnOS ₆	Hexagonal <i>P6₃mc</i>	U	Ijjaali 2005 ⁸⁷
Ln ₂ Fe ₂ O ₃ S ₂ (Ln = La, Ce, Pr)	Tetragonal <i>I4/mmm</i>	U	Mayer 1992 ⁸⁸ Charkin 2011 ⁸⁹
LaCuOS	Tetragonal <i>P4/nmm</i>	S	Palazzi 1981, ⁹⁰ Doussier-Brochard 2010 ⁹¹
La ₅ Cu ₆ O ₄ S ₇	Orthorhombic <i>Imma</i>	U	Qiang Huang 2000 ⁹²
CeCu _x OS (x = 0.8 ; 1)	Tetragonal <i>P4/nmm</i>	S	Ueda 2003, ⁹³ Chan 2006 ⁹⁴
PrCuOS	Tetragonal <i>P4/nmm</i>	S	Lauxmann 2000 ⁹⁵
LnCuOS (Ln = Nd, Sm)	Tetragonal <i>P4/nmm</i>	S	Popovkin 1998 ⁹⁶
BiCuOS	Tetragonal <i>P4/nmm</i>	S	Kusainova 1994 ⁹⁷ , Sheets 2012 ⁹⁸

Ln_wM_xO_yS_z
(Ln = lanthanide or bismuth, M = 2nd and 3rd row transition metal in d-block)

La ₂ Nb ₃ O ₈ S ₂	Orthorhombic <i>Pnnm</i>	U	Brennan 1992, ⁹⁹ Cario 2003 ¹⁰⁰
La ₃ MO ₅ S ₂ (M = Nb, Ta)	Tetragonal <i>I4/mmm</i>	S	Cario 2007 ¹⁰¹
La _{-10.8} Nb ₅ O ₂₀ S ₁₀	Orthorhombic <i>Immm</i>	U	Boyer-Candalen 2000 ¹⁰²
Ce ₃ NbO ₄ S ₃	Orthorhombic <i>Pbam</i>	U	Altmannshofer 2008 ¹⁰³
Sm ₃ NbO ₄ S ₃	Orthorhombic <i>Pn2₁a</i>	U	Boyer-Candalen 2000(2) ¹⁰⁴
Gd ₃ NbO ₄ S ₃	Orthorhombic <i>Pn2₁a</i>	U	Kabbour 2003 ¹⁰⁵
La ₂ Ta ₃ O ₈ S ₂	Orthorhombic <i>Pnnm</i>	U	Brennan 1992 ⁹⁹
Sm ₂ Ta ₃ O ₈ S ₂	Orthorhombic <i>Pnnm</i>	U	Guo 1995 ¹⁰⁶
LaAgOS	Tetragonal <i>P4/nmm</i>	S	Palazzi 1980, ¹⁰⁷ Palazzi 1981(2) ¹⁰⁸
CeAg _x OS (x = 0.8 ; 1)	Tetragonal <i>P4/nmm</i>	S	Chan 2006 ⁹⁴
BiAgOS	Tetragonal <i>P4/nmm</i>	S	BaQais 2017 ¹⁰⁹

Ln_wM_xO_yS_z
(Ln = lanthanide, M = 2nd and 3rd row transition metal in p-block)

LaGaOS ₂ α	Orthorhombic <i>P2₁ab</i>	S	Guittard 1985 ⁶³
LaGaOS ₂ β	Orthorhombic <i>Pmca</i>	U	Jaulmes 1978 ¹¹⁰

$\text{La}_3\text{GaS}_5\text{O}$	Orthorhombic $Pnma$	S	Jaulmes 1983, ¹¹¹ Guittard 1985 ⁶³
$\text{La}_{3.33}\text{Ga}_6\text{S}_{12}\text{O}_2$	Tetragonal $P4_21m$	U	Mazurier 1982, ¹¹² Guittard 1985 ⁶³
$\text{Ce}_4\text{Ga}_2\text{O}_4\text{S}_5$	Tetragonal $I4/mmm$	S	Jaulmes 1982, ¹¹³ Guittard 1984 ¹¹⁴
$\text{Ln}_4\text{Ga}_{1.33}\text{O}_4\text{S}_4$ (Ln = La, Ce)	Tetragonal $P4/mmm$	S	Guittard 1985 ⁶³
$\text{Ln}_4\text{Ga}_2\text{O}_4\text{S}_5$ (Ln = Pr, Nd, Sm)	Orthorhombic $Pbca$	S	Guittard 1984 ¹¹⁴
LaInOS_2	Orthorhombic	<u>ND</u>	Kabbour 2004 ¹¹⁵
$\text{La}_5\text{In}_3\text{O}_3\text{S}_9$	Orthorhombic $Pbcm$	S	Kabbour 2004 ¹¹⁵
$\text{La}_{10}\text{In}_6\text{O}_6\text{S}_{17}$	Orthorhombic $Immm$	S	Gastaldi 1982 ¹¹⁶
$\text{Ln}_4\text{Sn}_2\text{O}_4\text{S}_6$ (Ln = La, Ce, Pr, Nd)	Orthorhombic $Pbnm$	S	Guittard 1984 ¹¹⁴
LnBiOS_2 (Ln = La, Ce, Pr, Nd, Gd, Dy)	Tetragonal $P4/nmm$	S	Céolin 1976, ¹¹⁷ Pardo 1976 ¹¹⁸ , Tanryverdiev 1995 ¹¹⁹

**$\text{Ln}_w\text{T}_x\text{O}_y\text{S}_z$ and $\text{Ca}_w\text{T}_x\text{O}_y\text{S}_z$
(Ln = lanthanide, T = metalloid)**

$\text{Ln}_4\text{Ge}_{1.5}\text{O}_4\text{S}_5$ (Ln = La, Ce, Pr, Nd)	Orthorhombic $Pbca$	S	Guittard 1984 ¹¹⁴
$\text{La}_4\text{As}_2\text{O}_4\text{S}_5$	Tetragonal $I4/mmm$	S	Jaulmes 1982 ¹¹³
LnSbOS_2 (Ln = La, Ce, Pr)	<u>Not described</u>	<u>ND</u>	Pardo 1976 ¹¹⁸
$\text{La}_4\text{Sb}_2\text{O}_4\text{S}_5$	X	X	Aliev 1997 ¹²⁰
$\text{La}_6\text{Sb}_4\text{O}_{12}\text{S}_3$	Tetragonal $I4_1/amd$	U	So 2004 ¹²¹
NdSbOS_2	Tetragonal $P4/nmm$	S	Pardo 1976 ¹¹⁸
$\text{CaSb}_{10}\text{O}_{10}\text{S}_6$	Monoclinic $C2/c$	<u>ND</u>	Nakai 1978 ¹²²

**$\text{A}_w\text{M}_x\text{O}_y\text{S}_z$
(A = alkaline or earth-alkaline, M = transition metal)**

$\text{K}_6\text{Ti}_6\text{OS}_{18}$	Triclinic $P1$	U	Tillinski 2001 ¹²³
$\text{Ba}_6\text{Ti}_5\text{OS}_{15}$	Orthorhombic $C222_1$	S	Sutorik 1994 ¹²⁴
CaFeOS	Hexagonal $P6_3mc$	S	Selivanov 2004, ⁶⁴ Delacotte 2015 ⁶⁵
$\text{Ca}_3\text{Fe}_4\text{S}_3\text{O}_6$ [c]	Tetragonal	<u>ND</u>	Selivanov 2004 ⁶⁴
CaCoOS	Hexagonal $P6_3mc$	S	Salter 2016 ⁶⁶

BaCoOS	Orthorhombic <i>Cmcm</i>	U	Valldor 2015, ⁶⁸ Salter 2016 ⁶⁶
CaZnOS	Hexagonal <i>P6₃mc</i>	S	Petrova 2003, ¹²⁵ Sambrook 2007 ⁶⁷
BaZnOS	Orthorhombic <i>Cmcm</i>	U	Broadley 2005 ⁶⁹
Others			
Zr _{1-x} Hf _x OS	Cubic <i>P2₁3</i>	U	Eisman 1982 ⁵
Pb ₁₄ Sb ₃₀ O ₅ S ₅₄ (scainiite) [d]	Monoclinic <i>C2/m</i>	U	Orlandi 1999 ¹²⁶

[a] S = selective, U = unselective, ND = not described. [b] Deducted from later works. [c] Structure not solved, only based on composition. [d] Natural compound.

Table 9: Quaternary oxysulfides $M^I_w M^II_x O_y S_z$.

In this table are not referenced the quaternary phases reported by Umarji *et al.* in 1980: $M_2Mo_6S_6O_2$ ($M = Co, Ni, Cu$) and $PbMo_6S_6O_2$.¹²⁷ A few years after this publication, Selwyn *et al.* tried to obtain the copper-based phase and demonstrated that Umarji *et al.* reached only a mixture of the Chevrel phase $Cu_{2.7}Mo_6S_8$, Mo and MoO_2 .¹²⁸ Then Selwyn *et al.* also concluded that obtaining the ternary $Mo_6S_6O_2$ oxysulfide from the claimed $M_2Mo_6S_6O_2$ was impossible.

V.1.3.3. Quinary oxysulfides

Quinary oxysulfides also exist, but are not exhaustively listed here. Most of them are layered compounds with selective interactions and contain earth-alkaline atoms, as evidenced by Teske in 1985 with $CaLaGa_3OS_6$, $SrLaGa_3OS_6$, $La_2ZnGa_2OS_6$ and $Sr_2ZnGe_2OS_6$.¹²⁹ A similar $Sr_2MnGe_2OS_6$ phase was synthesized and studied recently.¹³⁰ Doped phosphors $CaLaGa_3OS_6$ ^{131–135} and $SrLaGa_3OS_6$ ^{134,136–138} were extensively studied by Zhang, Yu, and Zhang since 2005. Zhu, Hor and Otschi also detailed different quinary oxysulfide families: (i) the $Sr_2Cu_2MO_2S_2$ ($M = Mn$,¹³⁹ Co ,^{140,141} Zn ,¹³⁹ Ni ¹⁴²) and $Ba_2Cu_2CoO_2S_2$ ^{140,141} family that displays an unusual square planar MO_2 layer and the two perovskite-based families (ii) $Sr_3Cu_2M_2O_5S_2$ ($M = Sc$,¹⁴² Fe ¹⁴³) and (iii) Sr_2CuMO_3S ($M = Sc$,¹⁴⁴ Cr ,¹⁴³ Fe ,¹⁴³ Ga ,¹⁴⁵ In ¹⁴³) with the work of Ogino on scandium. Later, Blandy transformed $Sr_2Cu_2MnO_2S_2$ in $Sr_2Cu_{1.5}MnO_2S_2$ by oxidative deintercalation of copper to obtain a mixed-valent perovskite.¹⁴⁶

The study of the quasi-binary system $La_2O_2S-AgGaS_2$ ($La_2O_2S - 0.75 Ga_2S_3 - 0.75 Ag_2S$) by Carcaly *et al.* led to the formation of $La_4Ag_{1.5}Ga_{1.5}O_4S_5$ in which silver and gallium are randomly distributed in the same sites.¹⁴⁷ Along with $La_3MO_5S_2$ ($M = Nb, Ta$; Table 9), Cario *et al.* reported bilanthanide lamellar $La_2YMO_5S_2$ phases very close to the $Ln_2Ti_2O_5S_2$

structure.¹⁰¹ The works of Tranchitella on La/Ti quaternary oxysulfide (Table 9) led him to the quinary compound $\text{Sr}_{5.8}\text{La}_{4.4}\text{Ti}_{7.8}\text{S}_{24}\text{O}_4$ with the same $[(\text{Ti}_4\text{S}_2\text{O}_4)(\text{TiS}_6)_{4/2}]^{12-}$ layer than $\text{La}_{14}\text{Ti}_8\text{S}_{33}\text{O}_4$.⁷⁵ $\text{La}_5\text{Ti}_2\text{MS}_5\text{O}_7$ ($\text{M} = \text{Cu}, \text{Ag}$), an alkaline-free structure with perovskite layers was also evidenced by Meignen¹⁴⁸ and studied for its photocatalytic properties for water reduction and oxidation.¹⁴⁹ Meignen *et al.* also prepared $\text{La}_5\text{Ti}_{\sim 3.25}\text{Zr}_{\sim 0.25}\text{S}_5\text{O}_{9.25}$ with mixed Ti/Zr sites.¹⁵⁰ In 2003, Rutt *et al.* obtained $\text{KY}_2\text{Ti}_2\text{O}_5\text{S}_2$ by topotactic potassium intercalation of potassium in $\text{Y}_2\text{Ti}_2\text{O}_5\text{S}_2$.¹⁵¹ As a perspective, in 2015 Yee *et al.* designed by DFT modeling a new high-temperature superconductor $\text{Ca}_2\text{HgCuO}_2\text{S}_2$ whose superconducting transition temperature should be close to mercury cuprates' ones.¹⁵²

V.1.4. Conclusion

Our vision of the existing oxysulfide compositions is now almost complete. In this context, a revised periodic table is presented in Figure 86.

The periodic table of oxysulfides (April 2018)

One cation maximum
($\text{M}_x\text{O}_y\text{S}_z$ only)

One cation minimum
($\text{M}_x\text{O}_y\text{S}_z, \text{A}_w\text{B}_x\text{O}_y\text{S}_z, \dots$)

Two cations minimum
($\text{A}_w\text{B}_x\text{O}_y\text{S}_z, \text{A}_v\text{B}_w\text{C}_x\text{O}_y\text{S}_z, \dots$)

Nanoscaled
 $\text{M}_x\text{O}_y\text{S}_z$

H Hydrogen																		He Helium
Li Lithium	Be Beryllium									B Boron	C Carbon	N Nitrogen	O Oxygen	F Fluorine	Ne Neon			
Na Sodium	Mg Magnesium									Al Aluminum	Si Silicon	P Phosphorus	S Sulfur	Cl Chlorine	Ar Argon			
K Potassium	Ca Calcium	Sc Scandium	Ti Titanium	V Vanadium	Cr Chromium	Mn Manganese	Fe Iron	Co Cobalt	Ni Nickel	Cu Copper	Zn Zinc	Ga Gallium	Ge Germanium	As Arsenic	Se Selenium	Br Bromine	Kr Krypton	
Rb Rubidium	Sr Strontium	Y Yttrium	Zr Zirconium	Nb Niobium	Mo Molybdenum	Tc Technetium	Ru Ruthenium	Rh Rhodium	Pd Palladium	Ag Silver	Cd Cadmium	In Indium	Sn Tin	Sb Antimony	Te Tellurium	I Iodine	Xe Xenon	
Cs Cesium	Ba Barium		Hf Hafnium	Ta Tantalum	W Tungsten	Re Rhenium	Os Osmium	Ir Iridium	Pt Platinum	Au Gold	Hg Mercury	Tl Thallium	Pb Lead	Bi Bismuth	Po Polonium	At Astatine	Rn Radon	
Fr Francium	Ra Radium																	
			La Lanthanum	Ce Cerium	Pr Praseodymium	Nd Neodymium	Pm Promethium	Sm Samarium	Eu Europium	Gd Gadolinium	Tb Terbium	Dy Dysprosium	Ho Holmium	Er Erbium	Tm Thulium	Yb Ytterbium	Lu Lutetium	
			Ac Actinium	Th Thorium	Pa Protactinium	U Uranium	Np Neptunium	Pu Plutonium	Am Americium	Cm Curium	Bk Berkelium	Cf Californium	Es Einsteinium	Fm Fermium	Md Mendelevium	No Nobelium	Lr Lawrencium	

Figure 86: Periodic table revised for the oxysulfide compounds. In blue are indicated the elements that can be found in synthetic or natural oxysulfides. Blue shades indicate the compositions (ternary, quaternary and more) that can be achieved for each element. Surrounded in violet are the elements for which $\text{M}_x\text{O}_y\text{S}_z$ nanoparticles can be found.

This periodic table underlines two crucial points:

- (i) The lack of ternary transition metal oxysulfides, as a large part of the *d*-block contains elements which need a lanthanide or an alkaline-earth metal to form an oxysulfide compound.
- (ii) Nanoscaled phases of transition metal oxysulfides are very limited (Co, Zn). The following section is dedicated to them.

V.2. Transition metal oxysulfides nanoparticles

Transition metal bulk oxysulfides are quite rare. Zinc, titanium, molybdenum and tungsten oxysulfide were nevertheless obtained. Most often, they were obtained under the form of amorphous thin films or particles.

Because of the electronegativity anion size differences between the oxygen and sulfur, transition metals will preferentially bind to one of them (in the hard and soft acids and bases theory, oxygen is a hard base and sulfur a soft base). Also, maintaining sulfur in a reduced state, *id est* avoiding sulfates or other oxidized sulfur species, is difficult because these later species contain strong and stable bonds such as S=O, making them thermodynamic pits.

V.2.1. Challenging synthesis, tricky characterization

We previously detailed numerous syntheses of $\text{Ln}_2\text{O}_2\text{S}$ nanoparticles. It is an exception in the oxysulfide family, as it remains to the best of our knowledge the only structure for which monophasic crystalline nanoparticles could be formed. Today, a vast and promising land of metal oxysulfide nanoparticles, especially involving transition metals, must be explored. With such nanoparticles with transitions metals and chalcogens, new applications could emerge, such as heterogeneous catalysis, photocatalysis, battery materials, superconduction, and so on.

Several advantages are intrinsically brought by soft reaction conditions (compared with typical synthesis of bulk crystals) and the nanoscale. Mild temperatures and small grain size can unlock metastable structures. Also, diffusion processes are much faster over nanometric distances and lead to efficient substitution reactions with nanoscaled materials. It opens new synthetic strategies to transform preformed oxide, sulfide or metal nanoparticles in oxysulfide nanoparticles.

However, synthesizing transition metal ternary oxysulfides is particularly challenging. The ionic radius difference between O^{II} (1.26 Å) and S^{II} (1.70 Å) associated with the variable affinities with the metal make the substitution reactions highly difficult. Energy input by heating is especially not recommended for nanoparticles synthesis because of excessive growth and sintering.

Despite these difficulties, transition metal oxysulfide nanoparticles were already prepared. A few examples will be detailed in the next sections. The main issue consists of identifying and evidencing the oxysulfide nature of the compound. Because excessive heating tends to

stabilize sulfate or separate oxides and sulfides rather than crystallize an oxysulfide structure, the reported structures can be amorphous and/or impure.

Identification and characterization of such phases is much harder than crystalline nanoparticles. In particular, inductively coupled plasma atomic emission spectroscopy (ICP-AES), X-ray fluorescence (XRF) and energy dispersive X-ray spectroscopy (EDS) are suitable techniques to evidence the presence of sulfur, but the determination of the nanoparticles' precise oxygen content remains a challenge. High resolution transmission electron microscopy and energy filtered transmission electron microscopy (EFTEM) constitute an elegant solution, but requires well-dispersed nanoparticles and will not provide accurate quantitative data. Moreover, it is hard to conclude about the precise localization of the atoms: are they in the whole particle or only at the surface (because of ligands for instance)?

The identification of the nature of the chemical bonds and oxidation states inside the material is a supplementary issue, yet this is required to differentiate oxysulfides from sulfates. It becomes highly problematic when the composition of a solid is unclear. Infrared and Raman spectroscopies are particularly appropriate for amorphous oxysulfide identification because M–O and M–S bonds generally present very distinguishable signatures. However, only qualitative analysis is possible. X-Ray photoemission spectroscopy (XPS) brings some clues but investigates only the very surface. X-ray absorption spectroscopy, such as XANES or EXAFS (at O K-edge, S K-edge, M K, L or M-edge) is able to characterize the whole sample and gives precious information on the oxidation states and chemical bonds. However, surface and core cannot be distinguished and only average information is obtained, so that one should be very careful about hypothesis and interpretations. Furthermore, it must be noticed that the required energies for the different edges involves the use of different X-ray ranges (soft for oxygen, tender for sulfur, hard for the metal K-edge) and consequently the use of distinct beamlines. The analysis of the pair distribution function of the diffuse background of X-ray diffraction patterns (PDF) is expected to bring solutions as it can be applied to the analysis of amorphous compounds. Still, it remains a poorly studied technique in the field of nanoparticles analysis.

Finally, we emphasized the fact that oxysulfide nanoparticles can be metastable or unstable phases. It reinforces the difficulty to store, transfer, manipulate and characterize them (for instance in air-filled room atmosphere and devices or when heating upon irradiation by electron or X-ray beams).

V.2.2. Amorphous and crystalline cobalt oxysulfide

In 2016, Nelson *et al.* reported the formation of cobalt oxysulfide CoO_xS_y hollow nanoparticles.¹⁵³ The strategy consisted in the substitution of oxygen anions by sulfur anions in cobalt oxide hollow nanoparticles, using ammonium sulfide dissolved in oleylamine at 100 °C (Figure 87A). The sulfur content was adjustable *via* the nominal $(\text{NH}_4)_2\text{S}$ amount, with a saturation of the sulfur content at $y \approx 1.3$. With low sulfur contents ($y < 0.2$), the particles keep the crystalline structure of CoO but with higher sulfur contents, the nanoparticles became amorphous (Figure 87F). The hollow nanosphere morphology was preserved during the whole experiment (Figure 87B to Figure 87E).

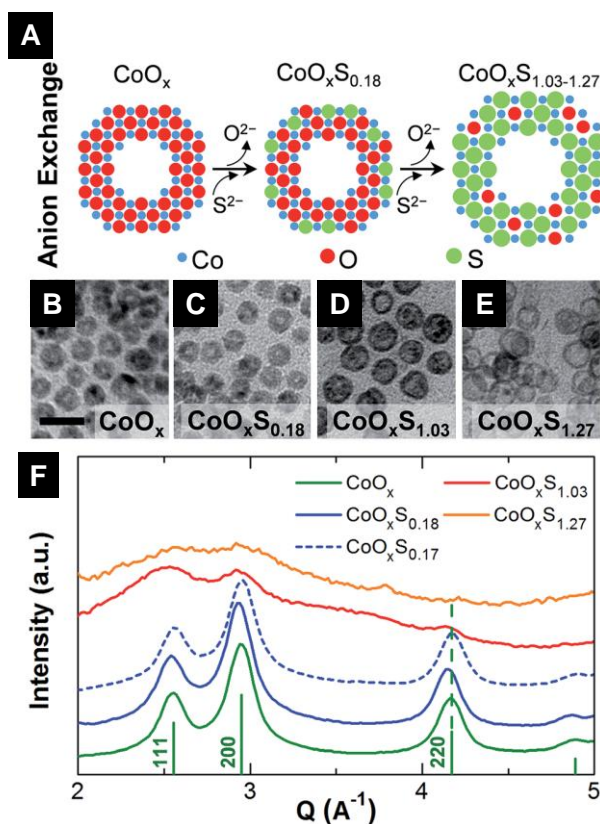


Figure 87: Adapted from Nelson *et al.*¹⁵³ (A) Synthetic strategy of CoO_xS_y hollow nanoparticles. TEM micrographs of CoO_xS_y nanoparticles with $y = 0$ (B); 0.18 (C); 1.03 (D); 1.27 (E). Rotationally averaged SAED patterns of the various CoO_xS_y nanoparticles. Reference lines in green indicate CoO Bragg peaks (JCPDS 00-048-1719).

No direct proof of the oxidation state of sulfur is brought by the authors. Nevertheless, annealing the sulfur-rich nanoparticles led to the formation of cobalt sulfides (possibly in a mixture with CoO). It supported the presence of reduced sulfur in the nanoparticles.

V.2.3. Crystalline $\text{ZnO}_{1-x}\text{S}_x$ nanoparticles

Crystalline zinc oxysulfide was obtained at the nanoscale. In 2009, Park *et al* carried out the substitution of oxygen atoms in ZnO by sulfur using hexamethyldisilathiane and obtained ZnS crystalline hollow nanoparticles.¹⁵⁴ The driving force of the reaction with ZnO is the formation of very stable Si-O bonds.

During the substitution process, the authors were able to isolate ZnO@ZnS core-shell crystalline nanoparticles, which are composed by a core of ZnO and a shell of isostructural ZnS wurtzite structure.

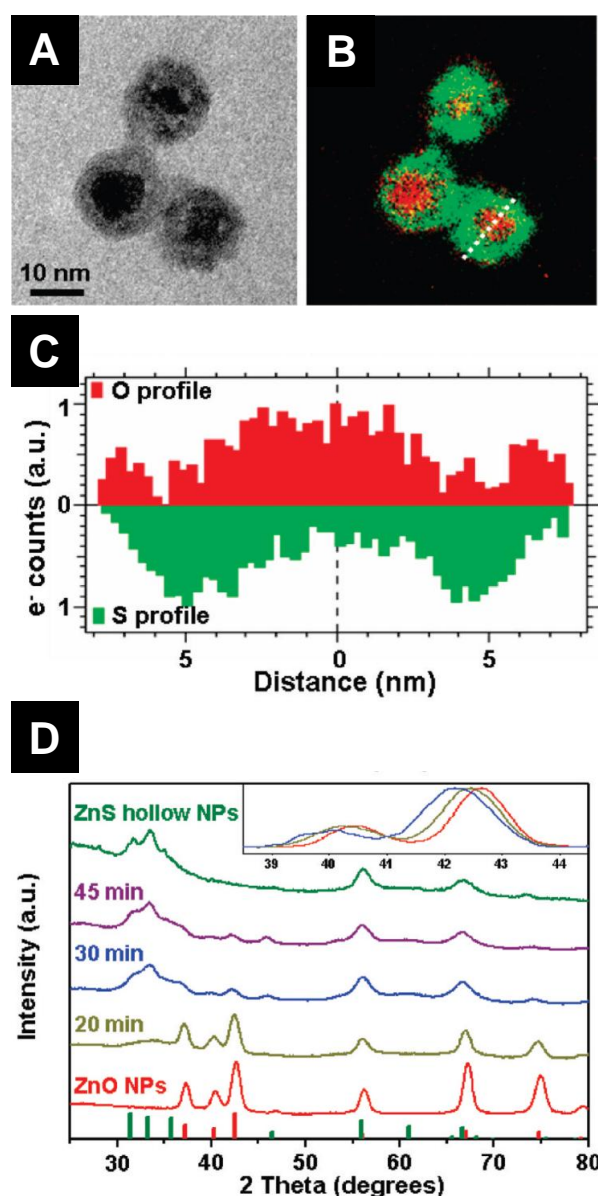


Figure 88: Adapted from Park *et al.*¹⁵⁴ TEM (A) and EFTEM (B) images of ZnO@ZnS nanoparticles. (C) Oxygen and sulfur composition along the cross-section in (B). (D) XRD patterns of the nanoparticles from ZnO to ZnS through ZnO@ZnS core-shell nanoparticles. Inset: Normalized pattern

in the $[38.5^\circ; 44.5^\circ]$ 2θ region. The small shifts of the diffraction peaks towards low 2θ values indicate a lattice dilatation caused by sulfur insertion.

The process was accompanied by the so-called “nanoscale Kirkendall effect”, which refers to the hollowing of the nanoparticles as a consequence of unbalanced diffusion rates.¹⁵⁵ Because Zn^{II} diffuse outwards faster than S^{II} inwards, the reaction finally led to a hollow ZnS structure. HRTEM and EFTEM also showed that the final ZnS nanoparticles were obtained through the formation of heteroepitaxial $\text{ZnO}@\text{ZnS}$ intermediates that release the high interface energy by the diffusion of the core into the shell. The composition analyses of core-shell intermediates indeed showed that oxygen is not only localized in the core of the nanoparticle, but also in the shell. It suggested that the substitution process with hexamethyldisilathiane took place in the shell region where oxygen had migrated.

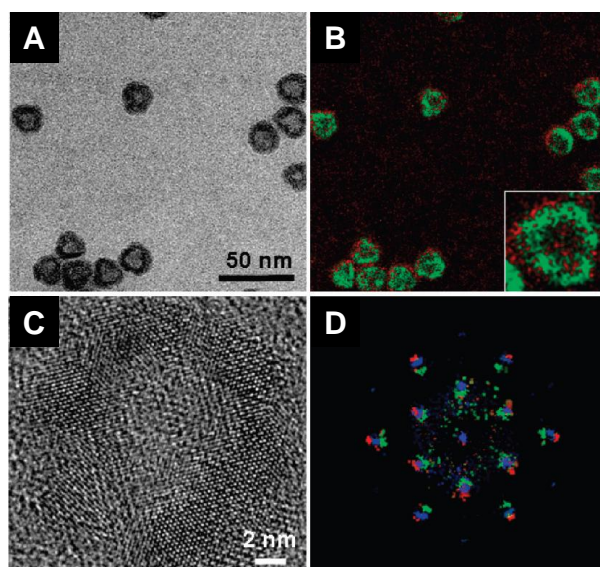


Figure 89: Adapted from Park *et al.*¹⁵⁴ TEM, EFTEM and HRTEM of annealed core-shell nanoparticles. EFTEM strongly suggest the formation of a $\text{ZnO}_{1-x}\text{S}_x$ nanoalloy. (D) FFT image of (C) overlaid on FFT image of the precursor $\text{ZnO}@\text{ZnS}$ core-shell nanoparticles (red: ZnO; green: ZnS; blue: annealed nanoparticles). These images support the heteroepitaxial formation of the ZnS shell and $\text{ZnO}_{1-x}\text{S}_x$ when thermally annealed.

The reaction resulted in the formation of crystalline $\text{ZnO}_{1-x}\text{S}_x$ located in the shell. Furthermore, the authors were able to obtain pure hollow $\text{ZnO}_{1-x}\text{S}_x$ nanoparticles by thermally annealed the core-shell intermediates. Interestingly, the diffusion processes spontaneously occurred without sulfurating reagents and led to hollow $\text{ZnO}_{1-x}\text{S}_x$ alloys.

The research on zinc oxysulfide nanoparticles has grown in the last years. Pandey *et al.* managed to obtain the whole composition range ($0 \leq x \leq 1$) of nanoparticles.^{156,157} They obtained $\text{ZnO}_{1-x}\text{S}_x$ crystalline nanoparticles by a solution combustion method. $\text{Zn}(\text{acetate})_2$

and thiourea were incorporated in a mixture of ethanol and ethylene glycol (4:1) and then placed in a hot furnace (350 °C) for 2 hours. They showed that the bandgap varied with the sulfur content and that $\text{ZnO}_{1-x}\text{S}_x$ nanoparticles can photocatalyze the degradation of methyl orange. In 2017, Zhang *et al.* underlined the importance of doped zinc oxide to understand the intriguing ferromagnetic properties of certain d^0 components and used the same combustion method than Pandey.¹⁵⁸ As a consequence of oxidation by air, they measured a significant amount of sulfate groups at the surface of their nanoparticles using XPS. Abdullah *et al.* synthesized $\text{ZnO}_{1-x}\text{S}_x$ nanoparticles using zinc(II) acetate and thioacetamide for the photocatalysis of the hydrogen evolution reaction.¹⁵⁹ Gultom *et al.* in the same group also showed that nickel-doped $\text{ZnO}_{1-x}\text{S}_x$ nanoparticles were suitable for hydrogen production.¹⁶⁰

V.2.4. Other proposed transition metal oxysulfides

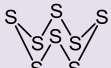

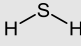

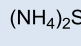

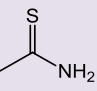

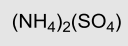

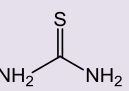

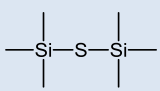

Crystalline nano-aggregates of cobalt nickel oxysulfides $(\text{CoNi})\text{O}_y\text{S}_z$ were claimed by Liu in 2013.¹⁶¹ However, the author noticed using XPS that sulfur only existed in oxidized species (S^{IV} , S^{VI}) in the material. By definition, it cannot be called “oxysulfide” but should rather be named “oxysulfate”.

In 2017, Liu *et al.* reported “fullerene-like oxysulfide hollow nanospheres”.¹⁶² The name is also abusively employed in this case, as the authors demonstrated that their nanoparticles are composed of crystalline nickel sulfide mixed with amorphous nickel oxide.

V.3. Conclusion

In light of the literature results, it seems that the synthesis of transition metal oxysulfides is much more challenging than lanthanide oxysulfides for both bulk and nanoscaled phases. It seems that transition metals do not easily allow the two different anions to form ternary $M_xO_yS_z$ crystalline structures (O^{II} and S^{-I} or S^{-II}).

However, three strategies can be envisaged to synthesize nanoscaled transition metal oxysulfides (Figure 91). First, the partial substitution of one anion by the other, as successfully carried out by Nelson *et al.* and Park *et al.* by replacing O^{II} by S^{-II} (Figure 91A).^{153,154} It required a water-free environment and more reactive species than elemental sulfur in amines, namely ammonium sulfide and hexamethyldisilathiane (Figure 90).

Elemental sulfur   <p>Good solubility and enhanced reactivity in amines. Reacts in graphite to form <i>in situ</i> CS₂.</p> <p>mp: 115 °C bp: 444 °C</p>	
Hydrogen sulfide   <p>Used as diluted gas in argon or nitrogen. Sulfiding and reducing.</p> <p>bp: -60 °C</p>	Ammonium sulfide   <p>Sold as aqueous solution (decomposes at room temperature). Allows O-S substitution in organic medium.</p> <p>Sol. in H₂O: 1281 g/L (293 K)</p>
Thioacetamide   <p>Good solubility in water and organic solvents.</p> <p>mp: 110 °C Sol. in H₂O: 163 g/L (298 K)</p>	Ammonium sulfate   <p>Leads to sulfates: reduction step required</p> <p>Sol. in H₂O: 74.4 g/L (293 K)</p>
Thiourea   <p>Good solubility in water and organic solvents.</p> <p>mp: 173 °C Sol. in H₂O: 142 g/L (298 K)</p>	Hexamethyldisilathiane   <p>Allows O-S substitution in organic medium (very sensitive to water)</p> <p>bp: 164 °C</p>

Nanoparticles synthesis source

Ln₂O₂S
 M_xO_yS_z (M = Co, Zn)
 No nanoparticles synthesis

Figure 90: Sulfur sources typically used for the sulfidation processes leading to oxysulfides (mp = melting point, bp = boiling point, Sol. = solubility).

In this thesis, great efforts were made to transpose our synthesis procedure using metal complexes and elemental sulfur in amines to directly get nanoparticles of transition metal oxysulfides. It represents the second strategy (Figure 91B). We thought that, starting from the

colloidal synthesis of $\text{Ln}_2\text{O}_2\text{S}$, we could obtain crystals or amorphous phases of $\text{M}_x\text{O}_y\text{S}_z$ of unknown compositions.

The third strategy is to change the targeted product and move to quaternary oxysulfides (Figure 91C). The exhaustive list presented in Table 9 is the proof that many compositions can be achieved this way, sometimes because the transition metal can be majorly bonded to one of the anion (selective bonding). In general, whatever the bonding type is in the solid, they represent a rich library of compositions whose properties can be promising in various fields, taking benefit for instance from the presence of two different cations just like in our $\text{Gd}_{2(1-y)}\text{Ce}_{2y}\text{O}_2\text{S}$ nanoparticles gadolinium is a stabilizing matrix and cerium an electronic disruptor.

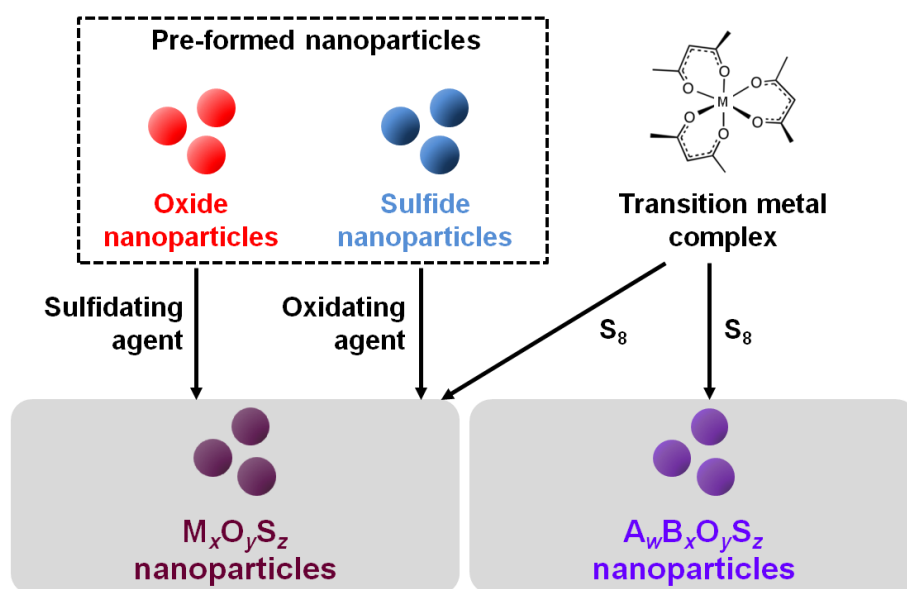


Figure 91: Strategies to get transition metal oxysulfide nanoparticles: substitution on pre-formed nanoparticles, $\text{Ln}_2\text{O}_2\text{S}$ nanoparticles synthesis adaptation to monometallic $\text{M}_x\text{O}_y\text{S}_z$ and bimetallic $\text{A}_w\text{B}_x\text{O}_y\text{S}_z$ oxysulfide nanoparticles.

In the next chapter, we investigate the transposition of the $\text{Ln}_2\text{O}_2\text{S}$ synthesis to the transition metal oxysulfide synthesis. Monometallic and bimetallic compositions were targeted using mainly first-row transition metals (Ti, V, Cr, Fe, Co, Cu, Zn) but indium and bismuth were also studied in the *p* block of the periodic table.

References

- (1) Hauser, O. Notiz Über Die Darstellung Der Oxysulfide Des Zirkoniums Und Thoriums. *Zeitschrift für Anorg. Chemie* **1907**, 53 (1), 74–77.
- (2) McCullough, J. D.; Brewer, L.; Bromley, L. A. The Crystal Structure of Zirconium Oxysulfide, ZrOS. *Acta Crystallogr.* **1948**, 1 (6), 287–289.
- (3) Jellinek, F. A Tetragonal Form of Zirconium Oxide Sulfide, ZrOS. *Acta Chem. Scand.* **1962**, 16, 791–792.
- (4) Stocks, K.; Eulenberger, G.; Hahn, H. Darstellung Und Kristallstruktur von HfOS. *Zeitschrift für Anorg. und Allg. Chemie* **1980**, 463 (1), 105–109.
- (5) Eisman, G. A.; Steinfink, H. The Synthesis of HfOS. *J. Solid State Chem.* **1982**, 43 (2), 225–226.
- (6) Kupčík, V. Die Kristallstruktur Des Kermesits, Sb₂S₂O. *Naturwissenschaften* **1967**, 54 (5), 114–114.
- (7) Boller, H. Die Kristallstruktur von Bi₂O₂Se. *Monatshefte für Chemie* **1973**, 104 (4), 916–919.
- (8) Koyama, E.; Nakai, I.; Nagashima, K. Crystal Chemistry of Oxide–chalcogenides. II. Synthesis and Crystal Structure of the First Bismuth Oxide–sulfide, Bi₂O₂S. *Acta Crystallogr. Sect. B Struct. Sci.* **1984**, 40 (2), 105–109.
- (9) Zhang, X.; Liu, Y.; Zhang, G.; Wang, Y.; Zhang, H.; Huang, F. Thermal Decomposition of Bismuth Oxysulfide from Photoelectric Bi₂O₂S to Superconducting Bi₄O₄S₃. *ACS Appl. Mater. Interfaces* **2015**, 7 (7), 4442–4448.
- (10) Meng, S.; Zhang, X.; Zhang, G.; Wang, Y.; Zhang, H.; Huang, F. Synthesis, Crystal Structure, and Photoelectric Properties of a New Layered Bismuth Oxysulfide. *Inorg. Chem.* **2015**, 54 (12), 5768–5773.
- (11) Meyer, B. K.; Merita, S.; Polity, A. On the Synthesis and Properties of Ternary Copper Oxide Sulfides (Cu₂O_{1-x}S_x). *Phys. status solidi - Rapid Res. Lett.* **2013**, 7 (5), 360–363.
- (12) Bakke, J. R.; Tanskanen, J. T.; Hägglund, C.; Pakkanen, T. A.; Bent, S. F. Growth Characteristics, Material Properties, and Optical Properties of Zinc Oxysulfide Films Deposited by Atomic Layer Deposition. *J. Vac. Sci. Technol. A Vacuum, Surfaces, Film.* **2012**, 30 (1), 01A135.
- (13) Deulkar, S. H.; Huang, J.-L.; Neumann-Spallart, M. Zinc Oxysulfide Thin Films Grown by Pulsed Laser Deposition. *J. Electron. Mater.* **2010**, 39 (5), 589–594.
- (14) Thankalekshmi, R. R.; Rastogi, A. C. Structure and Optical Band Gap of ZnO_{1-x}S_x Thin Films Synthesized by Chemical Spray Pyrolysis for Application in Solar Cells. *J. Appl. Phys.* **2012**, 112 (6), 063708.
- (15) Polat, İ.; Aksu, S.; Altunbaş, M.; Yılmaz, S.; Bacaksız, E. The Influence of Diffusion Temperature on the Structural, Optical and Magnetic Properties of Manganese-Doped Zinc Oxysulfide Thin Films. *J. Solid State Chem.* **2011**, 184 (10), 2683–2689.
- (16) Polat, İ.; Aksu, S.; Altunbaş, M.; Bacaksız, E. Microstructural, Optical and Magnetic Properties of Cobalt-Doped Zinc Oxysulfide Thin Films. *Mater. Chem. Phys.* **2011**, 130 (1–2), 800–805.
- (17) Polat, İ.; Aksu, S.; Altunbaş, M.; Bacaksız, E. The Influence of Diffusion Temperature on the Structural, Optical, and Magnetic Properties of Nickel-Doped Zinc Oxysulfide Thin Films. *Phys. Status Solidi* **2012**, 209 (1), 160–166.
- (18) Lee, D.-S.; Jeong, H.-D. Distinct Band Gap Tunability of Zinc Oxysulfide (ZnOS) Thin Films Synthesized from Thioacetate-Capped ZnO Nanocrystals. *Appl. Sci. Conver. Technol.* **2014**, 23 (6), 376–386.
- (19) Platzer-Björkman, C.; Törndahl, T.; Abou-Ras, D.; Malmström, J.; Kessler, J.; Stolt, L. Zn(O,S) Buffer Layers by Atomic Layer Deposition in Cu(In,Ga)Se₂ Based Thin Film Solar

- Cells: Band Alignment and Sulfur Gradient. *J. Appl. Phys.* **2006**, *100* (4), 044506.
- (20) Sinsermsuksakul, P.; Hartman, K.; Bok Kim, S.; Heo, J.; Sun, L.; Hejin Park, H.; Chakraborty, R.; Buonassisi, T.; Gordon, R. G. Enhancing the Efficiency of SnS Solar Cells via Band-Offset Engineering with a Zinc Oxysulfide Buffer Layer. *Appl. Phys. Lett.* **2013**, *102* (5), 053901.
 - (21) Inoue, M.; Ueda, Y.; Negishi, H.; Sasaki, M.; Ohba, T.; Kitano, Y.; Komura, Y. Effect of Sulphur Doping on the Electrical Properties of γ -Mo₄O₁₁ Crystals. *J. Less Common Met.* **1986**, *115* (2), 261–268.
 - (22) Olofinjana, B.; Egharevba, G. O.; Eleruja, M. A.; Jeynes, C.; Adediji, A. V.; Akinwunmi, O. O.; Taleatu, B. A.; Mordi, C. U.; Ajayi, E. O. B. Synthesis and Some Properties of Metal Organic Chemical Vapour Deposited Molybdenum Oxysulphide Thin Films. *J. Mater. Sci. Technol.* **2010**, *26* (6), 552–557.
 - (23) Tchangbedji, G.; Odink, D. A.; Ouvrard, G. V₂O₄S — a New Transition Metal Oxysulfide as Positive for Lithium Batteries. *J. Power Sources* **1993**, *44* (1–3), 577–581.
 - (24) Tchangbédji, G.; Prouzet, E. P.; Ouvrard, G. A New Soft Chemistry Synthesized Vanadium Oxysulfide. *Mater. Sci. Forum* **1994**, *152–153*, 319–322.
 - (25) Ouvrard, G.; Tchangbédji, G.; Deniard, P.; Prouzet, E. Structural, Physical and Electrochemical Characteristics of a Vanadium Oxysulfide, a Cathode Material for Lithium Batteries. *J. Power Sources* **1995**, *54* (2), 246–249.
 - (26) Meunier, G.; Dormoy, R.; Levasseur, A. New Positive-Electrode Materials for Lithium Thin Film Secondary Batteries. *Mater. Sci. Eng. B* **1989**, *3* (1–2), 19–23.
 - (27) Meunier, G.; Dormoy, R.; Levasseur, A. New Amorphous Titanium Oxysulfides Obtained in the Form of Thin Films. *Thin Solid Films* **1991**, *205* (2), 213–217.
 - (28) Levasseur, A.; Vinatier, P.; Gonbeau, D. X-Ray Photoelectron Spectroscopy: A Powerful Tool for a Better Characterization of Thin Film Materials. *Bull. Mater. Sci.* **1999**, *22* (3), 607–614.
 - (29) Gonbeau, D.; Guimon, C.; Pfister-Guillouzo, G.; Levasseur, A.; Meunier, G.; Dormoy, R. XPS Study of Thin Films of Titanium Oxysulfides. *Surf. Sci.* **1991**, *254* (1–3), 81–89.
 - (30) Dupin, J. .; Gonbeau, D.; Martin-Litas, I.; Vinatier, P.; Levasseur, A. Amorphous Oxysulfide Thin Films MO_yS_z (M=W, Mo, Ti) XPS Characterization: Structural and Electronic Peculiarities. *Appl. Surf. Sci.* **2001**, *173* (1–2), 140–150.
 - (31) Martinez, H.; Benayad, A.; Gonbeau, D.; Vinatier, P.; Pecquenard, B.; Levasseur, A. Influence of the Cation Nature of High Sulfur Content Oxysulfide Thin Films MO_yS_z (M=W, Ti) Studied by XPS. *Appl. Surf. Sci.* **2004**, *236* (1–4), 377–386.
 - (32) Lindic, M. H.; Martinez, H.; Benayad, A.; Pecquenard, B.; Vinatier, P.; Levasseur, A.; Gonbeau, D. XPS Investigations of TiO_yS_z Amorphous Thin Films Used as Positive Electrode in Lithium Microbatteries. *Solid State Ionics* **2005**, *176* (17–18), 1529–1537.
 - (33) Lindic, M.-H.; Pecquenard, B.; Vinatier, P.; Levasseur, A.; Martinez, H.; Gonbeau, D.; Petit, P.-E.; Ouvrard, G. Characterization of Rf Sputtered TiO_yS_z Thin Films. *Thin Solid Films* **2005**, *484* (1–2), 113–123.
 - (34) Dubois, V.; Pecquenard, B.; Soulé, S.; Martinez, H.; Le Cras, F. Dual Cation- and Anion-Based Redox Process in Lithium Titanium Oxysulfide Thin Film Cathodes for All-Solid-State Lithium-Ion Batteries. *ACS Appl. Mater. Interfaces* **2017**, *9* (3), 2275–2284.
 - (35) Yang, G.; Yan, Z.; Xiao, T. Low-Temperature Solvothermal Synthesis of Visible-Light-Responsive S-Doped TiO₂ Nanocrystal. *Appl. Surf. Sci.* **2012**, *258* (8), 4016–4022.
 - (36) Ramacharyulu, P. V. R. K.; Praveen Kumar, J.; Prasad, G. K.; Sreedhar, B. Sulphur Doped Nano TiO₂: Synthesis, Characterization and Photocatalytic Degradation of a Toxic Chemical in Presence of Sunlight. *Mater. Chem. Phys.* **2014**, *148* (3), 692–698.
 - (37) Smith, L. A. C.; Trudeau, M. L.; Provencher, M.; Smith, M. E.; Antonelli, D. M. Low-Temperature Synthesis and Electrochemical Properties of Mesoporous Titanium Oxysulfides.

- (38) Martin, I.; Vinatier, P.; Levasseur, A.; Dupin, J. .; Gonbeau, D. XPS Analysis of the Lithium Intercalation in Amorphous Tungsten Oxysulfide Thin Films. *J. Power Sources* **1999**, 81–82, 306–311.
- (39) Martin-Litas, I.; Vinatier, P.; Levasseur, A.; Dupin, J. .; Gonbeau, D.; Weill, F. Characterisation of r.f. Sputtered Tungsten Disulfide and Oxysulfide Thin Films. *Thin Solid Films* **2002**, 416 (1–2), 1–9.
- (40) Martin-Litas, I.; Vinatier, P.; Levasseur, A.; Dupin, J. C.; Gonbeau, D. Promising Thin Films (WO_{1.05}S₂ and WO_{1.35}S_{2.2}) as Positive Electrode Materials in Microbatteries. *J. Power Sources* **2001**, 97–98, 545–547.
- (41) Martin-Litas, I.; Vinatier, P.; Levasseur, A.; Dupin, J. C.; Gonbeau, D. Electrochemical Properties of Tungsten Oxysulphide Thin Films as Positive Electrodes for Lithium Microbatteries. *Bull. Mater. Sci.* **2003**, 26 (7), 673–681.
- (42) Abraham, K. M.; Pasquariello, D. M.; Willstaedt, E. B. Lithium/Molybdenum Oxysulfide Secondary Batteries. *J. Electrochem. Soc.* **1989**, 136 (2), 576.
- (43) Pasquariello, D. M.; Dunn, W. J.; Abraham, K. M. Rechargeable Lithium-Molybdenum Oxysulfide Batteries. In *Proceedings of the 34th International Power Sources Symposium*; IEEE, 1990; pp 94–97.
- (44) Abraham, K. M.; Pasquariello, D. M. Synthesis, Characterization, and Lithium Battery Applications of Molybdenum Oxysulfides. *Chem. Mater.* **1993**, 5 (9), 1233–1241.
- (45) Afanasiev, P.; Bezverkhy, I. Genesis of Vesicle-Like and Tubular Morphologies in Inorganic Precipitates: Amorphous Mo Oxysulfides. *J. Phys. Chem. B* **2003**, 107 (12), 2678–2683.
- (46) Genuit, D.; Bezverkhy, I.; Afanasiev, P. Solution Preparation of the Amorphous Molybdenum Oxysulfide MoOS₂ and Its Use for Catalysis. *J. Solid State Chem.* **2005**, 178 (9), 2759–2765.
- (47) Schmidt, E.; Weill, F.; Meunier, G.; Levasseur, A. New Amorphous Molybdenum Oxysulfides Obtained in the Form of Thin Films and Their Characterization by TEM. *Thin Solid Films* **1994**, 245 (1–2), 34–39.
- (48) Schmidt, E.; Meunier, G.; Levasseur, A. Electrochemical Properties of New Amorphous Molybdenum Oxysulfide Thin Films. *Solid State Ionics* **1995**, 76 (3–4), 243–247.
- (49) Buck, V. Lattice Parameters of Sputtered MoS₂ Films. *Thin Solid Films* **1991**, 198 (1–2), 157–167.
- (50) Levasseur, A.; Schmidt, E.; Meunier, G.; Gonbeau, D.; Benoist, L.; Pfister-Guillouzo, G. New Amorphous Molybdenum Oxysulfide Thin Films Their Characterization and Their Electrochemical Properties. *J. Power Sources* **1995**, 54 (2), 352–355.
- (51) Schmidt, E.; Sourisseau, C.; Meunier, G.; Levasseur, A. Amorphous Molybdenum Oxysulfide Thin Films and Their Physical Characterization. *Thin Solid Films* **1995**, 260 (1), 21–25.
- (52) Muijsers, J. C.; Weber, T.; Vanhardeveld, R. M.; Zandbergen, H. W.; Niemantsverdriet, J. W. Sulfidation Study of Molybdenum Oxide Using MoO₃/SiO₂/Si(100) Model Catalysts and Mo-IV₃-Sulfur Cluster Compounds. *J. Catal.* **1995**, 157 (2), 698–705.
- (53) Weber, T.; Muijsers, J. C.; van Wolput, J. H. M. C.; Verhagen, C. P. J.; Niemantsverdriet, J. W. Basic Reaction Steps in the Sulfidation of Crystalline MoO₃ to MoS₂, As Studied by X-Ray Photoelectron and Infrared Emission Spectroscopy. *J. Phys. Chem.* **1996**, 100 (33), 14144–14150.
- (54) Yufit, V.; Nathan, M.; Golodnitsky, D.; Peled, E. Thin-Film Lithium and Lithium-Ion Batteries with Electrochemically Deposited Molybdenum Oxysulfide Cathodes. *J. Power Sources* **2003**, 122 (2), 169–173.
- (55) Golodnitsky, D.; Yufit, V.; Nathan, M.; Shechtman, I.; Ripenbein, T.; Strauss, E.; Menkin, S.; Peled, E. Advanced Materials for the 3D Microbattery. *J. Power Sources* **2006**, 153 (2), 281–

- (56) Golodnitsky, D.; Nathan, M.; Yufit, V.; Strauss, E.; Freedman, K.; Burstein, L.; Gladkikh, A.; Peled, E. Progress in Three-Dimensional (3D) Li-Ion Microbatteries. *Solid State Ionics* **2006**, *177* (26–32), 2811–2819.
- (57) Qiao, Y.; Hu, X.; Liu, Y.; Liang, G.; Croft, M. C.; Huang, Y. Surface Modification of MoOxSy on Porous TiO₂ Nanospheres as an Anode Material with Highly Reversible and Ultra-Fast Lithium Storage Properties. *J. Mater. Chem. A* **2013**, *1* (47), 15128.
- (58) Stewart, M. J.; Media; Riddlewood; Price, J. A. Antimony Oxysulfide as a Polycondensation Catalyst. 3438945, 1969.
- (59) Marcon, J.-P. Oxysulfures De Plutonium. *Comptes Rendus Hebd. l'Académie des Sci. - Série C* **1967**, *264* (17), 1475–1476.
- (60) Tien, V.; Guittard, M.; Dugué, J.; Flahaut, J. Les Combinaisons U₂R_{2n}–2O_{2n}Sn+1 Formées Par Les Lanthanides Légers (R = Ce à Tb) Avec n = 2 et 3 et Dans Le Cas Du Lanthane Avec N = 2 à 6. *J. Solid State Chem.* **1988**, *73* (1), 11–18.
- (61) Okabe, T.; Van Tendeloo, G.; Van Landuyt, J.; Amelinckx, S.; Guittard, M. Long-Period Stacking Variants in the Homologous Series U₂La_{2n}–2O_{2n}Sn+1. *J. Solid State Chem.* **1988**, *72* (2), 376–389.
- (62) Cody, J. A.; Ibers, J. A. Synthesis and Characterization of the New Rare-Earth/Transition-Metal Oxysulfides La₆Ti₂S₈O₅ and La₄Ti₃S₄O₈. *J. Solid State Chem.* **1995**, *114* (2), 406–412.
- (63) Guittard, M.; Jaulmes, S.; Loireau-Lozac'h, A. M.; Mazurier, A.; Berguer, F.; Flahaut, J. Étude Du Système La₂S₃–La₂O₃–Ga₂O₃–Ga₂S₃: Description Structurale Des Phases Quaternaires et Approche Du Diagramme de Phase. *J. Solid State Chem.* **1985**, *58* (3), 276–289.
- (64) Selivanov, E. N.; Chumarev, V. M.; Gulyaeva, R. I.; Mar'evich, V. P.; Vershinin, A. D.; Pankratov, A. A.; Korepanova, E. S. Composition, Structure, and Thermal Expansion of Ca₃Fe₄S₃O₆ and CaFeSO. *Inorg. Mater.* **2004**, *40* (8), 845–850.
- (65) Delacotte, C.; Pérez, O.; Pautrat, A.; Berthebaud, D.; Hébert, S.; Suard, E.; Pelloquin, D.; Maignan, A. Magnetodielectric Effect in Crystals of the Noncentrosymmetric CaOFeS at Low Temperature. *Inorg. Chem.* **2015**, *54* (13), 6560–6565.
- (66) Salter, E. J. T.; Blandy, J. N.; Clarke, S. J. Crystal and Magnetic Structures of the Oxide Sulfides CaCoSO and BaCoSO. *Inorg. Chem.* **2016**, *55* (4), 1697–1701.
- (67) Sambrook, T.; Smura, C. F.; Clarke, S. J.; Ok, K. M.; Halasyamani, P. S. Structure and Physical Properties of the Polar Oxysulfide CaZnOS. *Inorg. Chem.* **2007**, *46* (7), 2571–2574.
- (68) Valldor, M.; Rößler, U. K.; Prots, Y.; Kuo, C.-Y.; Chiang, J.-C.; Hu, Z.; Pi, T.-W.; Kniep, R.; Tjeng, L. H. Synthesis and Characterization of Ba[CoSO]: Magnetic Complexity in the Presence of Chalcogen Ordering. *Chem. - A Eur. J.* **2015**, *21* (30), 10821–10828.
- (69) Broadley, S.; Gál, Z. A.; Corà, F.; Smura, C. F.; Clarke, S. J. Vertex-Linked ZnO₂S₂ Tetrahedra in the Oxysulfide BaZnOS: A New Coordination Environment for Zinc in a Condensed Solid. *Inorg. Chem.* **2005**, *44* (24), 9092–9096.
- (70) Guittard, M.; Vovan, T.; Julien-Pouzol, M.; Jaulmes, S.; Laruelle, P.; Flahaut, J. Mise En Evidence et Etude Structurale d'une Famille de Composés En Feuillet de Formule Générale (UO)₂RS₃ (R = Gd à Lu et Y). *Zeitschrift für Anorg. und Allg. Chemie* **1986**, *540* (9–10), 59–66.
- (71) Jaulmes, S.; Julien-Pouzol, M.; Dugué, J.; Laruelle, P.; Vovan, T.; Guittard, M. Structure de l'oxysulfure d'uranium et de Lutécium, (UOS)₄LuS. *Acta Crystallogr. Sect. C Cryst. Struct. Commun.* **1990**, *46* (7), 1205–1207.
- (72) Goga, M.; Seshadri, R.; Ksenofontov, V.; Gülich, P.; Tremel, W. Ln₂Ti₂S₂O₅ (Ln = Nd, Pr, Sm): A Novel Series of Defective Ruddlesden–Popper Phases. *Chem. Commun.* **1999**, *7* (11),

- (73) Boyer, C.; Deudon, C.; Meerschaut, A. Synthesis and Structure Determination of the New $\text{Sm}_2\text{Ti}_2\text{O}_5\text{S}_2$ Compound. *Comptes Rendus l'Académie des Sci. - Ser. IIC* **1999**, 2 (2), 93–99.
- (74) Meignen, V.; Lafond, A.; Cario, L.; Deudon, C.; Meerschaut, A. A New Lanthanum Titanium Oxysulfide, $\text{La}_{16}\text{Ti}_5\text{S}_{17+x}\text{O}_{17}$, with $x = 0.75$ (9). *Acta Crystallogr. Sect. C Cryst. Struct. Commun.* **2003**, 59 (7), i63–i64.
- (75) Tranchitella, L. J.; Fettingner, J. C.; Eichhorn, B. W. Synthesis and Structural Analysis of $\text{Sr}_{5.8}\text{La}_{4.4}\text{Ti}_{7.8}\text{S}_{24}\text{O}_4$ and $\text{La}_{14}\text{Ti}_8\text{S}_{33}\text{O}_4$: Two New Oxysulfides Containing a Common $[(\text{Ti}_4\text{S}_2\text{O}_4)(\text{TiS}_6)]_{12}$ -Layer. *Chem. Mater.* **1996**, 8 (9), 2265–2271.
- (76) Cario, L.; Deudon, C.; Meerschaut, A.; Rouxel, J. Synthesis and Structure Determination of $\text{La}_8\text{Ti}_{10}\text{S}_{24}\text{O}_4$. *J. Solid State Chem.* **1998**, 136 (1), 46–50.
- (77) Tranchitella, L. J.; Fettingner, J. C.; Heller-Zeisler, S. F.; Eichhorn, B. W. $\text{La}_{8+x}\text{Ti}_{8+y}\text{S}_{24}\text{O}_4$ Compounds Where $x + y \leq 2$: A Series of Phases with Mixed-Valent Titanium. *Chem. Mater.* **1998**, 10 (8), 2078–2085.
- (78) Deudon, C.; Meerschaut, A.; Cario, L.; Rouxel, J. Preparation and Crystal Structure Determination of $\text{La}_{20}\text{Ti}_{11}\text{S}_{44}\text{O}_6$. *J. Solid State Chem.* **1995**, 120 (1), 164–169.
- (79) Cody, J. A.; Deudon, C.; Cario, L.; Meerschaut, A. Synthesis and Structure Determination of a New Cerium Titanium Oxysulfide [$\text{Ce}_{20}\text{Ti}_{11}\text{S}_{44}\text{O}_6$]. *Mater. Res. Bull.* **1997**, 32 (9), 1181–1192.
- (80) Boyer-Candalen, C.; Deudon, C.; Meerschaut, A. Synthesis and Structure Determination of $\text{Nd}_{16}\text{Ti}_5\text{S}_{17}\text{O}_{17}$. *J. Solid State Chem.* **2000**, 152 (2), 554–559.
- (81) Meignen, V.; Meerschaut, A.; Cario, L.; Lafond, A. Synthesis and Crystal Structure of a New Oxysulfide $\text{Gd}_{6+x}\text{Ti}_4\text{XS}_{10}\text{YO}_{6+y}$ (Where $x \sim 0.04$ and $y \sim 0.27$). *Zeitschrift für Naturforsch. - Sect. B J. Chem. Sci.* **2004**, 59 (9), 4–9.
- (82) Vovan, T.; Dugué, J.; Guittard, M. Oxysulfures Mixtes de Vanadium et de Terre Rare de Formule Générale $\text{R}_5\text{V}_3\text{S}_6\text{O}_7$ (R = Lanthane à Néodyme). *Comptes Rendus l'Académie des Sci. - Série II* **1981**, 292 (13), 957–959.
- (83) Dugué, J.; Tien, V.; Laruelle, P. Structure de l'oxysulfure de Lanthane et de Vanadium, $\text{La}_5\text{V}_3\text{O}_7\text{S}_6$. *Acta Crystallogr. Sect. C Cryst. Struct. Commun.* **1985**, 41 (8), 1146–1148.
- (84) Vovan, T.; Dugué, J.; Guittard, M. Oxysulfures Mixtes de Chrome III et de Terres Rares. *Mater. Res. Bull.* **1978**, 13, 1163–1166.
- (85) Dugué, J.; Vovan, T.; Villers, J. Etude Structurale Des Oxysulfures de Chrome(III) et de Terres Rares. I. Structure de l'Oxysulfure LaCrOS_2 . *Acta Crystallogr.* **1980**, B36, 1291–1294.
- (86) Dugué, J.; Vovan, T.; Villers, J. Etude Structurale Des Oxysulfures de Chrome(III) et de Terres Rares. II. Structure de l'Oxysulfure CeCrOS_2 . *Acta Crystallogr.* **1980**, B36, 1294–1297.
- (87) Ijjaali, I.; Deng, B.; Ibers, J. A. Seven New Rare-Earth Transition-Metal Oxychalcogenides: Syntheses and Characterization of $\text{Ln}_4\text{MnOSe}_6$ (Ln=La, Ce, Nd), $\text{Ln}_4\text{FeOSe}_6$ (Ln=La, Ce, Sm), and La_4MnOS_6 . *J. Solid State Chem.* **2005**, 178 (5), 1503–1507.
- (88) Mayer, J. M.; Schneemeyer, L. F.; Siegrist, T.; Waszczak, J. V.; Van Dover, B. New Layered Iron-Lanthanum-Oxide-Sulfide and -Selenide Phases: $\text{Fe}_2\text{La}_2\text{O}_3\text{E}_2$ (E= S, Se). *Angew. Chemie Int. Ed. English* **1992**, 31 (12), 1645–1647.
- (89) Charkin, D. O.; Plotnikov, V. A.; Sadakov, A. V.; Omel'yanovskii, O. E.; Kazakov, S. M. Synthesis of Novel Rare Earth—Iron Oxide Chalcogenides with the $\text{La}_2\text{Fe}_2\text{O}_3\text{Se}_2$ Structure. *J. Alloys Compd.* **2011**, 509 (27), 7344–7348.
- (90) Palazzi, M. Préparation et Affinement de La Structure de $(\text{LaO})\text{CuS}$. *Comptes Rendus Hebd. l'Académie des Sci. - Série II* **1981**, 292, 789–791.
- (91) Doussier-Brochard, C.; Chavillon, B.; Cario, L.; Jobic, S. Synthesis of P-Type Transparent

- LaOCuS Nanoparticles via Soft Chemistry. *Inorg. Chem.* **2010**, *49* (7), 3074–3076.
- (92) Huang, F. Q.; Brazis, P.; Kannewurf, C. R.; Ibers, J. A. Synthesis, Structure, Electrical Conductivity, and Band Structure of the Rare-Earth Copper Oxychalcogenide $\text{La}_5\text{Cu}_6\text{O}_4\text{S}_7$. *J. Solid State Chem.* **2000**, *155* (2), 366–371.
 - (93) Ueda, K.; Takafuji, K.; Hosono, H. Preparation and Crystal Structure Analysis of CeCuOS . *J. Solid State Chem.* **2003**, *170* (1), 182–187.
 - (94) Chan, G. H.; Deng, B.; Bertoni, M.; Ireland, J. R.; Hersam, M. C.; Mason, T. O.; Van Duyne, R. P.; Ibers, J. A. Syntheses, Structures, Physical Properties, and Theoretical Studies of CeM_xOS ($\text{M} = \text{Cu}, \text{Ag}$; $x \approx 0.8$) and CeAgOS . *Inorg. Chem.* **2006**, *45* (20), 8264–8272.
 - (95) Lauxmann, P.; Schleid, T. CuPrOS: Kein Einprägsames Akronym, Vielmehr Ein Echtes Quaternäres Chalkogenid Mit Aufgefüllter PbFCl-Struktur. *Zeitschrift für Anorg. und Allg. Chemie* **2000**, *626* (11), 2253–2255.
 - (96) Popovkin, B. A.; Kusainova, A. M.; Dolgikh, V. A.; Akselrud, L. G. New Layered Phases of the MOCuX ($\text{M} = \text{Ln}, \text{Bi}$; $\text{X} = \text{S}, \text{Se}, \text{Te}$) Family: A Geometric Approach to the Explanation of Phase Stability. *Russ. J. Inorg. Chem.* **1998**, *43* (10), 1471–1475.
 - (97) Kusainova, A. M.; Berdonosov, P. S.; Akselrud, L. G.; Kholodkovskaya, L. N.; Dolgikh, V. A.; Popovkin, B. A. New Layered Compounds with the General Composition (MO) (CuSe), Where $\text{M} = \text{Bi}, \text{Nd}, \text{Gd}, \text{Dy}$, and BiOCuS : Syntheses and Crystal Structure. *J. Solid State Chem.* **1994**, *112* (1), 189–191.
 - (98) Sheets, W. C.; Stampler, E. S.; Kabbour, H.; Bertoni, M. I.; Cario, L.; Mason, T. O.; Marks, T. J.; Poeppelmeier, K. R. Facile Synthesis of BiCuOS by Hydrothermal Methods. *Inorg. Chem.* **2007**, *46* (25), 10741–10748.
 - (99) Brennan, T. D.; Ibers, J. A. Metal-Metal Bonding and Mixed-Valent Tantalum in $\text{La}_2\text{Ta}_3\text{S}_2\text{O}_8$. *J. Solid State Chem.* **1992**, *98* (1), 82–89.
 - (100) Cario, L.; Kabbour, H.; Guillot-Deudon, C.; Meerschaut, A. A Mixed-Valent Niobium Oxy sulfide, $\text{La}_2\text{Nb}_3\text{S}_2\text{O}_8$. *Acta Crystallogr. Sect. C Cryst. Struct. Commun.* **2003**, *59* (6), i55–i56.
 - (101) Cario, L.; Popa, A. F.; Lafond, A.; Guillot-Deudon, C.; Kabbour, H.; Meerschaut, A.; Clarke, S. J.; Adamson, P. Cation Deficient Layered Ruddlesden–Popper-Related Oxy sulfides $\text{La}_2\text{LnMS}_2\text{O}_5$ ($\text{Ln} = \text{La}, \text{Y}$; $\text{M} = \text{Nb}, \text{Ta}$). *Inorg. Chem.* **2007**, *46* (23), 9584–9590.
 - (102) Boyer-Candalen, C.; Meerschaut, A. Synthesis and Structure Determination of the New Compound $\text{La}_{\sim 10.8}\text{Nb}_5\text{O}_{20}\text{S}_{10}$. *J. Solid State Chem.* **2000**, *152* (2), 348–352.
 - (103) Altmannshofer, S.; Johrendt, D. Synthesis, Crystal Structure and Magnetism of the New Oxy sulfide $\text{Ce}_3\text{NbO}_4\text{S}_3$. *Zeitschrift für Anorg. und Allg. Chemie* **2008**, *634* (8), 1361–1364.
 - (104) Boyer-Candalen, C.; Meerschaut, A.; Palvadeau, P. Crystal Structure Determination of the New Compound $\text{Sm}_3\text{NbO}_4\text{S}_3$. *Mater. Res. Bull.* **2000**, *35* (10), 1593–1601.
 - (105) Kabbour, H.; Cario, L.; Deudon, C.; Meerschaut, A. A Gadolinium and Niobium Oxide Sulfide, $\text{Gd}_3\text{NbS}_3\text{O}_4$. *Acta Crystallogr. Sect. E Struct. Reports Online* **2003**, *59* (7), i101–i102.
 - (106) Guo, G.; Wang, Y.; Chen, J.; Zhuang, H.; Huang, J.; Zhang, Q. Samarium Tantalum Oxy sulfide, $\text{Sm}_2\text{Ta}_3\text{S}_2\text{O}_8$. *Acta Crystallogr. Sect. C Cryst. Struct. Commun.* **1995**, *51* (10), 1964–1966.
 - (107) Palazzi, M.; Carcaly, C.; Flahaut, J. Un Nouveau Conducteur Ionique $(\text{LaO})\text{AgS}$. *J. Solid State Chem.* **1980**, *35* (2), 150–155.
 - (108) Palazzi, M.; Jaulmes, S. Structure Du Conducteur Ionique $(\text{LaO})\text{AgS}$. *Acta Crystallogr. Sect. B Struct. Crystallogr. Cryst. Chem.* **1981**, *37* (7), 1337–1339.
 - (109) BaQais, A.; Curutchet, A.; Ziani, A.; Ait Ahsaine, H.; Sautet, P.; Takanabe, K.; Le Bahers, T. Bismuth Silver Oxy sulfide for Photoconversion Applications: Structural and Optoelectronic

- Properties. *Chem. Mater.* **2017**, 29 (20), 8679–8689.
- (110) Jaulmes, S. Oxysulfure de Gallium et de Lanthane LaGaOS 2. *Acta Crystallogr. Sect. B Struct. Crystallogr. Cryst. Chem.* **1978**, 34 (8), 2610–2612.
 - (111) Jaulmes, S.; Mazurier, A.; Guittard, M. Structure de l'oxypentasulfure de Gallium et de Trilanthane, GaLa₃OS₅. *Acta Crystallogr. Sect. C Cryst. Struct. Commun.* **1983**, 39 (12), 1594–1597.
 - (112) Mazurier, A.; Guittard, M.; Jaulmes, S. Structure Cristalline d'un Oxysulfure Isotype de La Mélilite, La_{3,33}Ga₆O₂S₁₂. *Acta Crystallogr. Sect. B Struct. Crystallogr. Cryst. Chem.* **1982**, 38 (2), 379–382.
 - (113) Jaulmes, S.; Godlewski, E.; Palazzi, M.; Etienne, J. Deux Structures Isotypes à Sites Anioniques et Cationiques Lacunaires: (CeO)₄Ga₂S₅ et (LaO)₄As₂S₅. *Acta Crystallogr. Sect. B Struct. Crystallogr. Cryst. Chem.* **1982**, 38 (6), 1707–1710.
 - (114) Guittard, M.; Benazeth, S.; Dugue', J.; Jaulmes, S.; Palazzi, M.; Laruelle, P.; Flahaut, J. Oxysulfides and Oxyselenides in Sheets, Formed by a Rare Earth Element and a Second Metal. *J. Solid State Chem.* **1984**, 51 (2), 227–238.
 - (115) Kabbour, H.; Cario, L.; Moëlo, Y.; Meerschaut, A. Synthesis, X-Ray and Optical Characterizations of Two New Oxysulfides: LaInS₂O and La₅In₃S₉O₃. *J. Solid State Chem.* **2004**, 177 (4–5), 1053–1059.
 - (116) Gastaldi, L.; Carré, D.; Pardo, M. P. Structure de l'oxysulfure d'indium et de Lanthane In₆La₁₀O₆S₁₇. *Acta Crystallogr. Sect. B Struct. Crystallogr. Cryst. Chem.* **1982**, 38 (9), 2365–2367.
 - (117) Céolin, R.; Rodier, N. Structure Cristalline de l'oxysulfure de Cérium et de Bismuth CeBiOS 2. *Acta Crystallogr. Sect. B Struct. Crystallogr. Cryst. Chem.* **1976**, 32 (5), 1476–1479.
 - (118) Pardo, M.-P.; Céolin, R.; Guittard, M. Sur Les Oxysulfures à Deux Éléments Métalliques, Terre Rare et Bismuth, Ou Terre Rare et Antimoine. *Comptes rendus Hebd. l'Académie des Sci. - Série C* **1976**, 283, 735–738.
 - (119) Tanryverdiev, V. S.; Aliev, O. M.; Aliev, I. I. Synthesis and Physicochemical Properties of LnBiOS₂. *Inorg. Mater.* **1995**, 31 (11), 1361–1363.
 - (120) Aliev, O. M.; Tanryverdiev, V. S. The Synthesis and Some Physical Properties of Rare-Earth Oxysulfostibnites. *Zhurnal Neorg. Khimii* **1997**, 42 (11), 1918–1921.
 - (121) So, W.-W.; LaCour, A.; Aliev, V. O.; Dorhout, P. K. Synthesis and Characterization of a New Quaternary Lanthanum Oxythioantimonite: La₆Sb₄O₁₂S₃. *J. Alloys Compd.* **2004**, 374 (1–2), 234–239.
 - (122) Nakai, I.; Nagashima, K.; Koto, K.; Morimoto, N. Crystal Chemistry of Oxide–chalcogenide. I. The Crystal Structure of Sarabauite CaSb₁₀O₁₀S₆. *Acta Crystallogr. Sect. B Struct. Crystallogr. Cryst. Chem.* **1978**, 34 (12), 3569–3572.
 - (123) Tillinski, R.; Näther, C.; Winkler, B.; Bensch, W. Synthesis and Crystal Structure of K₆Ti₆S₁₈O: A New Coordination Compound Containing Discrete Ti₆O Units in a Chalcogenide Environment. *Zeitschrift für Anorg. und Allg. Chemie* **2001**, 627 (12), 2576–2580.
 - (124) Sutorik, A. C.; Kanatzidis, M. G. Ba₆Ti₅S₁₅O: A New Metal/Oxysulfide Resulting from the Inclusion of BaO into the BaTiS₃ Structure Type. *Chem. Mater.* **1994**, 6 (10), 1700–1704.
 - (125) Petrova, S. A.; Mar'evich, V. P.; Zakharov, R. G.; Selivanov, E. N.; Chumarev, V. M.; Udoveva, L. Y. Crystal Structure of Zinc Calcium Oxysulfide. *Dokl. Chem.* **2003**, 393 (1–3), 255–258.
 - (126) Orlandi, P.; Moëlo, Y.; Meerschaut, A.; Palvadeau, P. Lead-Antimony Sulfosalts from Tuscany (Italy). I. Scainiite, Pb₁₄Sb₃₀S₅₄O₅, the First Pb-Sb Oxy-Sulfosalt, from Buca Della Vena Mine. *Eur. J. Mineral.* **1999**, 11 (6), 949–954.

- (127) Umarji, A. M.; Rao, G. V. S.; Sankaranarayana, V.; Rangarajan, G.; Srinivasan, R. Synthesis and Properties of O-Containing Chevrel Phases, $AxMo_6S_6O_2$ ($A=Co, Ni, Cu$ and Pb). *Mater. Res. Bull.* **1980**, *15* (7), 1025–1031.
- (128) Selwyn, L. .; McKinnon, W. .; Dahn, J. . Lack of Oxygen Substitution in the Chevrel Compound Mo_6S_8 . *Solid State Commun.* **1987**, *64* (7), 1025–1028.
- (129) Teske, C. L. Über Oxidsulfide Mit Akermanitstruktur $CaLaGa_3S_6O$, $SrLaGa_3S_6O$, $La_2ZnGa_2S_6O$ Und $Sr_2ZnGe_2S_6O$. *Zeitschrift für Anorg. und Allg. Chemie* **1985**, *531* (12), 52–60.
- (130) Endo, T.; Doi, Y.; Wakeshima, M.; Suzuki, K.; Matsuo, Y.; Tezuka, K.; Ohtsuki, T.; Shan, Y. J.; Hinatsu, Y. Magnetic Properties of the Melilite-Type Oxysulfide $Sr_2MnGe_2S_6O$: Magnetic Interactions Enhanced by Anion Substitution. *Inorg. Chem.* **2017**, *56* (5), 2459–2466.
- (131) Yu, R.; Wang, J.; Zhang, M.; Zhang, J.; Yuan, H.; Su, Q. A New Blue-Emitting Phosphor of Ce^{3+} -Activated $CaLaGa_3S_6O$ for White-Light-Emitting Diodes. *Chem. Phys. Lett.* **2008**, *453* (4–6), 197–201.
- (132) Zhang, G.; Wang, J.; Chen, Y.; Su, Q. Two-Color Emitting of Ce^{3+} and Tb^{3+} Co-Doped $CaLaGa_3S_6O$ for UV LEDs. *Opt. Lett.* **2010**, *35* (14), 2382.
- (133) Zhang, G.; Liu, C.; Wang, J.; Kuang, X.; Su, Q. An Intense Charge Transfer Broadband Sensitized Near-Infrared Emitting $CaLaGa_3S_6O:Yb^{3+}$ Phosphor Suitable for Solar Spectral Converter. *Opt. Express* **2011**, *19* (24), 24314.
- (134) Yu, R.; An, Y.; Wang, C.; Wang, H.; Wu, Y.; Chen, J.; Wang, Z.; Zhang, J. Tunable Yellowish-Green to Green $(Ca_{1-x}Sr_x)LaGa_3S_6O:Eu^{2+}$ Phosphors for Potential LED Application. *Electrochem. Solid-State Lett.* **2012**, *15* (1), J1.
- (135) Zhang, G.; Liu, C.; Wang, J.; Kuang, X.; Su, Q. A Dual-Mode Solar Spectral Converter $CaLaGa_3S_6O:Ce^{3+}, Pr^{3+}$: UV-Vis-NIR Luminescence Properties and Solar Spectral Converting Mechanism. *J. Mater. Chem.* **2012**, *22* (5), 2226–2232.
- (136) Zhang, X.; Zhang, J.; Xu, J.; Su, Q. Luminescent Properties of Eu^{2+} -Activated $SrLaGa_3S_6O$ Phosphor. *J. Alloys Compd.* **2005**, *389* (1–2), 247–251.
- (137) Yu, R.; Deng, B.; Zhang, G.; An, Y.; Zhang, J.; Wang, J. Luminescence Properties of Ce^{3+} -Activated $SrLaGa_3S_6O$ and Application in White LEDs. *J. Electrochem. Soc.* **2011**, *158* (8), J255.
- (138) Zhang, G.; Cui, Q.; Liu, G. Efficient Near-Infrared Quantum Cutting and Downshift in Ce^{3+} - Pr^{3+} Codoped $SrLaGa_3S_6O$ Suitable for Solar Spectral Converter. *Opt. Mater.* **2016**, *53*, 214–217.
- (139) Zhu, W. J.; Hor, P. H. Unusual Layered Transition-Metal Oxysulfides: $Sr_2Cu_2MO_2S_2$ ($M=Mn, Zn$). *J. Solid State Chem.* **1997**, *130* (2), 319–321.
- (140) Zhu, W. J.; Hor, P. H.; Jacobson, A. J.; Crisci, G.; Albright, T. A.; Wang, S.-H.; Vogt, T. $A_2Cu_2CoO_2S_2$ ($A = Sr, Ba$), A Novel Example of a Square-Planar CoO_2 Layer. *J. Am. Chem. Soc.* **1997**, *119* (50), 12398–12399.
- (141) Smura, C. F.; Parker, D. R.; Zbiri, M.; Johnson, M. R.; Gál, Z. A.; Clarke, S. J. High-Spin Cobalt(II) Ions in Square Planar Coordination: Structures and Magnetism of the Oxysulfides $Sr_2CoO_2Cu_2S_2$ and $Ba_2CoO_2Cu_2S_2$ and Their Solid Solution. *J. Am. Chem. Soc.* **2011**, *133* (8), 2691–2705.
- (142) Ottschi, K.; Ogino, H.; Shimoyama, J.; Kishio, K. New Candidates for Superconductors; A Series of Layered Oxysulfides $(Cu_2S_2)(Sr_{n+1}MnO_{3n-1})$. *J. Low Temp. Phys.* **1999**, *117* (3/4), 729–733.
- (143) Zhu, W. J.; Hor, P. H. Crystal Structure of New Layered Oxysulfides: $Sr_3Cu_2Fe_2O_5S_2$ and Sr_2CuMO_3S ($M=Cr, Fe, In$). *J. Solid State Chem.* **1997**, *134* (1), 128–131.
- (144) Ogino, H.; Shimoyama, J.; Kishio, K.; Katsura, Y.; Tsuboi, M.; Yamanoi, K.; Cadatal-

- Raduban, M.; Nakazato, T.; Shimizu, T.; Sarukura, N. Excitonic Luminescence in Two-Dimensionally Confined Layered Sulfide Oxides. *Appl. Phys. Lett.* **2012**, *101* (19), 191901.
- (145) Zhu, W. J.; Hor, P. H. Sr₂CuGaO₃S, a Rare Example of Square Pyramidal Gallium. *Inorg. Chem.* **1997**, *36* (17), 3576–3577.
- (146) Blandy, J. N.; Abakumov, A. M.; Christensen, K. E.; Hadermann, J.; Adamson, P.; Cassidy, S. J.; Ramos, S.; Free, D. G.; Cohen, H.; Woodruff, D. N.; Thompson, A. L.; Clarke, S. J. Soft Chemical Control of the Crystal and Magnetic Structure of a Layered Mixed Valent Manganite Oxide Sulfide. *APL Mater.* **2015**, *3* (4), 041520.
- (147) Carcaly, C.; Flahaut, J.; Guittard, M.; Palazzi, M. Un Composé à Structure Feuilletée (LaO)4Ag1,5Ga1,5S5. *Mater. Res. Bull.* **1981**, *16* (11), 1367–1374.
- (148) Meignen, V.; Cario, L.; Lafond, A.; Moëlo, Y.; Guillot-Deudon, C.; Meerschaut, A. Crystal Structures of Two New Oxysulfides La₅Ti₂MS₅O₇ (M=Cu, Ag): Evidence of Anionic Segregation. *J. Solid State Chem.* **2004**, *177* (8), 2810–2817.
- (149) Suzuki, T.; Hisatomi, T.; Teramura, K.; Shimodaira, Y.; Kobayashi, H.; Domen, K. A Titanium-Based Oxysulfide Photocatalyst: La₅Ti₂MS₅O₇ (M = Ag, Cu) for Water Reduction and Oxidation. *Phys. Chem. Chem. Phys.* **2012**, *14* (44), 15475.
- (150) Meignen, V.; Meerschaut, A.; Cario, L.; Lafond, A. Synthesis and Crystal Structure of a New Oxychalcogenide La₅Ti_{3.25}Zr_{0.25}S₅O_{9.25}. *J. Solid State Chem.* **2005**, *178* (5), 1637–1643.
- (151) Rutt, O. J.; Hill, T. L.; Gál, Z. A.; Hayward, M. A.; Clarke, S. J. The Cation-Deficient Ruddlesden–Popper Oxysulfide Y₂Ti₂O₅S₂ as a Layered Sulfide: Topotactic Potassium Intercalation To Form KY₂Ti₂O₅S₂. *Inorg. Chem.* **2003**, *42* (24), 7906–7911.
- (152) Yee, C.-H.; Birol, T.; Kotliar, G. Guided Design of Copper Oxysulfide Superconductors. *Europhys. Lett.* **2015**, *111* (1), 17002.
- (153) Nelson, A.; Fritz, K. E.; Honrao, S.; Hennig, R. G.; Robinson, R. D.; Suntivich, J. Increased Activity in Hydrogen Evolution Electrocatalysis for Partial Anionic Substitution in Cobalt Oxysulfide Nanoparticles. *J. Mater. Chem. A* **2016**, *4* (8), 2842–2848.
- (154) Park, J.; Zheng, H.; Jun, Y.; Alivisatos, A. P. Hetero-Epitaxial Anion Exchange Yields Single-Crystalline Hollow Nanoparticles. *J. Am. Chem. Soc.* **2009**, *131* (39), 13943–13945.
- (155) Wang, W.; Dahl, M.; Yin, Y. Hollow Nanocrystals through the Nanoscale Kirkendall Effect. *Chem. Mater.* **2013**, *25* (8), 1179–1189.
- (156) Pandey, S. K.; Pandey, S.; Pandey, A. C.; Mehrotra, G. K. Zinc Oxysulfide Ternary Alloy Nanocrystals: A Bandgap Modulated Photocatalyst. *Appl. Phys. Lett.* **2013**, *102* (23), 1–6.
- (157) Pandey, S. K.; Pandey, S.; Parashar, V.; Yadav, R. S.; Mehrotra, G. K.; Pandey, A. C. Bandgap Engineering of Colloidal Zinc Oxysulfide via Lattice Substitution with Sulfur. *Nanoscale* **2014**, *6* (3), 1602–1606.
- (158) Zhang, H.; Liu, G.; Cao, Y.; Chen, J.; Shen, K.; Kumar, A.; Xu, M.; Li, Q.; Xu, Q. The Magnetic and Adsorption Properties of ZnO_{1-x}S_x Nanoparticles. *Phys. Chem. Chem. Phys.* **2017**, *19* (39), 26918–26925.
- (159) Abdullah, H.; Kuo, D.-H.; Chen, X. High Efficient Noble Metal Free Zn(O,S) Nanoparticles for Hydrogen Evolution. *Int. J. Hydrogen Energy* **2017**, *42* (9), 5638–5648.
- (160) Gultom, N. S.; Abdullah, H.; Kuo, D.-H. Enhanced Photocatalytic Hydrogen Production of Noble-Metal Free Ni-Doped Zn(O,S) in Ethanol Solution. *Int. J. Hydrogen Energy* **2017**, *42* (41), 25891–25902.
- (161) Liu, L. Nano-Aggregates of Cobalt Nickel Oxysulfide as a High-Performance Electrode Material for Supercapacitors. *Nanoscale* **2013**, *5* (23), 11615.
- (162) Liu, J.; Yang, Y.; Ni, B.; Li, H.; Wang, X. Fullerene-Like Nickel Oxysulfide Hollow Nanospheres as Bifunctional Electrocatalysts for Water Splitting. *Small* **2017**, *13* (6), 1602637.

Chapter VI

Attempts at transposing $\text{Ln}_2\text{O}_2\text{S}$ synthesis to nanoscaled transition metal oxysulfides

Table of contents

VI.1. Motivation	197
VI.2. Synthesis of bimetallic $\text{Ln}_w\text{M}_x\text{O}_y\text{S}_z$ oxysulfide nanoparticles.....	199
VI.2.1. Titanium-, vanadium- and chromium-based bimetallic oxysulfides	199
VI.2.2. Iron-, cobalt- and copper-based bimetallic oxysulfides	203
VI.2.3. Gadolinium-indium bimetallic oxysulfide	205
VI.2.3. Conclusion	206
VI.3. Synthesis of $\text{M}_x\text{O}_y\text{S}_z$ nanoparticles: first attempts.....	208
VI.3.1. Results from powder XRD patterns	208
VI.3.2. First-row transition metals	208
VI.3.3. Attempts with zirconium, indium and bismuth.....	210
VI.3.4. Conclusion	212
VI.4. Conclusion	213
References	214

VI.1. Motivation

This chapter is dedicated to the synthesis of oxysulfide nanoparticles containing transition metals. At the beginning of the project, our experience on the formation mechanism of lanthanide oxysulfide nanoparticles was much lower developed than exposed in chapter 3. As we progressed on this pathway, we also performed a series of tests to attempt the colloidal synthesis of monometallic and bimetallic transition metal oxysulfides. This chapter, more than the others, is a source of reflexion and perspectives.

As mentioned in the previous chapter, there is a wide range of compositions that were never achieved at the nanoscale (Figure 86). For transition metals, only cobalt and zinc oxysulfide nanoparticles were obtained with new synthetic strategies dealing with strong sulfidating agents (S^{II} in $(NH_4)_2S$ and hexamethyldisilathiane).

Transition metal oxysulfide nanoparticles																	
H Hydrogen	<div> <div></div> d-block transition metals <div></div> Nanoscaled $M_xO_yS_z$ (M = transition metal) </div>																He Helium
Li Lithium	Be Beryllium											B Boron	C Carbon	N Nitrogen	O Oxygen	F Fluorine	Ne Neon
Na Sodium	Mg Magnesium											Al Aluminum	Si Silicon	P Phosphorus	S Sulfur	Cl Chlorine	Ar Argon
K Potassium	Ca Calcium	Sc Scandium	Ti Titanium	V Vanadium	Cr Chromium	Mn Manganese	Fe Iron	Co Cobalt	Ni Nickel	Cu Copper	Zn Zinc	Ga Gallium	Ge Germanium	As Arsenic	Se Selenium	Br Bromine	Kr Krypton
Rb Rubidium	Sr Strontium	Y Yttrium	Zr Zirconium	Nb Niobium	Mo Molybdenum	Tc Technetium	Ru Ruthenium	Rh Rhodium	Pd Palladium	Ag Silver	Cd Cadmium	In Indium	Sn Tin	Sb Antimony	Te Tellurium	I Iodine	Xe Xenon
Cs Cesium	Ba Barium		Hf Hafnium	Ta Tantalum	W Tungsten	Re Rhenium	Os Osmium	Ir Iridium	Pt Platinum	Au Gold	Hg Mercury	Tl Thallium	Pb Lead	Bi Bismuth	Po Polonium	At Astatine	Rn Radon
Fr Francium	Ra Radium																
		La Lanthanum	Ce Cerium	Pr Praseodym	Nd Neodymium	Pm Promethium	Sm Samarium	Eu Europium	Gd Gadolinium	Tb Terbium	Dy Dyprosium	Ho Holmium	Er Erbium	Tm Thulium	Yb Ytterbium	Lu Lutetium	
		Ac Actinium	Th Thorium	Pa Protactin	U Uranium	Np Neptunium	Pu Plutonium	Am Americium	Cm Curium	Bk Berkelium	Cf Californium	Es Einsteinium	Fm Fermium	Md Mendelev	No Nobelium	Lr Lawrenc	

Figure 92: Periodic table revised for the transition metal oxysulfide nanoparticles. The transition metals that are investigated in this chapter are indicated in dark red and dark violet.

We thus decided explore possible candidates for crystalline transition metal oxysulfide nanoparticles. We mainly focused our work on the transition metals from titanium to copper for their good availability, price, and presence in the bimetallic $Ln_wM_xO_yS_z$ compositions (Figure 86 and Chapter 5, Table 1).

We started with bimetallic compositions to be close to the compositions that were already reported. By mixing the two desired metals in the stoichiometry expected in the final phase, we hoped to crystallize one of the previously reported bimetallic oxysulfide phase. We imagined that the nanoscale could also enable us to form new phases. Then, we conducted other tests that aimed the synthesis of $M_xO_yS_z$ nanoparticles, with “M” a single transition metal.

In this chapter, the reaction conditions are similar to those used for the lanthanide oxysulfide nanoparticles: the reactants are oleylamine, oleic acid, 1-octadecene and elemental sulfur, an optional alkaline source and the metal precursor (often acetylacetonate or acetate complex).

VI.2. Synthesis of bimetallic $\text{Ln}_w\text{M}_x\text{O}_y\text{S}_z$ oxysulfide nanoparticles

VI.2.1. Titanium-, vanadium- and chromium-based bimetallic oxysulfides

Titanium, vanadium and chromium can all be found in bimetallic compositions: bulk $\text{Ln}_5\text{V}_3\text{O}_7\text{S}_6$ ($\text{Ln} = \text{La, Ce, Pr, Nd}$) for vanadium,^{1,2} bulk LnCrOS_2 ($\text{Ln} = \text{La, Ce, Pr, Nd, Sm}$) for chromium³⁻⁵ and various compositions for titanium, such as bulk $\text{Ln}_2\text{Ti}_2\text{S}_2\text{O}_5$ ($\text{Ln} = \text{Pr, Nd, Sm}$) lamellar phase with selective bonding),^{6,7} $\text{La}_4\text{Ti}_3\text{O}_8\text{S}_4$,⁸ $\text{La}_6\text{Ti}_2\text{O}_5\text{S}_8$,⁸ and so on.

Our idea was to form similar compositions in similar conditions than our successful synthesis of gadolinium oxysulfide nanoparticles. One will notice that gadolinium may not be the most judicious lanthanide to be used here, as the reported compositions are obtained only for bigger lanthanide cations (basically from lanthanum to samarium). Nevertheless, we decided to keep gadolinium as starting lanthanide because of our good knowledge about the $\text{Gd}_2\text{O}_2\text{S}$ nanoparticles and the possibility to reach unknown phases.

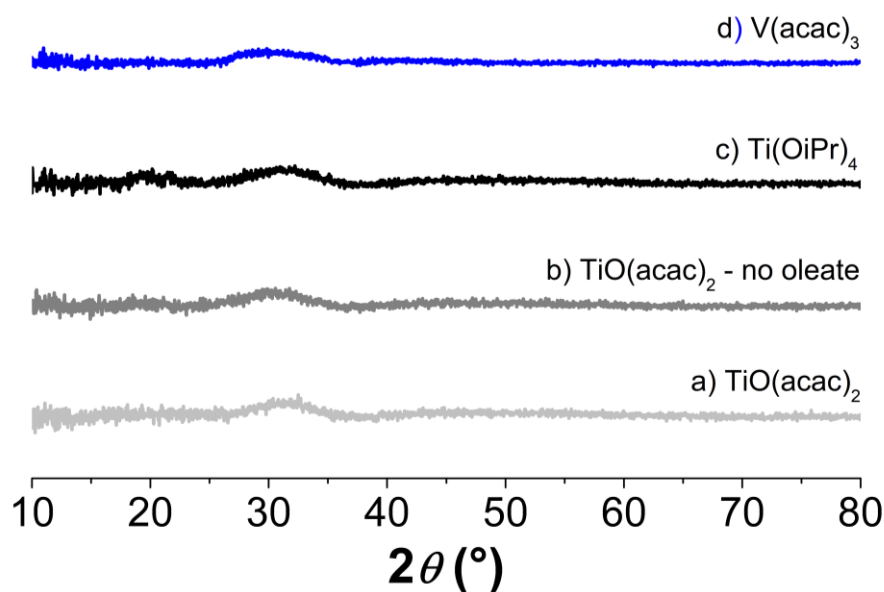


Figure 93: Powder XRD patterns of the synthetic attempts aiming $\text{Gd}_2\text{Ti}_2\text{O}_5\text{S}_2$ and $\text{Gd}_5\text{V}_3\text{O}_7\text{S}_6$ nanoparticles. The protocol of the synthesis of $\text{Gd}_2\text{O}_2\text{S}$ nanoplates was adapted by adding $\text{TiO}(\text{acac})_2$ (a, [CL006] and b, [CL011]), $\text{Ti}(\text{OiPr})_4$ (c, [CL115]) and $\text{V}(\text{acac})_3$ (d, [CL055]). For (b), oleic acid and $\text{Na}(\text{oleate})$ were not used.

With the same conditions than $\text{Gd}_2\text{O}_2\text{S}$ nanoparticles synthesis (oleylamine, oleic acid, 1-octadecene, sodium oleate, elemental sulfur and $\text{Gd}(\text{acac})_3$) and using $\text{Ti}^{\text{IV}}\text{O}(\text{acac})_2$ and $\text{V}^{\text{III}}(\text{acac})_3$, the respective $\text{Gd}_2\text{Ti}_2\text{O}_5\text{S}_2$ ($\eta = 24\%$) and $\text{Gd}_5\text{V}_3\text{O}_7\text{S}_6$ ($\eta \approx 100\%$) syntheses both yielded amorphous powders (Figure 93a and d). It is the sign that the second metal intervened in the reaction, as $\text{Gd}_2\text{O}_2\text{S}$ nanoparticles did not form as usual.

The system dealing with titanium was further explored. The reaction was tried with neither sodium nor oleic acid to see the influence of the coordinating species (Figure 93b). We also carried out the reaction with the tetrapropoxide compound $\text{Ti}^{\text{IV}}(\text{OiPr})_4$ to avoid the oxo ligand in $\text{Ti}^{\text{IV}}\text{O}(\text{acac})_2$ that we believed very strongly bonded to titanium (Figure 93c). All the reactions resulted in amorphous products. Amorphous powders of $\text{Gd}_w\text{Ti}_x\text{O}_y\text{S}_z$ and $\text{Gd}_w\text{V}_x\text{O}_y\text{S}_z$ (c and d in Figure 93) were then annealed under inert atmosphere (argon) to get an insight of what could be in the sample (Figure 94).

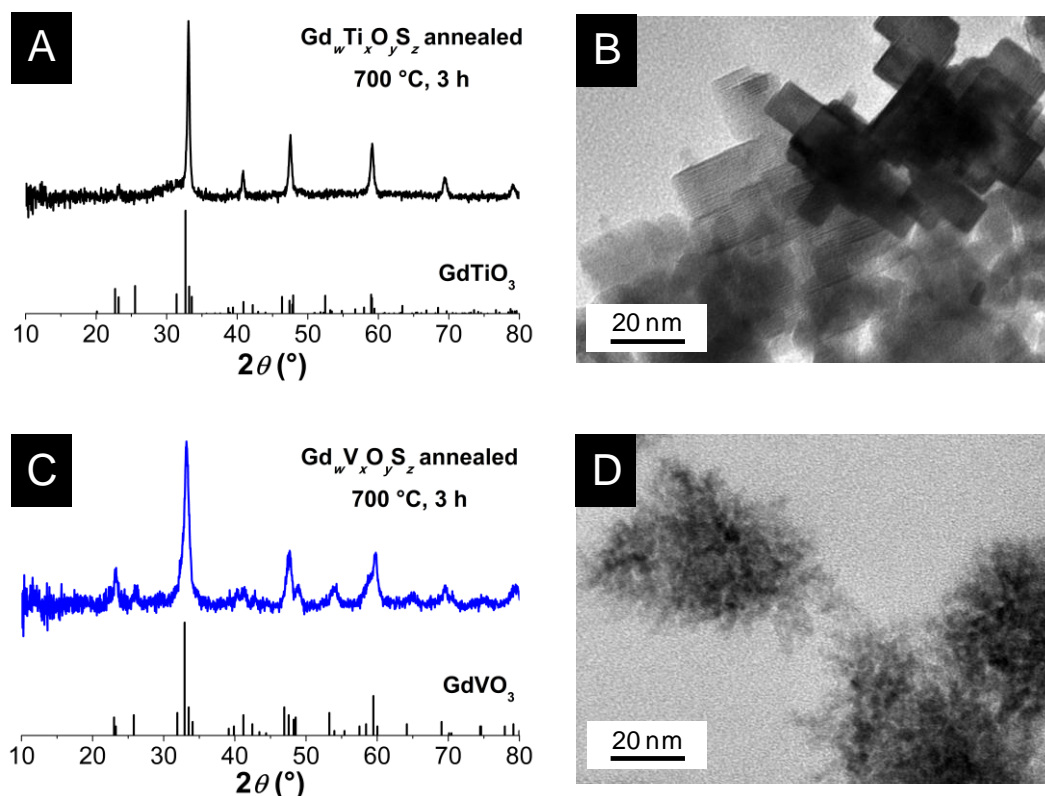


Figure 94: GdTiO_3 powder XRD pattern (A, [CL118]) and TEM micrograph (B) formed by annealing of $\text{Gd}_w\text{Ti}_x\text{O}_y\text{S}_z$. GdVO_3 powder XRD pattern (C, [CL124]) and TEM micrograph (D) formed by annealing of $\text{Gd}_w\text{V}_x\text{O}_y\text{S}_z$. XRD pattern references are JCPDS files 70-2296 (GdTiO_3) and 25-0205 (GdVO_3).

During annealing, the amorphous products crystallized (Figure 94A and C). For both of them, the GdMO_3 phase was observed but with pretty different morphologies: assemblies of 10 nm^3 nanocubes for GdTiO_3 (Figure 94B) and very small nanoparticles ($< 5 \text{ nm}$) for GdVO_3 (Figure 94D). EDS revealed that sulfur was mostly absent from the two products ($\text{S}:\text{Ti} \approx 1 \%$ and $\text{S}:\text{V} \approx 5 \%$), in agreement with the yellow supernatants obtained when the particles were centrifuged after the reaction leading to the amorphous product. But we cannot exclude that a small amount of sulfur substituted oxygen atoms in the lattice. The annealed samples are both black, while the amorphous (Gd,Ti) and (Gd,V) products were respectively white and black.

For chromium, reported compositions were targeted, namely bulk LaCrOS_2 and bulk NdCrOS_2 . We chose these two phases because lanthanum chromium oxysulfide has a different crystallographic structure than the other LnCrOS_2 , and we wanted to see which one would grow in our conditions. The results of the two reactions performed with $\text{Cr}^{\text{III}}(\text{acac})_3$ for one hour and without $\text{Na}(\text{oleate})$ are presented in Figure 95.

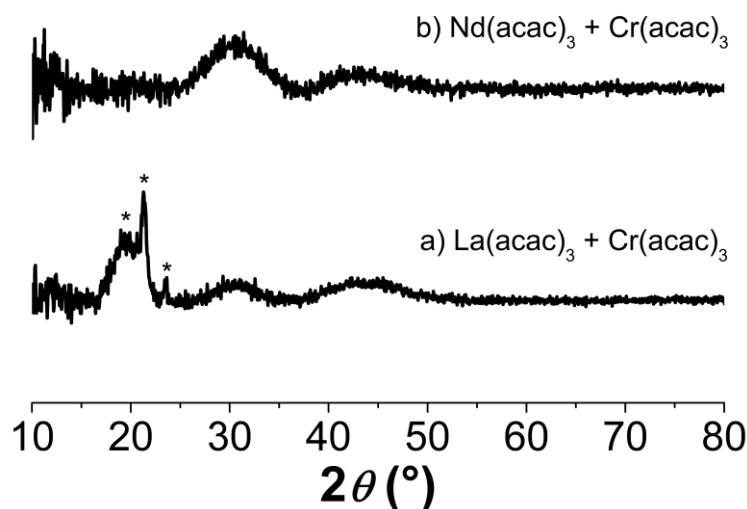


Figure 95: Powder XRD patterns of the synthetic attempts aiming LaCrOS_2 (a, [CL320]) and NdCrOS_2 (b, [CL321]). The stars indicate the presence of remaining sulfur and impurity from the solvent.

Again, amorphous phases were obtained and indicated that the growth of lanthanide oxysulfide nanoparticles was inhibited ($\eta(\text{LaCrOS}_2) = 51\%$ and $\eta(\text{NdCrOS}_2) \approx 100\%$). The green color of the samples is also the sign that chromium reacted. The products were then annealed at $900\text{ }^\circ\text{C}$ under argon (they were still amorphous after annealing at $700\text{ }^\circ\text{C}$, Figure 96B) and led this time to a mixture of LnCrO_3 ($\text{Ln} = \text{La}$ or Nd) and $\text{Ln}_2\text{O}_2\text{S}$ ($\text{Ln} = \text{La}$ or Nd , Figure 96). Interestingly, for the reaction with lanthanum, a third phase formed and could not be identified (Figure 96A).

These first tests on titanium, vanadium and chromium (d^n layer with $n < 5$) with gadolinium all led to bimetallic amorphous compounds. For gadolinium coupled with titanium or vanadium, sulfur did not bond to any metal and was mainly eliminated during the nanoparticles isolation and washing. For chromium, it seems that sulfur remained in the amorphous product. Nevertheless, at high temperature, it concentrated in the $\text{Ln}_2\text{O}_2\text{S}$ phase.

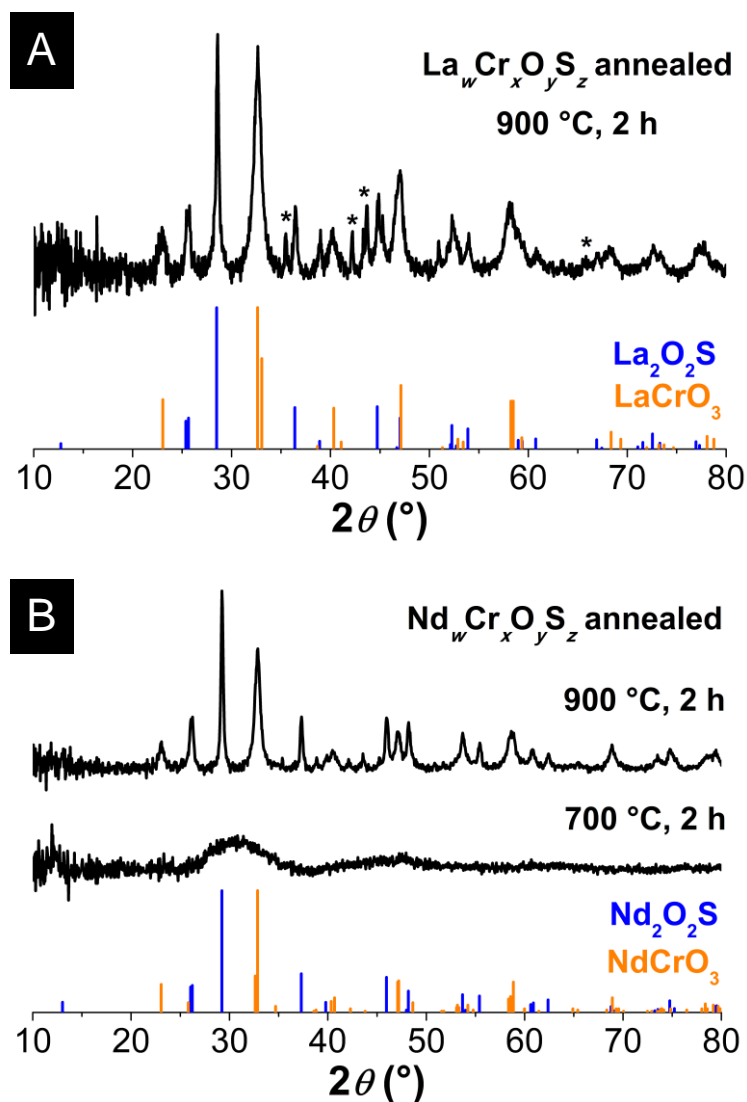


Figure 96: Powder XRD patterns of annealed $\text{Ln}_w\text{Cr}_x\text{O}_y\text{S}_z$ amorphous products for $\text{Ln} = \text{La}$ (A, [CL331]) and Nd (B, [CL325, CL327]). XRD pattern references are JCPDS files 71-2098 ($\text{La}_2\text{O}_2\text{S}$), 51-1589 (LaCrO_3), 65-3452 ($\text{Nd}_2\text{O}_2\text{S}$) and 39-1429 (NdCrO_3). The stars on A indicate unidentified peaks.

Interestingly, even if we have no clear evidence that we reached oxysulfide nanoparticles, our reactions with titanium, vanadium and chromium showed that **nanoscale was conserved** (even after annealing above 700 °C) and that **the nanoparticles contained more or less sulfur**.

What can we expect on these systems now? For the $\text{Ln}-\text{Cr}$ system, it is possible that the amorphous phase constitute a real bimetallic oxysulfide. Further analyses of composition, structure and oxidation states could be performed to unveil its nature.

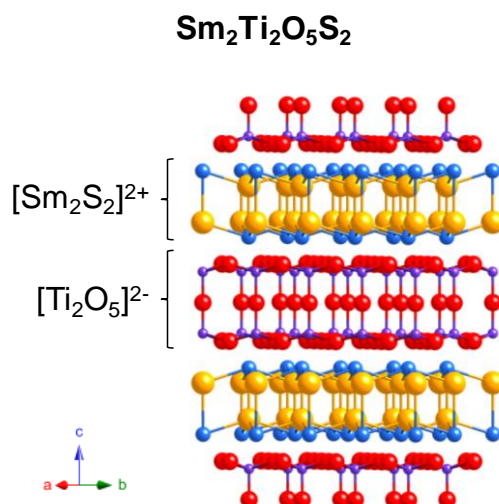


Figure 97: Sm₂Ti₂S₂O₅ layered structure. Selective bonding is illustrated by the preferential Ti-O and Sm-S bonds in the solid.

For the Ln-Ti system, the conclusions obtained in Chapter III are truly promising, especially for the Ln₂Ti₂S₂O₅ compound. Starting with a more adapted lanthanide (samarium or neodymium for instance), the lamellar phase (Figure 97) is an ideal candidate for the synthesis in the Na(oleate)-promoted *in situ* reactor. Some tests will be soon performed to determine the feasibility of the reaction.

VI.2.2. Iron-, cobalt- and copper-based bimetallic oxysulfides

Copper-based bimetallic oxysulfides exist and the main studied bulk phases LnCuOS (Ln = La,^{9,10} Ce,^{11,12} Pr,¹³ Nd,¹⁴ Sm¹⁴) and BiCuOS contained Cu^I (*d*¹⁰).^{15,16} It encouraged us to try to incorporate Cu^{II} in new bimetallic compositions. For cobalt, there is simply no reported bimetallic oxysulfide phase.

Co(acac)₂ and Cu(acac)₂ were thus used along with Gd(acac)₃ as metal precursors in the same conditions than the Gd₂O₂S nanoparticles synthesis ([CL139], [CL172]). The results for these two metals are presented on (Figure 98).

The behavior for these two metals is similar and distinct from the previous results obtained for titanium, vanadium and chromium. The diffraction patterns indicate the crystallization of Gd₂O₂S nanoparticles. However, in both cases, the pattern is slightly modified and additional peaks are present (Figure 98). For instance, in the experiment with copper, the intensity of the (100) peak at 27 ° of Gd₂O₂S is decreased but a peak grew at 33 °. The (110) peak at 45 ° is also larger.

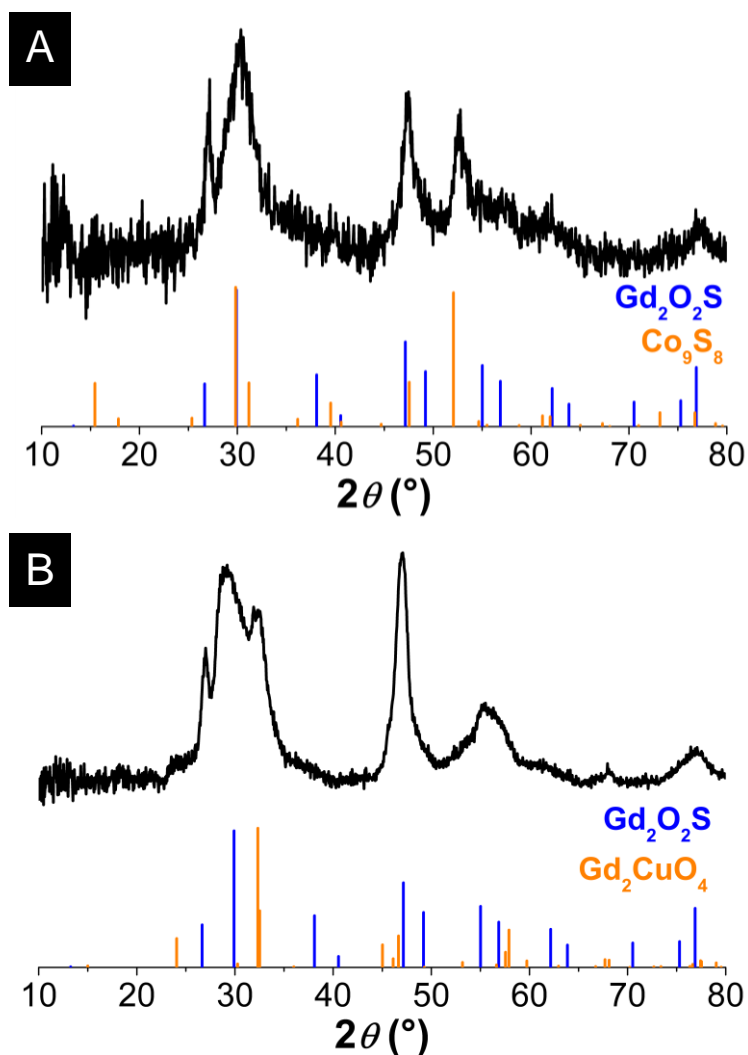


Figure 98: Powder XRD patterns of the product of the synthetic attempt of gadolinium-cobalt (A, [CL139]) and gadolinium-copper oxysulfide nanoparticles (B, [CL172]) using Gd_2O_2S nanoparticles synthetic conditions. XRD pattern references are JCPDS files 26-1422 (Gd_2O_2S), 65-6801 (Co_9S_8) and 77-0522 (Gd_2CuO_4).

Even with the hypothesis that all the products are crystalline enough to be detected by XRD, several scenarios can be proposed. First, there is no interaction between the two metals. The second metal crystallized likely in an oxide or a sulfide phase on its own, but the presence of Gd_2O_2S complicates its identification. Metallic nanoparticles or oxysulfide nanoparticles are even possible. Second, the *d*-block transition metal is inserted in the $[Gd_2O_2]$ layers of the Gd_2O_2S nanoplate, by substitution of Gd. This hypothesis is unlikely as cobalt and copper cations are at the +II oxidation state and are much smaller than gadolinium cations. Plus, the cations in Gd_2O_2S have a coordination number of seven that transition metals do not easily accept. Nevertheless, we can imagine a small fraction of inserted transition metal.¹⁷ Third, the transition metal can be involved in the two previous situations. In the case of cobalt, Co_9S_8

nanoparticles could have crystallized and with copper, Gd_2CuO_4 likely crystallized (Figure 98). At present, we cannot conclude on what happens for these two metals.

For iron, $\text{Ln}_2\text{Fe}_2\text{O}_3\text{S}_2$ structures were reported with $\text{Ln} = \text{La}, \text{Ce}, \text{Pr}$.^{18,19} The products of the reaction in the conditions of $\text{Gd}_2\text{O}_2\text{S}$ nanoplates synthesis are more obvious. It seems that no bimetallic phase was formed and that only iron sulfide (thin peaks in Figure 99) crystallized along with $\text{Gd}_2\text{O}_2\text{S}$ nanoparticles (Figure 99).

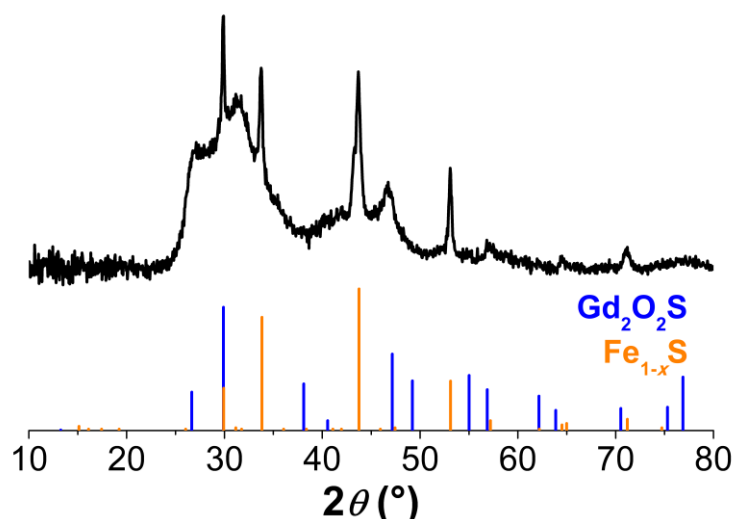


Figure 99: Powder XRD pattern of the product of the synthetic attempt of $\text{Gd}_2\text{Fe}_2\text{O}_3\text{S}_2$ nanoparticles using $\text{Gd}_2\text{O}_2\text{S}$ nanoparticles synthetic conditions [CL138]. XRD pattern references are JCPDS files 26-1422 ($\text{Gd}_2\text{O}_2\text{S}$) and 29-0724 (Fe_{1-x}S).

For iron, cobalt and copper, the crystallization of bimetallic oxysulfide nanoparticles was not achieved. The choice of the lanthanide is however perfectible, as gadolinium was not reported to crystallize with these metals.

VI.2.3. Gadolinium-indium bimetallic oxysulfide

A last test is presented here. Indium is a metal of the fifth period, and is involved in several bimetallic oxysulfide compositions with lanthanum (Chapter V, Table 1). We suspected that indium was thus able to form the same kind of bimetallic compositions with gadolinium.

We aimed $\text{Gd}_5\text{In}_3\text{O}_3\text{S}_9$ as a first step with the synthetic conditions of $\text{Gd}_2\text{O}_2\text{S}$ nanoparticles synthesis, and realized that we obtained a mixture of products, namely $\text{Gd}_2\text{O}_2\text{S}$ and NaInS_2 . We then confirmed that NaInS_2 was formed by using similar conditions without gadolinium and sodium and sulfur amounts adjusted to stoichiometry (Figure 100B).

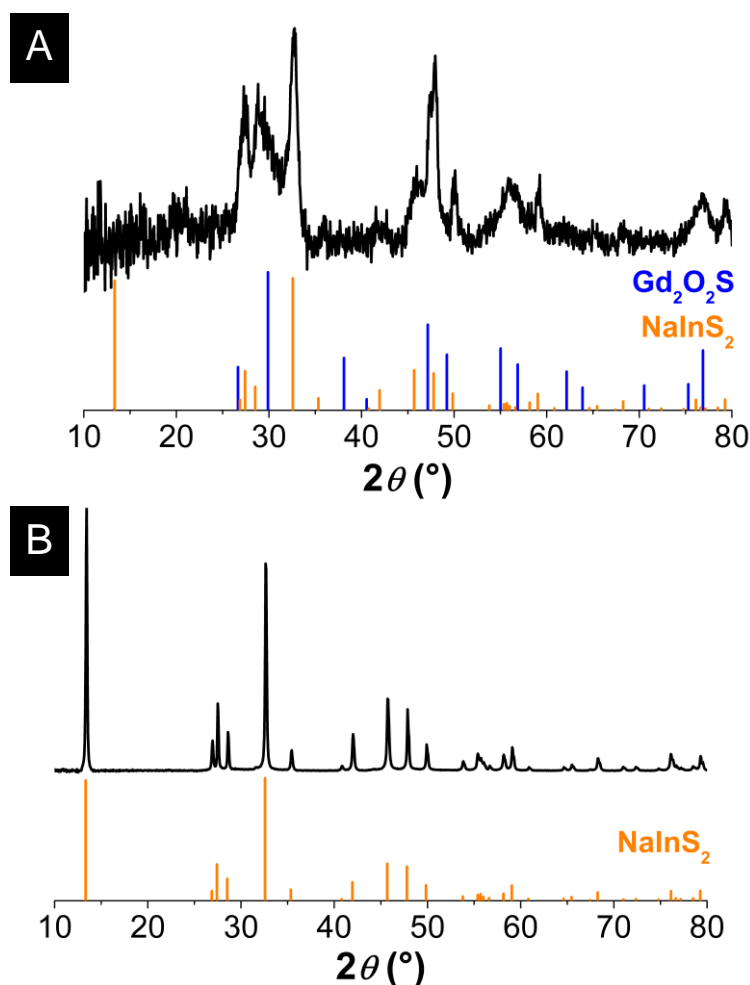


Figure 100: Powder XRD patterns of the attempt of $Gd_5In_3S_9O_3$ nanoparticles (A, [CL002]) and of the synthesis of $NaInS_2$ (B, [CL274]). XRD pattern references are JCPDS files 26-1422 (Gd_2O_2S) and 74-0135 ($NaInS_2$).

Again, the bimetallic composition was not reached.

VI.2.3. Conclusion

Bimetallic oxysulfide nanoparticles mixing lanthanide with first row transition metals and indium were not formed, despite the rather easy formation of Ln_2O_2S nanoplates. Sometimes, the transition metal interferes with the Ln_2O_2S formation (Ti, V, Cr). Otherwise, the second metal (Co, Fe, In) crystallizes in independent phases (oxide or sulfide).

Our exploratory approach was justified by the objective to achieve new compositions *via* the nanoscale. Unfortunately, we will have to be more reasonable on the choice of the aimed products, because most of our attempts were not successful. Nevertheless, when the targeted phase was already reported (case of chromium), the results were rather encouraging: sulfur

was still inside the amorphous products and the lanthanide and chromium crystallized together in an oxide when annealed, showing that one is at the vicinity of the other.

In the light of the results of Chapter III, one can suppose that reported lamellar phases such as $\text{Ln}_2\text{Ti}_2\text{O}_5\text{S}_2$, LaInOS_2 or LnBiOS_2 (Chapter V, Table I) in presence of the suitable lanthanide and an alkali additive are more likely to crystallize than our previous targeted products.

VI.3. Synthesis of $M_xO_yS_z$ nanoparticles: first attempts

The question of this section is: are we able to use the colloidal synthesis of Ln_2O_3S nanoparticles to form ternary transition metal oxysulfides? The previous section is not encouraging, but we can think that without gadolinium, the transition metal is able to crystallize along with oxygen and sulfur. Here, there is almost no reference of reported structures, except for bismuth (Bi_2O_3S notably), zinc ($ZnO_{1-x}S_x$) and titanium (amorphous thin films).

VI.3.1. Results from powder XRD patterns

In a mixture oleylamine/oleic acid/1-octadecene/elemental sulfur, nine metals were tested with or without an alkali complex.

The results obtained with the various metals are summarized in Figure 101 and Table 10.

VI.3.2. First-row transition metals

Titanium and vanadium complexes led to amorphous products (Figure 101A and B, Table 10). Upon annealing (700 °C, 3 h), the amorphous product obtained from $V(acac)_3$ and $Na(oleate)$ led majorly to crystals of V_2O_3 and a small amount of VO_2 (data not shown). It implies that sulfidation of vanadium using elemental sulfur is unlikely in these conditions. The use of lithium and sodium in the case of vanadium promoted the formation of nanoparticles. Without an alkali, no solid could be isolated. For titanium, aluminum was used instead of Na, because of its small ionic radius close to titanium ($r(Al^{III}(VI)) = 0.68 \text{ \AA}$; $r(Ti^{IV}(VI)) = 0.75 \text{ \AA}$). The white powder obtained was also amorphous (Figure 101A).

Iron, cobalt and copper led to various crystallized phases, including metals at the (0) oxidation state, oxides and sulfides (Figure 101C, D and E, Table 10). The alkali complex plays a role on the selectivity of the reaction, again demonstrating the crucial role of the oleate layer. For zinc, the reaction was performed without sodium oleate and led to a probable mixture of ZnO and ZnS where ZnO is likely the major product (based on XRD pattern, Figure 101F).

For the first-row transition metals, we found similar trends than for the bimetallic nanoparticles, with amorphous products for the lightest (Ti, V) and crystallized oxides and/or sulfides for the heaviest (Fe, Co, Cu).

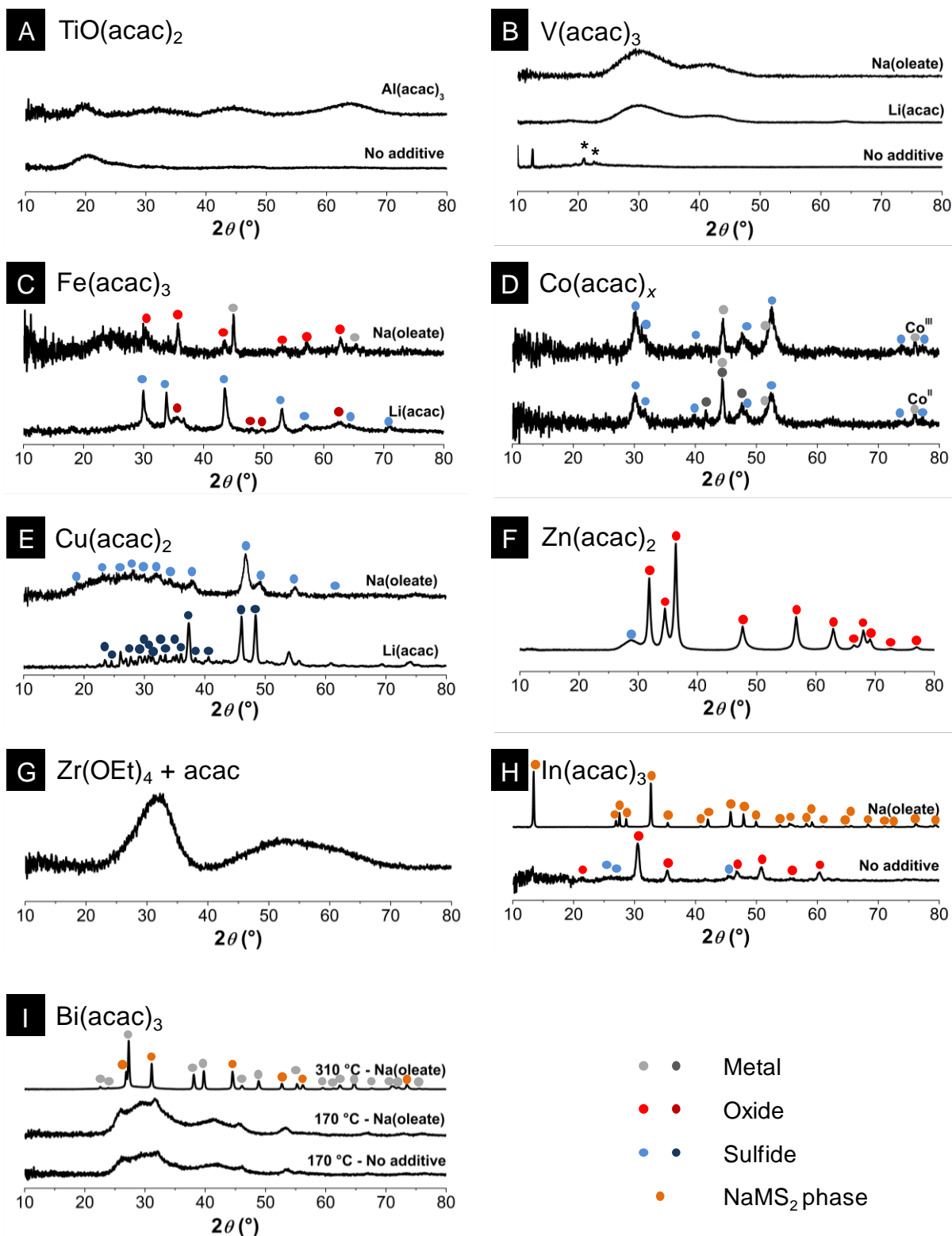
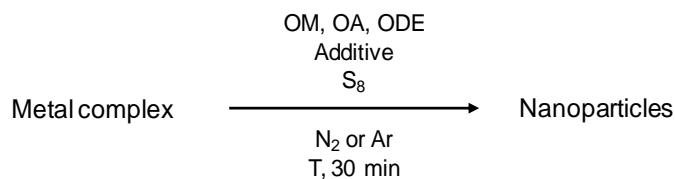


Figure 101: Powder XRD patterns of the various attempts of $\text{M}_x\text{O}_y\text{S}_z$ synthesis with transition metals (major peaks indexed from references). (A) Titanium. (B) Vanadium. Stars indicate a common impurity coming from the solvent. (C) Iron. JCPDS 06-0696 (Fe, gray), 82-1533 (Fe_3O_4 , light red), 39-1346 (Fe_2O_3 , dark red) and 65-1894 (FeS, blue). (D) Cobalt. JCPDS 15-0806 (Co, light gray), 89-4308 (β -Co, dark gray) and 65-6801 (Co_9S_8 , blue). (E) Copper. JCPDS 23-0958 (Cu_7S_4 , light blue) and 33-0490 (Cu_2S , dark blue). (F) Zinc. JCPDS 89-0510 (ZnO, red) and 83-1717 (ZnS, blue). (G) Zirconium.

(H) Indium. JCPDS 06-0416 (In_2O_3 , red), 71-1813 (In_2S_3 , blue) and 74-0135 (NaInS_2 , orange). (I) Bismuth. JCPDS 44-1246 (Bi, gray) and 75-0065 (NaBiS_2 , orange).



Index	Metal complex	S_8 (equiv. vs. metal)	Additive (1 equiv. vs. metal)	Temperature	Phase(s) according to XRD
[CL007]	$\text{TiO}(\text{acac})_2$	1	X	310 °C	Amorphous
[CL287]	$\text{TiO}(\text{acac})_2$	0.5	$\text{Al}(\text{acac})_3$	310 °C	Amorphous
[CL054]	$\text{V}(\text{acac})_3$	0.5	X	310 °C	No solid
[CL062]	$\text{V}(\text{acac})_3$	0.5	$\text{Na}(\text{oleate})$	310 °C	Amorphous
[CL070]	$\text{V}(\text{acac})_3$	0.5	$\text{Li}(\text{acac})$	310 °C	Amorphous
[CL089]	$\text{Fe}(\text{acac})_3$	0.5	$\text{Na}(\text{oleate})$	310 °C	Fe_3O_4 + Fe
[CL426]	$\text{Fe}(\text{acac})_3$ ^[a]	1	$\text{Li}(\text{acac})$	310 °C	FeS + Fe_2O_3
[CL162]	$\text{Co}(\text{acac})_2$	0.5	$\text{Na}(\text{oleate})$	310 °C	Co_9S_8 + Co
[CL163]	$\text{Co}(\text{acac})_3$	0.5	$\text{Na}(\text{oleate})$	310 °C	Co_9S_8 + Co
[CL090]	$\text{Cu}(\text{acac})_2$	0.5	$\text{Na}(\text{oleate})$	310 °C	Cu_7S_4
[CL288]	$\text{Cu}(\text{acac})_2$	0.5	$\text{Li}(\text{acac})$	310 °C	Cu_2S
[CL261]	$\text{Zn}(\text{acac})_2$	0.5	X	310 °C	ZnO (+ ZnS)
[CL274]	$\text{In}(\text{acac})_3$	2	$\text{Na}(\text{oleate})$	310 °C	NaInS_2
[CL299]	$\text{In}(\text{acac})_3$	1	X	310 °C	In_2O_3 (+ In_2S_3)
[CL571]	$\text{Zr}(\text{OEt})_4$ + acac	1	X	310 °C	Amorphous
[MA019]	$\text{Bi}(\text{ac})_3$	0.5	$\text{Na}(\text{oleate})$	310 °C	Bi + NaBiS_2
[CL027]	$\text{Bi}(\text{ac})_3$	0.5	$\text{Na}(\text{oleate})$	170 °C	Bi + ?
[CL033]	$\text{Bi}(\text{ac})_3$	0.5	X	170 °C	Bi + ?

Table 10: Synthetic attempts for transition metal ternary oxysulfides based on powder XRD patterns.
[a] Performed without oleic acid.

VI.3.3. Attempts with zirconium, indium and bismuth

We used $\text{Zr}(\text{OEt})_4$ combined with acetylacetone to form the $\text{Zr}(\text{acac})_4$ precursor in situ. Similarly to its tetravalent neighbor titanium, zirconium led to an amorphous product (Figure

101G). The broad peaks could also correspond to very small ZrO_2 nanoparticles. EDS confirmed that there was no sulfur in the product, but more surprisingly, SEM images showed well-organized structures in the range of several dozen micrometers (Figure 102)! We were not able to explain such arrangements with such a diffractogram.

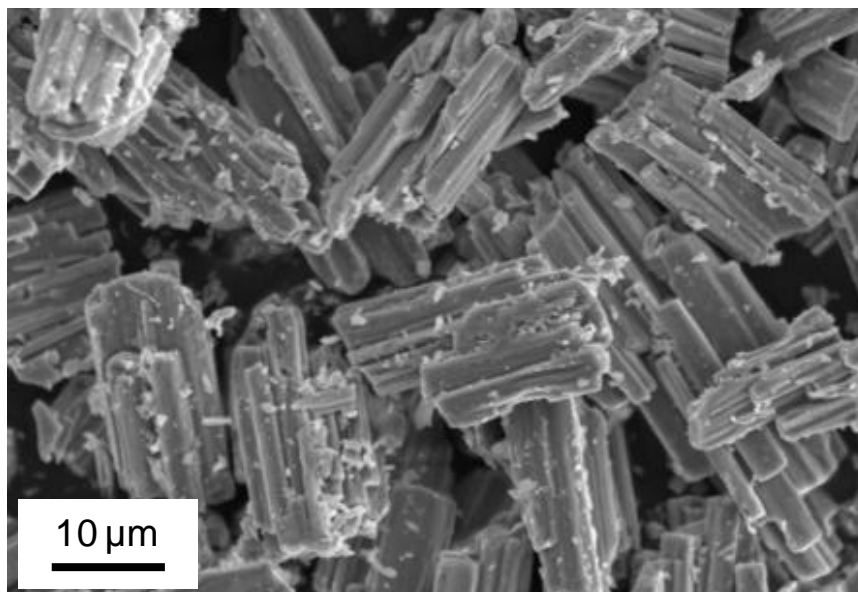


Figure 102: SEM image of the product obtained with $\text{Zr}(\text{OEt})_4$ and acetylacetone.

As presented in the previous section (VI.2.), indium and sodium crystallized in NaInS_2 . Bismuth acted in a similar way when $\text{Na}(\text{oleate})$ was used, with crystallization of NaBiS_2 (Figure 101I, Table 10). Without additive, indium led to the oxide In_2O_3 and probably a small amount of In_2S_3 , harder to identify on the powder XRD pattern (Figure 101H).

Because the melting point of bismuth is quite low ($\text{mp}(\text{Bi}) = 271\text{ }^\circ\text{C}$), bismuth (0) crystals were also observed in a significant quantity at $310\text{ }^\circ\text{C}$ (Figure 101H, Table 10). For bismuth at lower temperature without additive ($170\text{ }^\circ\text{C}$), several phases likely crystallized, leading to broad signals on the pattern that could not be properly assigned.

Because of the competitive crystallization of NaMS_2 ($\text{M} = \text{In}, \text{Bi}$), the crystallization of the $\text{M}_x\text{O}_y\text{S}_z$ oxysulfide will be challenging if we consider that sodium is also required for indium and bismuth. Adjusting the sodium quantity could help. We showed in Chapter III that only 0.5 equiv *vs.* Gd were sufficient to crystallize $\text{Gd}_2\text{O}_2\text{S}$. But here, if all the sodium is involved in the NaMS_2 , the oleate lamellar phase may not be stabilized and enables further crystallization of indium or bismuth oxysulfide. Adding more sodium, on the contrary, will probably consume all the available bismuth in NaMS_2 and there will not be any available

metal for oxysulfide nanoparticles crystallization. LiMS_2 and KMS_2 are also reported structures and might have crystallized if we would have decided to change the alkali cation.

Nevertheless, the crystallization of such NaMS_2 phase is of importance. It confirms that the transition metal and the alkali are in the vicinity of each other during the synthesis, likely in the 1.5 nm thick space between the oleate layers. It also suggests that we can have some clear evidence of the presence of sodium inside the nanoparticles when the metal and the alkali crystallize together.

VI.3.4. Conclusion

The goal was simple: we wanted to use similar conditions than $\text{Gd}_2\text{O}_2\text{S}$ synthesis to obtain ternary transition metal oxysulfides. When the tests were performed, we had only a little knowledge on the synthesis mechanism. A range of *d*- and *p*-transition metals was screened the most often as acetylacetonate complexes with elemental sulfur in the same mixture oleylamine/oleic acid/1-octadecene. An alkali complex (Na^I , Li^I) was often added, as we estimated it was useful for the oxysulfide synthesis. Remarkably, its absence generally led to little amounts of powder, and confirmed that the organization of the oleate chains with these cations is helping in the crystallization of a product, whether it is an oxysulfide or not.

VI.4. Conclusion

The exploratory approach we conducted here was not successful in obtaining new oxysulfide nanoparticles. With transition metals, the optimal conditions determined for the $\text{Ln}_2\text{O}_2\text{S}$ nanoparticles synthesis must be changed to control the selectivity and yield oxysulfide products.

Nevertheless, some points are satisfying. First, some sulfide nanoparticles crystallized. It means that elemental sulfur dissolved in oleylamine is still a suitable sulfidating agent for several metals (Fe, Co, Cu, In, Bi). Second, the alkali presence is still efficient to guide the crystallization of nanoparticles. Without alkali, some metals did not form any solid. Third, we isolated several amorphous products whose structures after annealing are encouraging ($\text{La}_w\text{Cr}_x\text{O}_y\text{S}_z$ and $\text{Nd}_w\text{Cr}_x\text{O}_y\text{S}_z$). In fact, the targeted phases of bimetallic oxysulfides were the most often not reported and thus very challenging to obtain. We will focus our next attempts on already reported phases.

Also, one must notice that we used a limited set of parameters. The short time reaction and the relatively low temperature for such chemistry can represent a hindrance for the crystallization of oxysulfide nanoparticles. Some reactions were performed for a longer time: 3 hours for $\text{Gd}_w\text{Ti}_x\text{O}_y\text{S}_z$ and 5 hours for $\text{Nd}_w\text{Cr}_x\text{O}_y\text{S}_z$. The products were still amorphous. Nevertheless, structural changes could have occurred during this longer reaction time.

In parallel of this study, we also tried to find a new efficient way to synthesize transition metal oxysulfides. In the literature, oxide nanoparticles were converted in oxysulfide nanoparticles (Chapter V).^{20,21} We thought that we could alternatively oxidize sulfide nanoparticles. In the next chapter, we detail how to form amorphous nickel oxysulfide using a synthesis developed for the formation of nickel sulfide nanoparticles.

References

- (1) Vovan, T.; Dugué, J.; Guittard, M. Oxysulfures Mixtes de Vanadium et de Terre Rare de Formule Générale $R_5V_3S_6O_7$ (R = Lanthane à Néodyme). *Comptes Rendus l'Académie des Sci. - Série II* **1981**, 292 (13), 957–959.
- (2) Dugué, J.; Tien, V.; Laruelle, P. Structure de l'oxysulfure de Lanthane et de Vanadium, $La_5V_3O_7S_6$. *Acta Crystallogr. Sect. C Cryst. Struct. Commun.* **1985**, 41 (8), 1146–1148.
- (3) Vovan, T.; Dugué, J.; Guittard, M. Oxysulfures Mixtes de Chrome III et de Terres Rares. *Mater. Res. Bull.* **1978**, 13, 1163–1166.
- (4) Dugué, J.; Vovan, T.; Villers, J. Etude Structurale Des Oxysulfures de Chrome(III) et de Terres Rares. I. Structure de l'Oxysulfure $LaCrOS_2$. *Acta Crystallogr.* **1980**, B36, 1291–1294.
- (5) Dugué, J.; Vovan, T.; Villers, J. Etude Structurale Des Oxysulfures de Chrome(III) et de Terres Rares. II. Structure de l'Oxysulfure $CeCrOS_2$. *Acta Crystallogr.* **1980**, B36, 1294–1297.
- (6) Goga, M.; Seshadri, R.; Ksenofontov, V.; Gütllich, P.; Tremel, W. $Ln_2Ti_2S_2O_5$ (Ln = Nd, Pr, Sm): A Novel Series of Defective Ruddlesden–Popper Phases. *Chem. Commun.* **1999**, 7 (11), 979–980.
- (7) Boyer, C.; Deudon, C.; Meerschaut, A. Synthesis and Structure Determination of the New $Sm_2Ti_2O_5S_2$ Compound. *Comptes Rendus l'Académie des Sci. - Ser. IIC* **1999**, 2 (2), 93–99.
- (8) Cody, J. A.; Ibers, J. A. Synthesis and Characterization of the New Rare-Earth/Transition-Metal Oxysulfides $La_6Ti_2S_8O_5$ and $La_4Ti_3S_4O_8$. *J. Solid State Chem.* **1995**, 114 (2), 406–412.
- (9) Palazzi, M. Préparation et Affinement de La Structure de $(LaO) CuS$. *Comptes Rendus Hebd. l'Académie des Sci. - Série II* **1981**, 292, 789–791.
- (10) Doussier-Brochard, C.; Chavillon, B.; Cario, L.; Jobic, S. Synthesis of P-Type Transparent $LaOCuS$ Nanoparticles via Soft Chemistry. *Inorg. Chem.* **2010**, 49 (7), 3074–3076.
- (11) Ueda, K.; Takafuji, K.; Hosono, H. Preparation and Crystal Structure Analysis of $CeCuOS$. *J. Solid State Chem.* **2003**, 170 (1), 182–187.
- (12) Chan, G. H.; Deng, B.; Bertoni, M.; Ireland, J. R.; Hersam, M. C.; Mason, T. O.; Van Duyne, R. P.; Ibers, J. A. Syntheses, Structures, Physical Properties, and Theoretical Studies of CeM_xOS (M = Cu, Ag; $x \approx 0.8$) and $CeAgOS$. *Inorg. Chem.* **2006**, 45 (20), 8264–8272.
- (13) Lauxmann, P.; Schleid, T. $CuPrOS$: Kein Einprägsames Akronym, Vielmehr Ein Echtes Quaternäres Chalkogenid Mit Aufgefüllter $PbFCl$ -Struktur. *Zeitschrift für Anorg. und Allg. Chemie* **2000**, 626 (11), 2253–2255.
- (14) Popovkin, B. A.; Kusainova, A. M.; Dolgikh, V. A.; Akselrud, L. G. New Layered Phases of the $MOCuX$ (M = Ln, Bi; X = S, Se, TE) Family: A Geometric Approach to the Explanation of Phase Stability. *Russ. J. Inorg. Chem.* **1998**, 43 (10), 1471–1475.
- (15) Kusainova, A. M.; Berdonosov, P. S.; Akselrud, L. G.; Kholodkovskaya, L. N.; Dolgikh, V. A.; Popovkin, B. A. New Layered Compounds with the General Composition $(MO)(CuSe)$, Where M = Bi, Nd, Gd, Dy, and $BiOCuS$: Syntheses and Crystal Structure. *J. Solid State Chem.* **1994**, 112 (1), 189–191.
- (16) Sheets, W. C.; Stampfer, E. S.; Kabbour, H.; Bertoni, M. I.; Cario, L.; Mason, T. O.; Marks, T. J.; Poeppelmeier, K. R. Facile Synthesis of $BiCuOS$ by Hydrothermal Methods. *Inorg. Chem.* **2007**, 46 (25), 10741–10748.
- (17) Tan, S.; Li, D. Enhancing Oxygen Storage Capability and Catalytic Activity of Lanthanum Oxysulfide (La_2O_2S) Nanocatalysts by Sodium and Iron/Sodium Doping. *ChemCatChem* **2017**, 82071, 1–10.
- (18) Mayer, J. M.; Schneemeyer, L. F.; Siegrist, T.; Waszczak, J. V.; Van Dover, B. New Layered Iron-Lanthanum-Oxide-Sulfide and -Selenide Phases: $Fe_2La_2O_3E_2$ (E = S, Se). *Angew. Chemie*

Int. Ed. English **1992**, *31* (12), 1645–1647.

- (19) Charkin, D. O.; Plotnikov, V. A.; Sadakov, A. V.; Omel'yanovskii, O. E.; Kazakov, S. M. Synthesis of Novel Rare Earth—Iron Oxide Chalcogenides with the $\text{La}_2\text{Fe}_2\text{O}_3\text{Se}_2$ Structure. *J. Alloys Compd.* **2011**, *509* (27), 7344–7348.
- (20) Park, J.; Zheng, H.; Jun, Y.; Alivisatos, A. P. Hetero-Epitaxial Anion Exchange Yields Single-Crystalline Hollow Nanoparticles. *J. Am. Chem. Soc.* **2009**, *131* (39), 13943–13945.
- (21) Nelson, A.; Fritz, K. E.; Honrao, S.; Hennig, R. G.; Robinson, R. D.; Suntivich, J. Increased Activity in Hydrogen Evolution Electrocatalysis for Partial Anionic Substitution in Cobalt Oxysulfide Nanoparticles. *J. Mater. Chem. A* **2016**, *4* (8), 2842–2848.

Chapter VII

Towards nickel oxysulfide nanoparticles

Table of contents

VII.1. Molecular approach: nickel sulfide nanoparticles <i>via</i> $\text{Ni}^{(0)}$ and $\text{S}^{(0)}$	219
VII.1.1. Motivation and expectations	219
VII.1.2. Synthesis of nickel sulfides: exploiting the reactivity of $[\text{Ni}^{(0)}(\text{cod})_2]$	220
VII.1.2.1. Preliminary test: reaction of $\text{Ni}^{(0)}$ with $\text{S}^{(0)}$	220
VII.1.2.2. Looking for the room temperature stable nickel sulfide nanoparticles	222
VII.1.2.3. Towards NiS_2 : exploring the Ni_xS_z system up to 260 °C.....	225
VII.1.2.3.1. In 1-octadecene	225
VII.1.2.3.2. Reactions in molten sulfur	228
VII.1.3. Conclusion and perspectives.....	231
VII.2. From metal sulfides to metal oxysulfides	233
VII.2.1. Controlled oxidation of metal sulfides nanoparticles	233
VII.2.2. Amorphous nickel oxysulfide from $[\text{Ni}(\text{cod})_2]$, S_8 and O_2	236
VII.3. Conclusion	241
References	242

VII.1. Molecular approach: nickel sulfide nanoparticles *via* $\text{Ni}^{(0)}$ and $\text{S}^{(0)}$

VII.1.1. Motivation and expectations

To form transition metal oxysulfide nanoparticles, we tried to reuse the $\text{Ln}_2\text{O}_2\text{S}$ synthesis (Chapter VI). Because of the mitigated results of this strategy, we performed in parallel a series of experiments aiming the synthesis of metal sulfide nanoparticles. In the literature, the two reported transition metal oxysulfide nanoparticles (of cobalt¹ and zinc²) were obtained from preformed oxide nanoparticles. We thought that we could also oxidize preformed sulfide nanoparticles to yield similar transition metal oxysulfides.

Which metal(s) to target? In the *d*-block transition metals, all the first-row metals are available from titanium to zinc (scandium is lanthanide-like), are rather affordable and can form sulfides. Among them, we decided to focus on nickel for which we had a good expertise, and for which the design of metal (0), metal borides and metal phosphides are possible at mild temperatures.^{3,4} Besides, it is close to cobalt and zinc.^{1,2}

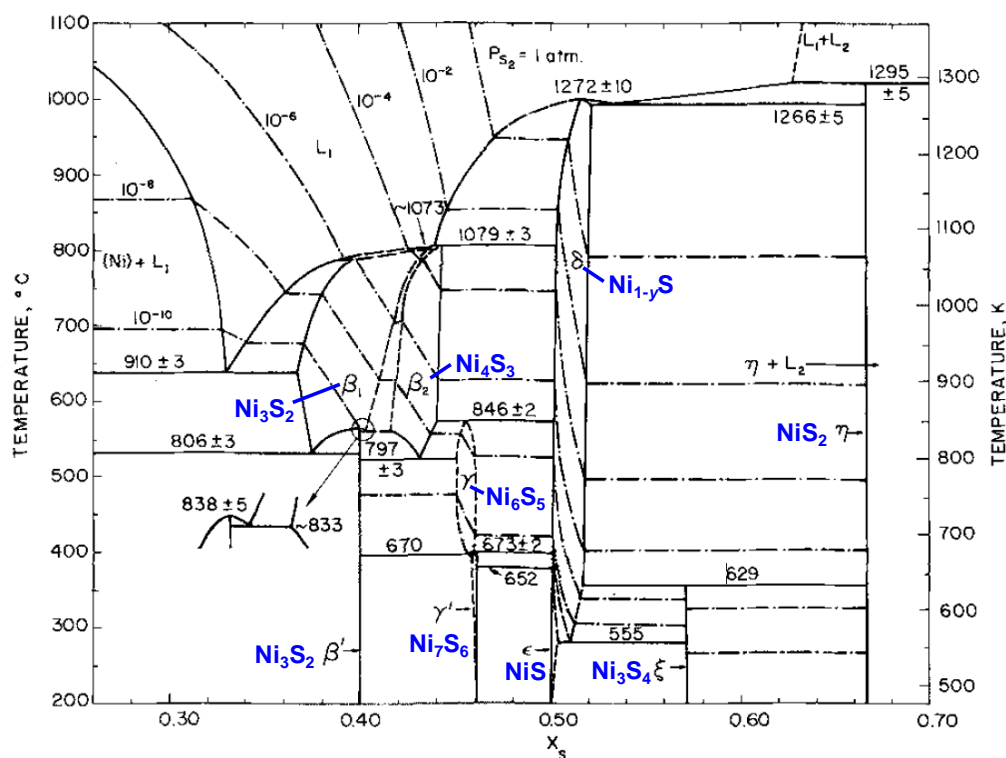


Figure 103: Nickel-sulfur phase diagram for 200 - 1100 °C adapted from Lin *et al.*⁵

The nickel-sulfur system is rich (Figure 103).⁵ With increasing sulfur fraction, crystalline Ni_3S_2 (β_1 , β_2), Ni_4S_3 (β_2), Ni_7S_6 (γ'), Ni_6S_5 (γ), NiS (ϵ), Ni_{1-y}S (δ), Ni_3S_4 (ξ) and NiS_2 (η) are found in the phase diagram. The system is also quite complex for sulfur fractions between

0.44 and 0.48. Stølen *et al.* reported an updated version of the region between 600 and 900 K (327 - 627 °C) in 1994 (Figure 104).⁶ From the two diagrams, we can expect five nickel sulfide phases to be stable below 280 °C: Ni₃S₂, Ni₉S₈, NiS, Ni₃S₄ and NiS₂. It encouraged us to target these phases for the synthesis of nickel sulfide nanoparticles.

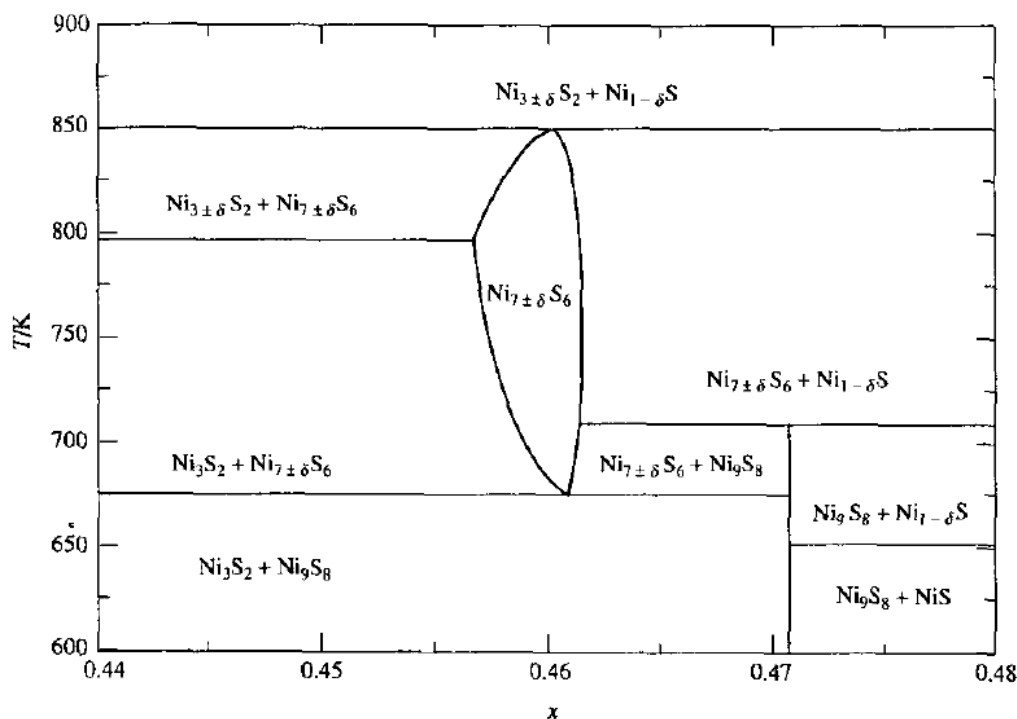


Figure 104: Nickel-sulfur phase diagram for sulfur fractions in the range 0.44-0.48 by Stølen *et al.*⁶

The synthesis of nanoscaled nickel sulfides was extensively studied. It is challenging to selectively obtain each of the pure phases with the same route (i.e. with no major change of operating conditions). However, few versatile methods are referenced on the versatile syntheses of nickel sulfides nanoparticles, using H₂S/H₂ on nickel nanoparticles deposited on graphene,⁷ elemental sulfur on Ni plates,⁸ or single source decomposition,^{9,10} or injection method.^{11,12}

VII.1.2. Synthesis of nickel sulfides: exploiting the reactivity of [Ni⁽⁰⁾(cod)₂]

VII.1.2.1. Preliminary test: reaction of Ni⁽⁰⁾ with S⁽⁰⁾

To form nickel sulfide nanoparticles, we can use different approaches. Classically, a source of Ni^{II} (most of the nickel complexes) could react with S^{-II} (H₂S, thiourea, thioacetamide, ammonium sulfide, Na₂S...). Nanoparticles of reduced metal could also be sulfidated by an adequate agent.

Because of the availability of a $\text{Ni}^{(0)}$ complex, namely $[\text{Ni}^{(0)}(\text{cod})_2]$ (cod = 1,5-cyclooctadiene), we chose to try the reaction between molecular $\text{Ni}^{(0)}$ and $\text{S}^{(0)}$ (elemental sulfur, Figure 105). In $[\text{Ni}(\text{cod})_2]$, the cyclooctadiene ligands are weakly coordinated to the metal and at least one can easily leave its coordination sphere. Plus, $\text{Ni}^{(0)}$ and $\text{S}^{(0)}$ can exchange two electrons (donation from the metal to sulfur) to formally obtain common and stable oxidation states of nickel and sulfur: Ni^{II} and $\text{S}^{-\text{II}}$.

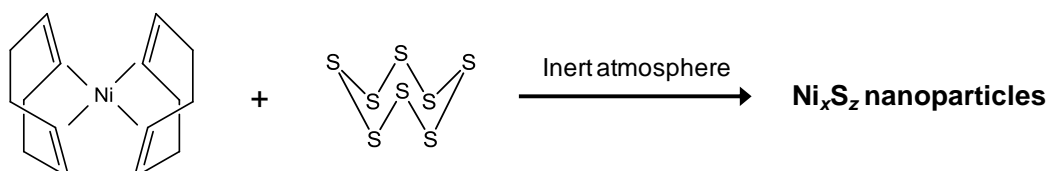


Figure 105: Synthetic strategy to get nickel sulfide nanoparticles.

The $[\text{Ni}(\text{cod})_2]$ complex is particularly sensitive to oxygen. For a preliminary test [CL029], a yellow solution of $[\text{Ni}(\text{cod})_2]$ (2.2×10^{-2} M) was prepared in anhydrous THF in inert atmosphere ($\text{H}_2\text{O} < 0.5$ ppm; $\text{O}_2 < 0.5$ ppm). Dehydrated elemental sulfur was then introduced as a powder in the solution (2 equiv. vs. Ni). As soon as the sulfur flakes touched the solution, they became black and the solution rapidly turned black **at room temperature**. After the sulfur addition, the Schlenk tube was gently heated (80°C) under vacuum to remove the cyclooctadiene ligands and THF.

After two washing steps with THF/ethanol mixtures under air, a black paste was obtained and characterized by XRD and TEM.

Polydisperse nanoparticles were obtained (Figure 106B). Big spherical crystalline hollow nanoparticles with a diameter of 20 - 100 nm and smaller objects (5 - 10 nm) coexisted. NiS_2 is stable at low temperature and was expected to form, considering than 2 equivalents of sulfur vs. Ni were introduced. Instead, crystalline Ni_3S_4 was observed (Figure 106A).

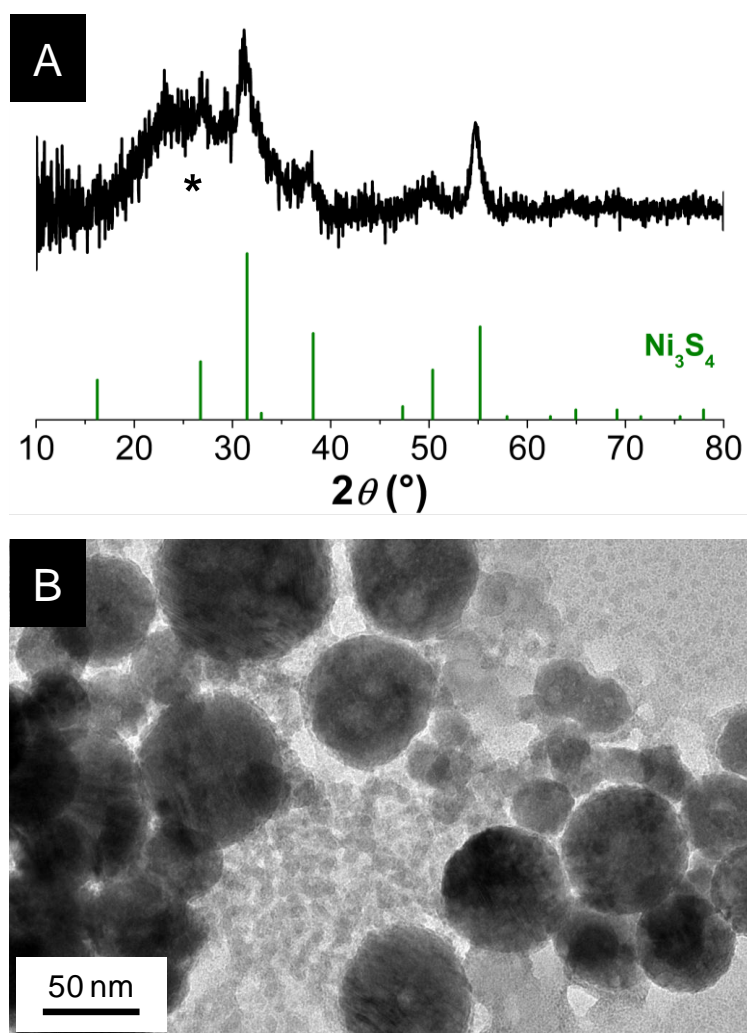


Figure 106: (A) XRD pattern of the black paste of nickel sulfide. The XRD pattern reference is 47-1739 (Ni_3S_4). The star indicates the broad signal of a glass slide on which is deposited the paste. (B) TEM micrographs of the Ni_xS_z nanoparticles.

VII.1.2.2. Looking for the room temperature stable nickel sulfide nanoparticles

After this first encouraging test, the setup of the reaction was revised. The addition of sulfur flakes was replaced by the dropwise addition of a S_8 solution in THF, making the sulfur introduction more regular and slower. The reaction was stirred for a few hours to favor a quantitative reaction of the nickel source. The powder was separated from cyclooctadiene by centrifugation (one or two washing steps with THF were required) to avoid the heating of the solution.

Now that we found out that we were able to obtain crystalline nickel sulfides at room temperature, we tried to obtain pure Ni_3S_2 (the richest in nickel), NiS (the 1:1 composition), Ni_3S_4 (the one already obtained) and NiS_2 (the richest in sulfur). The sulfur amount was

adjusted and the reactions carried out for one night at least. The XRD patterns of the black powders are presented in Figure 107.

Interestingly, two phases of crystalline sulfide nanoparticles were obtained from the reactions at ambient temperature: Ni_3S_2 and Ni_3S_4 . With less than 2/3 equiv. of sulfur vs. Ni, the phase was Ni_3S_2 (Figure 107f). For more than 4/3 equiv. vs. Ni, the nanoparticles crystallized in the Ni_3S_4 phase (Figure 107a and b). Nickel did not accept more sulfur in these conditions. However, for the 1:1 composition, an amorphous product was obtained. Based on EDS, the product was probably amorphous NiS.

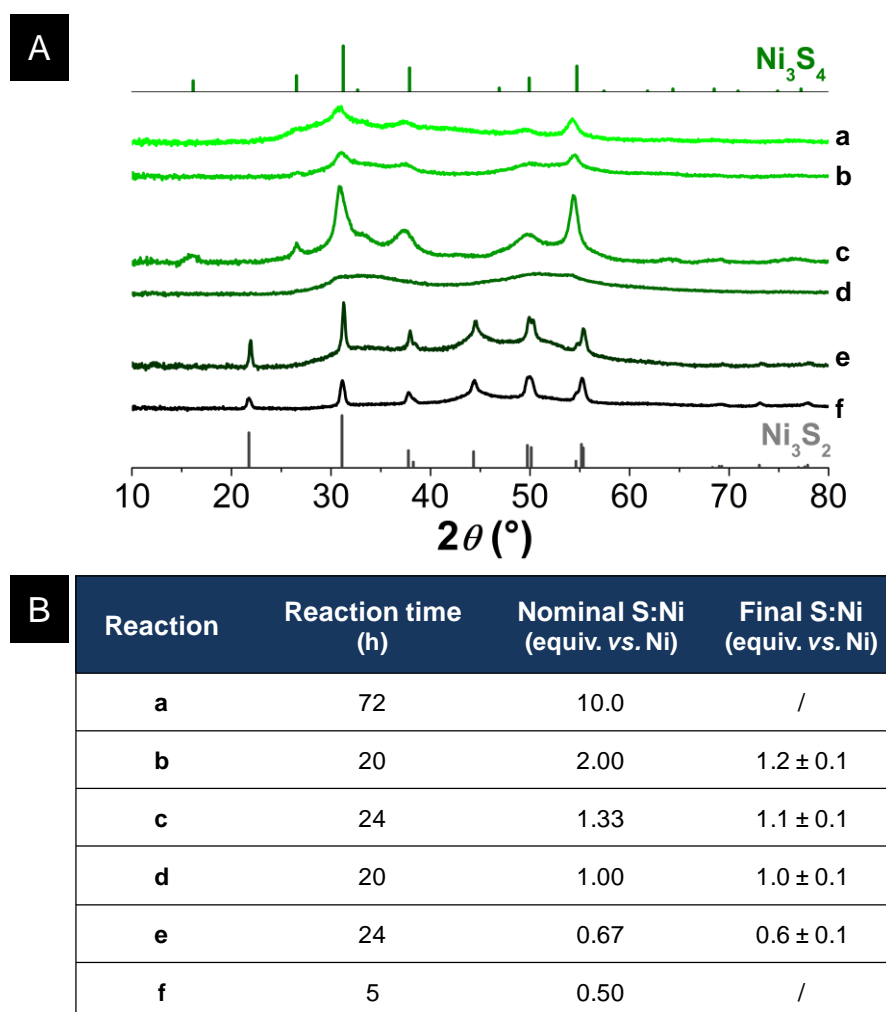


Figure 107: (A) Powder XRD patterns of Ni_xS_z nanoparticles (a:[CL051]; b: [CL385]; c: [CL476]; d: [CL376]; e: [CL475]; f: [CL346]). XRD pattern references are JCPDS files 44-1418 (gray, Ni_3S_2) and 47-1739 (green, Ni_3S_4). (B) Experimental conditions for the study. The final S/Ni ratio was obtained by EDS.

One will also notice that for 2/3 equiv. of sulfur vs. Ni, there is a clear amorphous contribution on the XRD pattern (Figure 107e). Because the whole powder was attracted by a

magnet, the amorphous phase was attributed to non-sulfidated $\text{Ni}^{(0)}$. The final structure of the nanoparticles is probably a small core of amorphous Ni metal surrounded by crystalline Ni_3S_2 . The same trend is observed for 4/3 equiv. of S vs. Ni (Figure 107c). As the powder did not show any attraction to a magnet, we can propose that it was not amorphous $\text{Ni}^{(0)}$ this time. We can imagine that an amorphous core (maybe less rich in S than Ni_3S_4) remains. Globally, EDS shows that a small fraction of sulfur does not properly react. The nanoparticles obtained for 2/3 and 4/3 equiv. of S vs. Ni were observed by TEM (Figure 108).

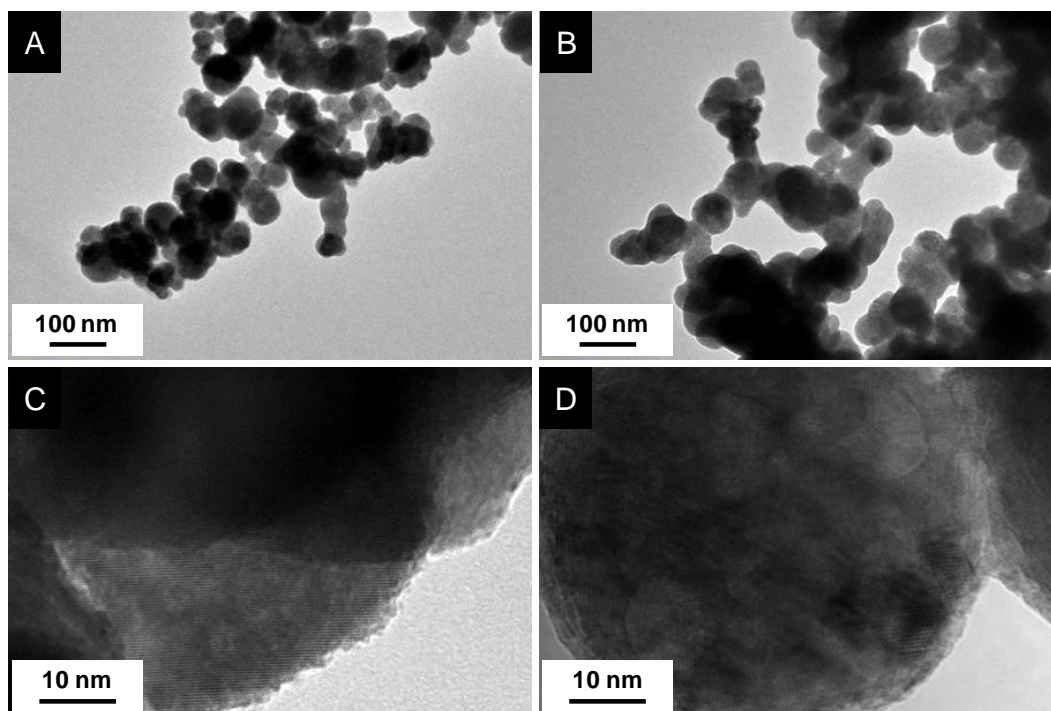


Figure 108: TEM micrographs of Ni_3S_2 nanoparticles (A and C, [CL475]) and Ni_3S_4 nanoparticles (B and D, [CL476]).

The nanoparticles were still spherical, polydisperse and polycrystalline (Figure 108A and B), but seemed to be more regular than these from our preliminary experiment (Figure 106B). There is no clear evidence of a core-shell structure, which we expected from the XRD patterns and the EDS analysis (Figure 107). However, we observed holes in the spheres and a majority of the nanoparticles are well crystallized (Figure 108C and D).

The holes could evidence the presence of unbalanced diffusion processes during the syntheses. The difference between the diffusion rates of sulfur and nickel in preformed nanoparticles could explain this peculiar porous morphology. It can be justified by the large size of sulfur anions compared to the nickel cations. This phenomenon is commonly called “nano-Kirkendall effect”.¹³

We were satisfied to obtain different nickel sulfides at room temperature with a reproducible morphology. The sulfur stoichiometry controls the formation of crystalline Ni_3S_2 , amorphous NiS and crystalline Ni_3S_4 with minor impurities coming from a small fraction of unreacted sulfur. However, whatever the sulfur loading above 4/3 equiv. vs. Ni , we were unable to form NiS_2 . It motivated us to heat the synthesis mixture.

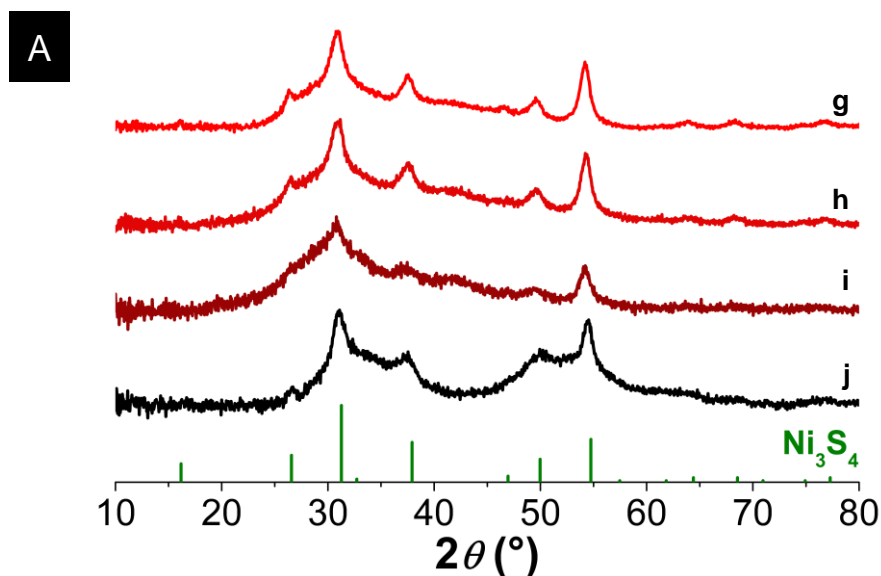
VII.1.2.3. Towards NiS_2 : exploring the Ni_xS_z system up to 260 °C

VII.1.2.3.1. In 1-octadecene

The sulfur-richest phase of the Ni_xS_z system, NiS_2 , could not be obtained at room temperature from solutions of $[\text{Ni}(\text{cod})_2]$ and S_8 in THF even with 10 equiv. of S vs. Ni . In the literature, this phase was obtained only with a temperature above 200 °C,^{7,9–12,14} with first traces detected at 160 °C.⁸

We thus decided to heat the reaction mixture. For temperatures below 80 °C (THF boiling point), the Schlenk was directly heated. For temperatures above 80 °C, a solvent exchange was required. Degassed 1-octadecene was added in the black solution. The cyclooctadiene and THF were gently evaporated under vacuum. The mixture could then be heated at any temperature below 310 °C.

Several tests were conducted with 2 equiv. of S vs. Ni (Figure 109). For the low temperatures (up to 150 °C), the reaction was conducted during 24 hours at least. For 260 °C, based on other works,^{9,11} we performed the reaction for only one hour. Ni_3S_4 nanocrystals were obtained regardless of the reaction temperature (Figure 109).



B

Reaction	Nominal S:Ni (equiv. vs. Ni)	Temperature (° C)	Reaction time (h)
g	2	25	24 ^[a]
h	2	50	72
i	2	150	72
j	2	260	1

[a] Same result for 72 hours.

Figure 109: Temperature investigation of the reaction $[\text{Ni}(\text{cod})_2] + \text{S}_8$ with 2 equiv. of S vs. Ni. (A) Powder XRD patterns (g:[CL437]; h: [CL052]; i: [CL042]; j: [CL385]). XRD pattern reference is JCPDS file 47-1739 (Ni_3S_4). (B) Experimental conditions.

Following this, several parameters could be adjusted to obtain NiS_2 at 260 °C: concentration of the precursors, reaction time or S:Ni ratio. Because the concentration of $[\text{Ni}(\text{cod})_2]$ was already high (10^{-1} M) and the reaction time likely sufficient, we chose to play on the S:Ni ratio. The reaction was thus performed with 10 equiv. of S vs. Ni (Figure 110).

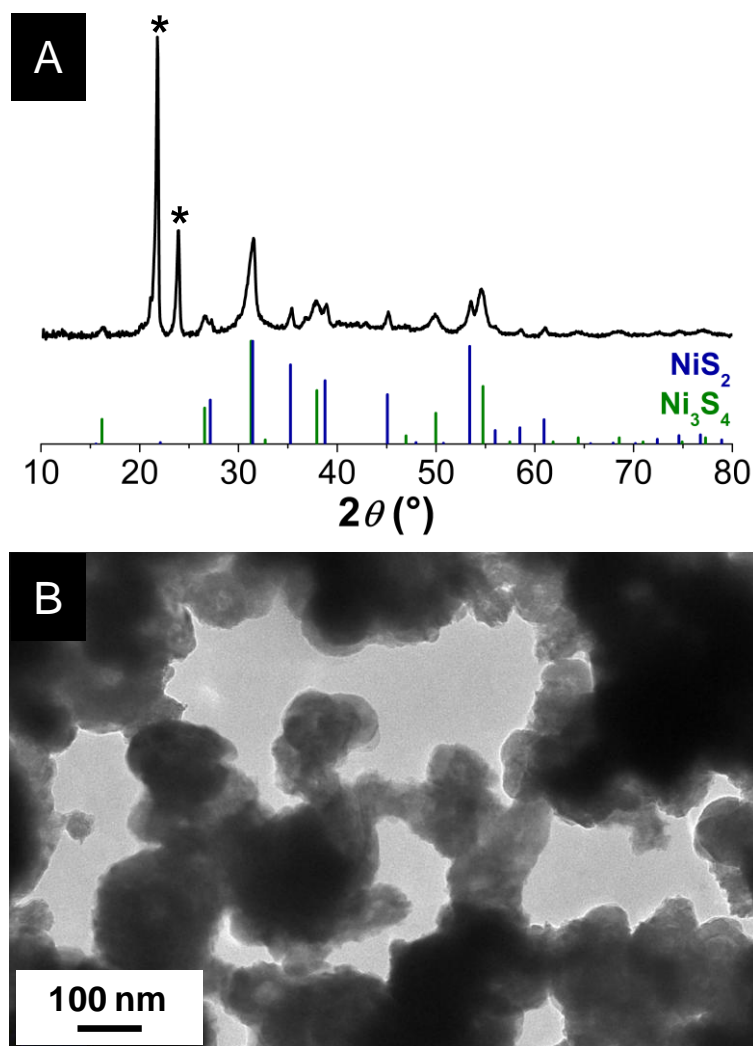


Figure 110: Power XRD pattern (A) and TEM micrograph (B) of the reaction product of $[\text{Ni}(\text{cod})_2] + \text{S}_8$ in 1-octadecene at 260 °C with 10 equiv. of S vs. Ni [CL442]. XRD pattern references are JCPDS files 47-1739 (Ni_3S_4) and 73-0574 (NiS_2). Stars indicate a common impurity coming from the solvent.

NiS_2 nanocrystals were finally obtained. They form a mixture with Ni_3S_4 nanoparticles. Using 10 equiv. of S vs. Ni was a good idea but still not enough to get the pure NiS_2 phase. We did not try to perform the reaction for a longer time, but we can expect that it will lead to a better NiS_2 yield. We also carried out the reaction for other S:Ni ratios, leading to the results presented on (Figure 111).

For 1 equiv. of S vs. Ni (NiS targeted), Ni_9S_8 and NiS were obtained (Figure 111). For 1.33 equiv. (Ni_3S_4 targeted), NiS and Ni_3S_4 were formed (Figure 111). With the other results already detailed, it seems that at high temperature just as well as at room temperature, a sulfur defect is observed and the targeted product cannot be obtained from stoichiometric conditions.

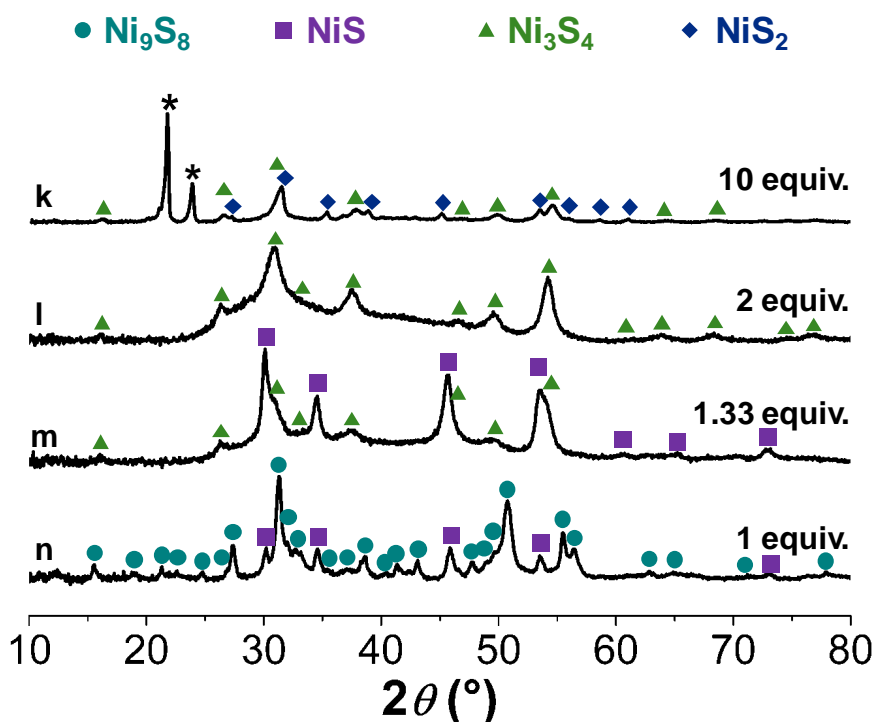


Figure 111: Powder XRD patterns of the products obtained from $[\text{Ni}(\text{cod})_2] + \text{S}_8$ at 260 °C (k: [CL415]; l: [CL438]; m: [CL437]; n: [CL442]). XRD pattern references are JCPDS files 78-1886 (light blue, Ni_9S_8), 77-1624 (violet, NiS), 47-1739 (green, Ni_3S_4) and 73-0574 (dark blue, NiS_2). Stars indicate a common impurity coming from the solvent.

These reactions were also a good way to have a clue about the nature of the amorphous products obtained at room temperature. For 1 equiv. of S vs. Ni, the amorphous product may thus be a mixture of Ni_9S_8 and NiS . For 1.33 equiv., the presence of amorphous NiS is likely and explains the final S:Ni ratio (1.1 ± 0.1) lower than 1.33.

VII.1.2.3.2. Reactions in molten sulfur

Even with an excess of sulfur (10 equiv. vs. Ni), pure nanoscaled NiS_2 could not be obtained in 1-octadecene. Therefore, we forced the nickel to be in a far more sulfur-concentrated medium by performing the reaction in molten sulfur.

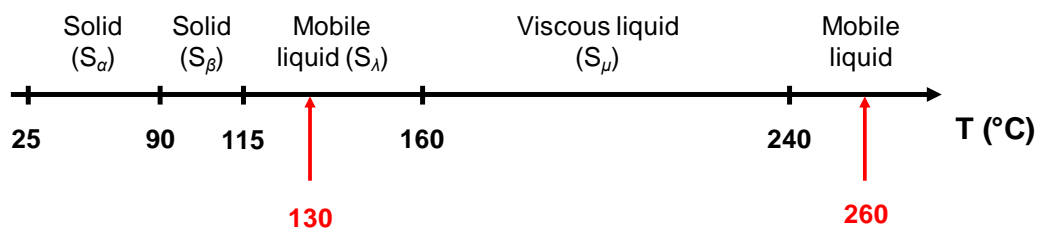


Figure 112: Elemental sulfur behavior upon heating and chosen reaction temperatures (red).

However, elemental sulfur is not a convenient solvent (Figure 112).¹⁵ It remains solid (S_α) up to around 115 °C and then melts to form a deep red mobile liquid (S_λ). At 159 °C, sulfur rings start to break and form long chains of sulfur atoms (S_μ). Consequently, the liquid becomes very viscous. A thermal conductivity drop accompanies this evolution, making the liquid very hard to heat. But after 200 °C, the chains retrieve some mobility and the viscosity decreases. A mobile fluid is observed above 240 °C.

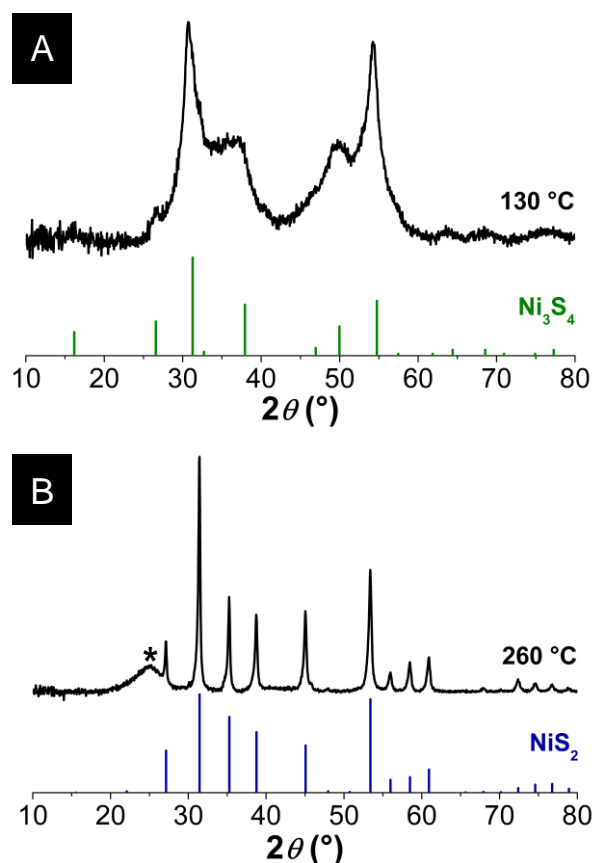


Figure 113: Powder XRD patterns of the products of the syntheses in molten sulfur at 130 °C (A, [CL408]) and 260 °C (B, [CL410]). XRD pattern references are JCPDS files 47-1739 (green, Ni_3S_4) and 73-0574 (dark blue, NiS_2). The star indicates amorphous sulfur.

Two windows were possible for the reaction in molten sulfur: the 115 - 160 °C range and above 240 °C. We decided to investigate the two ranges and chose 130 °C and 260 °C as

reaction temperatures (Figure 112). The yellow solid $[\text{Ni}(\text{cod})_2]$ was added in around 10 g of elemental sulfur in a three-necked flask under inert atmosphere. After a few minutes, the solid started to turn black. It was rapidly heated under inert atmosphere up to the reaction temperature.

The products obtained after ~ 1 h are presented in Figure 113. If the reaction still yields Ni_3S_4 at 130°C , **the reaction at 260°C in molten sulfur yields crystalline NiS_2 as the only crystalline species**. However, for the latter sample, the mass of the product is much higher than expected ($\eta \approx 500\%$). Removing the polymerized sulfur chains is a challenging process even with numerous washing steps. Thus a significant amount of sulfur remains in the final product. Accordingly, the XRD pattern shows an amorphous contribution around 25° (Figure 113B). For the product obtained from the reaction at 130°C , washing with butylamine, THF and ethanol was sufficient to eliminate all the remaining sulfur. It is undoubtedly the formation of the viscous S_μ liquid that forms the amorphous sulfur which is challenging to remove.

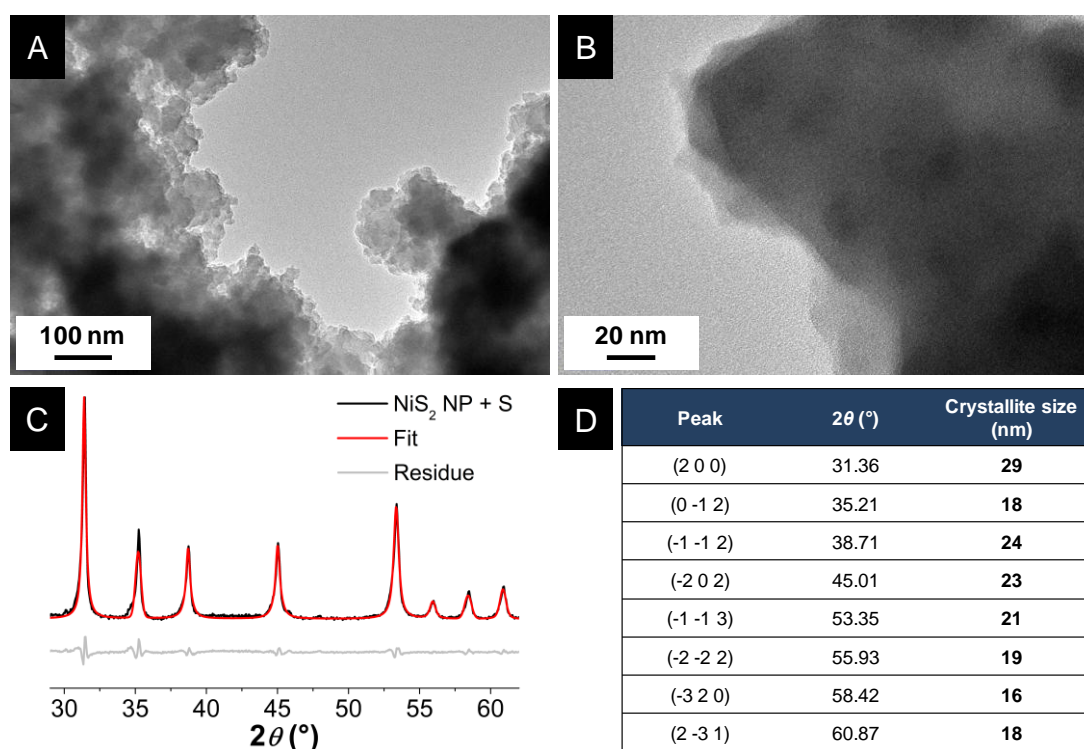


Figure 114: (A and B) TEM micrographs of NiS_2 nanoparticles in amorphous sulfur. (C) Fit of the powder XRD pattern of the $\text{NiS}_2 + \text{S}$ nanoparticles. (D) Crystallite size obtained by the Scherrer's formula using the full width half maxima from the fit parameters.

On the TEM micrographs, we see aggregated nanocrystals embedded in an amorphous gangue which must correspond to the amorphous sulfur (Figure 114). Because of the sulfur, the

nanocrystals could not be observed at high magnifications, but we can estimate from TEM images that their size is comprised between 20 and 40 nm. This size is in agreement with the crystallite size calculated via the Scherrer's formula, with typical sizes between 15 and 30 nm (Figure 114D).

VII.1.3. Conclusion and perspectives

The synthesis of nickel sulfides with a new strategy at room temperature was successful and ended up with crystalline Ni_3S_2 and Ni_3S_4 , both of them with a low amount of amorphous impurity $\text{Ni}^{(0)}$ (ferromagnetic) and NiS respectively. The nanoparticles are spherical and aggregated. To the best of our knowledge, this is the first synthesis of crystalline nickel sulfide nanoparticles at ambient temperature.

Mixtures of $\text{Ni}_9\text{S}_8/\text{NiS}$, $\text{NiS}/\text{Ni}_3\text{S}_4$, $\text{Ni}_3\text{S}_4/\text{NiS}_2$ were obtained at higher temperature (260 °C) and confirmed that a defect of sulfur is always observed in the final product. Using molten sulfur, pure NiS_2 nanoparticles were finally reached, but were trapped in amorphous sulfur.

Remarkably, we were able with $[\text{Ni}(\text{cod})_2]$ and S_8 to obtain all the phases described below 280 °C in the phase diagram (Figure 103, Figure 104 and Figure 115). It is likely that using a larger excess of sulfur may provide the pure Ni_xS_y phases at 260 °C and/or room temperature, depending on the targeted sulfide.

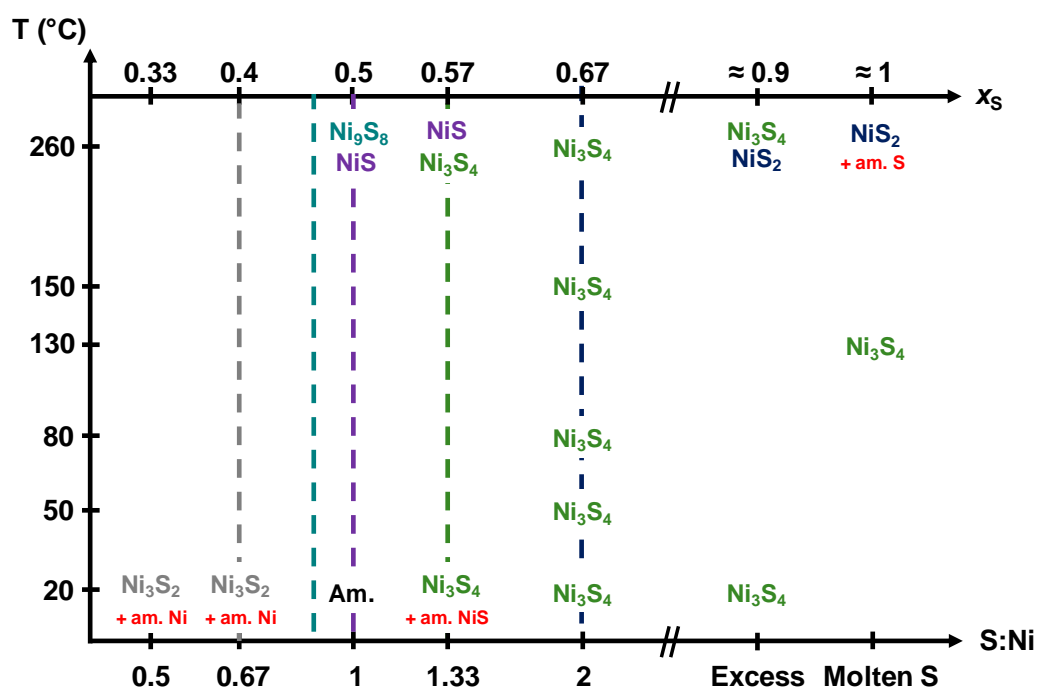


Figure 115: Phase speciation obtained for the $[\text{Ni}(\text{cod})_2] + \text{S}_8$ system. The bottom axis represents the nominal S:Ni ratio, and the top axis is the nominal sulfur fraction ($x_S = n_S / (n_S + n_{\text{Ni}})$). The vertical

dashed lines indicate the position of the pure phases; from left to right: Ni_3S_2 (gray), Ni_9S_8 (light blue), NiS (violet), Ni_3S_4 (green) and NiS_2 (dark blue).

The nanoparticles of Ni_3S_2 (+ amorphous Ni), Ni_3S_4 (+ amorphous NiS) and NiS_2 (+ amorphous S) were tested for the electrocatalytic reduction of CO_2 . Even if their activity was quite low for such reactions, they turned out to show significant activity for proton reduction (data not shown). This work is still ongoing for the valorization of Ni_xS_z non-noble and stable catalysts for proton reduction.

VII.2. From metal sulfides to metal oxysulfides

VII.2.1. Controlled oxidation of metal sulfides nanoparticles

Our first idea was to use the sulfide nanoparticles to turn them into oxysulfide nanoparticles. Why do we choose oxygen insertion rather than sulfur insertion? We thought that it was easier to insert oxygen anions ($r(\text{O}^{\text{II}}) = 1.26 \text{ \AA}$) by diffusion in the sulfide structure than sulfide ions ($r(\text{S}^{\text{II}}) = 1.70 \text{ \AA}$) in an oxide.

Several oxide donors are possible. However, they must be strong enough to incorporate oxygen (formally at a negative oxidation state) into the structure, but without oxidizing the sulfur atoms into sulfites or sulfates.

What sulfide could bear oxide insertion? The ideal choice would be a pure crystalline phase in which nickel can accept supplementary anions. We did not obtain pure phases from our sulfide synthesis, but we chose the “ Ni_3S_2 ” sample that contains crystalline Ni_3S_2 nanoparticles with a little amount of $\text{Ni}^{(0)}$.

Oxygen from air was first chosen as oxygen provider. The calcination of nickel sulfide nanoparticles powder was conducted based on works on iron and cobalt sulfides, which were synthesized by sulfidation of $\text{Fe}^{(0)}$ and $\text{Co}^{(0)}$ nanoparticles. The syntheses of the latter metal nanoparticles [CL126a for $\text{Fe}^{(0)}$, CL127a for $\text{Co}^{(0)}$] and sulfides nanoparticles [CL126b for Fe_xS_z , CL127b for Co_xS_z] are detailed in the experimental section.

The temperature of the oxidation by air of Ni_3S_2 nanoparticles was fixed to 250°C and the reaction time to 3 hours. Under air, the nanoparticles formed a mixture of sulfide products with Ni_3S_2 , Ni_9S_8 , NiS and Ni_3S_4 nanostructures, according to XRD (Figure 116B).

Moreover, nickel oxide NiO also crystallized (Figure 116B). From the XRD pattern broad peaks, we can say that the NiO nanocrystals were pretty small. On the TEM micrographs, small nanospheres with a diameter between 5 to 10 nm (Figure 117) were detected. This crystallization of both NiO and sulfides which contain more sulfur than in Ni_3S_2 has already been observed by the XPS study of the oxidation of Ni_3S_2 by Buckley and Woods.¹⁶

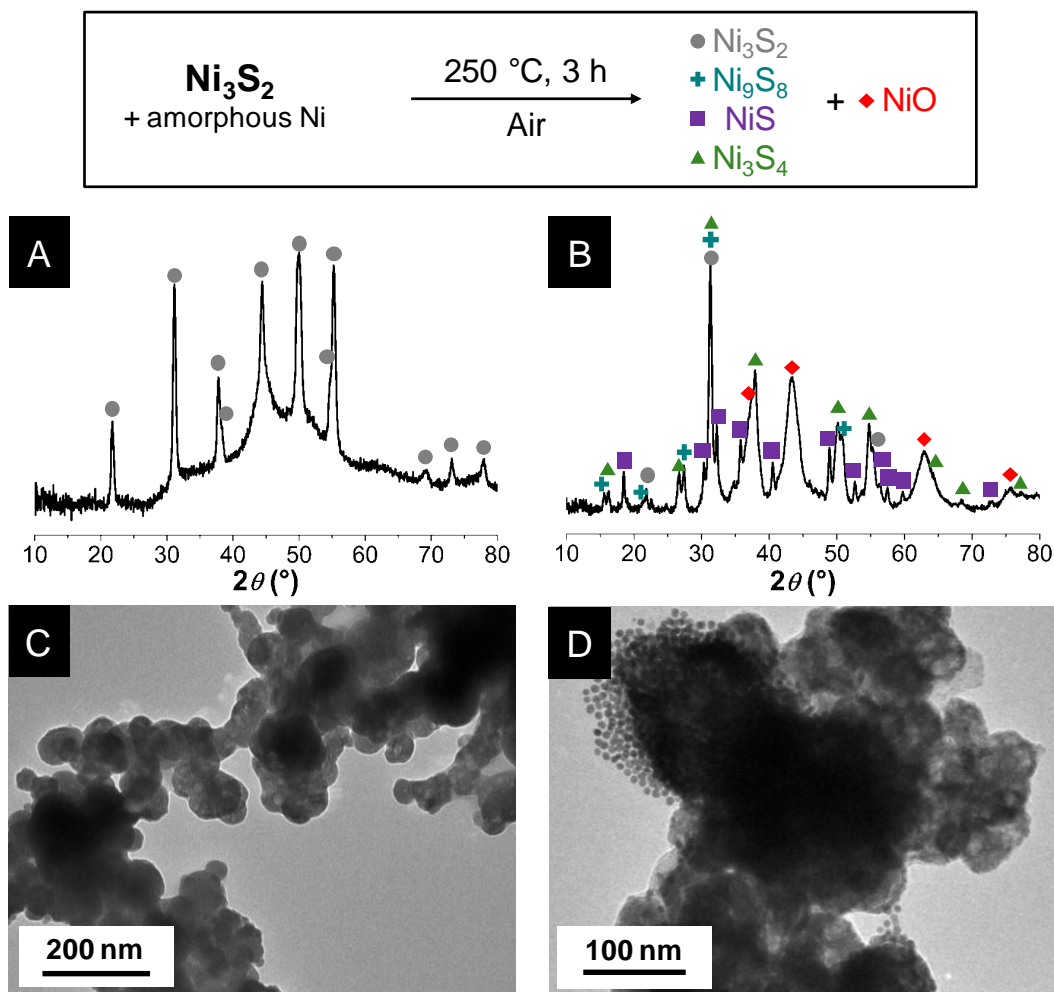


Figure 116: Calcination of the Ni_3S_2 nanoparticles (+ amorphous Ni) at $250\text{ }^\circ\text{C}$ for 3 hours. XRD patterns of the initial powder (A, [CL346]) and the powder after calcination (B, [CL348]). XRD pattern references are JCPDS files 44-1418 (gray circles, Ni_3S_2), 78-1886 (light blue crosses, Ni_9S_8), 12-0041 (violet squares, NiS), 47-1739 (green triangles, Ni_3S_4) and 47-1049 (red diamonds, NiO). TEM micrographs before (C) and after calcination (D).

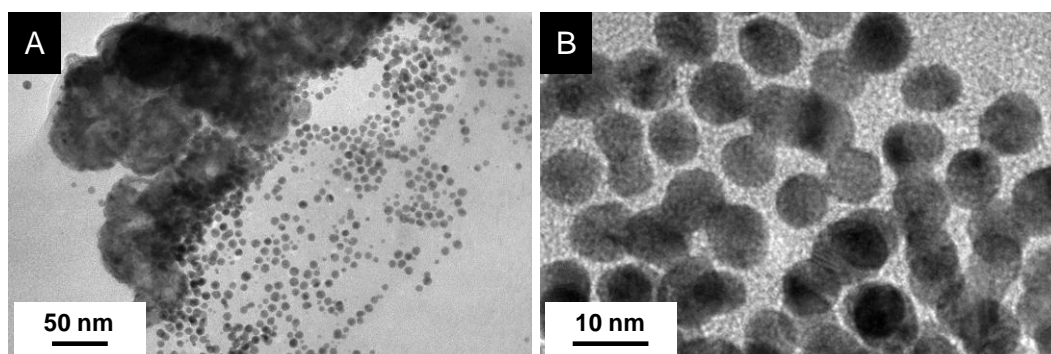


Figure 117: NiO nanoparticles formed during the calcination of Ni_3S_2 nanoparticles.

A fairly similar result was obtained for iron and cobalt sulfides. However, the starting materials were already complex mixtures of sulfides Fe_xS_z and Co_xS_z .

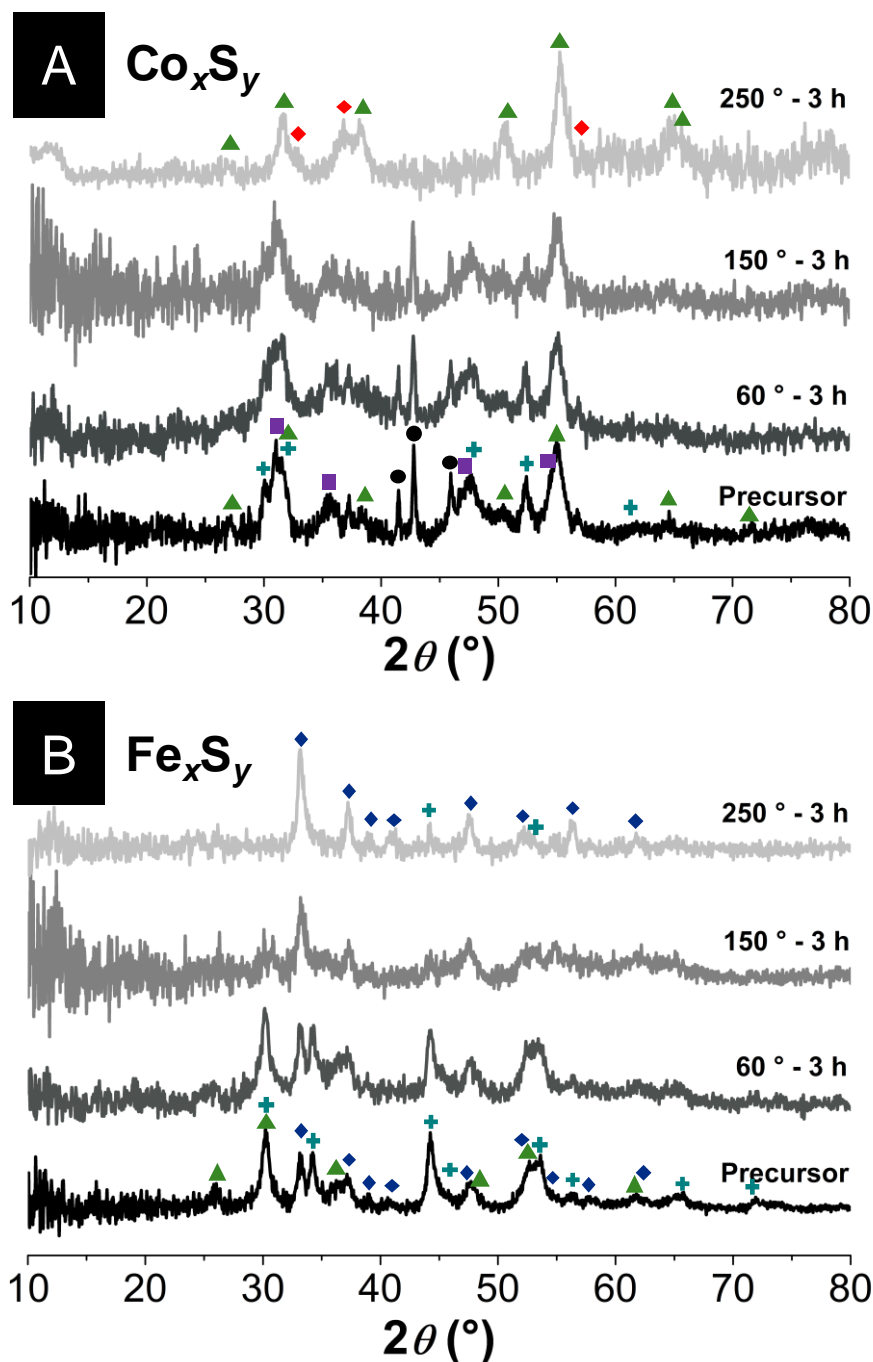


Figure 118: (A) Calcination of the sulfides mixture of cobalt with XRD pattern references JCPDS files being 88-2325 and 89-4308 (black circles, Co and Co- β respectively), 86-2273 (light blue crosses, Co_9S_8), 65-8977 (violet squares, CoS), 47-1738 (green triangles, Co_3S_4) and 70-2855 (red diamonds, CoO). (B) Calcination of the sulfides mixture of iron with XRD pattern references being JCPDS files 89-1954 (light blue crosses, Fe_7S_8), 89-1998 (green triangles, Fe_3S_4), 37-0475 and 42-1340 (dark blue diamonds, FeS_2 , marcasite and pyrite respectively).

After calcination at 250 °C, the crystallization of the sulfur-richest sulfides was fostered (Figure 118). For cobalt, the mixture of $\text{Co}^{(0)}$, Co_9S_8 , CoS, Co_3S_4 became Co_3S_4 and CoO after the calcination at 250 °C for 3 hours (Figure 118A). Up to 150 °C, no significant

variations of the XRD pattern of the mixture was observed. For iron, FeS₂-pyrite crystallization was favored starting from Fe₇S₈, Fe₃S₄ and FeS₂-marcasite (Figure 118B). After calcination at 150 °C, the mixture was already strongly affected. We suspect that iron oxide nanoparticles were also formed in this case. Altogether, this method of calcination under air is likely not suitable for the formation of oxysulfide nanoparticles, even if we cannot be completely sure that no oxysulfide was formed from the XRD patterns. We can for instance imagine an oxysulfide structure very close to a sulfide or an oxide.

For nickel, we also tried to use an aqueous solution of H₂O₂. Our first attempt, with a large excess of oxidant, showed that Ni₃S₂ degraded and was oxidized in hydrated nickel sulfate Ni(SO₄)·xH₂O.

We could have tried various other soft chemical oxidation processes, but we decided to switch back to the formation of the nickel sulfides from the [Ni(cod)₂] complex.

VII.2.2. Amorphous nickel oxysulfide from [Ni(cod)₂], S₈ and O₂.

This section is based on the idea that once the nickel sulfide crystallized, it is hard to oxidize it in a nickel oxysulfide without segregating nickel oxide and nickel sulfides or forming nickel sulfates.

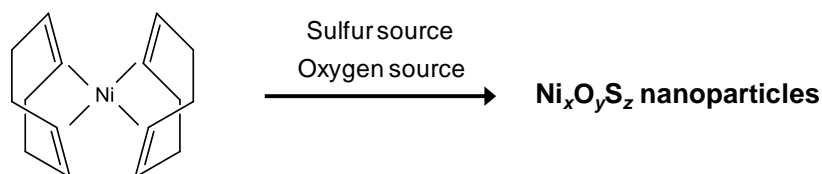
We thus came back to the sulfide synthesis: at ambient temperatures, a solution of elemental sulfur is added to a solution of [Ni(cod)₂] under inert atmosphere. Is it possible to add an oxidant in a controlled quantity during the reaction to form a nickel oxysulfide with a similar synthetic route?

Various oxygen and sulfur sources were combined. With elemental sulfur, bubbling O₂ and metachloroperbenzoic acid (*m*-CPBA, organic soft oxidant) were used. A solution of (NH₄)₂S in water was used as both oxygen and sulfur source. Hydrated sodium sulfide Na₂S·9H₂O was also tested. The results obtained using these syntheses are summarized in Figure 119.

The easiest interpretation is the reaction with Na₂S·9H₂O. From XRD, we know that we formed sodium sulfite and sodium sulfate, two undesired products obtained from sulfur oxidation.

However, the other results were encouraging. With elemental sulfur, bubbling O₂ and *m*-CPBA yielded an amorphous black powder (Figure 119, Figure 120). Used as a source of both oxygen and sulfur, (NH₄)₂S also led to an amorphous product (Figure 119, Figure 120). These results are different from the case where no oxygen source is added (crystallization of

Ni₃S₂ with some amorphous Ni), and mean that oxygen is involved in the nanoparticles formation. Also, none of these products were ferromagnetic at ambient temperature, meaning that there is no remaining Ni⁽⁰⁾.



Sulfur source	Oxygen source	Phase(s) from XRD	S:Ni (EDX)
S ₈	X	Ni ₃ S ₂	0.6 ± 0.1
S ₈	O ₂ (during and after S ₈ addition)	Amorphous	0.3 ± 0.1
S ₈	O ₂ (before, during and after S ₈ addition)	Amorphous	0.4 ± 0.1
S ₈	<i>m</i> -CPBA	Amorphous	1.0 ± 0.1
(NH ₄) ₂ S	H ₂ O	Amorphous	1.0 ± 0.1 ^[a]
Na ₂ S·9H ₂ O	Na ₂ S·9H ₂ O	Na ₂ SO ₃ Na ₂ SO ₄	X

[a] After annealing under argon at 200 °C, 1 h.

Figure 119: XRD and EDS results of the attempts of forming nickel oxysulfide by simultaneous oxidation and sulfidation of [Ni(cod)₂]. The nominal S:Ni ratio is 0.67 for all the reactions.

From EDS in Figure 119, the results obtained from the use of O₂ (bubbling air) are particularly encouraging: the sulfur amount (S:Ni ≈ 0.4) is not high enough to correspond to any stable sulfide phase (at least S:Ni = 0.67). It could indicate that both oxygen and sulfur stabilize nickel cations in these amorphous compounds.

Before further investigation, these amorphous compounds were annealed under inert atmosphere to try to crystallize what are possibly amorphous nickel oxysulfide nanoparticles. Because nickel oxysulfide may not be very stable, mild conditions were chosen (200 °C, 1 h). In spite of the fact that no oxysulfide crystallized, this thermal treatment was informative on the nature of the bonds in the nanoparticles (Figure 121).

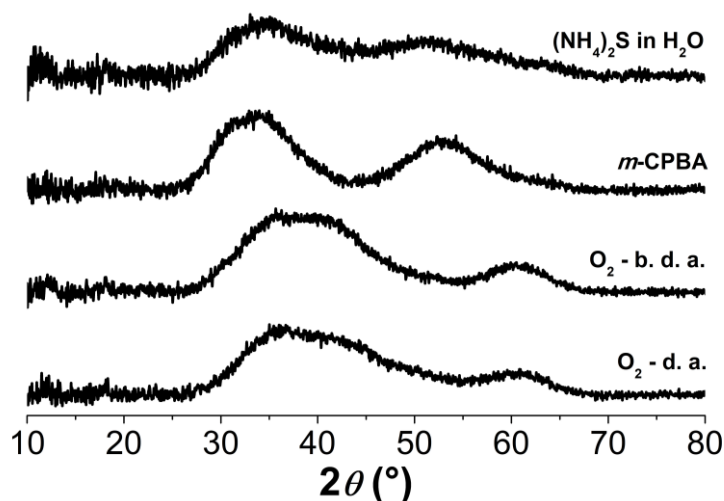


Figure 120: XRD patterns of the particles obtained from the simultaneous oxidation and sulfidation of $[\text{Ni}(\text{cod})_2]$. Abbreviations: “b.” stands for “before”, “d.” for “during” and “a.” for “after” and these three refer to the bubbling time of air compared to the dropwise sulfur addition. For instance, the sample “b. d. a.” means that air bubbled before, during and after the addition of the sulfur solution in THF.

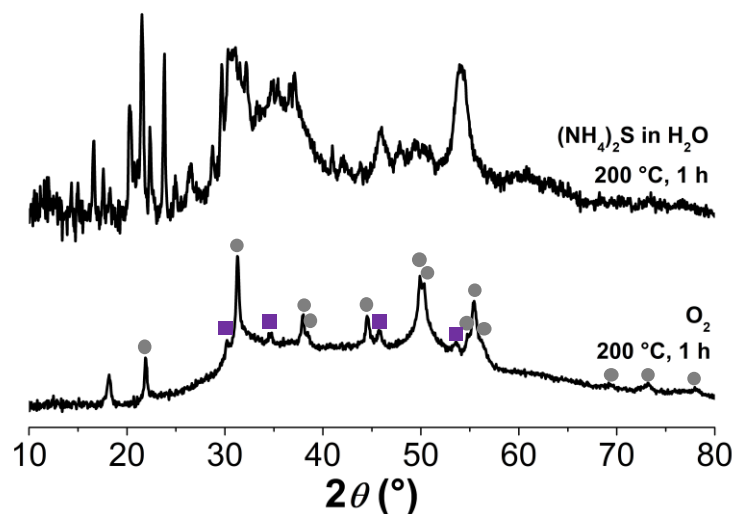


Figure 121: XRD patterns of annealed $\text{Ni}_x\text{O}_y\text{S}_z$ nanoparticles previously formed using bubbling O_2 (bottom) and $(\text{NH}_4)_2\text{S}$ (top). Annealing was performed under argon at $200\text{ }^\circ\text{C}$ for 1 h. For simplicity, the attribution of the peaks of the top pattern is not presented, but a large majority of the peaks can be attributed to a mixture of $\text{Ni}(\text{SO}_4)\cdot 6\text{H}_2\text{O}$ and $\text{Ni}(\text{SO}_4)\cdot 7\text{H}_2\text{O}$ (JCPDS files 33-0955 and 88-0280 respectively). The broad peak at 54° could not be attributed. For the bottom pattern, the references are JCPDS files 44-1418 (gray circles, Ni_3S_2) and 65-0830 (violet squares, NiS).

Annealing the product obtained using $(\text{NH}_4)_2\text{S}$, a complex mixture of compounds was obtained (Figure 121). The nickel sulfates $\text{Ni}(\text{SO}_4)\cdot 6\text{H}_2\text{O}$ and $\text{Ni}(\text{SO}_4)\cdot 7\text{H}_2\text{O}$ are only two products among the mixture. The S:Ni ratio of 1.0 given by the EDS after annealing is

consistent with the sulfates obtained, even if other products are present (Figure 120). We can expect similar result for of the reaction with *m*-CPBA, because the supernatant collected from the reaction at ambient temperature had a blue-green color characteristic of nickel sulfates, the S:Ni ratio of the amorphous product is also 1.0, and the XRD pattern is almost identical to the one obtained with (NH₄)₂S (Figure 120).

The most interesting case for us is the annealing of the product obtained *via* bubbling air during the synthesis (Figure 121). Nickel sulfides Ni₃S₂ and NiS crystallized and a significant amorphous contribution is still present. The presence of nickel sulfides is encouraging as it demonstrates that the sulfates were not formed, neither during the synthesis at ambient temperature neither during the annealing. The nickel sulfates would have crystallized at such temperatures, just like in the annealing of the amorphous products obtained using *m*-CPBA and (NH₄)₂S. It is a good sign that we obtained an amorphous nickel oxysulfide using O₂ and S₈.

That is why we carried out further analyses on amorphous nanoparticles obtained from the reaction of [Ni(cod)₂], S₈ and O₂ (Figure 122). XPS was performed by Christophe Méthivier at the Laboratory of Surface Reactivity (LRS, Paris).

The TEM micrographs of the nanoparticles (Figure 122D and E) show that we have nanoparticles. They are aggregated but isolated nanoparticles seem to measure between 20 and 40 nm. In Figure 122E, it seems that very small objects are embedded by a less-contrasting solid. Anyway, no lattice fringe was observed even at high magnifications (for now, no electronic diffraction was performed).

From the XPS spectrum of nickel, we know that we have oxidized nickel (the first component is centered at 855.7 eV) and no more Ni⁽⁰⁾ which would have resulted in a fine peak at a binding energy of below 853 eV.^{17,18} Sulfur analysis indicates that both reduced (red component in Figure 122) and oxidized sulfur (violet component in Figure 122B) are significantly present with binding energies of 162.0 eV¹⁶ and 167.8 eV¹⁹ respectively. The presence of sulfate could be related to surface oxidation. A third species (orange component in Figure 122B) whose binding energy is 163.6 eV was not attributed with certainty. However, this component is in the region of elemental sulfur. The O 1s spectrum may be complex but we observe a peak centered at a binding energy of 531.3 eV. This value is common for hydroxide species and Ni(OH)₂ in particular,¹⁹ but Kim *et al.* argued that this peak can also characterize oxygen species bonded to Ni^{III} cations whose signal is at a binding

energy of 855.8 eV (formally “Ni₂O₃” described as a surface defect structure of NiO).^{17,20} At present, it is hard for us to conclude about this point.

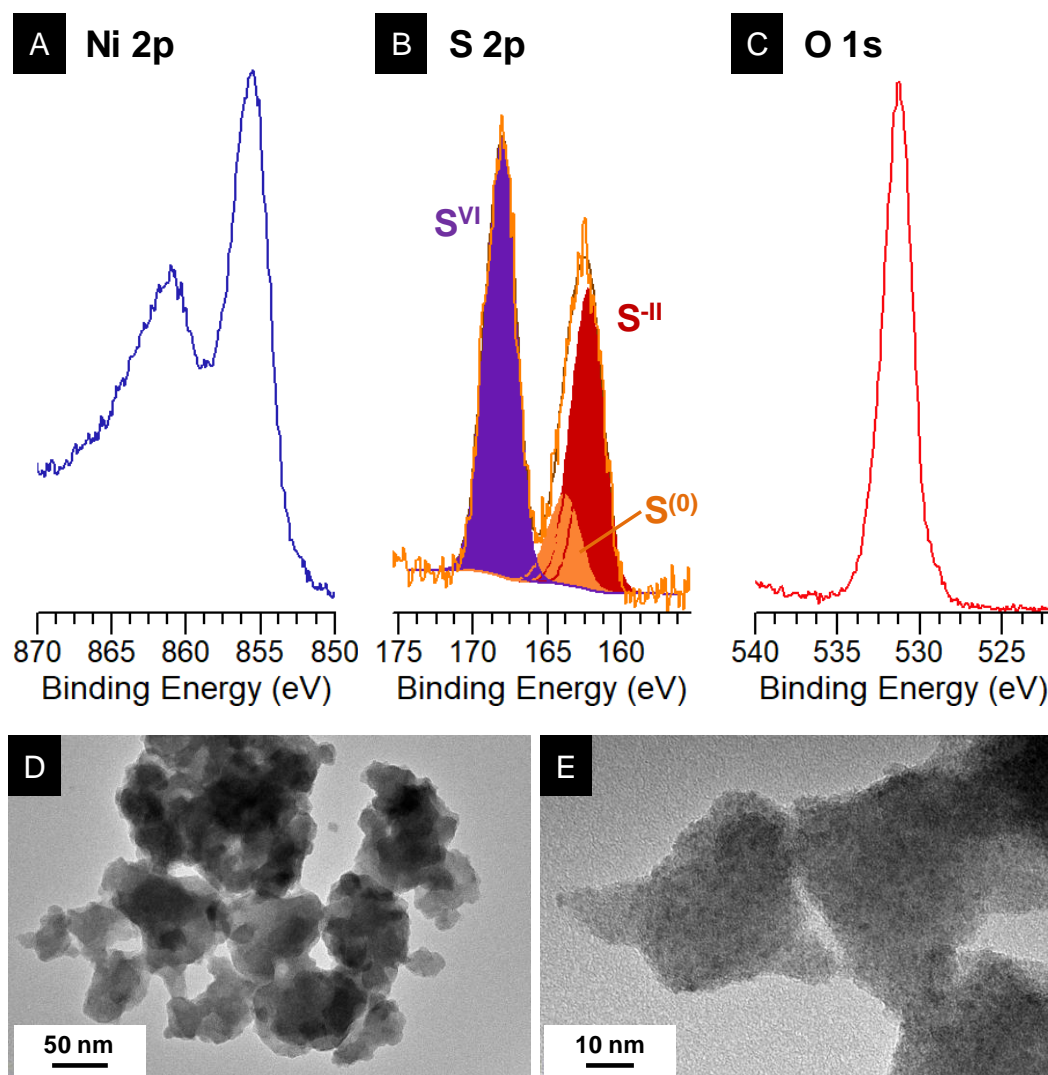


Figure 122: Ni 2p (A), S 2p (B) and O 1s (C) XPS spectra of amorphous Ni_xO_yS_z nanoparticles obtained from [Ni(cod)₂], S₈ and O₂ at ambient temperature [CL486]. (D and E) TEM micrographs of amorphous Ni_xO_yS_z nanoparticles.

The complex morphology of the nanoparticles has not been elucidated yet. However, if we admit that we have a single phase, the presence of reduced sulfur and oxygen confirms that we have amorphous oxysulfide nanoparticles.

VII.3. Conclusion

In this last chapter, we successfully obtained different nickel sulfide nanoparticles *via* a new method at ambient temperature, using a highly reactive complex of $\text{Ni}^{(0)}$ and elemental sulfur. In spite of the fact that the oxidizing treatments of these sulfides did not yield the targeted oxysulfide products, the synthesis of the sulfide nanoparticles inspired us and led to the direct formation of amorphous nanoparticles containing both sulfur and oxygen. Among them, amorphous oxysulfide nanoparticles $\text{NiO}_y\text{S}_{\sim 0.4}$ were obtained from the concomitant oxidation and sulfidation of $[\text{Ni}(\text{cod})_2]$ using O_2 and S_8 respectively. At present, the synthetic protocol needs further development to demonstrate repeatability and reproducibility. Performing the reaction with dried air could also unveil the true nature of oxygen in the amorphous oxysulfide nanoparticles (Ni^{II} hydroxide or Ni^{III} oxide).

Hopefully, this work will lead to other oxysulfide compounds at nanoscale. Some attempts with another $\text{M}^{(0)}$ complex, namely $\text{Co}_2(\text{CO})_8$, were carried out. Because the carbonyl ligands are more difficult to remove than the cyclooctadiene ones, the system requires higher temperature to start forming nanoparticles. This work is in progress.

In parallel, hexamethyldisilathiane was directly used on different $\text{M}(\text{acac})_2$ complexes ($\text{M} = \text{Co}, \text{Ni}, \text{Cu}$; 1 equiv. of HMDST, 100 °C, 2 h). The strong sulfidating agent reacted differently on the three complexes but formed nanoparticles for the three metals: sulfide nanoparticles for cobalt and copper, and an identified product for Ni. We hope to perform additional reactions to complete this preliminary work.

We can also think about reacting $\text{M}^{(0)}$ nanoparticles with controlled oxygen and sulfur amount. The selectivity of the process may be more complex to master, because of the diffusion rate differences of the species. Segregation of oxide and sulfide could also happen. Altogether, this chapter illustrates the arduous path to transition metal oxysulfide nanoparticles, with promising results in the case of nickel.

References

- (1) Nelson, A.; Fritz, K. E.; Honrao, S.; Hennig, R. G.; Robinson, R. D.; Suntivich, J. Increased Activity in Hydrogen Evolution Electrocatalysis for Partial Anionic Substitution in Cobalt Oxsulfide Nanoparticles. *J. Mater. Chem. A* **2016**, *4* (8), 2842–2848.
- (2) Park, J.; Zheng, H.; Jun, Y.; Alivisatos, A. P. Hetero-Epitaxial Anion Exchange Yields Single-Crystalline Hollow Nanoparticles. *J. Am. Chem. Soc.* **2009**, *131* (39), 13943–13945.
- (3) Carenco, S.; Wu, C.-H.; Shavorskiy, A.; Alayoglu, S.; Somorjai, G. A.; Bluhm, H.; Salmeron, M. Synthesis and Structural Evolution of Nickel-Cobalt Nanoparticles Under H₂ and CO₂. *Small* **2015**, *11* (25), 3045–3053.
- (4) Carenco, S.; Portehault, D.; Boissière, C.; Mézailles, N.; Sanchez, C. Nanoscaled Metal Borides and Phosphides: Recent Developments and Perspectives. *Chem. Rev.* **2013**, *113* (10), 7981–8065.
- (5) Lin, R. Y.; Hu, D. C.; Chang, Y. a. Thermodynamics and Phase Relationships of Transition Metal-Sulfur Systems: II. The Nickel-Sulfur System. *Metall. Trans. B* **1978**, *9* (4), 531–538.
- (6) Stølen, S.; Fjellvåg, H.; Grønvold, F.; Seim, H.; Westrum, E. F. Phase Stability and Structural Properties of Ni_{7±8}S₆ and Ni₉S₈ Heat Capacity and Thermodynamic Properties of Ni₇S₆ at Temperatures from 5 K to 970 K and of Ni₉S₈ from 5 K to 673 K. *J. Chem. Thermodyn.* **1994**, *26* (9), 987–1000.
- (7) Tilley, R. D.; Jefferson, D. A. The Synthesis of Nickel Sulfide Nanoparticles on Graphitized Carbon Supports. *J. Phys. Chem. B* **2002**, *106* (42), 10895–10901.
- (8) Yu, S.-H.; Yoshimura, M. Fabrication of Powders and Thin Films of Various Nickel Sulfides by Soft Solution-Processing Routes. *Adv. Funct. Mater.* **2002**, *12* (4), 277.
- (9) Kumar, N.; Raman, N.; Sundaresan, A. Temperature Evolution of Nickel Sulphide Phases from Thiourea Complex and Their Exchange Bias Effect. *J. Solid State Chem.* **2013**, *208*, 103–108.
- (10) Roffey, A.; Hollingsworth, N.; Islam, H.; Mercy, M.; Sankar, G.; Catlow, C. R. A.; Hogarth, G.; de Leeuw, N. H. Phase Control during the Synthesis of Nickel Sulfide Nanoparticles from Dithiocarbamate Precursors. *Nanoscale* **2016**, *8* (21), 11067–11075.
- (11) Karthikeyan, R.; Thangaraju, D.; Prakash, N.; Hayakawa, Y. Single-Step Synthesis and Catalytic Activity of Structure-Controlled Nickel Sulfide Nanoparticles. *CrystEngComm* **2015**, *17*, 5431–5439.
- (12) Beal, J. H. L.; Etchegoin, P. G.; Tilley, R. D. Transition Metal Polysulfide Complexes as Single-Source Precursors for Metal Sulfide Nanocrystals. *J. Phys. Chem. C* **2010**, *114* (9), 3817–3821.
- (13) Wang, W.; Dahl, M.; Yin, Y. Hollow Nanocrystals through the Nanoscale Kirkendall Effect. *Chem. Mater.* **2013**, *25* (8), 1179–1189.
- (14) Zuo, X.; Yan, S.; Yang, B.; Li, G.; Zhang, H.; Tang, H.; Wu, M.; Ma, Y.; Jin, S.; Zhu, K. Template-Free Synthesis of Nickel Sulfides Hollow Spheres and Their Application in Dye-Sensitized Solar Cells. *Sol. Energy* **2016**, *132*, 503–510.
- (15) Wells, A. F. Elementary Sulphur, Selenium, and Tellurium. In *Structural Inorganic Chemistry*; Oxford: Clarendon Press, 1975; pp 570–604.
- (16) Buckley, A. N.; Woods, R. Electrochemical and XPS Studies of the Surface Oxidation of Synthetic Heazlewoodite (Ni₃S₂). *J. Appl. Electrochem.* **1991**, *21* (7), 575–582.
- (17) Kim, K. S.; Winograd, N. X-Ray Photoelectron Spectroscopic Studies of Nickel-Oxygen Surfaces Using Oxygen and Argon Ion-Bombardment. *Surf. Sci.* **1974**, *43* (2), 625–643.
- (18) Hüfner, S.; Wertheim, G. K. Systematics of Core Line Asymmetries in XPS Spectra of Ni. *Phys. Lett. A* **1975**, *51* (5), 301–303.

- (19) Legrand, D. L.; Nesbitt, H. W.; Bancroft, G. M. X-Ray Photoelectron Spectroscopic Study of a Pristine Millerite (NiS) Surface and the Effect of Air and Water Oxidation. *Am. Mineral.* **1998**, 83 (11–12 Part 1), 1256–1265.
- (20) Kim, K. S.; Davis, R. E. Electron Spectroscopy of the Nickel-Oxygen System. *J. Electron Spectros. Relat. Phenomena* **1972**, 1 (3), 251–258.

Conclusion and perspectives

Table of contents

Ln ₂ O ₂ S nanoparticles	247
Nucleation and growth of the nanoparticles	247
Optical properties	247
Safe-by-design nanoparticles	248
Polyvalent nanoparticles	248
Magnetic properties of Gd ₂ O ₂ S	249
Transition metal (oxy)sulfide nanoparticles	250
Ln _w M _x O _y S _z nanoparticles synthesis in OM/OA/ODE	250
M _x O _y S _z synthesis	250
Electrochemical proton and CO ₂ reduction	251
And more	251
References	252

Ln₂O₂S nanoparticles

Nucleation and growth of the nanoparticles

Lanthanide oxysulfide nanoparticles synthesized in high boiling point organic solvents were deeply investigated in this PhD thesis. So far, the proposed formation mechanism is mostly qualitative. An ongoing work could enable the quantification of the processes involved in the nanoparticles formation (volume fraction of crystallized particles, energy barrier for nucleation and growth, and so on).

Besides, EXAFS at Gd-L_{III} edge is under exploitation to determine the structure of the intermediate species during the reaction. This is a challenging interpretation, because the EXAFS spectra require a reference structure for the fit, and the significant amount of ligands causes a non-negligible perturbation to the Gd environment in Gd₂O₂S nanocrystals (in particular, there are much more Gd-O bonds due to the Gd-carboxylate interactions at the surface).

Moreover, the influence of sodium may be the object of a new series of SAXS-WAXS experiments, in which the formation and role of the oleate layers will be precisely investigated.

Optical properties

The synthesis of Ce₂O₂S, motivated by the peculiar electronic and optical properties of the bulk phase, turned out to be an inspiration for the design of air-stable bimetallic (Ln,Ce)₂O₂S (Ln = Pr, Eu, Gd) nanoparticles which absorb light in the visible range. We believe that such absorbent nanoparticles will enable the design of new photocatalysts working in the visible range. Some preliminary tests were conducted on the degradation of a dye (rhodamine B) with a homemade setup (Figure 123) to select the best candidate for such applications. Mitigated results were obtained but efforts are made to improve the quality of the (Gd,Ce)₂O₂S nanoparticles dispersion in water (this part of the work is conducted by Anh-Minh Nguyen in our laboratory).



Figure 123: Photocatalysis tests with our homemade setup. The blue-green light ($\lambda = 501$ nm) is produced by 9 LED and the pink solutions are a dispersion of (Gd,Ce)₂O₂S nanoparticles in aqueous rhodamine B solutions.

Safe-by-design nanoparticles

Besides, the same (Gd,Ce)₂O₂S nanoparticles are now studied *in vitro* to determine their toxicity (still by Anh-Minh Nguyen). The safe-by-design approach aims at reducing potential toxicity of nanomaterials during the design phase. Thus, the cytotoxicity of the nanoparticles was studied on murine macrophage cell line. Cerium is likely responsible for the cytotoxicity of the nanoplates. Preliminary results of synchrotron techniques (μ XRF, μ XANES on the beamline ID21 at ESRF synchrotron) show that oxidation state of cerium in nanoparticles in contact with the cells seems to change. *In vivo* toxicity is also considered to compare with the *in vitro* model.

Polyvalent nanoparticles

We verified during this PhD thesis that luminescent properties could still be obtained with our nanoparticles, especially with europium (Figure 124).

In analogy with bimodal imaging, we expect that more complex nanoparticles, such as trimetallic compositions, could be designed to obtain polyvalent nanoparticles (absorption, fluorescence, catalysis, magnetic properties). For instance, (Gd,Ce,Eu)₂O₂S nanoparticles were obtained following the same synthetic route.

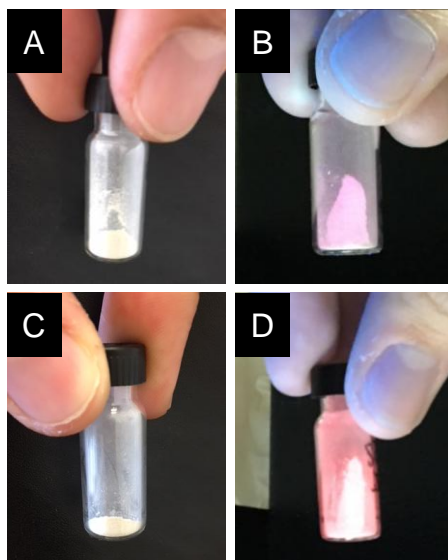


Figure 124: $\text{Gd}_{1.98}\text{Eu}_{0.02}\text{O}_2\text{S}$ nanoparticles (A, B) and $\text{Gd}_{1.8}\text{Eu}_{0.2}\text{O}_2\text{S}$ nanoparticles (C, D) under visible light (A, C) and under UV irradiation (365 nm). The nanoparticles exhibit the typical fluorescence of the Eu^{3+} recombination centers (red light of $^5\text{D}_0 \rightarrow ^7\text{F}_j$ transitions) under UV excitation.

Magnetic properties of $\text{Gd}_2\text{O}_2\text{S}$

The magnetic properties of $\text{Gd}_2\text{O}_2\text{S}$ are also under investigation, because we show a significant difference between the properties of the bulk phase and the nanoparticles. The surface is likely to play a preponderant role, and many attempts for the synthesis of $\text{Gd}_2\text{O}_2\text{S}$ nanoparticles of intermediary sizes (20 - 100 nm) were conducted. At present, these attempts did not succeed, but we are confident that the various available protocols will enable the formation of $\text{Gd}_2\text{O}_2\text{S}$ nanoparticles with the required dimensions. We hope that we will then be able to extract more easily the parameters that are critical for the change of behavior of the magnetic moment at low temperature.

Transition metal (oxy)sulfide nanoparticles

$\text{Ln}_w\text{M}_x\text{O}_y\text{S}_z$ nanoparticles synthesis in OM/OA/ODE

Bimetallic oxysulfide crystalline nanoparticles with a *d*-block transition metal were not achieved yet. However, we identified some phases whose synthesis in the OM/OA/ODE/A(oleate)/S₈ system (A = Li, Na, K) seems possible in the light of the results on the formation mechanism of $\text{Ln}_2\text{O}_2\text{S}$ nanoparticles. For instance, lamellar lanthanide titanium oxysulfides are good candidates for this synthesis, and will be targeted shortly.

The GdTiO_3 and GdVO_3 nanoparticles doped with sulfur are also interesting cases and may be further investigated. Some studies showed that even a low amount of sulfur was sufficient to significantly modify the properties oxides, such as titanium oxide nanostructures for instance.¹⁻³

$\text{M}_x\text{O}_y\text{S}_z$ synthesis

In OM/OA/ODE, similarly to the bimetallic nanoparticles, some phases seem to be good candidates for future synthetic attempts. In particular, post-transition metals Bi (lamellar $\text{Bi}_2\text{O}_2\text{S}$) and indium should be the object of new tests.

For the *d*-block first row transition metals, the challenge is much harder. What we could play on is the heating kinetics. This is actually a general remark: during the whole PhD thesis, the influence on the heating ramp was not investigated. However, it could be useful to perform swifter temperature ramps (*via* the use of microwave ovens for instance) to change the kinetics of the system. It is well illustrated by the case of the syntheses of cobalt and iron sulfides for instance, for which we obtain complex mixtures of products corresponding to thermodynamic local minima. Microwave heating was proposed early on the $\text{Ln}_2\text{O}_2\text{S}$ synthesis but it was not performed owing to time constraints.

The synthesis of amorphous nickel oxysulfides nanoparticles has to be optimized. The volume and duration of the bubbling air flow will be controlled and measured properly. Other complexes or $\text{M}^{(0)}$ nanoparticles could be tested to achieve new oxysulfide compositions. In parallel, the preliminary tests with the direct use of hexamethyldisilathiane on transition metal complexes are promising for the formation of nanoparticles containing both sulfur and oxygen anions. Other sulfur sources (thioacetamide, thiourea...) were also poorly investigated.

The PhD thesis of Thi Kim-Chi Lê at the LCMCP (2017 - 2020) targets the formation of nanostructures of molybdenum oxysulfides. So far, molybdenum oxysulfides nanoparticles

were not obtained for this challenging synthesis, but electrochemically active composite nanoparticles $(\text{Gd},\text{Mo})_x\text{O}_y\text{S}_z$ were obtained, with a synthetic route inspired from these of $(\text{Gd},\text{Ce})_2\text{O}_2\text{S}$.

Electrochemical proton and CO₂ reduction

A study of the electrocatalytic proton and CO₂ reduction of our nickel sulfide nanoparticles (Ni_3S_2 + amorphous Ni, Ni_3S_4 + amorphous NiS and NiS_2 + amorphous S) is being conducted at the *Collège de France* in collaboration with David Wakerley and Victor Mougél. The amorphous nickel oxysulfide nanoparticles will be investigated soon. The first results were showing that the nickel sulfide nanoparticles tend to catalyze much better proton reduction over CO₂ reduction, but that latter activity was still significant for a non-noble catalyst. Both of the activities are currently investigated, while the process to cover the gas diffusion layer with a maximum of nanoparticles of catalyst is being optimized with the Ni_3S_2 nanoparticles.

And more...

The most remarkable aspect of the oxysulfide family is its small number of protagonists. New compositions are regularly reported, mostly bimetallic. We can expect that new phases will emerge with cheap and available transition metals such as iron, cobalt, copper and imagine that novel properties will be found (heterogeneous catalysis, luminescence, superconductivity). The bottom-up synthesis of nanoparticles is a tremendous tool for such challenging syntheses, and we hope that novel compositions are about to be formed and stabilized by such techniques.

References

- (1) Yang, G.; Yan, Z.; Xiao, T. Low-Temperature Solvothermal Synthesis of Visible-Light-Responsive S-Doped TiO₂ Nanocrystal. *Appl. Surf. Sci.* **2012**, 258 (8), 4016–4022.
- (2) Ramacharyulu, P. V. R. K.; Praveen Kumar, J.; Prasad, G. K.; Sreedhar, B. Sulphur Doped Nano TiO₂ : Synthesis, Characterization and Photocatalytic Degradation of a Toxic Chemical in Presence of Sunlight. *Mater. Chem. Phys.* **2014**, 148 (3), 692–698.
- (3) Smith, L. A. C.; Trudeau, M. L.; Provencher, M.; Smith, M. E.; Antonelli, D. M. Low-Temperature Synthesis and Electrochemical Properties of Mesoporous Titanium Oxysulfides. *ChemElectroChem* **2016**, 3 (2), 256–265.

Experimental section

Table of Contents

Note	255
ES.1. Syntheses and thermal treatments.....	255
ES.1.1. Synthesis of $\text{Gd}_{2(1-y)}\text{Ce}_{2y}\text{O}_2\text{S}$ nanoparticles	255
ES.1.2. Bulk $\text{Gd}_2\text{O}_2\text{S}$ synthesis	256
ES.1.3. Synthesis of $\text{Ln}_w\text{M}_x\text{O}_y\text{S}_z$ nanoparticles and $\text{M}_x\text{O}_y\text{S}_z$ nanoparticles.....	257
ES.1.4. Annealing $\text{Ln}_w\text{M}_x\text{O}_y\text{S}_z$ nanoparticles	257
ES.1.5. Synthesis of nickel sulfide nanoparticles using $[\text{Ni}(\text{cod})_2]$ and elemental sulfur..	257
ES.1.5.1. For $T \leq 80\text{ }^\circ\text{C}$	257
ES.1.5.2. For $80 < T \leq 260\text{ }^\circ\text{C}$	258
ES.1.5.3. In molten sulfur	258
ES.1.6. Iron (0) and iron sulfide nanoparticles.....	258
ES.1.7. Cobalt (0) and cobalt sulfide nanoparticles	259
ES.1.8. Calcination of Fe, Co and Ni sulfides.....	259
ES.1.9. $\text{Ni}_x\text{O}_y\text{S}_z$ amorphous oxysulfide nanoparticles.....	260
ES.2. Synchrotron-based techniques	261
ES.2.1. X-ray absorption near-edge Spectroscopy (XANES).....	261
ES.2.2. Near ambient pressure X-ray photoelectron spectroscopy (NAP-XPS).....	261
ES.2.3. Extended X-ray absorption fine structure (EXAFS)	263
ES.3. Other characterization techniques.....	264
ES.3.1. X-ray diffraction on powder (XRD)	264
ES.3.2. Transmission electron microscopy (TEM) and high resolution TEM (HRTEM) .	265
ES.3.3. Scanning electron microscopy (SEM) and energy dispersive X-ray spectroscopy (EDS).....	266
ES.3.4. UV-visible diffuse reflectance	266

ES.3.5. Fourier transform infrared spectroscopy (FTIR)	266
ES.3.6. Pair distribution function analysis (PDF)	267
ES.3.7. Thermogravimetric analysis coupled with mass spectrometry (TGA-MS).....	268
ES.3.8. Small angle X-ray scattering (SAXS) and wide angle X-ray scattering (WAXS)	269
ES.3.9. Vibrating sample magnetometry (VSM)	270
ES.3.10. Superconductive quantum interference device magnetometry (SQUID).....	271
ES.4. Density functional theory calculations (DFT)	271
References	273

Note

Some sections of this experimental section were extracted from the article “*Synthesis of Ce_2O_2S and $Gd_{2(1-y)}Ce_{2y}O_2S$ Nanoparticles and Reactivity from In situ X-ray Absorption Spectroscopy and X-ray Photoelectron Spectroscopy*” from Larquet *et al.*,¹ while others will be used for other manuscripts.

ES.1. Syntheses and thermal treatments

ES.1.1. Synthesis of $Gd_{2(1-y)}Ce_{2y}O_2S$ nanoparticles

Bimetallic oxysulfides nanoparticles were prepared *via* a solvothermal reaction including a mixture of organic solvents and metallic complexes. Oleylamine (OM; technical grade, 70 %), oleic acid (OA; technical grade, 90 %), sulfur (S_8 ; ≥ 99.5 %) and sodium oleate (Na(oleate); ≥ 99 %) were purchased from Sigma-Aldrich. 1-octadecene (ODE; technical grade, 90 %) was purchased from Acros Organics. Gadolinium acetylacetonate hydrate ($Gd(acac)_3 \cdot xH_2O$; 99.9 %) and cerium acetylacetonate hydrate ($Ce(acac)_3 \cdot xH_2O$; 99.9 %) were purchased from Strem Chemicals. All products were used as received without further purification.

In a typical synthesis of Ce_2O_2S , $Ce(acac)_3 \cdot xH_2O$ (0.50 mmol), S_8 (0.032 mmol), Na(oleate) (0.50 mmol), OM (17 mmol), OA (2.5 mmol) and ODE (32.5 mmol) were added in a 100 mL three-neck flask at room temperature. The brown solution was heated to 120 °C under vacuum for 20 minutes to remove water and other impurities with low boiling points. The mixture was then heated to 310 °C and stirred at this temperature for 30 min under purified N_2 . Then it was left to cool under N_2 to room temperature and was directly transferred to an inert-atmosphere glovebox (H_2O : ≤ 0.5 ppm, O_2 : ≤ 0.5 ppm). The crude product can be dispersed into anhydrous THF. After several centrifugations in anhydrous THF, a brown paste of Ce_2O_2S nanoparticles was obtained.

In a typical synthesis of $GdCeO_2S$, $Gd(acac)_3 \cdot xH_2O$ (0.25 mmol), $Ce(acac)_3 \cdot xH_2O$ (0.25 mmol), S_8 (0.032 mmol), Na(oleate) (0.50 mmol), OM (17 mmol), OA (2.5 mmol) and ODE (32.5 mmol) were added in a 100 mL three-neck flask at room temperature. The brown solution was heated to 120 °C under vacuum for 20 minutes to remove water and other impurities with low boiling points. The mixture was then heated to 310 °C and stirred at this temperature for 30 minutes under purified N_2 . The transparent solution gradually became turbid starting from 280 °C. Then the mixture was left to cool to room temperature under N_2 . The nanoparticles were isolated using ethanol and washed at least three times using a

THF/ethanol (1:5) mixture to remove the remaining reagents and organic matter. A 40 to 90 mg amount of dried $\text{Gd}_{2(1-y)}\text{Ce}_{2y}\text{O}_2\text{S}$ nanoparticles was thus obtained depending on the initial cerium loading.



Figure 125: Picture of running syntheses of $(\text{Gd,Ce})_2\text{O}_2\text{S}$ nanoparticles. The three-necked flasks are disposed in the white heating mantles. Coolers are placed above the flasks to prevent any liquid from going in the tubes. The ramp on the top of the pictures enables to pump the reacting medium or provide inert gas.

It should be noted that a significant decrease of the reaction yield (measured after several washing of the nanoparticles in air) is observed along with the amount of cerium introduced in the nanoparticles: starting from 0.5 mmol of lanthanide precursor, a yield of around 75 % vs. Gd (100 mg of powder) was obtained for $y = 0$ % ($\text{Gd}_2\text{O}_2\text{S}$) while a yield of 35 % (45 mg) was obtained for $y = 70$ % ($\text{Gd}_{0.6}\text{Ce}_{1.4}\text{O}_2\text{S}$). For this estimation, 30 wt% of ligands are considered.

ES.1.2. Bulk $\text{Gd}_2\text{O}_2\text{S}$ synthesis

1.00 g of $\text{Gd}_2(\text{SO}_4)_3 \cdot 8\text{H}_2\text{O}$ was placed in an alumina crucible which was then disposed in a horizontal tube furnace. The furnace was then flushed by a flow of gaseous dihydrogen in argon (Ar/H_2 with 5 % H_2) for 20 min. The temperature was then heated up to 1100 °C at 5 °C/min, before a temperature dwell of 24 hours. The product was left to cool to room temperature under Ar/H_2 and a white powder was obtained (around 500 mg, $\eta \approx 100$ %).

ES.1.3. Synthesis of $\text{Ln}_w\text{M}_x\text{O}_y\text{S}_z$ nanoparticles and $\text{M}_x\text{O}_y\text{S}_z$ nanoparticles

The syntheses of bimetallic and monometallic nanoparticles containing *d*-block transition metals were conducted similarly to $\text{Ln}_2\text{O}_2\text{S}$ synthesis (310 °C, 30 min unless otherwise specified; see the protocol in ES.1.1). When two metals are used, both of them were introduced directly in the mixture of organic solvents at ambient temperature without preliminary step, except for the reaction with zirconium ($\text{Zr}(\text{OEt})_4$ was introduced in the mixture containing the organic solvents, sulfur and 4 equiv. of acetylacetone vs. Zr) . The reactants amounts depend on the targeted phase and are defined in Chapter VI.

ES.1.4. Annealing $\text{Ln}_w\text{M}_x\text{O}_y\text{S}_z$ nanoparticles

Several amorphous powders of $\text{Ln}_w\text{M}_x\text{O}_y\text{S}_z$ nanoparticles were annealed under atmosphere. The powder was loaded in a long quartz tube which was then placed in a vertical tube furnace. The quartz tube was flushed with argon for 10 minutes then heated up to the annealing temperature still under argon at 10 °C/min. Once the reaction was over, the tube was flushed with argon and let to cool to room temperature. The powder was then extracted from the tube.

ES.1.5. Synthesis of nickel sulfide nanoparticles using $[\text{Ni}(\text{cod})_2]$ and elemental sulfur

ES.1.5.1. For $T \leq 80$ °C

In a typical synthesis of Ni_3S_2 , a yellow 10^{-1} M solution of $[\text{Ni}(\text{cod})_2]$ (138 mg, 0.5 mmol) in THF (5 mL) was prepared in a Schlenk tube inside an inert-atmosphere glovebox (H_2O : ≤ 0.5 ppm, O_2 : ≤ 0.5 ppm). Still in the glovebox, a transparent solution of thoroughly degassed elemental sulfur S_8 (10.7 mg, 0.042 mmol, $\text{S}:\text{Ni} = 2/3$) in THF (5 mL) was added dropwise into the first solution, which immediately turned black. The Schlenk tube was closed and extracted from the glovebox and the mixture was stirred during 16 h to 24 h. The nanoparticles were then isolated with THF (10 mL) and washed once with THF (15 mL). If the nanoparticles are hard to isolate, THF/ethanol mixtures can help. A 30 mg amount of black nanoparticles was thus obtained ($\eta = 75$ %).

The initial sulfur amount can be adjusted to obtain amorphous NiS (16.0 mg of S_8) or crystalline Ni_3S_4 (21.4 mg of S_8) with similar yields. The solution can be heated up to 80 °C with this method.

ES.1.5.2. For $80 < T \leq 260$ °C

For reaction temperatures above 80 °C, the mixture was prepared similarly to the previous section, but in a three-necked flask. Once the flask was extracted from the glovebox, THF and cyclooctadiene were cautiously removed from the Schlenk tube under vacuum at ambient temperature or by gently heating using a heating mantle at 30 °C. When half of the solvent was removed, 10 mL of degassed 1-octadecene were added in the Schlenk tube under inert atmosphere. After full evaporation of THF and cyclooctadiene, the mixture was heated up to the desired temperature under inert atmosphere (for the reactions at 260 °C, the mixture reacted for 1 h). Then, the flask was left to cool to room temperature. The nanoparticles were isolated using ethanol and washed at least three times using a THF/ethanol (1:5) mixture to remove the remaining reagents and organic matter.

ES.1.5.3. In molten sulfur

In a typical procedure, around 10 g of degassed elemental sulfur were loaded in a three-neck flask inside an inert-atmosphere glovebox (H_2O : ≤ 0.5 ppm, O_2 : ≤ 0.5 ppm). Then, 275 mg of $[\text{Ni}(\text{cod})_2]$ were added in the flask. The flask was closed and swiftly extracted from the glovebox and plugged to a Schlenk line. The mixture was then stirred and heated up under inert atmosphere.

Sulfur melts around 115 °C. The yellow mixture (both reactants are yellow) rapidly turned black because of the decomposition of $[\text{Ni}(\text{cod})_2]$ and/or formation of nickel sulfide species. For the reaction at 260 °C: the medium became very viscous around 160 °C and up to 240 °C. In this range, heating is slow because of a thermal conductivity drop of molten sulfur. After 240 °C, the medium became a mobile liquid again and was suitable for a reaction at 260 °C. After reaction, the mixture was left to cool to room temperature.

If the reaction was performed at 130 °C, all the sulfur could be removed by washing the nanoparticles with THF, ethanol and butylamine. If the reaction was performed at 260 °C, a large amount of sulfur could not be removed by washing with these solvents and remained on the NiS_2 nanoparticles.

ES.1.6. Iron (0) and iron sulfide nanoparticles

The formation of $\text{Fe}^{(0)}$ nanoparticles was conducted following the strategy reported by Peng *et al.*¹⁹ In a three-necked flask, 0.24 g of oleylamine and 15.8 g of 1-octadecene were loaded. The mixture was heated to 120 °C under vacuum for 20 minutes to remove water and other impurities with low boiling points. Under inert atmosphere, the medium was then heated up to

180 °C. Then, 0.7 mL of $\text{Fe}(\text{CO})_5$ (1.0 g, 5.2 mmol) was injected in the hot medium through a septum. The solution became dark green and a significant amount of vapor was formed, before becoming black within minutes. The solution was stirred 20 min at 180 °C and was left to cool to room temperature.

The $\text{Fe}^{(0)}$ nanoparticles were directly sulfidated. 333 mg of S_8 (1.30 mmol, S:Fe = 2) were swiftly added to the cooled mixture under inert atmosphere. The solution was degassed and then heated up to 200 °C. After 2 h, the solution was left to cool to room temperature. The nanoparticles were isolated using ethanol and washed at least three times using a THF/ethanol (1:5) mixture to remove the remaining reagents and organic matter. A black powder (230 mg, $\eta = 37\%$) was obtained.

ES.1.7. Cobalt (0) and cobalt sulfide nanoparticles

The formation of $\text{Co}^{(0)}$ nanoparticles was inspired by the synthesis of $\text{Ni}^{(0)}$ nanoparticles as described by Carenco *et al.*²⁰ In a three-necked flask, 15.6 g of oleylamine were loaded and degassed under vacuum at 50 °C for 10 min. The medium was left to cool down to room temperature still under vacuum. Under inert atmosphere, $\text{Co}(\text{acac})_2$ (1.5 , 5.8 mmol) was then added in the flask. A red gel immediately formed. The gel was heated up and rapidly dissolved into a solution that is heated up to 120 °C. Under vacuum, the solution was degassed for 20 minutes to remove water and other impurities with low boiling points. The mixture was then heated at 260 °C under inert atmosphere. The color of the solution was yellow-green and turned dark green then perfectly black. After two hours, the solution was left to cool to room temperature.

The $\text{Co}^{(0)}$ nanoparticles were directly sulfidated. 372 mg of S_8 (1.45 mmol, S:Co = 2) were swiftly added to the cooled mixture under argon. The solution was degassed and then heated up to 200 °C. After 2 h, the solution was left to cool to room temperature. The nanoparticles were isolated using ethanol and washed at least three times using a THF/ethanol (1:5) mixture to remove the remaining reagents and organic matter. A black powder (470 mg, $\eta = 66\%$) was obtained.

ES.1.8. Calcination of Fe, Co and Ni sulfides

The sulfide powder was placed in an open glass vial which is disposed in an oven which contains ambient air. The temperature was then increased up to the calcination temperature at

around 10 °C/min. After the reaction, the sample was extracted from the oven and the vial was closed. The latter was left to cool to room temperature.

ES.1.9. $\text{Ni}_x\text{O}_y\text{S}_z$ amorphous oxysulfide nanoparticles

Similar to the synthesis of Ni_3S_2 nanoparticles, a yellow 10^{-1} M solution of $[\text{Ni}(\text{cod})_2]$ (138 mg, 0.5 mmol) in THF (5 mL) was prepared in a Schlenk tube inside an inert-atmosphere glovebox ($\text{H}_2\text{O}: \leq 0.5$ ppm, $\text{O}_2: \leq 0.5$ ppm). Still in the glovebox, a transparent solution of thoroughly degassed elemental sulfur S_8 (10.7 mg, 0.042 mmol, S:Ni = 2/3) in THF (5 mL) was prepared. The two Schlenk tubes were extracted from the glovebox. Through a septum, air was bubbled directly in the $[\text{Ni}(\text{cod})_2]$ solution for around 10 min. The medium progressively turned black. Then the dropwise addition of sulfur started also through the septum, while air still bubbled. After the addition, air was bubbled for additional 10 min. The Schlenk tube was then closed and the reaction was stirred at room temperature for 24 h. The nanoparticles were then isolated with THF (10 mL) and washed once with THF (15 mL). A black powder was obtained (≈ 50 mg).

ES.2. Synchrotron-based techniques

At the SOLEIL synchrotron facility, the analyses were conducted using an electron energy of 2.7 GeV and an average ring current of 450 mA.

ES.2.1. X-ray absorption near-edge Spectroscopy (XANES)

Sulfur K-edge and cerium L-edge XANES data were collected on the LUCIA beamline. The incoming photons were selected with a Si (111) double crystal monochromator. 2 to 3 mg of the sample were diluted in *ca* 40 mg of graphite and were compressed to form a 6 mm diameter pellet (pressure: 2 t). Up to seven pellets were fixed with carbon adhesive tape on a copper plate placed in a sample holder inside the measurement chamber (Figure 126). During typical analyses, the pressure in the chamber was maintained around 10^{-2} mbar. Measurements were performed in fluorescence mode using a Bruker silicon drift detector, with an outgoing photon angle of 10° . All data were normalized to the edge jump and calibrated to the maximum of the first peak of sodium thiosulfate (2470.8 eV).



Figure 126: Picture of pellets of graphite and (Gd,Ce)₂O₂S nanoparticles fixed on a copper plate for XANES analysis.

ES.2.2. Near ambient pressure X-ray photoelectron spectroscopy (NAP-XPS)

X-ray photoelectron spectroscopy was performed on the TEMPO B beamline at SOLEIL on the NAP-XPS end-station (Figure 127). Samples were deposited from a 30 mg.mL⁻¹ solution of dispersed nanoparticles in pure THF onto gold-coated (100 nm layer) silica wafers by dip-coating (Figure 128). Spectra were measured under vacuum (10^{-9} mbar), under 0.2 mbar H₂O

pressure or under 0.4 mbar H₂O and O₂ pressure (0.2 mbar each). In order to mitigate beam damage, measurements were performed on several spots on the sample surface.

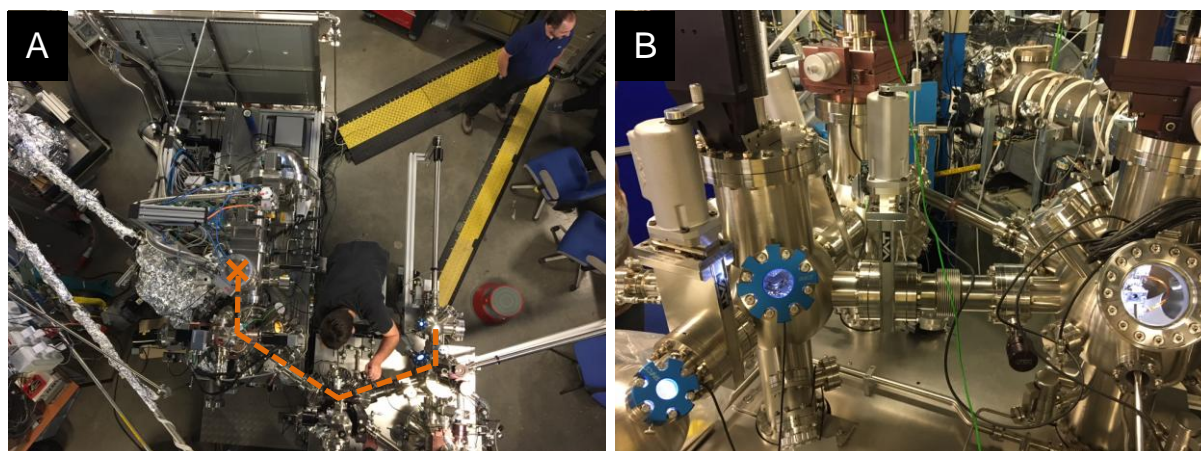


Figure 127: Pictures of the TEMPO B beamline, from the top (A) and from the side (B). On A is indicated the samples pathway to the analysis chamber (orange cross).

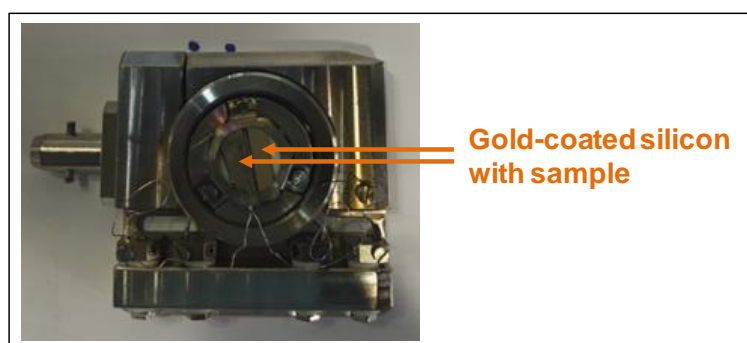


Figure 128: Picture of the samples fixed on the sample holder for NAP-XPS experimentations. The length of the gold-coated silicon samples is around 1 cm.

Spectrum processing was carried out using the CasaXPS software package. Binding energies were calibrated using the Au $4f_{7/2}$ peak at 84.0 eV. Shirley background was used for gadolinium and cerium regions (137 - 153 eV for Gd $4d$; 876 - 893 eV, 893 - 912 eV and 913 - 921 eV for Ce $3d$). All spectra were collected with an incident photon energy of 735 eV for Gd $4d$ and S $2p$, and 1100 eV for Ce $3d$. Pass energy of 50 eV was used. A linear background was used for sulfur regions (158 - 175 eV). All peaks were fitted using the Gaussian-Lorentzian line shape GL(30) (30 % Lorentzian and 70 % Gaussian) as an approximation of the Voigt curve.² The doublet splitting of Gd $4d$ peaks was let free as a significant difference appeared between the regular and the satellite peaks. The two components of a doublet were set with an equal FWHM value. See references below of typical XPS analyzes on S, Gd and Ce.³⁻⁶

Species		B. E. (eV)	Doublet splitting (eV)	FWHM (eV)	Color
S ^{-II}	S 2p _{3/2}	161.0 - 162.5	1.16	≤ 3	Red
S ^{IV}	S 2p _{3/2}	167.0 - 170.0	1.16	≤ 3	Pink
S ^{VI}	S 2p _{3/2}	170.0 - 172.0	1.16	≤ 3.5	Purple
Gd ^{III}	Gd 4d _{5/2}	142.0 - 144.0	5.15 ± 0.1	≤ 4	Light green
	Gd 4d _{3/2}	147.0 - 149.0			
	Gd 4d _{5/2} sat.	140.0 - 142.0	3.1 ± 0.2	≤ 4	Dark green
	Gd 4d _{3/2} sat.	144.0 - 146.0			
Ce ^{III}	Ce 3d _{5/2} a	880.6 - 881.0	18.2	≤ 4	Purple
	Ce 3d _{5/2} b	884.9 - 885.7	18.2	≤ 4	Pink
Ce ^{IV}	Ce 3d _{5/2} a	882.4 - 883.0	18.6	≤ 3.5	Yellow
	Ce 3d _{5/2} b	888.2 - 888.8	18.6	≤ 5.5	Red
	Ce 3d _{5/2} c	898.0 - 898.8	18.6	≤ 3.5	Orange

Table 11: Fitting parameters used in CasaXPS. Under the column “B.E.” is indicated the constraint applied to the peak position.

ES.2.3. Extended X-ray absorption fine structure (EXAFS)

EXAFS at Gd and Ce L_{III}-edge was performed on the SAMBA beamline at the SOLEIL synchrotron facility. For solids, the nanoparticles were diluted in graphite and compressed to 6 mm diameter pellets similarly to XANES (see the XANES section and Figure 129A). For liquids, the colloidal solutions were injected with a syringe in a cell delimited by two kapton windows (Figure 129B).

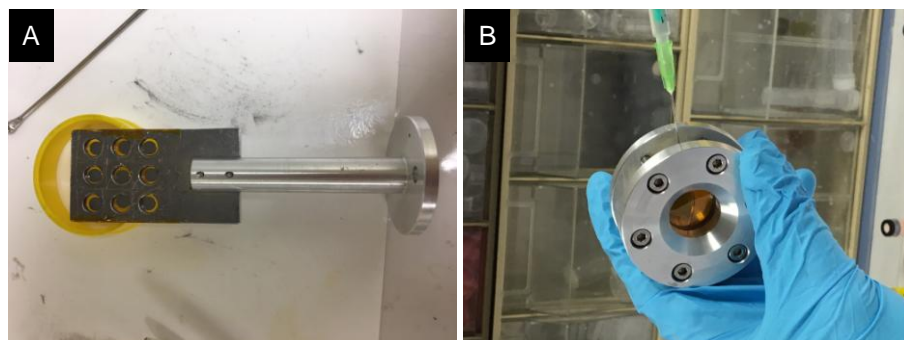


Figure 129: (A) Pellets of graphite and (Gd,Ce)₂O₂S nanoparticles fixed on the SAMBA sample holder. (B) Liquid cell with injection of a colloidal solution sampled during the synthesis of Gd₂O₂S nanoplates.

ES.3. Other characterization techniques

ES.3.1. X-ray diffraction on powder (XRD)

The X-ray diffraction patterns of dry powders were measured on a Bruker D8 diffractometer using Cu K α radiation at 1.5406 Å. Typical diffractograms were collected with steps of 0.05 ° and a scanning speed of 5 s/point. The backgrounds of the patterns were subtracted using the EVA software.

When low-noise Si monocrystals sample holders were used, the angular position 2θ was corrected by adjusting the sample height (correction around 0.5 to 1 mm, see Figure 131). The shift of the diffraction patterns illustrates the height shift h of the sample on the low-noise sample holder ($\Delta 2\theta = \frac{-2h\cos(\theta)}{R}$) where R is the goniometer radius (217.5 mm).



Figure 130: Picture of a Si monocrystal used for XRD. The plastic dome next to it enables analysis under inert atmosphere when the sample is prepared in a glovebox.

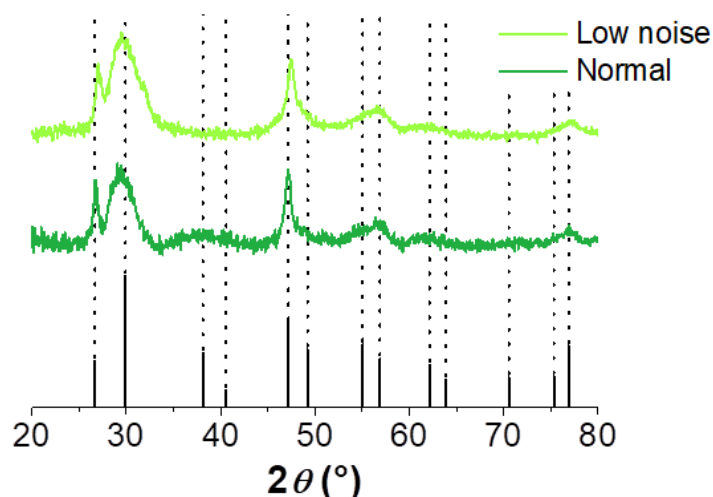


Figure 131: XRD patterns of Gd₂O₂S nanoparticles on normal polymer and low-noise silicium monocrystal sample holders. Black peaks correspond to Gd₂O₂S (JCPDS 26-1422).

A correction of around 0.6 mm is necessary for dry powders to get back to the correct peak positions and was equally applied for all the samples measured on a Si monocrystal for the

measure of the lattice parameter a via the (110) fit (Figure 4). The vertical dotted lines are a guide to the eye.

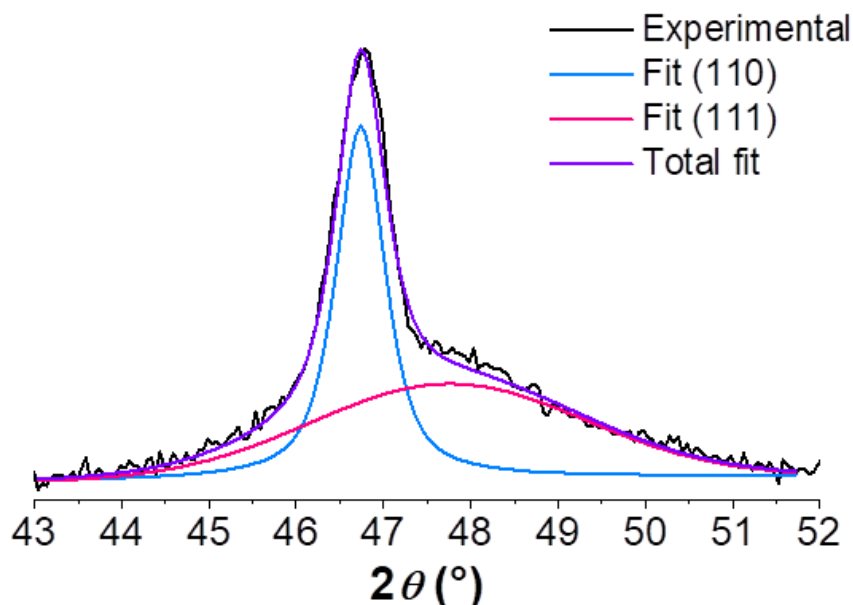


Figure 132: Experimental XRD pattern of $\text{Gd}_{0.6}\text{Ce}_{1.4}\text{O}_2\text{S}$ ($y = 70\%$) nanoparticles (black line) and corresponding fit (purple line) using two Pseudo-Voigt functions for the (110) and (111) diffraction peaks (blue line and pink line respectively).

To fit the (110) and the (111) peaks of $(\text{Gd,Ce})_2\text{O}_2\text{S}$ nanoparticles, two Pseudo-Voigt functions were used (Figure 132). The fit gave access to the crystallite size using the full width half maximum of the (110) peak here. Scherrer's equation is defined as follows:

$\tau = \frac{K\lambda}{\beta \cos(\theta)}$ where τ is the crystal domain size, K a shape factor (chosen as equal to 0.9), λ the incident wavelength (1.5406 Å), β the full width at half maximum of the peak (rad) and θ its angular position (rad).

ES.3.2. Transmission electron microscopy (TEM) and high resolution TEM (HRTEM)

A drop of a diluted solution of $\text{Gd}_{2(1-y)}\text{Ce}_{2y}\text{O}_2\text{S}$ dispersed in pure THF was allowed to dry on an amorphous carbon-coated copper grid. TEM images were collected with a TWIN 120 (TECNAI SPIRIT) at 120 kV and with a JEOL 100CF. HRTEM was performed on a FEG-TEM JEOL 2100F at 200 kV. For $\text{Ce}_2\text{O}_2\text{S}$, a drop of a diluted dispersion of the crude nanoparticles in THF was deposited on a copper grid inside the glovebox. The grid was stored under argon and swiftly inserted into the transmission electron microscope.

ES.3.3. Scanning electron microscopy (SEM) and energy dispersive X-ray spectroscopy (EDS)

A small amount of powder was deposited on a carbon adhesive tape on a scanning electron microscope sample holder. A layer of carbon was deposited on the samples for electronic conductivity. EDS analyses were performed on a SEM HITACHI S-3400N at 10 kV. Titanium was chosen as reference and analyses were performed on three to five different zones on each sample. The same device was used to take images of the deposited samples.

ES.3.4. UV-visible diffuse reflectance

Dry powders were loaded in the circular sample holder to make a uniform layer of solid. The UV-visible diffuse reflectance spectra were measured using an integration sphere of a Cary-WinUV 5000 spectrophotometer (AGILENT) between 250 nm and 800 nm at 1 nm.s^{-1} and corrected with a sample of BaSO_4 as reference. The $F(R)$ spectra were deducted using the formula $F(R) = \frac{(1-R)^2}{2R}$, where R is the reflectance. Depending on the bandgap (direct or indirect), linear zones could be extrapolated to 0 on the abscissa axis for the Tauc curve $(F(R)h\nu)^n = f(h\nu)$ where $n = 2$ for a direct bandgap and $n = \frac{1}{2}$ for an indirect bandgap.

ES.3.5. Fourier transform infrared spectroscopy (FTIR)

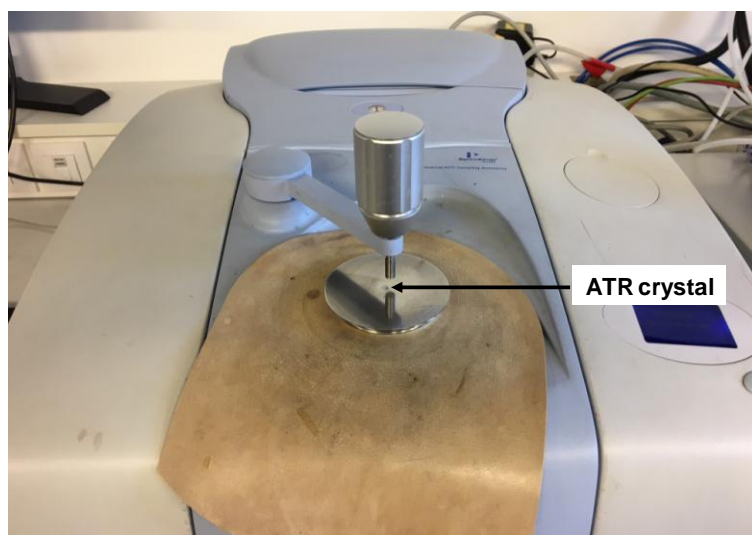


Figure 133: Picture of the FTIR device.

Infrared spectra were collected on a Spectrum 400 (PERKINELMER) spectrometer. The dry sample (1 to 3 mg) was deposited on the attenuated total reflectance (ATR) crystal (Figure 133). Transmittance was measured between 4000 cm^{-1} and 550 cm^{-1} with steps of 0.5 cm^{-1} .

ES.3.6. Pair distribution function analysis (PDF)

The reduced atomic PDF, $G(r)$, gives, from a structural model, the probability of finding a pair of atoms at a distance of r as follows:

$$G(r) = 4\pi[\rho(r) - \rho_0]$$

where $\rho(r)$ is the atomic pair-density and ρ_0 is the average atomic number density. As defined, peaks in the $G(r)$ function correspond to specific distances separating a pair of atoms.

$G(r)$ can also be extracted from an experimental XRD pattern. Indeed, $G(r)$ is the Fourier transform of the total structure function $S(Q)$:

$$G(r) = \left(\frac{2}{\pi}\right) \cdot \int_{Q=0}^{\infty} Q \cdot [S(Q) - 1] \cdot \sin(Qr) dQ$$

where Q is the magnitude of the scattering vector ($Q = 4\pi \sin(\theta) / \lambda$), 2θ being the angle between the incoming and outgoing X-ray, λ is the X-ray wavelength, and $S(Q)$ is the total scattering structure function which is the corrected and normalized experimental intensity.

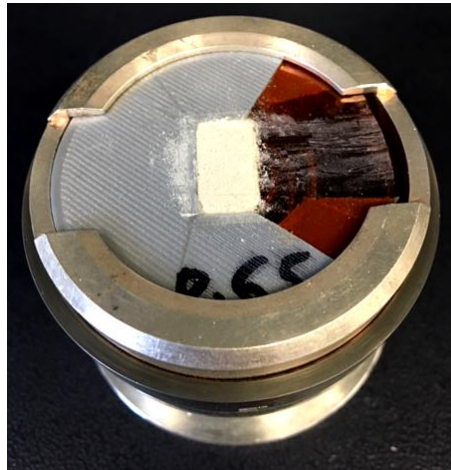


Figure 134: Homemade sample holder developed by Capucine Sassoie, Mohamed Selmane and Thomas Kress (LCMCP) used for the diffraction measurement (PDF) analysis with $\text{Gd}_2\text{O}_2\text{S}$ nanoparticles.

The experimental data were recorded from a standard laboratory D8 advance diffractometer equipped with a Mo anode ($\lambda_{\text{K}\alpha} = 0.7107 \text{ \AA}$), in the reflection mode, using a homemade sample holder designed to minimize its own signal (Figure 134). The large amount (100 mg) of analyzed powder allowed to process the signal with no further treatment such as sample holder background subtraction. Three patterns were recorded with increasing step time (step size = 0.05° , 2θ range; step time: 8 - 50° ; 25 s, $50 - 90^\circ$; 50 s, $90 - 150^\circ$; 100 s), converted in

count per second and merged to obtain the full XRD pattern. The XRD data were then processed using the program PDFGetX3, from $Q = 1.8$ to 15 \AA^{-1} to obtain $G(r)_{exp}$.⁷

On the other hand, the PDF data were modeled from the $\text{Gd}_2\text{O}_2\text{S}$ structure (PDF 04-008-6593) and compared with the experimental one using PDFGUI.⁸ Calculations in real space were performed for r from 1 to 20 \AA , way below the width of the hexagonal crystalline nanoplates, to reduce the effect of anisotropy. A mean size particle factor of 25 \AA was introduced for best attenuation in the high r region.^{9,10}

Real space calculated PDF were here compared without any further structure refinement (neither cell parameters nor atomic positions – thermal agitation were only adjusted to 0.01), given the complexity of correctly evaluating PDF from finite anisotropic nanoparticles.

ES.3.7. Thermogravimetric analysis coupled with mass spectrometry (TGA-MS)

TGA-MS was performed at the *Institute of Electronics, Microelectronics and Nanotechnology* (IEMN) in Lille by Djamila Hourlier. Thermogravimetry analysis (TGA) (Netzsch STA449F3 Jupiter apparatus) coupled with a quadrupole mass spectrometry (MS) (Aëolos QMS403D, 70 eV, electron ionisation) *via* a heated capillary system was applied to monitor the decomposition of materials during the annealing process and to determine the evolved gaseous species (Figure 135).



Figure 135: Picture of the TGA-MS apparatus.

Before each experiment, the TGA system was first evacuated and then flushed with the same ultrahigh purity gas which was used for the thermal treatment. The experiments were carried out under dynamic inert or reactive gas: He (99.999 % purity), 20 % O_2 in He (99.999 %

purity) or 3 % H₂ in Ar (99.999 % purity) at a flow rate of 50 cm³/min. The samples were heated in Al₂O₃ crucibles up to 900 °C or 1200 °C with a heating rate varying between 2 °C/min and 15 °C/min.

ES.3.8. Small angle X-ray scattering (SAXS) and wide angle X-ray scattering (WAXS)

The SAXS-WAXS experiments were directed by David Carrière at the *Center of Atomic Energy* (CEA). For the SAXS-WAXS experiments, the reaction medium was sampled at different temperatures. The reaction was never interrupted to prevent modifications of the reaction time. To take an aliquot, the flow of inert gas was turned off and the sample was swiftly taken off by a Pasteur pipette. The total sampled amount did not exceed half of the reaction medium (around 0.4 mL / sample, total volume of 16 mL) to maintain the same reaction dynamics in the flask. The hot sample is immediately cooled down by a water bath at ambient temperature under a quasi inert atmosphere. Because of the small volume of the sample, only a few seconds are necessary to cool the sample down to temperatures close to room temperature. The sample was then placed in the capillary, which was hermetically sealed because the analysis chamber is under vacuum (Figure 136B).

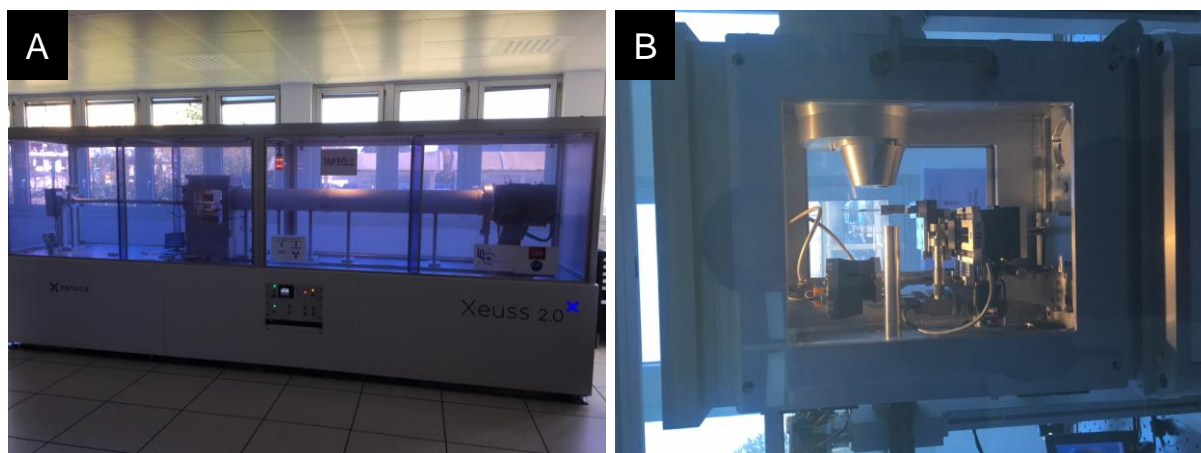


Figure 136: Picture of the SWAXS apparatus (A) with zoom on the sample chamber (B).

Small- and wide-angle X-ray scattering (SAXS/WAXS) measurements were performed with a commercial setup (Xeuss 2.0, Xenocs) at a wavelength of $\lambda = 1.54 \text{ \AA}$ using two complementary sample-to-detector distances to span wavevector ranges of $2.7 \times 10^{-3} \text{ \AA}^{-1} \leq q \leq 2.6 \times 10^{-3} \text{ \AA}^{-1}$ (SAXS) and $9.6 \times 10^{-2} \text{ \AA}^{-1} \leq q \leq 1.75 \text{ \AA}^{-1}$ (WAXS).

The sample-detector distance was calibrated with tetradecanol. The detector count was normalized to differential cross-sections per volume with Lupolen as a secondary reference ($I_{\text{max}} = 6 \text{ cm}^{-1}$), and with a photon count across the sample as a monitor of the direct beam.

Samples were contained in sealed glass capillaries with a 1.2 mm optical path, as determined by the scattering intensity of water ($1.6 \times 10^{-2} \text{ cm}^{-1}$), and measured under vacuum.

ES.3.9. Vibrating sample magnetometry (VSM)

The magnetization of the nanoparticles was measured between 5 K and 350 K by vibrating sample magnetometry using a Physical Property Measurement System (PPMS) from Quantum Design at the *Physical Measurements at Low Temperature* platform (MPBT) on the *Campus Pierre et Marie Curie* of *Sorbonne Université* with the help of Yannick Klein (IMPMC). Around 10 mg of the desired sample were placed into a sample holder vibrating at 40 Hz inside the magnetometer chamber thanks to a linear motor. Zero-field cooling (ZFC) and field cooling (FC) curves were obtained at 50 Oe for most of the samples (2500 Oe for $\text{Gd}_{0.2}\text{Ce}_{1.8}\text{O}_2\text{S}$ nanoparticles).

The molar susceptibility is deduced from the measured magnetization in emu using Equation 5. Its value is given for one mol of gadolinium (factor 2 in Equation 5).

$$\chi_{molGd} = \frac{M}{H} \frac{M_m(\text{Gd}_2\text{O}_2\text{S})}{2m}$$

M	Magnetization (emu)
H	Magnetic Field (Oe)
M_m	Molar mass (g.mol ⁻¹)
m	Sample mass (g)

Equation 5: Expression of the molar susceptibility of the sample normalized for one mole of gadolinium.

The Curie constant was obtained using a fitting with the generalized Curie law (Chapter IV). Its value (and the effective moment deduced from it) can be then corrected by the ligands amount. Otherwise, the susceptibility can directly be corrected (Equation 6).

$$\chi_{molGd,corr} = \frac{M}{H} \frac{M_m(Gd_2O_2S)}{2(m - m_{lig})}$$

M	Magnetization (emu)
H	Magnetic Field (Oe)
M_m	Molar mass (g.mol ⁻¹)
m	Sample mass (g)

Equation 6: Expression of the molar susceptibility normalized for one mol of gadolinium and corrected by the ligands mass m_{lig} .

ES.3.10. Superconductive quantum interference device magnetometry (SQUID)

The magnetization of the nanoparticles was measured between 2 K and 110 K with a SQUID using a Magnetic Property Measurement System (MPMS-XL) from Quantum Design at the MPBT platform with the help of David Hrabovsky (IMPMC) and Yanling Li (IPCM). Around 45 mg of the sample were placed into a sample holder in polycarbonate. Zero-field cooling (ZFC) and field cooling (FC) curves were obtained at 50 Oe for the Gd_2O_2S samples, giving the magnetic moment (emu). The molar susceptibility was obtained for the bulk phase using Equation 5. For the nanoparticles, the molar susceptibility was directly corrected as given in Equation 6.

ES.4. Density functional theory calculations (DFT)

The DFT calculations were performed by Lorenzo Paulatto (IMPMC). In the *ab-initio* simulation of rare-earth oxysulfides, we had one main difficulty to tackle: how to treat the very localized, but not completely chemically inert, *f* orbitals of the rare earth. The *4f* orbital contains 1 electron in the conventional isolated-atom structure of cerium, 7 electrons in gadolinium. The *4f* orbitals are localized inside a sphere of around 1 Å, centered on the atomic nucleus, but it is only partially filled and its binding energy is comparable with that of the chemically more active *5d* and *6s* orbitals. Even if these orbitals participate little in chemical bonds, their inclusion in the description of the valence structure is important to have an accurate band structure, especially in the lower energy valence bands.

The very strong self-interaction error, makes a simple DFT calculation impossible, to compensate the error, we have used the DFT+U technique.^{11,12} All calculations were done with the Quantum-ESPRESSO code^{13,14} using the PBE generalized gradient approximation.¹⁵

We used ultrasoft pseudopotentials with valence-bound $4f$ orbitals from the pslibrary.¹⁶ These pseudopotentials trade an excellent transferability with an extremely high plane-wave cutoff of 200 Ry.

We computed the correction U from finite-difference linear-response in a $2 \times 2 \times 2$ supercell of 40 atoms (extrapolated to $8 \times 8 \times 8$), which we found to give a value of the U parameter virtually identical to a $2 \times 2 \times 1$ supercell, and only a fraction of one eV higher than the value from unit cell calculation. The value we used are: 1.27 eV for Gd and 6.85 eV for Ce. The latter is not very different from literature values used for cerium oxides.¹⁷ We computed electronic structure of the bulk geometry using a grid of $4 \times 4 \times 2$ electronic k -points for the bulk materials, or $4 \times 4 \times 1$ in the slab geometry. For $\text{Ce}_2\text{O}_2\text{S}$, the relaxed crystal cell volume is a few percent (3 % Ce compound, 4 % Gd compound) larger than data available literature.¹⁸ This is expected as, contrary to literature, the $4f$ electron can in our simulation case contribute to the chemical bonds. We have summarized the relaxed geometry parameters in Table 12.

	Cell parameter		Internal parameters		Absolute magnetization (μ_B)
	a (Å)	c/a	Metal	O	
Gd₂O₂S	3.876	1.725	0.281	0.371	14.16
Ce₂O₂S	4.055	1.722	0.274	0.369	2.11

Table 12: Relaxed geometry parameters obtained for $\text{Gd}_2\text{O}_2\text{S}$ and $\text{Ce}_2\text{O}_2\text{S}$.

When simulating the 3-layer slab geometry, the relaxed structure does not reconstruct significantly from the bulk one as we observe a modest contraction of about 2 % of the superficial inter-layer distance. The dangling bonds of the exposed surface oxide cause the surface to become metallic; this effect is neutralized in reality by the presence of surface ligands. We found that adding hydrogen terminators on the surface can neutralize it with minimal changes to the structural properties; alternatively the system can be treated as metallic. In the latter case the Fermi energy will move over the gap. For practical reason we consider the excess electronic charge as a doping, and we will still refer to the gap and valence bands as they were identified in the surface-neutralized configuration.

References

- (1) Larquet, C.; Nguyen, A.-M.; Ávila-Gutiérrez, M.; Tinat, L.; Lassalle-Kaiser, B.; Gallet, J.-J.; Bournel, F.; Gauzzi, A.; Sanchez, C.; Carenco, S. Synthesis of Ce₂O₂S and Gd₂(1-y)Ce_{2y}O₂S Nanoparticles and Reactivity from in Situ X-Ray Absorption Spectroscopy and X-Ray Photoelectron Spectroscopy. *Inorg. Chem.* **2017**, *56* (22), 14227–14236.
- (2) For CasaXPS line shapes see http://www.casaxps.com/help_manual/line_shapes.htm.
- (3) Bêche, E.; Charvin, P.; Perarnau, D.; Abanades, S.; Flamant, G. Ce 3d XPS Investigation of Cerium Oxides and Mixed Cerium Oxide (Ce_xTi_yO_z). *Surf. Interface Anal.* **2008**, *40* (3–4), 264–267.
- (4) Uwamino, Y.; Ishizuka, T.; Yamatera, H. X-Ray Photoelectron Spectroscopy of Rare-Earth Compounds. *J. Electron Spectros. Relat. Phenomena* **1984**, *34* (1), 67–78.
- (5) Raiser, D.; Deville, J. P. Study of XPS Photoemission of Some Gadolinium Compounds. *J. Electron Spectros. Relat. Phenomena* **1991**, *57* (1), 91–97.
- (6) Smart, R. S. C.; Skinner, W. M.; Gerson, A. R. XPS of Sulphide Mineral Surfaces: Metal-Deficient, Polysulphides, Defects and Elemental Sulphur. *Surf. Interface Anal.* **1999**, *28* (1), 101–105.
- (7) Juhás, P.; Davis, T.; Farrow, C. L.; Billinge, S. J. L. PDFgetX3: A Rapid and Highly Automatable Program for Processing Powder Diffraction Data into Total Scattering Pair Distribution Functions. *J. Appl. Crystallogr.* **2013**, *46* (2), 560–566.
- (8) Farrow, C. L.; Juhas, P.; Liu, J. W.; Bryndin, D.; Božin, E. S.; Bloch, J.; Proffen, T.; Billinge, S. J. L. PDFfit2 and PDFgui: Computer Programs for Studying Nanostructure in Crystals. *J. Phys. Condens. Matter* **2007**, *19* (33), 335219.
- (9) Farrow, C. L.; Billinge, S. J. L. Relationship between the Atomic Pair Distribution Function and Small-Angle Scattering: Implications for Modeling of Nanoparticles. *Acta Crystallogr. Sect. A Found. Crystallogr.* **2009**, *65* (3), 232–239.
- (10) Gilbert, B. Finite Size Effects on the Real-Space Pair Distribution Function of Nanoparticles. *J. Appl. Crystallogr.* **2008**, *41* (3), 554–562.
- (11) Anisimov, V. I.; Zaanen, J.; Andersen, O. K. Band Theory and Mott Insulators: Hubbard U Instead of Stoner I. *Phys. Rev. B* **1991**, *44* (3), 943–954.
- (12) Cococcioni, M.; de Gironcoli, S. Linear Response Approach to the Calculation of the Effective Interaction Parameters in the LDA+U Method. *Phys. Rev. B* **2005**, *71* (3), 035105.
- (13) Giannozzi, P.; Baroni, S.; Bonini, N.; Calandra, M.; Car, R.; Cavazzoni, C.; Ceresoli, D.; Chiarotti, G. L.; Cococcioni, M.; Dabo, I.; Dal Corso, A.; de Gironcoli, S.; Fabris, S.; Fratesi, G.; Gebauer, R.; Gerstmann, U.; Gougoussis, C.; Kokalj, A.; Lazzeri, M.; Martin-Samos, L.; Marzari, N.; Mauri, F.; Mazzarello, R.; Paolini, S.; Pasquarello, A.; Paulatto, L.; Sbraccia, C.; Scandolo, S.; Sclauzero, G.; Seitsonen, A. P.; Smogunov, A.; Umari, P.; Wentzcovitch, R. M. QUANTUM ESPRESSO: A Modular and Open-Source Software Project for Quantum Simulations of Materials. *J. Phys. Condens. Matter* **2009**, *21* (39), 395502.
- (14) Giannozzi, P.; Andreussi, O.; Brumme, T.; Bunau, O.; Buongiorno Nardelli, M.; Calandra, M.; Car, R.; Cavazzoni, C.; Ceresoli, D.; Cococcioni, M.; Colonna, N.; Carnimeo, I.; Dal Corso, A.; de Gironcoli, S.; Delugas, P.; DiStasio, R. A.; Ferretti, A.; Floris, A.; Fratesi, G.; Fugallo,

- G.; Gebauer, R.; Gerstmann, U.; Giustino, F.; Gorni, T.; Jia, J.; Kawamura, M.; Ko, H.-Y.; Kokalj, A.; Küçükbenli, E.; Lazzeri, M.; Marsili, M.; Marzari, N.; Mauri, F.; Nguyen, N. L.; Nguyen, H.-V.; Otero-de-la-Roza, A.; Paulatto, L.; Poncé, S.; Rocca, D.; Sabatini, R.; Santra, B.; Schlipf, M.; Seitsonen, A. P.; Smogunov, A.; Timrov, I.; Thonhauser, T.; Umari, P.; Vast, N.; Wu, X.; Baroni, S. Advanced Capabilities for Materials Modelling with Quantum ESPRESSO. *J. Phys. Condens. Matter* **2017**, *29* (46), 465901.
- (15) Perdew, J. P.; Burke, K.; Ernzerhof, M. Generalized Gradient Approximation Made Simple [Phys. Rev. Lett. 77, 3865 (1996)]. *Phys. Rev. Lett.* **1997**, *78* (7), 1396–1396.
 - (16) Dal Corso, A. Pseudopotentials Periodic Table: From H to Pu. *Comput. Mater. Sci.* **2014**, *95*, 337–350.
 - (17) Loschen, C.; Carrasco, J.; Neyman, K. M.; Illas, F. Erratum: First-Principles LDA+U and GGA+U Study of Cerium Oxides: Dependence on the Effective U Parameter [Phys. Rev. B 75 , 035115 (2007)]. *Phys. Rev. B* **2011**, *84* (19), 199906.
 - (18) Mikami, M.; Nakamura, S. Electronic Structure of Rare-Earth Sesquioxides and Oxysulfides. *J. Alloys Compd.* **2006**, *408–412*, 687–692.
 - (19) Peng, S.; Wang, C.; Xie, J.; Sun, S. Synthesis and Stabilization of Monodisperse Fe Nanoparticles. *J. Am. Chem. Soc.* **2006**, *128* (33), 10676–10677.
 - (20) Carencio, S.; Boissière, C.; Nicole, L.; Sanchez, C.; Le Floch, P.; Mézailles, N. Controlled Design of Size-Tunable Monodisperse Nickel Nanoparticles. *Chem. Mater.* **2010**, *22* (4), 1340–1349.